

A Dissertation

entitled

**Experimental Investigations and Development of Analytical and Computational
Models for Microcracked Concrete Exposed to Elevated Temperatures**

by

Salim Khoso

Submitted to the Graduate Faculty as partial fulfillment of the requirements for the
Doctor of Philosophy Degree in Civil Engineering

Dr. Luis Alexander Mata, Committee Chair

Dr. Juan Jose Recalde, Committee Member

Dr. Douglas Karl Nims, Committee Member

Dr. Eddie Y. Chou, Committee Member

Dr. Serhan Guner, Committee Member

Dr. Amy Thompson,
Dean College of Graduate Studies

The University of Toledo

December 2021

© Copyright 2021, Salim Khoso

This document is copyrighted material. Under copyright law, no parts of this document may be reproduced without the expressed permission of the author.

An Abstract of

Experimental Investigations and Development of Analytical and Computational Models
for Microcracked Concrete Exposed to Elevated Temperatures

by

Salim Khoso

Submitted to the Graduate Faculty as partial fulfillment of the
Requirements for the Doctor of Philosophy Degree in Civil Engineering

The University of Toledo
December 2021

Assessment of the structural condition of damaged infrastructure and evaluation of new sustainably enhanced concrete materials require better understanding of how these materials will respond and behave under the application of various loads and elevated temperature exposures. Elevated temperatures are one of the factors causing damage to concrete at the level of microcracking, and the presence of microcracks in damaged concrete is fundamentally associated with a change in mechanical properties and an increase in fluid permeability. Current techniques to quantify the degree of microcracking non- or semi-destructively are limited, and microscopic analysis may be expensive and time-consuming for most evaluation applications. Hence, it becomes necessary to develop a technique with the capability to deliver quick, low-cost assessment of the engineering properties of materials for the purposes of asset management and decision making. Phase I of this research consisted of an experimental investigation to estimate changes in crack density parameter of concrete disks prior to and after temperature exposure of 300 °C, based on estimates of dynamic Young's modulus of elasticity from wet and dry conditions. Crack density parameter (ϵ) was estimated using a model for an elastic solid

with thin ellipsoidal cracks developed by O'Connell & Budiansky (1974) (O&B). Four sustainable concrete mixtures were investigated during this research study with a combination of two water-to-binder ratios of 0.4 and 0.5, and two fly ash cementitious replacement ratios of 40%, and 60%, which were compared to two control mixture with normal strength and high strength of conventional concrete with zero percent fly ash replacement. The experimental results showed significant improvement in the compressive strength for mixtures with fly ash content when compared with the traditional cement concrete. In the case of normal strength concrete (NSC), the compressive strength increased from 26.6 MPa to 30.1 MPa for concrete with 40% fly ash and 50.1 MPa for concrete with 60% fly ash. Whereas, in the case of high-strength concrete (HSC), the compressive strength increased significantly from 27.1 MPa to 32.5 MPa for mixture with 40% fly ash and 42.9 MPa for mixture with 60% fly ash. These results show that concrete with a higher percentage of fly ash content up to 60% could be used for structures exposed to a high temperature of about 300 °C. In Phase II, different cracked media models were analyzed to determine their applicability to estimate crack density parameter. The model by Hudson (1981) was applicable at low crack density parameters between 0 and 0.2, after which the second order correction predicted an increase in Young's modulus, which was not observed experimentally. Cheng's (1993) using Padé approximation applied to Hudson's model was not applicable to concrete because it showed minimal difference between the Young's modulus values for dry and soaked condition, whereas this difference was higher for experimental results. Finally, Hudson's model using only the first order correction was applicable to concrete, for which values of ϵ were obtainable. The ϵ obtained using Hudson's first order model yielded higher values than those predicted by the O&B

model. The mean ε for Normal strength and High strength mixtures using Hudson's model were 0.343 and 0.180 respectively whereas, for O&B model the mean ε obtained were 0.221 and 0.131 for Normal and High strength mixtures respectively. The extended (Recalde 2009) analytical technique showed that the crack density parameter and dynamic Young's modulus could easily be obtained using an iterative procedure. The results of the analysis suggest that the proposed method can be applied to quantify the elastic properties and crack density parameter of traditional and high SCM replacement mixtures, providing important understandings of the microstructural changes occurring in concrete due to high temperature exposures. In Phase III of this research, a finite element model (FEM) was developed using representative volume elements (RVE) of a solid with thin circular cracks. The elastic properties at crack density parameters ranging between 0.1 and 1.0 with randomly distributed cracks were evaluated for dry and water-saturated conditions. The FEM results when plotted showed similar trend in the decrease of Young's modulus with increase in ε values which was consistent with the experimental results up to the ε equal to 0.2 when compared to O&B model for soaked crack condition. The experimental investigations and the extension of analytical techniques from geophysics to concrete material supported by numerical modeling in this dissertation pave a way to determine a value for crack density parameter using non-destructive evaluation of wet and dry Young's modulus of elasticity of relatively thin concrete discs and the obtained results imply that these analytical techniques can be useful in providing important insight into the microstructural changes occurring in concrete due to various temperature exposures.

I dedicate my dissertation to God Almighty my creator who has been the source of inspiration and my strength throughout the period of my doctoral degree. Secondly, I dedicate this work to my parents who always supported and encouraged me and created ways for me to pursue higher studies with the power of prayers and shaping me for what I am today. To my wife Farzana and daughters Farah and Fareeha who sacrificed a lot for being away from me and waiting for my arrival back home for many years, and to my brothers and sisters for their love and patience. My love for you all can never be quantified.

I finally dedicate this dissertation to my cousin/friend Anina Fida who visited me thrice during my doctoral journey and kept on supporting me to accomplish my goal. Her unconditional love and her encouraging words to make impossible things to be possible will always remain in my mind. Anina, I cannot forget your continual and genuine reminder that the best is yet to come when I was going through tough times. Your positive attitude to bringing smiles to my lips during the unprecedented moments is something which I cannot forget. Thank you for being there and unveiling the beauty of life for me, and for your presence during the times when I needed a shoulder as a support especially during my doctoral journey. You surely have a big part in my life and in the endeavors which I have achieved so far.

Acknowledgements

I am very grateful to my supervisors, Dr. Luis A. Mata and Dr. Juan Jose Recalde, for their supervision and continuous support during my PhD journey. Their immense knowledge and experience have kept on encouraged me during my research work. I am also thankful to thank Dr. Douglas K. Nims, Dr. Serhan Guner, Dr. Eddie Y. Chou and all professors at UT for equipping me with knowledge and extensive professional guidance.

There were always great people during my Ph.D. journey among which I would give my sincere gratitude to my friend Asal Soltani for always being there. Her genuine support and dedications in expediting my PhD is unmatched and her part in my doctoral journey has been engraved in my mind and will stay there forever. I am also thankful to my friend Janet Raad for her continual support and help during research work. She would never say No to whatever I asked her, and was always ready to step forward and help me no matter what circumstances she was in. And I can never forget people in my life whom I learned from, which include Rafael Salgado, Shank Kulkarni, Ahmed H. Abdulgawad, Peter Rocco, Dr. Hussam Aldaussari, Dr. Mohammad T. Naqash, Tariq Rahim Rahimi, Yazan Sami, Mehdi Khoso, Shahid Channa, Fida Jatoi, Alina, Faryal, Fatima and Yousaf Sultan just to name a few that I cannot thank them as words fell short.

At the end, I would like to thank Fulbright for giving me this life-changing opportunity at UT. It was indeed a prestigious and unforgettable experience in my life.

Table of Contents

Table of Contents	viii
List of Tables	xvi
List of Figures	xxv
List of Abbreviations	xxxiv
List of Symbols	xxxvi
1.1 Background	1
1.2 Changes in Microstructure of Concrete	5
1.3 Problem Statement	7
1.4 Research Significance	8
Chapter Two.....	11
2.1 Background	11
2.1.1 Assessment of Damaged Concrete Condition	11
2.2 Analytical Procedure to Estimate Crack Density Parameter of Concrete.....	14

2.3 Microcracking and its effects on Concrete.....	15
2.4 Structural Fire and Temperatures Reached	18
2.5 Effect of Elevated Temperature on Concrete Properties.....	20
2.6 Micromechanical Modeling of Concrete.....	23
2.7 Finite Element Modeling of Concrete.....	24
2.8 The Representative Volume Element (RVE).....	25
Chapter Three.....	28
3.1 Overview of the Testing Program	28
3.2 Experimental Plan.....	29
3.3 Experimental Materials.....	30
3.3.1 Supplementary Cementitious Material	30
3.3.2 Type of Cement	31
3.3.3 Coarse and Fine Aggregate.....	31
3.3.4 Air Entraining Admixture.....	31

3.4	Experimental Methodology	33
3.5	Specimens Curing and Sample Preparation.....	34
3.6	Experimental Tests for Freshly Mixed Concrete	37
3.7	Mechanical Properties of Concrete	38
3.7.1	Compressive Strength Test.....	38
3.7.2	Modulus of Elasticity of Concrete	38
3.7.3	Microstructural Damage to Concrete Specimens	39
3.8	Testing Matrix for Concrete Discs	40
3.9	Resonant Characteristics of Concrete Discs.....	41
3.10	Determining Dynamic Young's Modulus of Elasticity.....	43
3.11	Air Permeability Index	46
3.12	Rate of Absorption of Water	48
3.12.1	Conditioning of specimens	48
	Chapter Four	51

4.1 Introduction	51
4.2 Compressive Strength Test Results	52
4.3 Modulus of Elasticity of Concrete	52
4.4 Signal Characteristics of Concrete Discs	54
4.5 Calculating Dynamic Young's Modulus of Elasticity	57
4.6 Changes in Fluid Penetrability Properties	58
4.7 Relationship between the Measured Properties	62
4.8 Statistical Analysis Results	65
4.8.1 Effect of Fly Ash on Air Permeability Index (API)	65
4.9 Summary	66
Chapter Five	69
5.1 Introduction	69
5.2 Problem Setting	70
5.3 Identification of analytical Model	72

5.3.1	Areas Explored	72
5.3.2	Selection of Analytical Model.....	74
5.4	Extension of Hudson’s (1981) Model to Concrete Material	85
5.5	Numerical Example on Hudson’s Model.....	90
5.5.1	Hudson’s Model with First Order Correction Only.....	91
5.5.2	Hudson’s Model with First and Second Order Corrections	93
5.5.3	Proposed Padé Approximation for Second Order by Cheng (1993)	94
5.6	Validating Hudson’s Extended Model with Cheng (1973) Model	96
5.7	Determination of CDP and Young’s Modulus using Hudson Extended Model	99
5.8	Comparing Hudson’s Extended Model Results with O’Connell and Budiansky Model	107
5.9	Difference in Elastic Modulus due to Temperature Exposure	129
5.10	Statistical Analysis Results	131
5.10.1	Effect of Elevated Temperature on the Dynamic Shear Modulus.....	131
5.10.2	Effect of Elevated Temperature on Crack Density Parameter	131

5.10.3 Relationship between the Decrease in G_d and increase of CDP for Damaged Specimens.....	132
5.11 Summary	133
Chapter Six.....	137
6.1 Introduction.....	137
6.1.1 Finite Element Modeling Approach in Abaqus Program.....	137
6.1.2 Material Elastic Properties.....	138
6.1.3 RVE Geometry and Material Properties.....	139
6.1.4 Modelling of Cracks	141
6.2 Python Scripting in Abaqus Software	142
6.2.1 Mesh Sensitivity Analysis in Abaqus.....	143
6.3 Analysis for Different Concrete Conditions.....	144
6.4 Generation of RVE.....	146
6.5 Homogenization of RVE.....	155
6.6 Abaqus EasyPBC Plugin.....	158

6.7 RVEs with one to eight cracks both in dry and soaked conditions	163
6.7.1 RVEs with Dry Permeated Cracks	163
6.7.2 RVEs with Wet Permeated Cracks	165
6.8 Numerical Analysis Results and Discussion	167
6.8.1 Case with Twenty-Four Cracks in RVE	167
6.8.3 Case with Eight Cracks in RVE	171
6.9 Comparing Numerical Analysis Results with Developed Analytical Models	179
6.10 Summary	186
Chapter Seven	190
7.1 Conclusions	190
7.1.1 Experimental Investigation (Phase I) Conclusions	190
7.1.2 Extension of Hudson’s model (Phase II)	192
7.1.3 Finite Element Modeling	195
7.2 Future Recommendations	197

References:.....	199
ACI 318-08 Building Code Requirements for Structural Concrete and Commentary ...	199
Appendix-A: Experimentally Obtained Air Permeability Index (API) Results	216
Appendix-B: Statistical Analysis Results	219
Appendix-C: Results for Crack Density Parameter and Young’s Modulus obtained using Hudson’s Extended Model and O’Connell and Budiansky Model.....	224
Appendix-D: Detail of RVEs with Number of Cracks and their Co-ordinates using ABAQUS Computer Program	234
Appendix-E: Detail of Elastic Properties of Different RVEs	237

List of Tables

3.1: Detail of mixture proportions	31
3.2: Characteristics of Traditional Concrete Mixtures.....	32
3.3: Characteristics of Sustainable Concrete Mixtures	32
3.4: Damage conditions and labeling of specimens.....	36
3.5: Damage Mechanism for Different Concrete Mixtures	39
3.6: Different conditions to measure dynamic shear modulus of discs.	41
4.1: Compressive strength test results.....	52
4.2: Modulus of Elasticity values for different concrete mixtures.....	53
4.3: Mean Resonant Frequency of concrete discs of one and two-inches damaged at high temperature exposure	56
4.4: Dynamic Young's Modulus of Elasticity of one and two-inches Concrete Discs for Different Moisture Conditioning and at High Temperature Exposure	57
4.5: Water absorbed in different time intervals	59

4.6: Air Permeability Index and Rates of Absorption of Water for Concrete Disc specimens from Four Mixture Groups for moisture conditioning before and after damage at High Temperature Exposure of 300 °C for Two different Thicknesses.	60
4.7: Means of Air Permeability Index for Undamaged and Damaged Disc Specimens...	65
4.8: Air Permeability Index for Different Concrete Mixture Groups before and after damage at 300 °C	66
5.1: The background moduli, 1 st and 2 nd order corrections used in Hudson Model	82
5.2: Comparison between Hudson’s Model for Rock Mechanics and Concrete Material	89
5.3: Input values for Numerical example.....	91
5.4: Results for (ϵ) and Young’s modulus for Control Normal and High Strength Undamaged Specimens using Hudson and O’Connell & Budiansky Models....	108
5.5: Results for (ϵ) and Young’s modulus for Mixtures with 40% and 60% fly ash damaged at 300 °C using Hudson’s Model.....	109
5.6: Results for (ϵ) and Young’s modulus for Mixtures with 40% and 60% fly ash damaged at 300 °C using O’Connell and Budiansky Model	110

5.7: Difference in percentage shown using two models for one and two-inch thick disc	113
5.8: Percentage difference in mean Young’s modulus for one-inch-thick disc	114
5.9: Hudson Model for one-inch.....	115
5.10: O’Connell and Budiansky Model for one-inch.....	115
5.11: Comparison of the Two Model Results	117
5.12: Hudson Model for two-inch.....	118
5.13: O’Connell and Budiansky Model for two-inch	119
5.14: O’Connell and Budiansky Model for two-inch	119
5.15: Mean values for change in ϵ and G_d values for different concrete Mixtures.....	132
6.1: Concrete Material Properties	141
6.2: Comparison of obtained results using three different mesh sizes.....	144
6.3: Details for crack radius and number of cracks in $200 \times 200 \times 200$ micron ³ RVE.....	148
6.4: Comparing dry (blue) and soaked (orange) results between one and Eight RVEs..	152
6.5: Young’s Modulus results Obtained Numerically with 24 cracks RVE	168

6.6: Young’s Modulus results Obtained Numerically with 16 cracks RVE	170
5.7: Young’s Modulus results Obtained Numerically with 8 cracks RVE	172
6.8: Young’s Modulus results obtained Numerically with 8 cracks RVE for both soaked and dry crack conditions	182
6.9: Normalized Young’s Modulus Results obtained Numerically with 8 cracks RVE for both soaked and dry crack conditions	184
C1: Results of CDP and Young’s modulus for Control Normal and High Strength Concrete using Hudson’s Model for two points.....	225
C2: Results of CDP and Young’s modulus for Normal and High Strength Concrete using Hudson’s Model for two points	226
C3: Results of CDP and Young’s modulus for Control specimens using Hudson’s Model for two points	227
C4: Results of CDP and Young’s modulus for damaged specimens using Hudson’s Model for five points	228
C5: Results of CDP and Young’s modulus for Control, Normal and High Strength Concrete using O’Connell and Budiansky Model for two points	229

C6: Results of CDP and Young’s modulus for damaged specimens using O’Connell and Budiansky Model for five points	230
C7: Results of CDP and Young’s modulus for damaged specimens using O’Connell and Budiansky Model for five points	231
C8: Results of CDP and Young’s modulus using O’Connell and Budiansky’s Model for two points.....	232
C9: Results of CDP and Young’s modulus for Control specimens using O’Connell and Budiansky’s Model for two points.....	233
E1: Elastic properties for single vertical crack RVE obtained using EasyPBC plugin in Abaqus for dry crack condition.....	238
E2: Elastic properties for single vertical crack RVE obtained using EasyPBC plugin in Abaqus for soaked crack condition.....	239
E3: Shear modulus results for single vertical crack RVE obtained using EasyPBC plugin in Abaqus for dry crack condition.	239
E4: Shear modulus results for single vertical crack RVE obtained using EasyPBC plugin in Abaqus for dry crack condition.	239

E5: Elastic properties for single horizontal crack RVE obtained using EasyPBC plugin in Abaqus for dry crack condition.....	240
E6: Elastic properties for single horizontal crack RVE obtained using EasyPBC plugin in Abaqus for saturated crack condition.	240
E7: Shear modulus results for single horizontal crack RVE obtained using EasyPBC plugin in Abaqus for dry crack condition.	241
E8: Shear modulus results for single horizontal crack RVE obtained using EasyPBC plugin in Abaqus for saturated crack condition.	241
E9: Elastic properties for single horizontal crack RVE obtained using EasyPBC plugin in Abaqus for dry crack condition.....	242
E10: Elastic properties for single horizontal crack RVE obtained using EasyPBC plugin in Abaqus for saturated crack condition.	242
E11: Shear modulus results for single inclined 45-degree crack RVE obtained using EasyPBC plugin in Abaqus for dry crack condition.....	243
E12: Shear modulus results for single inclined 45-degree crack RVE obtained using EasyPBC plugin in Abaqus for saturated crack condition.....	243

E13: Elastic properties for eight vertical crack RVE obtained using EasyPBC plugin in Abaqus for dry crack condition.....	244
E14: Elastic properties for eight vertical crack RVE obtained using EasyPBC plugin in Abaqus for saturated crack condition.	244
E15: Shear modulus results for eight vertical cracks RVE obtained using EasyPBC plugin in Abaqus for dry crack condition.	245
E16: Shear modulus results for eight vertical cracks RVE obtained using EasyPBC plugin in Abaqus for saturated crack condition.	245
E17: Elastic properties for eight horizontal crack RVE obtained using EasyPBC plugin in Abaqus for dry crack condition.....	246
E18: Elastic properties for eight horizontal crack RVE obtained using EasyPBC plugin in Abaqus for saturated crack condition.	246
E19: Shear modulus results for eight horizontal cracks RVE obtained using EasyPBC plugin in Abaqus for dry crack condition.	247
E20: Shear modulus results for eight horizontal cracks RVE obtained using EasyPBC plugin in Abaqus for saturated crack condition.	247

E21: Elastic properties for eight inclined 45-degree cracks RVE obtained using EasyPBC plugin in Abaqus for dry crack condition.	248
E21: Elastic properties for eight inclined 45-degree cracks RVE obtained using EasyPBC plugin in Abaqus for saturated crack condition.	248
E22: Shear modulus results for eight inclined 45-degree cracks RVE obtained using EasyPBC plugin in Abaqus for dry crack condition.	249
E23: Shear modulus results for eight inclined 45-degree cracks RVE obtained using EasyPBC plugin in Abaqus for saturated crack condition.	249
E24: Elastic properties for different RVEs using EasyPBC plugin.	251
E25: Shear modulus results for RVEs with increasing order of cracks obtained using EasyPBC plugin in Abaqus for dry crack condition.	252
E26: Elastic properties for different RVEs using EasyPBC plugin.	254
E27: Shear modulus results for RVEs with increasing order of cracks obtained using EasyPBC plugin in Abaqus for saturated crack condition.	255
E28: Elastic properties for RVEs with 24 randomly oriented cracks	257
E29: Shear modulus results for RVEs with 24 randomly oriented cracks obtained using EasyPBC plugin in Abaqus for dry crack condition.	258

E30: Elastic properties for RVEs with 24 randomly oriented cracks	260
E31: Shear modulus results for RVEs with 24 randomly oriented cracks obtained using EasyPBC plugin in Abaqus for saturated crack condition.....	261
E32: Young’s modulus values of 8 cracks in RVE with three different cases	262
E33: Normalized Young’s modulus plot values for 8 cracks in RVE with three different cases	262
E34: Details of crack radius used to model RVE with 8, 16 and 24 cracks	263

List of Figures

2.1: Resonant frequency test apparatus (McCoy et al. 2014)	13
2.2: Stress-Strain Relationship for Normal and High Strength Concretes (Afsar, 2012). 18	
2.3: Changes in elastic modulus of concrete as function of temperature (Kodur, 2014). 22	
3.1: Location of disc specimens sawn from 100 by 200 mm cylindrical specimens.....	35
3.2: (a) Water-cooled diamond studded saw cutter (b) and discs sawn using saw-cutter. 36	
3.3: Sawing position and labeling of disc specimens	37
3.4: Test setup for capturing vibration signal of concrete discs	42
3.5: Test Apparatus for Measurement of the Air Permeability Index, (Recalde, 2009)... 47	
3.6: Concrete discs put in desiccator for conditioning.....	49
3.7: Water absorption test setup.....	49
3.8: Schematic of the test setup.....	50
4.1: Modulus of Elasticity curve for different concrete mixtures	54

4.2: Obtained signals indicated by green lines and processed signals (Signal Express software).	56
4.3: Initial and Secondary Water absorption of NF40 concrete mixture	61
4.4: Initial and Secondary Water absorption of HF40 concrete mixture	61
4.5: Initial and Secondary Water absorption of NF60 concrete mixture	62
4.6: Initial and Secondary Water absorption of NF60 concrete mixture	62
4.7: Relationship Between E_d and API: (a) E_d versus API for Normal and High strength mixture groups with different fly ash content for one-inch-thick discs, (b) E_d versus API Relationship for two mixtures for two-inch thick discs.	64
5.1: Concrete solid with different constituents (Sadowski and Mathia, 2016).....	70
5.2: Diagram representing the upper and lower bounds on the elastic bulk and shear moduli (Mavko et al., 2009).....	73
5.3: Diagram representing the Effective Elastic Properties of a Solid with Circular Cracks: (a) Effect of Soft Fluid Saturation (b) Effect of Partial Saturation (O’Connell and Budiansky, 1974).....	80
5.4(a): An ellipsoid crack (b) A penny-shaped	84

5.5: Normalized elastic modulus for Hudson’s first order correction	92
5.6: (a) Effective moduli vs CDP (b) Young’s modulus vs CDP plots in soaked and dry conditions.....	92
5.7: (a) Normalized elastic Young’s modulus vs ϵ (b) Effective moduli vs ϵ for Hudson’s first and second order expansion for dry and soaked conditions.....	93
5.8: (a) Effective moduli vs ϵ (b) Young’s modulus vs ϵ plots generated using Padé approximation.....	96
5.9: (a) Normalized Young’s Modulus vs ϵ for dry (b) Normalized Young’s Modulus vs ϵ for soaked cracks using Hudson’s first and second order expansion.....	97
5.10: Comparison of 1 st , 2 nd and new Padé expansion for Normalized Young’s Modulus c_{11} for (a) Dry cracks condition and (b) Soaked cracks condition	98
5.11: Comparison of 1 st , 2 nd and new Padé expansion for Normalized Young’s Modulus c_{33} for (a) Dry cracks condition and (b) Soaked cracks condition	98
5.12: Comparison of 1 st , 2 nd and new Padé expansion for Normalized Young’s Modulus c_{44} for (a) Dry cracks condition and (b) Soaked cracks condition	99
5.13: Application of Hudson’s model on dry and soaked control specimens for (a) Normal and (b) High Strength concrete mixtures ‘NC and HC’	101

5.14: Application of Hudson’s model on dry and soaked control specimens for (a) Normal and (b) High Strength concrete mixture with 40% fly ash ‘NFHC’	102
5.15: Application of Hudson’s model on dry and soaked specimens for (a) Normal and (b) High Strength concrete mixtures with 60% fly ash ‘NF60 and HF60’	103
5.16: Application of Hudson’s model on dry and soaked control specimens for (a) Normal and (b) High Strength concrete mixture ‘NC and HC’	104
5.17: Application of Hudson’s model on dry and soaked damaged specimens at 300 °C (570 °F) with 40% fly ash content (a) Normal Strength (NF40) and High Strength (HF40) concrete mixtures	105
5.18: Application of Hudson’s model on dry and soaked damaged specimens at 300 °C (570 °F) with 60% fly ash content NF60 and HF60 (a) Normal Strength (NF60) and (b) High Strength (HF60) concrete mixtures	106
5.19: Comparison of Hudson’s model and O’Connell and Budiansky Model for Normal and High Strength Control mixture groups for one and two-inch thick discs.....	111
5.20: Comparison of Normalized Young’s Modulus for Normal Strength Concrete Mixtures damaged at 300 °C for one-inch thick disc specimens.....	121

5.21: Comparison of Normalized Young’s modulus for High Strength Concrete Mixtures damaged at 300 °C for one-inch thick disc specimens	122
5.22: Comparison of Normalized Young’s modulus for Normal and High Strength Concrete Mixtures damaged at 300 °C for one-inch thick disc specimens	123
5.23: Comparison of Normalized Young’s Modulus for Normal Strength Concrete Mixtures damaged at 300 °C for two-inch thick disc Specimens.....	124
5.24: Comparison of Normalized Young’s Modulus for High Strength Concrete Mixtures damaged at 300 °C for two-inch thick disc Specimens	125
5.25: Comparison of Normalized Young’s Modulus for Normal and High Strength Concrete Mixtures damaged at 300 °C for two-inch thick disc Specimens	126
5.26: Comparison of Normalized Young’s Modulus for Normal Strength Concrete Mixtures damaged at 300 °C for one-inch and two-inch thick disc Specimens .	127
5.27: Comparison of Normalized Young’s Modulus for High Strength Concrete mixtures damaged at 300 °C for one-inch and two-inch thick disc Specimens.....	128
5.28: Difference in Young’s modulus for all mixtures damaged at high temperatures (a) Specimens before damage (b) Specimens after damage.....	130
6.1: (a) smaller RVE (b) Larger RVE size to develop numerical models	139

6.2: FE model of one and two-inches thick concrete disc	140
6.3: Damaged RVE with dry cracks in concrete.....	142
6.4: Three different mesh sizes selected during simulation.....	144
6.5: Section of different RVEs for soaked concrete condition.	145
6.6: Section of different RVEs for dry concrete condition.....	145
6.7: EasyPBC plugin installed in Abaqus program	146
6.8: RVE with different number of cracks and their orientations.....	149
6.9: RVE containing 24 randomly oriented cracks meshed with quadratic Tet elements (C3D10), with a crack density as defined by equation 1.2 is, $\varepsilon = 0.2$	150
6.10: Comparison of elastic Young's modulus using single and eight RVEs for dry and soaked conditions.....	151
6.11: RVE in case of dry condition with cracks shown as empty voids.....	153
6.12: RVE in case of saturated condition with cracks shown in purple color.	153
6.13: RVE with different number of cracks and their orientations.....	154

6.14: Diagrams representing displacement boundary conditions required to estimate the effective elastic properties.	157
6.15: EasyPBC plugin main window in Abaqus program	158
6.16: EasyPBC plugin processing flowchart (Omeiry et al. 2019).....	160
6.17: Position of cracks in 100x100x100 micron ³ RVE in dry and soaked conditions..	161
6.18: Position of cracks in 200x200x200 micron ³ RVE in dry condition	162
6.19: Position of dry cracks in 200x200x200 micron ³ RVE starting from single crack to eight cracks	164
6.20: Position of wet cracks in 200x200x200 micron ³ RVE starting from single crack to eight cracks	166
6.21: Young’s Modulus Results of RVE with 24 Cracks for Dry and Soaked Cracks Condition.....	168
6.22: Normalized Young’s Modulus Results of RVE with 24 Cracks for Dry and Soaked Cracks Condition	169
6.23: Young’s Modulus Results of RVE with 16 Cracks for Dry and Soaked Cracks Condition.....	170

6.24: Normalized Young’s Modulus Results of RVE with 24 Cracks for Dry and Soaked Cracks Condition.	171
6.25: Young’s Modulus Results of RVE with 8 Cracks for Dry and Soaked Cracks Condition.....	173
6.26: Normalized Young’s Modulus Results of RVE with 8 Cracks for Dry and Soaked Cracks Condition	173
6.27: Comparison of Young’s Modulus with three Cases of 8 different crack orientations in RVE and average values of all three Cases for dry condition	174
6.28 Comparison of Normalized Young’s Modulus with three Cases of 8 different crack orientations in RVE and average values of three Cases for dry condition	174
6.29: Comparison of Young’s Modulus with three Cases of 8 different crack orientations in RVE and average values of all three Cases for soaked condition	175
6.30: Comparison of Normalized Young’s Modulus with three Cases of 8 different crack orientations in RVE and average values of all three Cases for soaked condition	175
6.31: Comparison of Young’s Modulus results obtained from RVEs with 8, 16 and 24 cracks for soaked cracks condition	177

6.32: Comparison of Normalized Young’s Modulus results obtained from RVEs with 8, 16 and 24 cracks for soaked cracks condition	177
6.33: Comparison of Young’s Modulus results obtained from RVEs with 8, 16 and 24 cracks for dry cracks condition.....	178
6.34: Comparison of Normalized Young’s Modulus results obtained from RVEs with 8, 16, and 24 cracks for dry cracks condition	178
6.35: Comparison of Numerically obtained Normalized Young’s Modulus results with different analytical models for soaked cracks condition.....	179
6.36: Comparison of Numerically obtained Normalized Young’s Modulus results with different analytical models for dry cracks condition	180
6.37: Error bars for Young’s modulus using FEA results for dry and soaked crack conditions.....	183
6.38: Error bars for Normalized Young’s modulus using FEA results for dry and soaked crack conditions	185
D1: Crack position and orientation in multiple RVEs	235
D2: Crack position and orientation in bundled multiple RVEs	236

List of Abbreviations

ANOVA	Analysis of Variance
ASI	Abaqus Scripting Interface
ASTM	American Society of Testing and Materials
CDP	Crack Density Parameter
CET	Construction Engineering and Technology
CO ₂	Carbon Dioxide
CPU	Central Processing Unit
D _{dmg}	Subscript indicating damage, e.g., E _{dmg} or
G _{dmg}	Young's modulus and shear modulus of damaged concrete disc, respectively.
EasyPBC	Easy Periodic Boundary Condition
FFT	Fast Fourier Transform
FE	Finite Element
FEA	Finite Element Analysis
FEM	Finite Element Method
G _{dry}	Shear modulus of Air-Dried Concrete
Specimen	
G _{wet}	Shear Modulus of Wet/Soaked Concrete
Specimen.	
GUI	Graphical User Interface
HSC	High Strength Concrete
HF-40	High Strength Concrete with 40% Fly Ash
Content	
HF-60	High Strength Concrete with 60% Fly Ash
Content	

ITZ	Interfacial Transition Zone
KUBC	Kinematic Uniform Boundary Conditions
NDT	Non-Destructive Testing
NSC.....	Normal Strength Concrete
NF-40	Normal Strength Concrete with 40% Fly Ash Content
NF-60	Normal Strength Concrete with 60% Fly Ash Content
OPC.....	Ordinary Portland Cement
PBC.....	Periodic Boundary Condition
RH.....	Relative Humidity
REV.....	Representative Elementary Volume
RVE.....	Representative Volume Element
SCMs.....	Supplementary Cementitious Materials (SCMs)
Skd	Soaked Condition of Concrete Disc
SUBC	Stress Uniform Boundary Conditions
Sec.....	Seconds
Tet.....	Tetrahedral
w/cm.....	Water to Cementitious Material Ratio

List of Symbols

A.....	Cross-Sectional Area of Concrete Disc
°C.....	Degree Celsius
d.....	Diameter of Concrete Disc
ε	Crack Density Parameter (dimensionless)
E_0	Young's Modulus of Undamaged Concrete
E_c	Static Young's Modulus of the Concrete Specimen
E_d	Dynamic Elastic Young's Modulus
°F.....	Degree Fahrenheit
f.....	Fundamental Cyclic Natural Frequency
f_i	The Volume Fraction of the ith Phase
f_1 and f_2	The Volume Fractions of the Individual Phases
f_c	Concrete Compressive Stress
f^c	Ultimate Compressive Stress of Concrete
ft ³	Cubic Foot
g.....	Grams
G_0	Un-cracked Shear Modulus
G.....	Shear Modulus
GPa.....	Giga Pascal
In.....	Inch
K'.....	Bulk Modulus of Inclusion Material

K_{dry}	Bulk Modulus of Dry Porous Material
K_{sat}	Bulk Modulus of Saturated Porous Material
K_0	Bulk Modulus of the Solid Material
K_{fl}	Effective Bulk Modulus of the Pore Fluid
K_1 and K_2	Bulk Moduli of Individual Phases,
kg/m^3	Kilograms Per Cubic Meter
L	Thickness of the Disc
lb/ft^3	Pounds Per Cubic Foot
lb/yd^3	Pounds Per Cubic Yard
M	Mass of Concrete Disc
M_i	The Elastic Moduli of the i th Phase.
M_0	Shear Modulus of Un-Cracked Concrete
M_v	Effective Elastic Moduli
psi	Pound-Force Per Square Inch
ϕ	The Crack Porosity
P	Mass Density of Concrete
λ	Lamé Constant of the Background Medium (Concrete in our case)
λ_0	Lamé Constant of Uncracked Concrete
r	Radius of Concrete Disc
Ω_0	Dimensionless Frequency Parameter Associated with the first Mode of Vibration.
μ	The Shear Modulus
μ'	Shear Modulus of Inclusion Material (for fluid μ' is taken as zero)
μ_1 and μ_2	Shear Moduli of Individual Phases
μ_{dry}	Shear Modulus of the Dry Porous Material
μ_{sat}	Shear Modulus of the Porous Material Saturated with Pore Fluid
ν	Poisson's Ratio
ν_0	Poisson's Ratio for Un-Cracked Concrete
ν_{dry}	Poisson's Ratio for Air Dried Concrete
ν_{wet}	Poisson's Ratio for Soaked Concrete
ν_s	Shear Wave Velocity
ν_p	Pulse Velocity

Chapter One

Introduction and Objectives

1.1 Background

Sustainability and asset management are two important areas in the construction industry that play pivotal roles in building infrastructure, facilitating the economic development of any country. The organizations that are involved in operations and providing the maintenance oversight of infrastructure elements may be interested to incorporate sustainable materials for building new structures or retrofitting existing structures ensuring that those construction materials provide adequate durability. Generally, Portland cement concrete is considered a sustainable man-made material for construction since it is environmentally friendly through all stages of its life span and it can help to achieve points towards LEED™ certification (U. S. Green Building Council 2008). Portland cement is the most important constituent in concrete, which has expressed concerns over the CO₂ emissions associated with cement production leaving a massive carbon footprint. It has been estimated that cement production reached ninety million metric tons during the year 2020 in the United States alone, in contrast to the 4.1 billion metric tons of cement produced globally every year (Garside 2021). Incorporating alternative or supplementary cementitious materials (SCMs) into concrete mixtures offsets the demand for using clinker in cement and ultimately improves the sustainability of

concrete. Most commonly used SCMs, sometimes also called admixtures, are mainly industrial byproducts, such as silica fume, slag, or fly ash. These admixtures could improve desirable concrete properties such as durability, strength and, flowability (Sakir et al., 2020; Khoso et al. 2019).

ASCE (2021) has given a general grade of “C-” for infrastructure needs that requires attention in rehabilitating, upgrading, and repairing many of the crumbling roads, bridges, and other structures. The use of sustainable concrete materials has considerable potential in the applications of any of the infrastructure elements which could reduce construction costs by reducing Portland cement content and could have far-reaching consequences on reducing CO₂ emissions. Replacements of sustainable construction materials in the appropriate ranges could enhance the strength and lower down the permeability of concrete, and improve the durability of structures throughout their service life.

The use of traditional cement concrete and concrete with additional supplementary cementitious material should ensure sufficient capacity to respond to aggressive environmental conditions and applied loads during their life span without excessive loss of serviceability. It is also important that concrete mixtures used with sustainable or supplementary cementitious material in construction should attain the anticipated levels of strength, stiffness, and durability in concrete structures exposed to several environmental conditions. The current knowledge regarding the damage mechanism and environmental effects to concrete has been achieved from the experiences and observations for traditional concrete, however, the long-term effects of concrete mixtures with enhanced sustainable materials and reduced amount of Portland cement content are limited.

The documentation and specifications required to achieve an adequate level of durability and strength in concrete structures exposed to several effects of environment were developed mainly as a result of failures of structures in practice. The current level of understanding of the durability of concrete has been attained by conducting various case studies largely based on concrete mixtures of Ordinary Portland cement (OPC) of moderate strength from well over ten decades of “trial and error”. Environmental effects such as sulfate attack, frost action, alkali-silica reactivity, and heat of hydration to concrete structures already in service were first identified even after years of construction. Standardized testing procedures may not appropriately be applicable for concrete mixtures with a reduced amount of Portland cement with different microstructure, because the current knowledge relies heavily on comparisons to field conducted experiences.

The current level of knowledge is mainly empirically based which is not necessarily applicable for all concrete mixtures since different mixtures could respond differently under similar environmental exposures. Original techniques developed to evaluate properties of moderate strength traditional concrete may not be suitable for mixtures with considerably different microstructures such as those mixtures with the characteristics of enhanced sustainability. According to (Mehta and Monteiro, 2017), Portland cement concrete with an increased volume of SCMs is known as enhanced sustainable concrete. The standard test methods available for moderate strength Portland cement concrete to evaluate frost attack may not be applied to concrete mixtures of high strength (ACI-318 2008) and the response of concrete of high strength under high-temperature exposures is

comparatively different than that of moderate strength concrete exposed to the same level of damage (Phan and Carino 1998; Recalde and Leming 2009).

Hence, it becomes very important to investigate the changes occurring in concrete at the microstructural level. Investigations into concrete characteristics could be done using an nondestructive testing (NDT) approach, which is the method of testing, inspecting, or assessing materials, elements, or assemblies without posing any effect to the serviceability of the component or to the system as a whole (Workman and Moore, 2012; Soltani et al. 2019). The main objective of NDT is to evaluate the quality of the material, assemblies, or members without destroying their capability to achieve their intended purpose (Helal and Mendis, 2015). Moreover, the approach of calculating the dynamic modulus of elasticity of concrete non-destructively based on measuring fundamental frequency was limited to concrete prisms and cylinders at elevated temperatures.

However, the implementation of methods based on resonant frequency could be further enhanced to evaluate concrete discs after exposure to severe conditions. Previous research has successfully used concrete disc specimens obtained by sawing the cylinders or cores (Leming et al., 1998; Dilek, 2008). Also, thin concrete discs cut from cylinders have been extensively used to calculate chloride ion permeability and air permeability of gradients in concrete members, which provides a better understanding of changes in mechanical properties of concrete from the exposed surface. Further research on the measurement of permeability tests and dynamic modulus of the same concrete specimen would enhance the knowledge of researchers and engineers significantly between these properties (McCoy et al., 2014; Dilek and Leming, 2005).

Although research studies conducted in North America have revealed that concrete production with high-performance is possible with reduced Portland cement content and replaced with fly ash up to 60% by mass of the total cement (Malhotra 2002; Khoso et al. 2016), however, there is still a need to conduct more research and to better understand the effects and damage mechanisms of these concrete mixtures. More research work is required to quantify the degradation and relationships between changes in different characteristics of traditional and sustainability-enhanced concrete mixtures related with an increase in the amount and interconnectivity of microcracks after damage events such as overloading or elevated temperature exposure. These studies could pave way for the application of concrete for infrastructure development with enhanced sustainability materials and provide opportunities to the agencies to intelligently select or specify traditional concrete mixtures with reduced content of Portland cement. Moreover, these studies could be advantageous for asset management by providing the analytical and forensic techniques for evaluating the deterioration mechanism in existing structures. Advanced tools with improved ability based on fundamental principles would prove advantageous to accurately quantify the damage in concrete at the microcracking level and providing important applications to sustainable construction and advance the design codes and specifications with an improved understanding of the long-term effects to the concrete mixtures under severe exposures.

1.2 Changes in Microstructure of Concrete

The relationship between microstructure and the material property has become a fundamental part of the investigation in modern material science research. Concrete, being a highly heterogeneous material, has a complex microstructure. Hence, creating realistic

models of the microstructure from which the material's behavior may be accurately predicted becomes extremely challenging. However, understanding the microstructural properties of individual concrete components, as well as their interrelationships, becomes useful for exercising control over the material properties (Mehta and Monteiro, 2014). To consider concrete deterioration, assess microstructural changes in concrete, and enhance the durability of concrete, analytical and numerical techniques are required to estimate the changes occurring in the effective elastic properties of concrete under elevated temperatures. Investigations of the relationship between changes in elastic properties and the development of an analytical techniques to estimate the changes in the microstructural level of concrete have been previously studied by (Recalde, 2009). However, the development of numerical models to predict the changes in the concrete microstructure with supplementary cementitious materials and the comparison with analytical data have not been previously reported.

Concrete cores obtained from large structural members could be evaluated in determining the existing structural capability, level of deterioration, crack density as well as the understating of the damaging factors such as entrapped air and other contents which affect the overall elastic properties of the material. Evaluation of smaller sections such as concrete cores in determining the dynamic elastic modulus and different conditions such as soaked and dry have provided important engineering properties and the deterioration mechanism along with damage gradients for the structures in service, have been studied and reported by (Dilek et al. 2003, Dilek and Leming 2007a, Dilek and Leming 2008, Recalde 2009, McCoy 2014). Concrete core samples of approximately 25 mm (1 in.) are feasible depth in determining Young's modulus of concrete and permeability related

results. Since many concrete mixtures with reduced Portland cement content claiming enhanced sustainable materials lack long-term experience making forensic analysis is far more challenging when compared to the traditional concrete mixtures.

1.3 Problem Statement

Current techniques to quantify the degree of microcracking non- or semi-destructively are limited and the lack of studies to quantify the degree of microcracking in concrete under elevated temperatures shows that there is a need for suitable alternative methods. Microscopic analysis may be expensive and time-consuming for most evaluation applications. The several advantages of additional methods to establish a quantitative relationship between changes in the microstructure of different concrete mixtures and the changes in their elastic properties would be useful in many applications. Few techniques have been used for forensics investigations in determining the crack density parameter (ε) and dynamic young's modulus (E_d) for the last decade by researchers (Recalde 2009, McCoy, 2014). To assess the structural condition of the concrete material and evaluation of new sustainably enhanced concrete materials, it is important to understand how these materials behave and respond to elevated temperature exposures. In this regard, an analytical model is a useful tool to measure the damage at the microstructural level of the concrete structure using small concrete disc specimens and to estimate the elastic properties non-destructively. To develop non-destructive testing techniques to quantify the degree of microcracking in concrete, it is necessary to understand resonant and stress wave propagation behavior in micro cracked concrete at a fundamental level. The shortage of studies on the microcracking level of concrete has hindered the development of a finite element method that could provide a better understanding and behavior of damaged

concrete under different conditions. Moreover, in order to accurately assess the response of concrete discs to high- temperature exposure, a finite element method need to be developed. Further studies to establish a quantitative relationship between microstructural changes of different concrete mixtures and changes in mechanical properties would be useful in many applications and for infrastructure development.

1.4 Research Significance

The analytical and numerical models presented in this research study to estimate dynamic elastic properties of concrete damaged at high temperatures would be useful in understanding the fundamental behavior of traditional as well as concrete with different supplementary cementitious materials. Analytical techniques to predict the response of enhanced sustainability concrete (ESC) to short-term fire exposure are limited, hence further procedures and the results presented in this research work could be of value to researchers and practicing engineers involved in assessing concrete mixtures with or without supplementary cementitious materials, exposed to high temperatures. The easily available tool for assessment of concrete and the ability to rapidly deliver the estimate of material properties and to quantify microstructural changes of existing concrete structures could be useful in many applications including forensic investigations and for agencies involved in the infrastructure development of any country.

1.5 Research Objectives

The research study presented in this dissertation is envisioned to expand the knowledge in analyzing the relationship between microstructural changes and changes in elastic properties of numerous concretes subjected to elevated temperature exposures. The dissertation presents the extension of analytical testing procedures to quantitatively measure the changes occurring in concrete considering crack density parameter of thin concrete disc specimens in dry and saturated conditions damaged before and after a short temperature exposure of 300 °C. The material used for damage investigation in this dissertation consists of concrete mixed with different percentages of fly ash, taking into consideration the sustainability of the material, and comparing it with traditional cement concrete. The analytical procedures used in this research work to investigate the changes in low- and high-strength concrete exposed to elevated temperatures are based on protocols developed by Leming, Nau, and Fukuda (1998). The analytical procedure used to estimate the crack density parameter and Young's modulus of concrete is an extension of the method originally presented by Hudson (1980, 1981), which was adapted to be applicable for thin concrete discs and to further determine the differences in elastic Young's modulus in empty and water-filled cracks.

The developed models in this research study have important implications in asset management and the sustainable development of infrastructure. An easily available tool for the assessment of concrete and the ability to rapidly deliver the estimate of material properties of existing concrete structures is valuable in managing the assets and for sustainable construction. The ability to use a simple analytical technique to quantify

engineering properties and microstructural changes based on fundamental analytical principles should enhance the knowledge of many researchers and practicing engineers in understanding the behavior of concrete specimens exposed to various conditions including elevated temperatures. Moreover, the ability of rapid assessment of engineering properties using such analytical techniques could also have important implications in the infrastructure development of any country with limited resources.

The research work conducted in this dissertation was intended to;

- (1) Collect experimental data in the beginning and to set a foundation for expanding analytical method developed by Hudson (1980, 1981) to thin concrete disc specimens and,
- (2) to adopt the extension of the analytical procedure to quantitatively determine the changes occurring in the elastic moduli of concrete specimens by estimating the crack density parameter of concrete discs under different conditions when exposed to short temperatures exposures and,
- (3) to use the testing methodology as a simple screening test to compare the material properties of traditional concrete to those obtained from mixtures with reduced Portland cement content used with supplementary cementitious materials with the properties of those obtained from traditional concrete.

Chapter Two

Literature Review

2.1 Background

2.1.1 Assessment of Damaged Concrete Condition

Every structural element used in the construction industry either made with traditional concrete or sustainable enhanced concrete should be capable of resisting loads and respond well to environmental exposures without excessive loss of serviceability. However, during the life span of existing concrete elements assessment of damage is required which is generally carried out by testing the concrete with load tests or inspecting visually. Assessment of structural concrete members by load testing, such as the method specified in ACI-318 Building Code (2019), could be an expensive and laborious process with high risks due to safety concerns. However, evaluation of concrete structural members through assessment of the concrete quality could be conducted using in-situ non-destructive testing procedures, or through obtaining smaller concrete cores the specifications of which are provided in ACI 214 Committee Report 214.4R-10 (2010) for core extraction and interpreting results. Analysis of the compressive strength of cores is typically considered to be adequate for evaluating the overall quality of the concrete, such as concerns about the quality of the concrete batch used during construction.

Evaluation of the compressive strength of cylindrical cores is generally considered to be sufficient for the concrete overall concrete quality, however, when concrete is exposed to environmental exposures such as elevated temperatures could not provide a better analysis of the strength due to damage gradients. The compressive strength of such cylindrical cores might therefore not be representative of the concrete quality in case of damage gradients with a limited depth compared to the length of the cylinder. Hence, the compressive strength of such cylindrical cores may not be expressive of the overall quality of concrete when the specimen contains damage gradients in limited thickness when compared to the cylinder length where the damage gradients keep on reducing with increased length. Many researchers (Dilek, Caldwell, Sharpe and Leming 2003; Dilek and Leming 2007a; Dilek and Leming 2008; Dilek 2006, Recalde 2009) carried out forensic investigations and on concrete cores with damage gradients using thin concrete disc specimens sawn from cylindrical cores. Evaluation of damage gradients was conducted by estimating the dynamic elastic modulus of disc specimen of approximately 25 mm (1 in.) thickness which showed a gradual decrease in the damage intensity when compared with top and bottom surfaces of the specimen.

Thin concrete disc specimens could easily be extracted and handled properly due to their smaller size for forensic investigation purposes. The dynamic elastic modulus of concrete (E_d) of thin concrete disc specimens could simply be estimated using a procedure developed by Leming, Nau, and Fukuda (1998). This method requires input values such as disc dimensions, mass, and resonant frequency of the disk to calculate dynamic Young's modulus of elasticity which was obtained from analysis of the signal generated by an accelerometer attached to one side of the disc in free-free vibration as shown in Figure 2.1.

This method to determine E_d is based on the theory developed and presented by Hutchinson (1979). The detail of the method developed by Leming, Nau and, Fukuda (1998) is presented in chapter three of this dissertation.

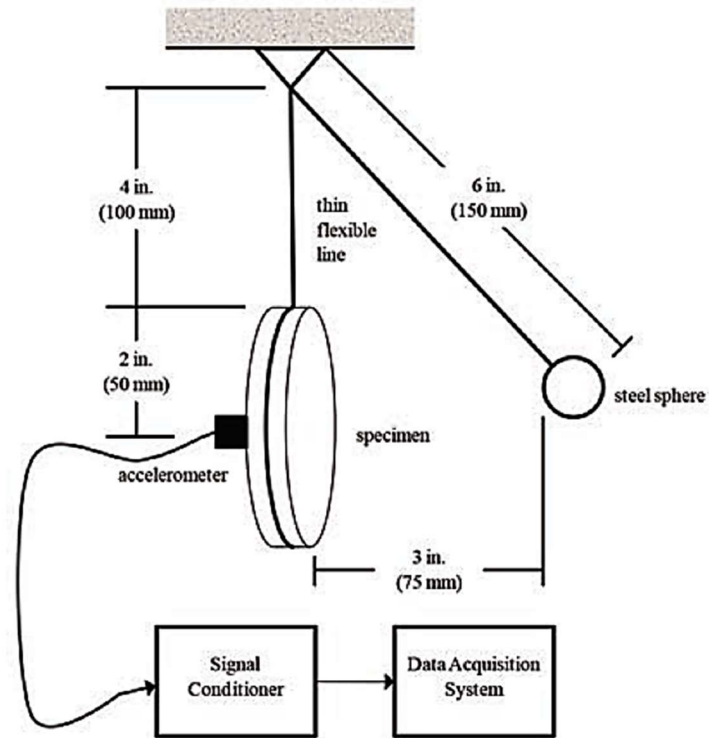


Figure 2.1: Resonant frequency test apparatus (McCoy et al. 2014)

Furthermore, McCoy et al. (2014) also adopted the method developed by Leming, Nau and, Fukuda (1998) where the study was conducted to determine the relationship between the changes occurring in the microstructure and the elastic properties of different concretes under moderately elevated temperature exposures. They described a method for estimating the crack density parameter (ε) of concrete, which is “the hypothetical number of mean-radius flat ellipsoidal cracks per unit volume of material. It is defined as $\varepsilon = N\langle a^3 \rangle$ for

circular cracks, where N is the number of cracks and $\langle a^3 \rangle$ is a measure of the mean crack radius α per unit volume” (Walsh, 1965). O’Connell and Budiansky (1974) studied the elastic media, containing randomly dispersed are oriented, flat, ellipsoidal cracks with and without the presence of using a method of self-consistent energy. The “crack density parameter for ellipsoidal cracks is defined as $\varepsilon = (2N/\pi) \langle \frac{A^2}{P} \rangle$, where $\langle \frac{A^2}{P} \rangle$ is the mean squared area to perimeter ratio of the cracks per unit volume”. The estimation of crack density parameter can be done by measuring the shear modulus and Poisson’s ratio values of undamaged and damaged material (McCoy et al., 2014).

2.2 Analytical Procedure to Estimate Crack Density Parameter of Concrete

An analytical procedure to estimate crack density parameter (ε) for thin circular concrete discs was developed by Recalde (2009). This approach was founded by using the analytical techniques derived from the O’Connell and Budiansky (1974) geophysical model. Moreover, Recalde (2009) analyzed dynamic shear modulus (G_d) of thin concrete discs nearly 25 mm (1 in.) thick with 100 mm (4 in.) diameter in dry and wet conditions (G_{dry} and G_{wet}). According to Recalde (2009), the exact knowledge of Poisson’s ratio ν and G_0 the un-cracked shear modulus was not required and could be assumed to estimate ε with an iterative solution by using the equations (2.1) through (2.4) given as

$$\frac{G_{dry}}{G_0} = 1 - \frac{32}{45} (1 - \nu_{dry}) \left[1 + \frac{3}{(2-\nu_{dry})} \right] \varepsilon \quad (2.1)$$

and

$$\frac{G_{wet}}{G_0} = 1 - \frac{32}{45} (1 - \nu_{wet}) \left[\frac{3}{(2-\nu_{wet})} \right] \varepsilon \quad (2.2)$$

The parameters in the given equation include G_{dry} , the shear modulus of air-dried concrete in 10^6 psi (GPa); G_{wet} , the shear modulus for saturated concrete in 10^6 psi (GPa); G_0 , the shear modulus for un-cracked concrete in 10^6 psi (GPa); ν_{dry} , the Poisson's ratio value for air- dried concrete; ν_{wet} , the Poisson's ratio for soaked concrete; and ε , the dimensionless crack density parameter, with

$$\varepsilon_{dry} = \frac{45 (\nu_0 - \nu_{dry})}{16 (1 - \nu_{dry}^2)} \left[\frac{(2 - \nu_{dry})}{(1 - 3\nu_0)(2 - \nu_{dry}) - 2(1 - 2\nu_0)} \right] \quad (2.3)$$

and

$$\varepsilon_{wet} = \frac{45 (\nu_0 - \nu_{wet})}{16 (1 - \nu_{wet}^2)} \frac{(2 - \nu_{wet})}{(2\nu_0 - 1)} \quad (2.4)$$

where ν_0 is the Poisson's ratio for un-cracked concrete. Values of G need to be obtained experimentally and Poisson's ratio can be assumed. Moreover, an iterative procedure could be applied to determine values for ν_{dry} , ν_{wet} , and G_0 such that $\varepsilon_{wet} = \varepsilon_{dry}$ and $0 < \nu_{dry} < \nu_{wet} < 0.5$ (McCoy et al., 2014). Recalde (2009) presented that the "sensitivity of ε is ± 0.01 for $0.15 \leq \nu_0 \leq 0.30$ ".

2.3 Microcracking and its effects on Concrete

In most cases, failure of concrete is related to cracking; therefore, it becomes very important to understand the crack formation, crack propagation, and factors influencing micro-cracking in concrete (Rajib, 2020). Micro-cracking may be defined as the formation of very small cracks in concrete which are not visible to the naked eye. Micro-cracking occurs naturally during the process of hydration in cement; however, it also happens when

the concrete undergoes compressive loads. Apart from this, micro-cracks also form when the concrete experiences elevated temperatures, which induces changes in the concrete solid ultimately breaking bonds between the cement and coarse aggregates. The effects of microscopic flaws on the macroscopic performance of other metals, flaws in ceramics, cracking in glass and limited study on concrete has been done by researchers (e.g., Cooper et al., 2017; Aldea et al., 1999; Tvergaard and Hutchinson, 1988; Slate and Hover, 1984). However, in the past few decades, increased attention has been given to understanding and characterizing the defects in concrete at the micro-cracking level (Vu et al., 2021). Since micro-cracking is not visible to the naked eye, Slate and Hover (1984) categorized the term 'micro-crack' as a crack with a thickness of around 100 μm that could be located using the technique developed by Slate and Olsefsky (1963). Micro-cracking has a severe impact on the overall concrete strength, which results in weakening bond strength between the mortar and aggregate, reduction in the capacity of concrete to carry loads, and growth of continuous cracks. Moreover, crack development in concrete increases strains with lateral expansion, resulting in stress development at later stages. Hsu et al. (1963) found that drying and shrinkage of concrete generated micro-cracks at the Interfacial transition zone (ITZ) prior to application of any external force. Concrete, while wet and in the process of being cured, also exhibits pre-existing micro-cracks (Jornet et al., 1993). In a study conducted by Ravindrarajah and Swamy (1989), the formation of visible cracks and plastic deformations of concrete were largely associated with concrete failure under the loading of any type. The development of such cracks is the result of internal micro-cracks under increased strains. Even prior the application of any type of external loading, the concrete solid contains micro-cracks that propagate further under various loading conditions,

resulting in reduced structural strength and ultimate failure of the system. Material scientists have conducted research studies on the formation of microscopic cracks and their effects due to short-term loading on concrete, including Hsu et al., (1963), who observed a growth in the trace width and trace length and number of micro-cracks with increasing strain at 30% of the ultimate strength of traditional concrete, showing deviation in the stress-strain curve from linear elastic behavior. Micro-cracks appear to increase in number and interconnect with each other at around 70 to 90% of the ultimate strength, causing a considerable divergence in the stress-strain curve and begin to show signs for failure (Recalde, 2009).

Carrasquillo et al. (1981) performed a comparative study on a progressive micro-cracking for different concrete mixtures under uniaxial compressive strengths ranging from 4500 psi to 11000 psi (31 to 76 MPa). This comparative study included the changes in the performance between normal and high strength concretes, such as change deviation in the elastic response and failure mechanism, which was explained by variations in micro-cracking. The crack progression occurred due to the formation of small cracks which when connected, resulted in deteriorating the concrete leading towards failure. Their study found that the cracks begin to combine and interact with each other in traditional concrete at about 70% of the maximum load carrying capacity paving a way towards the impending failure of the structural system. For the case of high strength concrete cracks formation was observed at about 90% of the ultimate concrete strength. Although high-strength concrete has far less micro-cracking as compared to the conventional normal-strength concrete, however, due to its nature of being more brittle it collapses suddenly without giving clear signs of failure and exhibiting fewer planes of failure. It is due to the homogenous nature

of concrete which makes concrete fail suddenly. The stronger the concrete is, the more brittle it becomes which could be seen in figure 2.2, in the stress and strain relationship. The slope of the stress-strain curve depends on the material's strength and is larger for high strength concrete as shown. This is because high-strength concrete has fewer strains prior reaching to the ultimate failure. When compared to ordinary concrete, high-strength concrete absorbs more loading effects, and its stress-strain curve increases in a vertical rather than horizontal manner (Afsar, 2012).

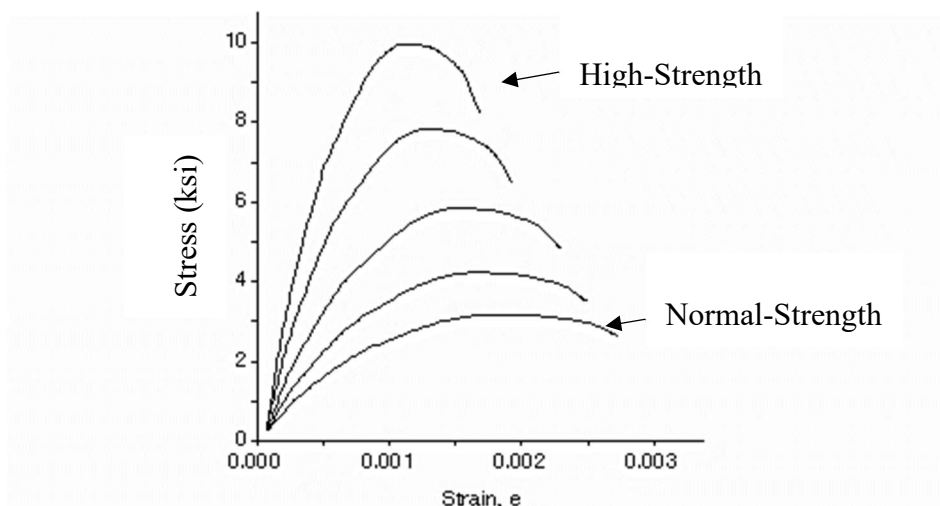


Figure 2.2: Stress-Strain Relationship for Normal and High Strength Concretes (Afsar, 2012)

2.4 Structural Fire and Temperatures Reached

The inherent fire-resistance properties of concrete make it more advantageous over other building materials; however, concrete buildings must be designed to withstand effects of fire that could occur at any stage throughout the life span. Although concrete and steel reinforcement lose strength as the temperature rises, structural elements still must be able

to carry a live load and dead load without collapse. Additionally, the expansion of structural components that are caused by fully developed fires must also be considered when designing structures. The requirements of building codes for fire resistance are often overlooked, resulting in severe and costly mistakes.

The ACI 318 strength requirements on concrete slab floor systems may require a smaller thickness than the requirement by the local building codes for a 2-hour fire- resistance system. This must be taken into consideration for a sound and safe design (David and Mahmoud, 2008). Generally, temperatures above 900°C are common in structures during the fire event, CIB W14 Report (1990). Initially, during the fire event in the building, there are a numerous change which occur in the physical and chemical properties of the cement. After a fire, some of these effects can be reversed on cooling, while others cannot be reversed, and may significantly deteriorate the concrete. Most of the porous concrete materials contain some amount of liquid water presented in pores. If the temperature surpasses the range of moisture plateaus of 100 – 140°C, this water will likely evaporate, resulting in a pressure building inside the concrete. When the temperature hits the 400°C mark, calcium hydroxide in cement begins to desiccate, producing more water vapor as well as causing the material to lose considerable strength. At higher temperatures, aggregates undergo other changes, such as quartz-based aggregates increasing in volume, which occurs due to the transformation of mineral, at a temperature of about 575°C, or aggregates of limestone decomposing at about 800°C. Moreover, due to the high temperature, a disintegration between cement and aggregates occur which results in cracks and ultimately spalling of concrete happens.

These chemical and physical changes will have a significant effect on the compressive strength and the elastic properties of concrete. Taking into account the temperature of 300°C, specimens have been damaged for relatively short exposure for two hours and the changes at the microstructural level have been determined in the research work conducted in this study.

2.5 Effect of Elevated Temperature on Concrete Properties

When traditional concrete is exposed to extreme temperature conditions, it begins to deteriorate due to changes in microstructure which eventually affect the mechanical properties of concrete resulting in weaker structural components to resist environmental conditions. The modulus of elasticity of concrete is generally considered to be one of the most affected property when the concrete is exposed to high temperatures (Babalola et al., 2021). The effects of elevated temperatures on the mechanical properties of concrete have been studied by many researchers since as early as 1950s (Malhotra, 1956; Schneider, 1988; Husem, 2006; Tomasz et al., 2017; Anupama et al., 2019). Compared to the compressive strength and tensile strength of the concrete, degradation in the modulus of elasticity occurs at a higher rate (Chen and Liu, 2004). This has been the consequence of the loss of free water and the development of cracks in concrete samples when subjected to elevated temperatures (Zhao et al., 2020; Rekha and Potharaju, 2015; Choe et al., 2015). Moreover, due to the repeated environmental conditions and changes in temperatures, the peak strength could loosen resulting in smaller crack formations in concrete components. Such external agencies could trigger the microcracking and allow water penetration through the cracks which eventually result in concrete deterioration and affect the concrete durability

(Kassir et al., 1996; Khoso et al., 2019). Effects of elevated temperatures on the mechanical properties of concrete have been extensively studied in the literature presented by (Kodur and Harmathy, 2008; Tang and Lo, 2009), which were mainly studied on fabricating of concrete cylinders of different sizes. For the research work conducted in this dissertation, Young's modulus (E) of the concrete was mainly a point of interest. The elastic modulus of concrete for many concrete types varies over a wide range at the room temperature which is mainly dependent on the water to cementitious material ratio, age of concrete, curing process, and the number of aggregates used (Kodur, 2014). The Young's modulus of concrete rapidly decreases with the temperature increase, and the fractional decline in the elastic property does not depend significantly on the type of aggregates (Cruz, 1966). In other studies, conducted by (Haramathy, 1993 and Bennetts, 1981), it is found that Young's modulus of normal strength concretes (NSC) reduces drastically as the temperature rises that that of lightweight concretes. High strength concrete (HSC) has also widely been used since the 1950s as a suitable alternative for normal strength concrete and is commonly used with silica fume to further increase the overall strength (Behnood and Ziari, 1988; Chowdhury, 2014). Figure 2.3 presents the change in the ratio of Young's modulus at target temperature when compared to that at room temperature for normal and high strength concretes (Kodur, 2014, EN, 1992-1-2, 2004 and Phan, 1996).

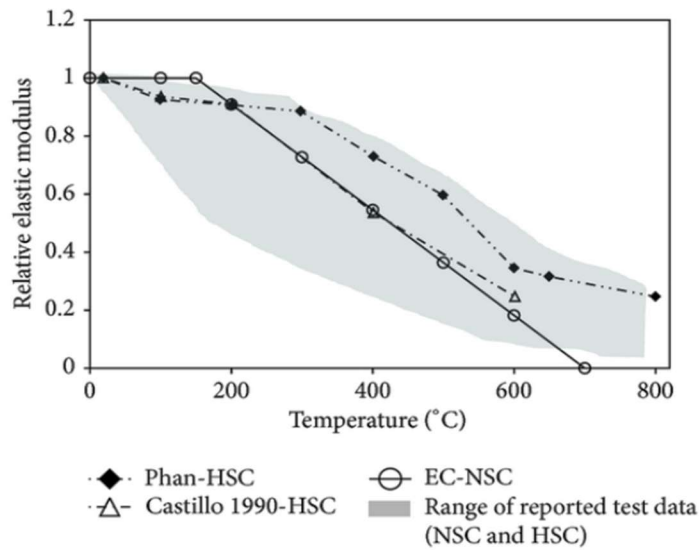


Figure 2.3: Changes in elastic modulus of concrete as a function of temperature (Kodur, 2014)

It could be observed in the above figure that the loss of Young's modulus trend for normal and high strength concretes compared to the temperature is identical, however, there is a considerable change reported in the test data. The reduction in the elastic modulus in both concrete mixtures could be attributed to the excessive stresses that occurred due to temperatures variation and changes occurring both physically and chemically in the microstructure of concrete (Kodur, 2014). The effect of high temperatures on elastic modulus was also studied by (Philleo, 1958) using dynamic procedures for temperature up to 370 °C (700 °F) where a decrease in elastic modulus of concrete was noticed. A similar study was carried out by (Dias et al., 1990) where a linear decrease of the residual dynamic elastic modulus of about 0.6 of the controlled elastic moduli was observed at a temperature exposure of 370 °C (570 °F). In general, the concrete subjected to high temperatures undergoes microstructural changes which drastically reduce the Young's modulus when compared to those placed in the ambient environments. In a study by (Chen et al., 2014),

a significant initial decrease in the elastic Young's modulus was observed at a temperature of 400 °C (750 °F) and further decrease with the increase in temperature, however, slower degradation rate when the temperature was 600 °C (1110 °F) and above. Concrete material could lose most of its Young's modulus of elasticity at 400 °C (750 °F) heating and cooling cycle (Zega and Maio, 2006; Chen et al., 2014). The degradation in the modulus of elasticity of concrete at a higher rate, when exposed to elevated temperatures, implies that the high temperature has a considerable damaging effect on the microstructure of the concrete material (Babalola et al., 2021; Chen et al., 2014).

2.6 Micromechanical Modeling of Concrete

Micromechanical modeling of materials has become an important and appropriate method to investigate the damage occurring under various conditions such as fatigue, heat, compression, and tension when compared to conventional materials. This approach is not limited to concrete materials, however; its application is widely spread to composite materials, aerospace structures, sports equipment and, many civil engineering structures (Burgarella et al., 2019). Estimating the elastic properties of various materials has become an active research area in the past few decades and is obtained either using macro or micromechanical techniques (Xia et. al, 2003). The micromechanical technique predicts the material's overall behavior based on known properties of its constituents, such as inclusion and matrix (Aboudi, 1991; Naseer et. al, 1993). In the past few years, efforts have been made to develop micromechanical models where the response depends on a three-dimensional scale of micro-heterogeneities (Dascalua et. al, 2008). However, in a macro-mechanical approach, the heterogeneous structure of the material is substituted by a

homogenous medium with anisotropic properties. A micromechanical technique is not only beneficial in getting the overall properties of the material; it also analyzes materials under different conditions such as dry and wet and produces elastic properties of the damaged concrete.

In order to validate experimentally obtained results, one would try to make a model with predefined input values of material and compare the produced results and behavior by numerical simulations. This would surely be with the idea of being able to numerically analyze the real material response occurring at the microstructural level of the concrete under different conditions using the finite element analysis approach.

2.7 Finite Element Modeling of Concrete

The finite element method (FEM) is universally considered to be one of the most important engineering breakthroughs in the field of civil engineering, specifically for the analysis of structural and materials science engineering. The development of computers and their capability have elevated the FEM approach to one of the most widespread methods to resolve engineering complications (Yucel, Arpaci, 2013 and Hosseini et. al, 2015). FEM is one of the conventional numerical analysis techniques used in numerous engineering fields in obtaining approximate solutions to continuum problems. The approach of finite element analysis was initially applied to stress analysis; however, it later became applicable in many other fields (Loarte and Sohrabi, 2017). The main advantage of FEM is its flexibility compared to classical methods (Cook, 1995). Hence, this advancement and increased use in computational speed available for analytical modeling and numerical analysis have provided the possibilities and promising routes for simulation

methods that could play a crucial role in analyzing the heterogeneous structure of materials at the microstructural level. Availability of such advanced numerical analysis tools has motivated me to conduct this work which is presented in the subsequent part of this research study, concentrating mainly on the behavior of damaged concrete at the micro-cracking level both in dry and soaked conditions and by creating a suitable numerical model exhibiting the microstructure of the concrete material. The approach consists of a numerical homogenization theory and practice, along with the modeling of the concrete matrix at the microstructural level by means of finite element methods on representative volume elements (RVEs). The numerical part of this research study mainly focuses on determining the effective elastic material properties of concrete composite for smaller volumes using computational techniques. Emphasis has been placed on creating an appropriate representative volume element (RVE) which presents the microstructure of randomly oriented penny-shaped cracks as inclusions in the concrete composite and by applying suitable 3D boundary conditions (Al Kassem, 2009). The numerical models would prove to deliver a better understanding of the experimentally obtained results and those obtained using analytical procedures.

2.8 The Representative Volume Element (RVE)

The “representative volume element (RVE) is the smallest volume across which a measurement can be conducted that yields a value representative of the entire system”. With periodic materials, selecting a periodic unit cell (which may or may not be unique) is simple, but in random media, the problem is far more challenging. The objective of generating smaller volume units is to estimate the mechanical properties such as Poisson’s

ratios, shear modulus, elastic modulus, thermal properties, hydrogeological properties, and other averaged values used to define the physical systems (Wikipedia 2021). Considering this approach, the estimation of the mechanical properties of the damaged concrete has widely become in use during recent times Sen et. al., 2015, Zhou et. al., 2015). Apart from experimental studies and analytical methods, micromechanical methods have become active in the research area to determine the overall properties of concrete materials. RVE represents the selected small part from the real specimen over which the properties could be determined that will yield a value representative of the whole. The optimal choice of RVE is usually that the RVE should have enough size to exhibit the feature of a composite material and as small as possible to make it computationally inexpensive (Ye and Wang, 2015). In the case of composites, a few studies have suggested that the “minimum size of the RVE is the smallest volume element of the composite that is statistically representative of the composite” (Drugan and Willis, 1996). The same RVE is defined by another researcher as a volume of the heterogeneous body that is macroscopically small enough and at the same time large enough to contain a sufficient number of inhomogeneities to be representative (LyDzba and Rozanski, 2014). Furthermore, the selected RVE should have the same volume fraction as that of the entire composite (Michel et. al., 1999). Micromechanical approaches provide global behaviors of the specimens from the known properties of inclusion and matrix through an RVE analysis (Xia et. al., 2006). The development of an RVE for analysis purposes has become a computationally effective approach towards estimating the effective elastic properties of the material using finite element methods (FEM). The availability of computer programs has provided the possibility to consider more intricate microstructure consisting of numerous inclusions

with dissimilar forms, dispersed orientations and variable aspect ratios, and uneven inclusions' distribution (Ye and Wang, 2015). To determine the effective elastic material properties, Abaqus is extensively used to Analyze different RVEs (Lubineau and Ladeveze, 2008). Furthermore, Abaqus provides code scripts through its kernel that are modified using Python for improved Finite element analysis and are used to line with Abaqus via the Abaqus Scripting Interface (ASI), which is a Python extension. ASI provides a suitable interface to the models and outcomes as a standard module of the Abaqus computer program (Zuo and Xie, 2015). This approach has been adopted in this research study to generate the behavior of concrete under high temperature using the experimental values and to compare with those obtained using analytically. To achieve the final objective of this research study, which is mainly based on numerical modeling, Python scripting is used and modified based on the RVE requirements to estimate the effective elastic properties of the concrete material under Periodic boundary conditions (PBCs). Introducing user-defined material properties to the RVE using Python scripting was observed to be efficient in reducing the time and avoiding developing different RVEs from scratch.

Chapter Three

Research Methodology

3.1 Overview of the Testing Program

The research work presented in this dissertation is carried out in three different phases. In phase I, an experimental investigation was conducted to collect data and to evaluate the effects of moisture content on the vibrational characteristics of thin concrete discs in free-free vibration. The experimental data collection was obtained from six different concrete mixtures prepared for normal strength and high strength concrete the details of which are presented in table 3.1. The experimental investigation intended to evaluate signal characteristics which may provide better understanding about the microstructural condition of the concrete. Prior determining the resonant frequency of specimens, the changes in the concrete microstructure were obtained by exposing the thin concrete disc to high temperature of 300 °C (500 °F). In Phase II, the data obtained from Phase I was used to introduce an analytical model to estimate the crack density parameter (CDP) of concrete using the resonant characteristic of circular discs and, the results were compared to previously developed models. Moreover, the changes in the microstructure, fluid penetrability and the mechanical properties of the damaged specimen at high-temperature exposure of 300 °C were examined. In Phase III, the analytically obtained results were

further compared with finite element model results and, the behavior of two different conditions soaked and dry was observed. The purpose of developing a numerical idea was to compare the damage mechanism behavior of concrete observed through the analytical tool and the potential to utilize these testing techniques on concrete mixtures other than traditional mixtures made with enhanced sustainability materials.

3.2 Experimental Plan

The experimental plan consists of conducting a comprehensive study in collecting data from specimens made with different concrete mixtures. A significant amount of ordinary Portland cement (OPC) was replaced by fly ash with proportions of 40% and 60%. The main purpose of using fly ash in concrete was to investigate how changes occur at the microstructural level of concrete when exposed to the different damaging environments, and when compared to traditional concrete, OPC-only based concrete mixtures. Moreover, concrete specimens were damaged by relatively short temperature exposure of 300 °C (570 °F) for two hours in the oven. Two different concrete conditions were considered for the testing purposes which consisted of:

- (1) dry concrete condition (DRY): where specimens used after 28 days curing kept dry before performing tests and,
- (2) soaked concrete condition (SKD): where specimens used after 28 days curing were directly used after taking them out of water for testing purposes.

The specimens in both conditions were then used to determine resonant frequency and to compare their similarity or dissimilarity to the responses of traditional concrete. The fly

ash replacement 0%, 40%, and 60% in concrete was used to carry out the experimental investigation during this dissertation.

3.3 Experimental Materials

The materials used to prepare concrete mixtures with supplementary cementitious material and to carry out the experimental investigations during this research work are presented below.

3.3.1 Supplementary Cementitious Material

In this experimental work, fly ash Class *C* as supplementary cementitious material (SCM) was used as cement replacement. Fly ash acts as an additional material mainly to contribute to improving the mechanical properties of concrete. The Fly ash utilized in this research work was attained from the Kuhlman Corporation, a concrete, and building materials supplier in Toledo, Ohio. The main objective of using fly ash in this research work is to observe the effect on the strength and the microstructural characteristics of concrete samples under elevated temperatures exposure. Mixtures examined during this study include both normal strength and high strength concrete with 0.5 and 0.4 water to cementitious material (w/c) ratio, respectively. For the purpose of validation, two traditional concrete mixtures of low strength and high strength were prepared in Phase I. Details of six mixture proportions are given in Table 3.1 and the characteristics of traditional concrete and sustainable concrete mixtures with different fly ash percentages are given in Table 3.2 and Table 3.3 respectively.

Table 3.1: Detail of mixture proportions

Concrete Type	Labeling	Fly Ash (%)	w/cm Ratio
Normal Strength	NC	0	0.5
	NF-40	40	0.5
	NF-60	60	0.5
High Strength	HC	20	0.4
	HF-40	40	0.4
	HF-60	60	0.4

3.3.2 Type of Cement

OPC Type II in accordance with ASTM C150 - 16 “Standard Specification for Portland Cement” was used in all concrete mixtures and fabricating cylindrical specimens. Fresh concrete mix tests were conducted the details of which are presented in the preceding sections.

3.3.3 Coarse Aggregate and Fine Aggregate

The coarse aggregate used in fabricating all six types of concrete mixtures was obtained locally from the nearby industry. A water absorption test for coarse aggregate was carried out after soaking the aggregates for 24 hours and which was equal to about 0.5%. Similarly, locally available round lake sand obtained from the Kuhlman Corporation was used as fine aggregate in preparing all concrete specimens. A water absorption test was also conducted for sand and the moisture content was found to be equal to 5.4%.

3.3.4 Air Entraining Admixture

Air entraining admixture was added in all six concrete mixtures, which generally stabilizes microscopic air bubbles in the concrete mix. This admixture is helpful in improving the durability of concrete when experiencing severe freezing and thawing weather condition.

Table 3.2: Characteristics of Traditional Concrete Mixtures

Property	Normal Strength Concrete (NC)	High Strength Concrete (HC)
Portland Cement lb/yd ³ (kg/m ³)	580	580
Fly ash (Class C) lb/yd ³ (kg/m ³)	0	0
Fine aggregate lb/yd ³ (kg/m ³)	1160 (688)	1160 (688)
Coarse aggregate lb/yd ³ (kg/m ³)	2320 (1375)	2320 (1375)
Water lb/yd ³ (kg/m ³)	290 (172)	230 (138)

Table 3.3: Characteristics of Sustainable Concrete Mixtures

Property	NF-40	HF-40	NF-60	HF-60
	Mixture composition			
Portland Cement lb/yd ³ (kg/m ³)	350 (207)	350 (207)	230 (138)	230 (138)
Fly ash (Class C) lb/yd ³ (kg/m ³)	230 (138)	230 (138)	350 (207)	350 (207)
Fine aggregate lb/yd ³ (kg/m ³)	1160 (688)	1160 (688)	1160 (688)	1160 (688)
Coarse aggregate lb/yd ³ (kg/m ³)	2320 (1375)	2320 (1375)	2320 (1375)	2320 (1375)
Water lb/yd ³ (kg/m ³)	290 (172)	230 (138)	290 (172)	230 (138)
Fresh concrete properties				
Slump, in. (mm)	(9) 229	(1.8) 46	(9.8) 249	(4.5) 114
Air content (%)	1.2	1.7	1.3	1.5
Unit weight, lb/ft ³ (kg/m ³)	145.5 (2330)	145.5 (2330)	145.5 (2330)	149.5 (2395)

3.4 Experimental Methodology

The experimental methodology consists of six different concrete mixtures. The mixtures include two traditional concrete mixtures, a normal strength (mixture NC) with average compressive strength of 26 MPa and high strength concrete (mixture HC) with average compressive strength of 27 MPa. Two mixtures of normal strength and high strength concrete with 0% cement replaced with fly ash were labeled as (NC) and (HC). Similarly, two mixtures with 40 percent fly ash as cement replacement (NF-40), and high strength concrete with 40 percent fly ash in the concrete mixture (HF-40). The other two mixtures were prepared using normal and high water-to-cementitious material ratio (w/cm) and cement replacement with fly ash of 60%, labeled as NF-60 and HF-60, respectively.

The mixtures and their respective labels are summarized as follows:

NC = Normal strength concrete with 0% fly ash in the mixture

HC = High strength concrete with 0% fly ash in concrete mixture

NF-40 = Normal strength concrete with 40% fly ash in the mixture

HF-40 = High strength concrete with 40% fly ash in concrete mixture

NF-60 = Normal strength concrete with 60% fly ash in the mixture

HF-60 = High strength concrete with 60% fly ash in concrete mixture

3.5 Specimens Curing and Sample Preparation

For the purpose of experimental investigation, in total five cylinders, 4 inches by inches (100 mm by 200 mm) were prepared for all six concrete mixtures. All cylinder specimens were fabricated by following the procedure specified in ASTM standards C-192-14 “Standard Practice for Making and Curing Concrete Test Specimens in the Laboratory.” The cylinders were cured for 28 days, in a tank totally immersed in water with a film of lime on top which was followed by recommendations specified by ASTM C206-14 “Standard Specification for Finishing Hydrated Lime.” After removing all cylinders from the curing period of 28 days, two concrete samples from each mixture group were tested to measure the compressive strength that was carried out in accordance with the ASTM C39/C39M-16 “Standard Test Method for Compressive Strength of Cylindrical Concrete Specimens.” One cylindrical specimen from each mixture was used to determine the elastic Young’s modulus, one cylinder from each mixture was kept as a control specimen and one cylinder was used to saw discs of 25 ± 3 mm and 50 ± 3 mm (1 and 2 in.) thick to determine the resonant frequency of each specimen before and after the high-temperature exposure. Each cylinder specimen was sawn into six discs the locations of which are shown in Figure 3.1.

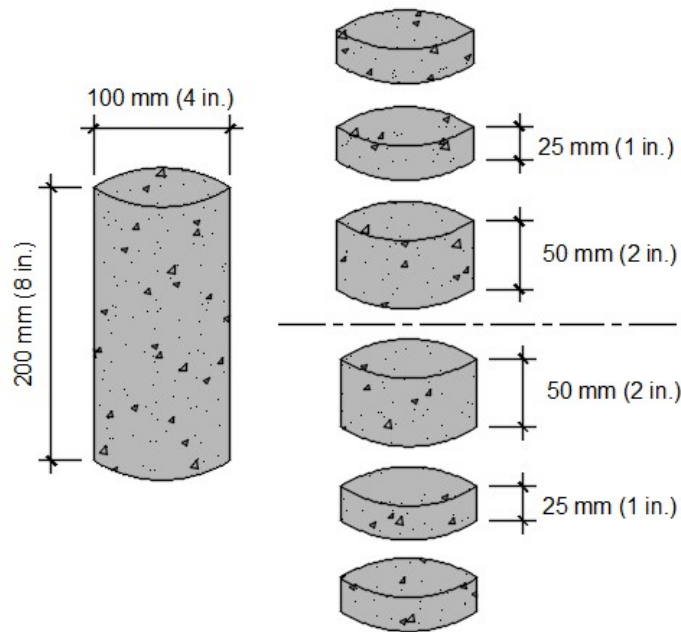


Figure 3.1: Location of disc specimens sawn from 100 by 200 mm (4 in. by 8 in.) cylindrical specimens

The first 25 mm (1 in.) disc was located between 30 and 55 mm from each side of the cylinder face, whereas the 50 mm thick disc was located between 60 and 110 mm from both faces of the cylinder, permitting 5 mm space for the saw cut. Discs on both the top and bottom faces of the cylinder were discarded due to irregularity in the surface and different mortar content caused by the finishing process during the fabrication of specimens. The resonant frequency of concrete discs was determined both in dry and soaked conditions. The purpose of testing the discs in the soaked condition is because the cracks and voids in the concrete get filled with water, making them heavier and harder for a sound wave to travel through the disc. Saw cutting of cylindrical specimens was done by using a water-cooled machine with a diamond-studded saw shown in figure 3.2 (a) and sawn discs of 25 mm and 50 mm are shown in figure 3.2 (b).



Figure 3.2: (a) Water-cooled diamond studded saw cutter (b) and discs sawn using saw-cutter.

Moreover, the methodology of sawing cylinders, labeling discs, damage levels, and the testing conditions are presented in Table 3.4 and figure 3.3. The details shown in table 3.3 were followed for all six concrete mixtures.

Table 3.4: Damage conditions and labeling of specimens.

Cylinder #	Description
1	: To determine compressive strength (f_c)
2	: To determine compressive strength (f_c)
3	: To determine modulus of Elasticity (E_c)
4	41A 42A 41B 42B
5	71Ca 72Ca 71Cb 72Cb

Cylinder 4	Cylinder 5
Top	Top
41A	71CA
42A	72CA
42B	72CB
41B	71CB
Bottom	Bottom

Figure 3.3: Sawing position and labeling of disc specimens

Furthermore, in concrete disc specimens, there is an addition of numbers 1 and 2, which identifies the thickness of disc where 1 shows 25 mm (1 in.) thick disc, and 2 shows for 50 mm (2 in.) thick concrete disc.

3.6 Experimental Tests for Freshly Mixed Concrete

Various tests for freshly mixed concrete in Phase-I have been conducted the details of which include the slump test of concrete and for all concrete mixtures used in this research work and was carried out in accordance with ASTM C143-14, “Standard Test Method for Slump of Hydraulic-Cement Concrete.” Another freshly mixed concrete test includes Unit Weight of Concrete and was conducted following the procedure specified in ASTM C-138-14, “Standard Test Method for Density (Unit Weight) of Concrete.” Air Content of Freshly Mixed Concrete was also determined using the pressure method specified by ASTM C 231-14, “Standard Test Method for Air Content of Freshly Mixed Concrete by the Pressure Method.”

3.7 Mechanical Properties of Concrete

3.7.1 Compressive Strength Test

Two concrete cylinders from each mixture were tested under compression loading. The compressive strength test was carried out in accordance with ASTM C39-16, “Standard test method for compressive strength of cylindrical concrete specimens.” This test was conducted on specimens cured for 28 days period in the water with a temperature equal to 23 ± 3 °C. The ultimate compressive load was determined and the average strength for each concrete mixture was calculated.

3.7.2 Modulus of Elasticity of Concrete

In concrete, the modulus of elasticity (E) is an indication of the capability of concrete to recall its original shape when undergoing stresses and strains. It is determined by dividing stress to strain as shown in equation (3.1), where stress is externally imposed load upon concrete and strain is the deformation occurring in concrete due to the external force.

$$E = \frac{\text{Stress}}{\text{Strain}} = \frac{\sigma}{\varepsilon} \quad (3.1)$$

Since E is stress divided by strain, one could expect concretes with higher values of E to be stronger, or more brittle, than concretes with a lower E value (Sean, 2003). The purpose of conducting this test was to find the variation in the elastic Young’s modulus ‘ E ’ of all concrete mixtures prepared with varying fly ash percentages and for normal and high water to cement ratios. The elastic Young’s modulus (E_c) of concrete was determined for specimens from each concrete mix using the calculated compressive strength test of concrete cylinders.

3.7.3 Microstructural Damage to Concrete Specimens

Microstructural damage was induced to selected specimens which was attained by exposing specimens to a relatively short period of the temperature of 300 °C (570 °F) in the oven for 2 hours. After exposing the disc specimens, the oven was turned off and the specimens were then left in the oven overnight which was later allowed to further cool down at the room temperature of nearly 25°C (80 °F) in the testing laboratory before performing further tests. The specimens were exposed to elevated temperature in order to produce mechanical damage caused due to the thermal expansion of various constituents and gas pressure of vapors entrapped inside the specimens without causing chemical decay (Phan and Carino 1998; Recalde and Leming 2009). The exposure time of two hours was selected for both 25 mm and 50 mm thick disc specimens. Once damaged, the specimens were sawn into discs for further tests. The microstructural damage mechanism to concrete discs for different groups is shown in Table 3.5.

Table 3.5: Damage Mechanism for Different Concrete Mixtures

Group	Damage Mechanism
A	Control specimens – No damage
C	In oven @ 300 °C for 2 hours

3.8 Testing Matrix for Concrete Discs

Two situations—undamaged and damaged—were established for conducting tests for the concrete discs. For the purpose of determining dynamic elastic Young's modulus (E_d), two specimen conditions, soaked and dry were considered. In the case of the soaked condition, discs were kept in half submerged in water for 24 hours with one face in contact with the air and then fully submerged for 24 hours, whereas in the dry condition, discs were kept in the oven at 50 °C to have constant mass before the damage. Upon removal of soaked discs from water, the surface was wiped out carefully to guarantee better contact between the accelerometer and test specimen for determining resonant frequency. Once the initial resonant frequency for undamaged specimens was measured to determine G_{skd} and to estimate $E_{d,skd}$, the concrete discs samples were left to dry in the oven at 50 °C for three days. The dried discs were later tested in dry condition to calculate G_{dry} and to estimate $E_{d,dry}$. Moreover, selected discs labeled with 'C' were exposed to 300 °C for two hours in the oven. After exposure, discs were kept in the oven overnight and were tested after cooling down. Once cooled, the discs were tested in dry condition and then soaked for 48 hours in water before testing in soaked (skd) condition to get the elastic moduli (G_d and E_d) in the damaged state. The mass of each disc was measured to the nearest 0.01 gram before conducting tests. The diameter and the thickness of discs were measured to the nearest 0.01 mm at three different locations around the perimeter and were the average value of all measurements were taken for each disc prior conducting further tests. Five different conditions to calculate the dynamic shear modulus are presented in table 3.6.

Table 3.6: Different conditions to measure dynamic shear modulus of discs.

1. G_d (Skd)	: Soaked before damage, after saw cutting
2. G_d (Dry)	: Dry at 50°C to constant mass before damage
3. G_d (Dry*)	: Exposed to 300 °C for 2-hours in muffle furnace to induce damage
4. G_d (Skd')	: Soaked after damage (24 hours with one face in contact with air, and 24 hours submerged)
5. G_d (Dry')	: Dry at 50 °C to constant mass after damage and after Skd' measurement

Legend: G_d = dynamic shear modulus, skd = soaked condition

3.9 Resonant Characteristics of Concrete Discs

During this part of the experimental investigation, the acceleration of the disc specimen in vibration was attained using a small piezoelectric accelerometer, which was attached to one side of the concrete disc, with soft and adhesive wax to ensure good contact and to guarantee better acoustical properties. In the testing procedure, the disc was suspended in the air with thin flexible wire and was excited by striking with a metal object, resulting in the creation of vibrations and energy in the disc. That energy is then transferred into a signal conditioner, which was attached to a computer, and displayed in a program called National Instruments “SignalExpress” where the signals were obtained. Signals from the accelerometer were determined at a sampling rate of 200,000 Hz. A minimum of 1100 data points were captured per signal. This was done due to the reason where the FFT function uses a base 2 logarithm for analysis purposes. Hence, it is required for the FFT

that the time series range to be calculated should contain a total number of data points to be accurately equal to 2^n (2 to the nth power) for example 512, 1024, 2048, etc. Therefore, 1100 or closer data points were captured to be able to evaluate a fixed length waveform containing points equal to 512, or 1024, or 2048, etc. For further analysis, the obtained frequency was further used to estimate the dynamic elastic Young's modulus of concrete, which is a parameter related to strength. Signal analysis was carried out using Fast Fourier Transform (FFT) and the resonant frequency of each disc was measured, which was then used to determine dynamic modulus of elasticity. The Resonant frequency was determined three times for each disc specimen and the average value was used for further calculations. The test setup for capturing the vibration signal of concrete discs is shown in figure 3.4 and the

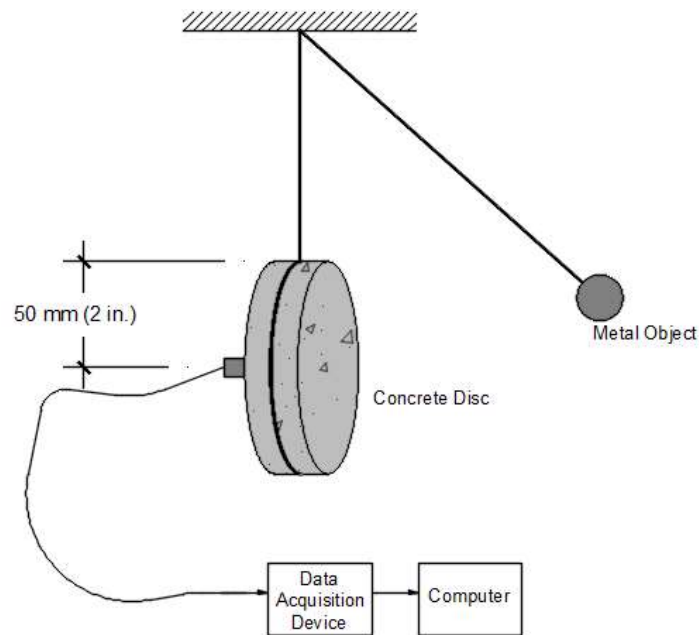


Figure 3.4: Test setup for capturing vibration signal of concrete discs

3.10 Determining Dynamic Young's Modulus of Elasticity

The procedure to calculate the dynamic Young's modulus of elasticity from the free resonance of concrete discs is presented in detail by (Leming et al., 1998) and is also used by (Recalde, 2009). The fundamentals for this testing approach originate from the theory developed by Hutchinson (1979) "assuming axisymmetric flexural vibration of thick, free circular plates, including shear and rotary inertia effects" (Recalde, 2009). The dynamic Young's modulus of a concrete disc under free-free vibration is presented as:

$$E_d = 2(1 + \nu)\rho \left(\frac{\pi f d}{\Omega_0}\right)^2 \quad (3.3)$$

where E_d = dynamic elastic (Young's) modulus, (Pa); ν = Poisson's ratio;

ρ = mass density of the disc specimen, kg/m³; f = fundamental cyclic natural frequency, Hz; d = diameter of the concrete disc, m; and Ω_0 = "dimensionless frequency parameter associated with the first mode of vibration", defined in terms of f as

$$\Omega_0 = \frac{\omega r}{v_s} = \frac{\pi f d}{v_s} \quad (3.4)$$

with

$$v_s = \frac{\sqrt{G}}{\sqrt{\rho}} \quad (3.5)$$

where v_s = shear wave velocity, m/s; G = shear modulus, Mpsi (GPa); and r = disc radius, m

The dynamic elastic modulus of concrete discs in both soaked and dry conditions was calculated by measuring f , d , and ρ . Poisson's ratio ν was estimated and Ω_0 was determined using an iterative solution that could easily be implemented using numerical solution with the evaluation capabilities of the Bessel function. Moreover, the thickness and the diameter of concrete discs were obtained as the average of at least three measurements taken at nearly equal spaces around the perimeter of discs, measured with an electronic device to the nearest of 0.1mm. The mass density of the disc specimen was calculated by dividing the mass of concrete disc over an equivalent volume of the cylinder and is given as:

$$\rho = \frac{M}{AL} \quad (3.6)$$

where M = mass of concrete disc, g; L = thickness of the disc, in; and A = cross-sectional area of the concrete disc, in², which is given as:

$$A = \frac{\lambda d^2}{4} \quad (3.7)$$

Poisson's ratio ν was estimated from the relationship to the stress wave velocities ratio in an elastic continuum as given in equation 3.8, where ν_p is the P-wave or compression wave velocity (Recalde 2009). The P-wave velocity was determined by measuring the length of flight time of longitudinal waves across the concrete disc diameter, which was carried out in accordance with ASTM Standard C597-16 "Standard Test Method for Pulse Velocity Through Concrete." The average value for the specimen diameter which was taken at three different locations spaced equally around the disc diameter was used as a representative ν_p for all the specimens for soaked and dry conditions. Pundit Pulse velocity apparatus was used to calculate the flight time for each specimen. Three measurements for

each specimen were determined, where the average of the value was used for further analysis purposes. The values which were clearly too high or too low were discarded and were due to the errors that sometimes occurred while contacting the transducers with a relatively small dimension (4 in.) of the specimen.

$$\left(\frac{v_p}{v_s}\right)^2 = \frac{2(1-\nu)}{1-2\nu} \quad (3.8)$$

Shear wave velocity was determined using an iterative process for Ω_0 and ν simultaneously, using the theory developed by Hutchinson (1979), and shown in equations 3.4 and 3.8. An estimate of dynamic shear modulus (G_d), instead of E_d , was determined from the relationship given in equation 3.9. Dynamic shear modulus G_d was estimated from the given relationship in order to minimize the dependency on ν for measuring elastic material constants (Recalde 2009):

$$v_s^2 = \frac{G_d}{\rho} \quad (3.9)$$

While conducting experimental tests with discs for frequency measurements, it was found that the accelerometer was difficult to attach to wet specimens with adhesive wax, and variability in signals was observed. The accelerometer was necessary to be attached firmly to the concrete disc allowing for measuring resonant frequency without any irregularities. However, after performing multiple trials and getting the accelerometer attached to the wet disc surface, the appropriate signals were measured. The adhesive wax was effective for attaching the accelerometer to dry concrete discs and the variability in results was not observed.

3.11 Air Permeability Index

The air permeability index of thin concrete discs used in this research work was determined using the procedure introduced by Schonlin and Hilsdorf (1988). According to Schonlin and Hilsdorf, the parameter is introduced as permeability “index” which is different than the permeability coefficients. The procedure identified by Schonlin and Hilsdorf is fundamentally a falling head, gas permeameter. In this method, the time is measured for a given pressure drop to occur between the top and bottom faces of the concrete disc specimen as air infuses through it. The Boyle-Marriotte law was used to develop the air permeability index equation, which assumes that the concrete disc is a homogenous porous medium. API is determined using the equation given as,

$$API = \frac{(p_1 - P_0)V_s}{(t_1 - t_0)[P_a - \frac{p_0 + p_1}{2}]} \frac{L}{A} \quad (3.10)$$

where;

API = air permeability index, m^2/s ,

P_0 = pressure inside the vacuum chamber measured at the start, Pa,

P_1 = pressure inside the vacuum chamber measured at the end, Pa,

P_a = atmospheric pressure, Pa,

$t_1 - t_0$ = time duration of measurement, sec

V_s = vacuum chamber volume, m^3 ,

L = disk thickness, m, and

A = cross-sectional area of the specimen, m^2

2

The testing apparatus used to measure the air permeability index is shown in Figure 3.5. The device consisted of a metallic vacuum chamber with a volume of 435 cm^3 . The

disc specimen was sealed on the side with a reusable impervious material to permit the transport of air only through the disc faces. A thin strip of soft clay is utilized to create a seal between the disc specimen and the chamber, an approach that has been used effectively in earlier research studies carried out by (Recalde and Leming 2009; Dilek *et al.* 2004; Dilek and Leming 2007a; Recalde 2005). Air from the chamber was released using a vacuum pump; the vacuum also firmly seated the specimen. The vacuum pump valve was shut when the vacuum reached a constant level of about 725 mm Hg (28.5 in. Hg). The time it took for the absolute pressure within the chamber to rise by any amount from the lowest attainable pressure was measured to the closest 0.01 second.

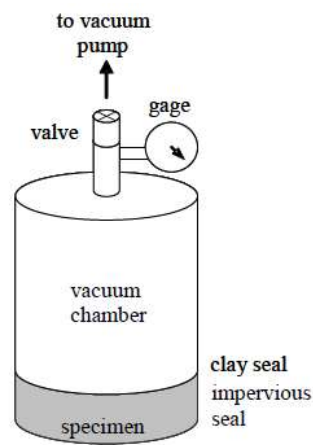


Figure 3.5: Test Apparatus for Measurement of the Air Permeability Index, (Recalde, 2009)

A reusable duct tape was used to seal the sides of concrete discs while determining the air permeability index, and the approach was also used in other research studies (Recalde and Leming 2009; Dilek *et al.* 2004; Dilek and Leming 2007a; Recalde 2005). Moreover, soft adhesive clay was found to be very effective for sealing the disc sides which provided better adhesion when compared to the duct tape when attached to concrete at locations where the coupling agent used for pulse velocity measurements had been absorbed.

3.12 Rate of Absorption of Water

The rate of Absorption of Water (Sorptivity) was determined in accordance with ASTM Standard C-1585 - 16 “Standard Test Method for Measurement of Rate of Absorption of Water by Hydraulic-Cement Concretes”. This test procedure is used to measure the rate of absorption of water by hydraulic cement concrete or mortar by calculating the rise in the total sample mass resulting due to the water absorption as a function of time when the specimen is exposed to water with one surface only. This test particularly measures the capillary rise absorption rate on concrete homogenous material like concrete. Concrete cylinders were fabricated and cured for the period of 28 days. After curing time, discs of 25 ± 3 mm and 50 ± 3 mm thick respectively were sawn from concrete cylinders using a saw cutter. The best possible concrete discs without any irregularities in dimensions were chosen for conducting the test. The diameter and thickness of the selected specimens were measured using an average of at least three dimensions.

3.12.1 Conditioning of specimens

The specimens shown in figure 3.6 were conditioned for three days in the oven at a temperature close to $50 \pm 2^{\circ}\text{C}$ and immersed in water as shown in figure 3.7 with a level of water not greater than 3 mm above the sample base. The relative humidity (RH) was kept in control in the desiccator with a saturated solution of potassium bromide. The saturated solution was kept at the bottom making sure the solution did not come in contact with test specimens. Relative humidity (RH) of 80% and 50°C conditioning was selected since it is specified in ASTM Standard C 1585 (2016). This test was conducted for soaked (SKD-condition), dry specimens (DRY-condition), and damaged discs (DMG-condition).

Selected discs were conditioned for three days by storing at 50⁰C and 80% RH, which was later kept in a sealed container for 15 days prior to testing for dynamic elastic properties and Sorptivity.



Figure 3.6: Concrete discs put in desiccator for conditioning



Figure 3.7: Water absorption test setup

Once the conditioning was done, the specimens were placed on a supported device inside the sealable polyethylene container and were kept at room temperature of 23⁰C ± 2⁰C for 15 days. The main purpose of conditioning inside the sealed container was to provide an

equilibration of the distribution of moisture in testing samples which were found to deliver an internal relative humidity of 50 to 70% which is comparable to the relative humidity determined in field structures. The total experiment test setup is shown schematically in figure 3.8.

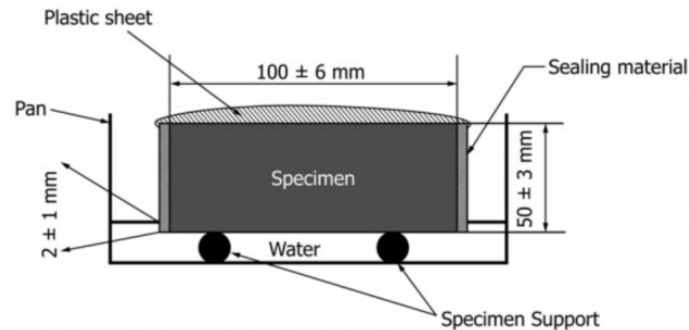


Figure 3.8: Schematic of the test setup

Moreover, test specimens were removed after 15 days of conditioning in a sealed container and the mass was measured and recorded to the nearest 0.1 g before sealing the peripheral surface and sides. After recording the mass, the test specimens were sealed with a sheet and duct tape to avoid water absorption into the sides of samples and to prevent evaporation of water held within the specimens. The specimen was covered at the top with the plastic sheet before it was wrapped with duct tape. After getting the specimens sealed, each disc was measured again, and the mass was recorded with the sides and non-tested surface sealed. Furthermore, the initial mass was recorded for further mass and to compare for the rate of absorption calculations. The water on the bottom of the specimen was wiped off with a towel and the weighing process was completed within the interval of 30 seconds between the subsequent specimens.

Chapter Four

Changes in Microstructure Properties due to Moisture Conditioning and High Temperature Damage (Phase-I)

4.1 Introduction

Mechanical properties of different concrete mixtures, free-free vibration signals, dynamic as well as the static modulus of elasticity, air permeability index, and the rate of water absorption of all disc specimens were obtained. Initially the compressive strength of various concrete groups was obtained, and discs were damaged at high temperature exposure of 300 °C (500 °F). Disc specimens in dry and wet conditions were used and the effect of moisture before and after the microstructural damage on signal characteristics of concrete specimens in free-free vibration was observed. Moreover, the dynamic Young's modulus calculated using the resonant frequency of different concrete discs was measured and was compared with different tests such as Air permeability index (API), and their relationships were observed. API was measured for damaged and undamaged specimens and for the specimens in dry and soaked conditions. Lastly, the water absorption ratio (Sorptivity) was measured for one-inch and two-inch thick disc specimens.

4.2 Compressive Strength Test Results

The compressive strength test result was determined for traditional concrete mixtures and of mixtures made with enhanced sustainability materials. The compressive strength test was carried out in accordance with ASTM C39-16, “Standard test method for compressive strength of cylindrical concrete specimens.” This compressive strength test was conducted on concrete specimens after the curing period of 28 days in fresh water having a temperature equal to 23 ± 3 °C. The ultimate compressive load was determined and the average strength for each concrete mixture was calculated the results of which are shown in Table 4.1.

Table 4.1: Compressive strength test results

Mixture Type	Labeling	Compressive Strength – MPa (psi)
Normal Strength Concrete	NC	26.6 (3860)
	NF-40	30.1 (4370)
	NF-60	50.1 (7270)
High Strength Concrete	HC	27.1 (3940)
	HF-40	32.5 (4710)
	HF-60	42.9 (6080)

4.3 Modulus of Elasticity of Concrete

Calculation of modulus of Elasticity was conducted in accordance with ASTM C 469/C469M-14 “Standard Test Method for Static Modulus of Elasticity and Poisson’s

Ratio of Concrete in Compression”. The purpose of conducting the test was to determine the variation in the modulus of elasticity ‘I’ of various groups of concrete prepared using different fly ash percentages in normal and high strength concrete. The Young’s modulus of elasticity (E_c) was calculated for specimens from each concrete mix using the already obtained compressive strength test from concrete cylindrical specimens. The determined value E_c for each mixture of concrete was then used to calculate secant modulus of elasticity (E_s), and the coefficient I for the secant modulus. for comparison purposes. The obtained results for Modulus of Elasticity are presented in table 4.2 and graphically represented in figure 4.1

Table 4.2: Modulus of Elasticity values for different concrete mixtures

S. No.	Mixture Type	F_c	Modulus of elasticity	Coefficient of Modulus
-	-	MPa (psi)	GPa (10^6 psi)	I
1	NF-40	26.9 (3900)	24.5 (3.55)	56996
2	HF-40	55.4 (8040)	35.2 (5.11)	56991
3	NF-60	33.4 (4850)	27.3 (3.97)	57025
4	HF-60	43.1 (6250)	31.1 (4.50)	56986

It could be observed in table 4.2 that concrete mixture HF-40 has the highest strength ($f_c = 8,040$ psi), followed by HF-60 ($f_c = 6250$ psi), NF-60 ($f_c = 4850$ psi), and NF-40 ($f_c = 3900$ psi). The HF-40 concrete mixture reveals the highest modulus of elasticity ($E = 5.11E+06$ psi) whereas NF-40 presents the lowest modulus of elasticity ($E = 3.55E+06$ psi).

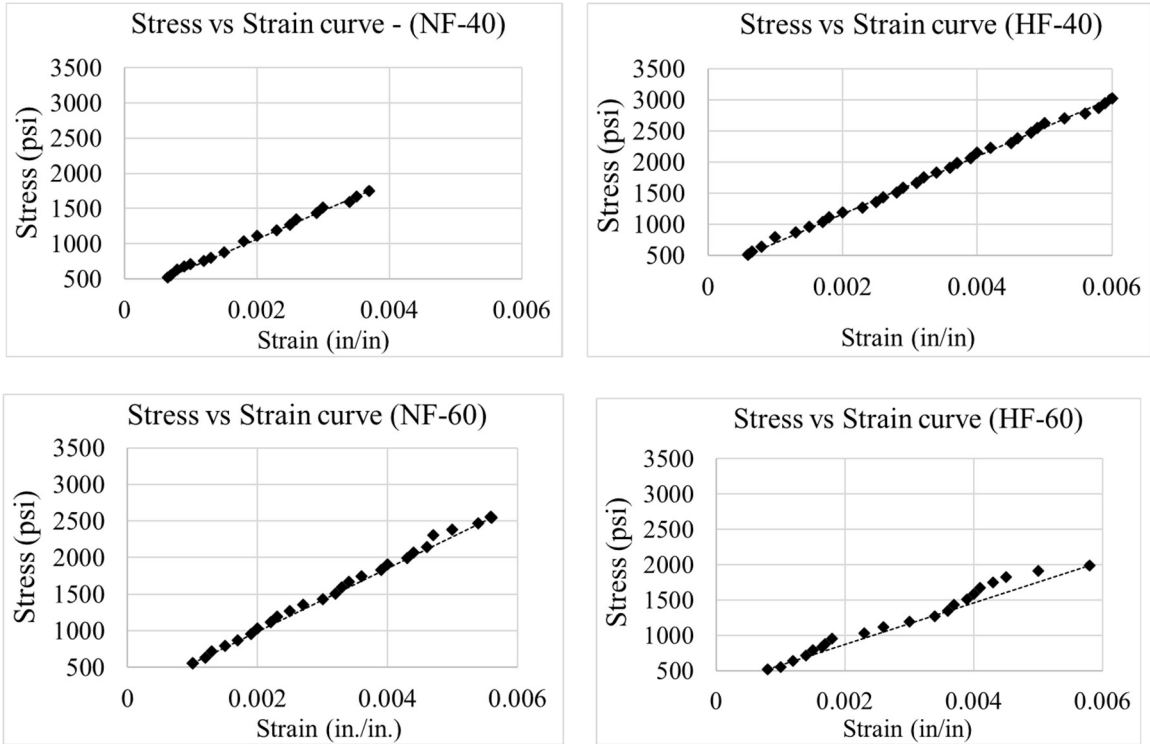


Figure 4.1: Modulus of Elasticity curve for different concrete mixtures

The second highest modulus of elasticity is exhibited by *HF-60* concrete mix ($E = 4.50E+06$) with the coefficient of ($C = 56,986$). The highest coefficient ($C = 57,025$) was demonstrated by concrete mixture *NF-60*. The calculated coefficients for all concrete mixtures seem to be reasonable and close to the generally accepted value of 57,000 which is given in equation 4.1 used to calculate Young’s modulus of elasticity of concrete in psi.

$$E = 57000 \sqrt{f'_c} \quad (4.1)$$

4.4 Signal Characteristics of Concrete Discs

Signal characteristics were obtained for disc specimens in dry and wet conditions. The acceleration of the disc specimen in vibration was determined using a small piezoelectric

accelerometer, which was attached to the one face of concrete disc. During this procedure, the disc was suspended in the air with thin flexible wire and was excited by striking with a metal object, resulting in the creation of vibrations and energy in the disc. That energy is then transferred into a signal conditioner, which was attached to a computer, and displayed in a program called National Instruments “SignalExpress” where the signals were obtained. For further analysis, the obtained frequency was used to compute the dynamic Young’s modulus of concrete, which is a parameter related to strength. Signal analysis was carried out using Fast Fourier Transform (FFT) and the resonant frequency of every disc was determined, which was further used to calculate dynamic modulus of elasticity. Resonant frequency was found at least three times for each specimen and the average value was taken. For the purpose of obtaining the frequency, the signals generated after striking the disc were analyzed by eliminating the portion of the signal at the impact and immediately after the impact, and selecting initial maximum acceleration as shown in figure 4.2 with green lines, after which all residual amplitudes in the signal were found having a lower value. This method of filtering was used to reduce the redundant or lower valued signals in the resonant frequency analysis, which is reported in previous studies (Recalde and Leming, 2009; Dilek and Leming, 2008). The selected maximum and lower values of acceleration were then processed for further data requirements. A sample size of 1024 data points was used for each analysis. The mean resonant frequency measured for all mixture types is presented in Table 4.3.

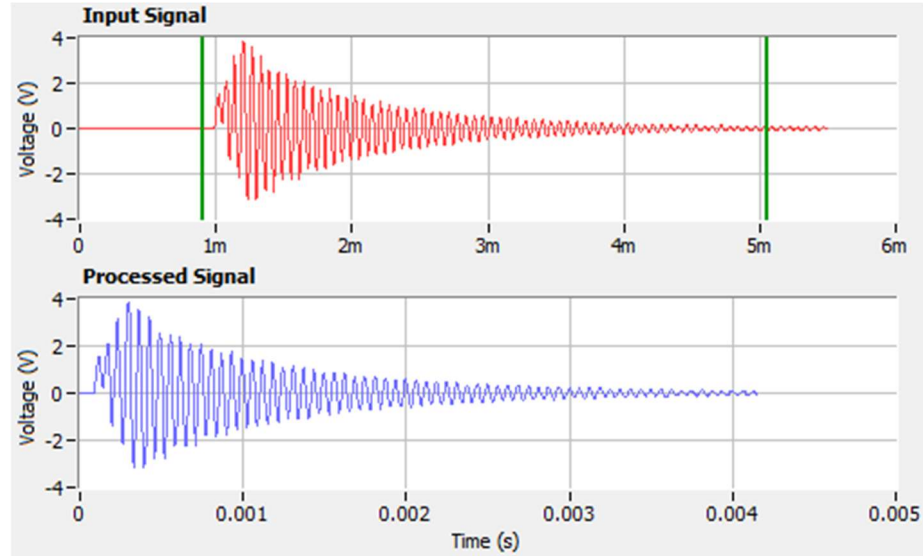


Figure 4.2: Obtained signals indicated by green lines and processed signals (Signal Express software).

Table 4.3: Mean Resonant Frequency of concrete discs of one and two-inches damaged at high temperature exposure

S.No.	Specimen	Resonant Frequency (Hz)				
		Dry	SKD	Dry*	SKD'	Dry'
1	NC-4-1A	12500	13281	7813	10156	9375
2	NC-4-2A	17188	17969	9375	14323	13021
3	HC-4-1A	14063	14063	8593	11197	10416
4	HC-4-2A	17969	18750	10156	14843	14843
5	HF40-7-1CA	9831	10546	5859	4427	5534
6	HF40-7-2CA	15885	17189	8073	8008	7943
7	HF60-7-1CA	9766	10286	4492	4818	4688
8	HF60-7-2CA	11621	16850	6380	6576	6771
9	NF40-7-1CA	6771	7682	3581	3711	3516
10	NF40-7-2CA	12109	15890	5990	5729	6380
11	NF60-7-1CA	7617	8203	4297	4688	4622
12	NF60-7-2CA	13021	14193	6120	7227	6771

4.5 Calculating Dynamic Young's Modulus of Elasticity

The Dynamic elastic Young's (E_d) from the free resonance of concrete discs was determined using the procedure presented by (Leming et al., 1998) and is explained in section 3.11. Calculated E_d for all concrete disc specimens from each mixture type and at each moisture condition is presented in Table 4.4. Equation 4.2 was used to calculate E_d for all mixture types before and after temperature exposure

$$E_d = 2(1 + \nu)\rho \left(\frac{\pi f d}{\Omega_0} \right)^2 \quad (4.2)$$

The obtained results shown in Table 4.4 for E_d consider the resonant frequency values measured shown in Table 4.3, measured density, dimensions of the discs and assumes a Poisson's ratio (ν) of 1/4.

Table 4.4: Dynamic Young's Modulus of Elasticity of one and two-inches Concrete Discs for Different Moisture Conditioning and at High Temperature Exposure

Specimen ID	Dynamic Young's Modulus of Elasticity, GPa (Mpsi)				
	Dry	SKD	Dry*	SKD'	Dry'
HF40-7-1CA	21.7 (3.38)	25.5 (3.96)	5.05 (0.87)	3.46 (0.58)	5.03 (0.84)
HF40-7-2CA	21.1 (3.37)	28.7 (4.45)	5.11 (0.87)	5.14 (0.87)	5.02 (0.85)
HF40-7-2CB	30.6 (4.42)	41.8 (5.95)	6.22 (1.05)	6.80 (1.15)	6.79 (1.14)
HF40-7-1CB	34.5 (4.49)	36.9 (5.12)	6.41 (1.10)	3.68 (0.63)	6.12 (1.02)
HF60-7-1CA	10.0 (1.68)	9.3 (1.54)	1.37 (0.24)	3.56 (0.60)	2.32 (0.40)
HF60-7-2CA	12.1 (1.99)	14.2 (2.24)	2.52 (0.43)	3.17 (0.53)	3.03 (0.52)
HF60-7-2CB	14.4 (2.30)	17.0 (2.71)	4.23 (0.72)	4.82 (0.81)	5.02 (0.84)
HF60-7-1CB	18.2 (2.82)	27.2 (3.86)	5.63 (0.96)	4.94 (0.82)	5.40 (0.89)
NF40-7-1CA	10.4 (1.73)	19.1 (2.89)	1.93 (0.33)	2.00 (0.34)	1.71 (0.29)
NF40-7-2CA	12.7 (2.05)	16.9 (2.62)	3.12 (0.54)	1.78 (0.31)	3.34 (0.56)
NF40-7-2CB	15.8 (2.52)	16.9 (2.66)	3.23 (0.55)	5.00 (0.84)	4.17 (0.70)
NF40-7-1CB	21.3 (3.19)	11.0 (1.83)	1.93 (0.33)	2.55 (0.44)	2.18 (0.37)
NF60-7-1CA	10.3 (1.71)	10.9 (1.81)	2.57 (0.44)	2.75 (0.47)	2.85 (0.49)
NF60-7-2CA	12.9 (2.12)	16.2 (2.62)	2.98 (0.51)	4.25 (0.71)	3.58 (0.60)
NF60-7-2CB	11.1 (0.17)	16.2 (2.54)	3.06 (0.53)	5.59 (0.92)	4.26 (0.72)
NF60-7-1CB	31.3 (4.19)	21.2 (3.22)	2.88 (0.50)	4.89 (0.82)	3.85 (0.65)

4.6 Changes in Fluid Penetrability Properties

Changes in Fluid penetrability properties were obtained through Air Permeability Index (API) and Rates of Absorption of Water (S) the details of which are presented in sections 3.12 and 3.13 respectively. The measurements of water absorbed for all mixture groups at different time intervals are given in Table 4.5. Moreover, the calculated values for API and Sorptivity for disc specimens from all different mixture groups are presented in Table 4.6. The changes obtained in Rates of Absorption of Water for concrete discs are shown in figures 4.3 to 4.6 where the graphs of water absorption versus the square root of time for each disc specimens are presented. Various research studies carried out in past observed little difference in API for undamaged concrete specimens with normal to high strengths. (Dilek et al. 2004; Dilek and Leming 2007a) hypothesized that API was susceptible to the interconnected microcracks presented in the concrete solid. Disc specimens damaged at high temperatures showed higher Initial Rates of Absorption of Water (S_i) for 50 mm thick disc specimens than undamaged specimens for all mixture groups. The Secondary Rates of water absorption (S_s) characteristics were different for specimens made from various mixtures with fly ash content. In most cases, as shown in Table 4.6, determining water absorption rates was not possible since the correlation coefficient (r) was less than 0.98 and ASTM C1585-16 mentions that when calculating the rates of water absorption, the correlation coefficient should always be greater than 0.98. These values were obtained using least square linear regression analysis. The experimentally obtained results of API for undamaged and damaged specimens are presented in Table A1 and Table A2 in Appendix-A.

Table 4.5: Water absorbed in different time intervals

Specimens	NF40-42A	NF40-72A	NF40-72B	HF40-42A	HF40-72A	HF40-72B	NF60-42A	NF60-72A	NF60-72B	HF60-42A	HF60-72CA	HF60-72CB
-	1:12:30	1:13:00	1:13:30	1:12:30	1:13:00	1:13:30	1:12:30	1:13:00	1:13:30	1:12:30	1:13:00	1:13:30
Weight	(g)	(g)										
Place	933.29	837.31	949.00	981.61	924.71	951.9	930.56	917.42	869.07	830.76	904.57	918.16
1'	935.91	843.66	954.82	984.14	927.08	954.12	934.07	925.74	874.48	833.23	909.57	923.69
5'	937.92	846.33	958.00	984.79	928.64	955.64	936.94	932.32	879.65	835.09	914.22	928.54
10'	938.99	849.03	960.22	985.33	929.67	956.66	939.01	937.45	883.12	836.31	917.32	931.84
20'	940.44	852.26	963.34	986.09	931.46	957.98	941.41	943.63	887.66	837.89	922.04	935.49
30'	941.7	855.11	965.92	986.67	932.87	959.28	943.15	947.96	890.84	839.18	924.88	938.52
1 h	944.09	860.75	970.85	987.99	935.73	961.56	945.99	954.89	894.87	842.07	929.75	944.06
2 h	947.18	867.54	975.36	989.53	939.61	964.77	948.58	961.6	902.84	845.62	934.54	949.84
3 h	949.28	871.56	978.17	990.64	942.38	967.13	950.48	962.3	905.21	847.81	936.28	951.87
4 h	950.95	872.52	979.85	991.41	944.18	968.86	951.63	962.44	905.73	849.64	936.76	952.49
5 h	952.39	872.75	980.57	991.9	945.42	970.27	952.39	962.49	905.78	851.1	937.14	952.75
6 h	953.18	873.05	980.66	992.4	946.07	971.34	953.08	962.63	906.94	851.85	937.15	952.78
1 D	956.32	874.03	982.06	994.5	947.07	973.45	954.6	963.16	906.49	856.17	937.9	953.59
2 D	956.55	874.56	982.49	994.94	947.36	973.91	955.08	963.96	907.3	856.59	938.41	954.04
3 D	956.84	874.88	982.84	995.28	947.68	974.19	955.52	964.6	908.11	856.71	939.17	954.62
4 D	957.36	875.36	983.39	995.61	948.03	974.39	955.8	965.04	908.41	857.21	939.74	955.13
5 D	957.49	875.7	984.03	995.96	948.36	974.7	955.92	965.3	908.75	857.25	940.11	955.35
6 D	957.34	876.1	984.44	996.17	948.74	975.04	956.01	965.63	908.98	857.42	940.56	955.98
7 D	957.56	876.5	984.66	996.18	949	975.2	956.25	965.92	909.17	857.58	940.61	956.04
8 D	957.77	876.82	984.99	996.46	949.02	975.41	956.45	966.17	909.33	857.92	940.73	956.28
9 D	958.04	876.83	985.11	996.74	949.35	975.61	956.53	966.33	909.62	858.36	940.95	956.48

“h” is hour, “D” shows day, “g” shows gram and “Place” is the weight of the specimen with adhesive and plastic wrap

Table 4.6: Air Permeability Index and Rates of Absorption of Water for Concrete Disc specimens from Four Mixture Groups for moisture conditioning before and after damage at High Temperature Exposure of 300 °C for Two different Thicknesses.

Mixture Group	Specimen	Air Permeability Index, (m ² /s)		Initial Rate of Absorption of Water, x10 ⁻⁴ mm/sec ^{0.5}
		Before Damage	After Damage	
NC	NC-7-1C	1.3E-06	4.9E-06	-
25 mm				
HC	HC-7-1C	1.9E-06	7.4E-06	-
25 mm				
NF40	NF40-7-1C	1.8E-05	2.4E-05	-
25 mm				
HF40	HF40-7-1C	2.9E-05	2.9E-05	-
25 mm				
NF60	NF60-7-1C	2.2E-05	2.9E-05	-
25 mm				
HF60	HF60-7-1C	1.7E-05	2.3E-05	-
25 mm				
NC	NC-7-2C	3.9E-06	2.5E-06	78
50 mm				
HC	HC-7-2C	4.4E-06	2.5E-06	104
50 mm				
NF40	NF40-7-1C	2.3E-05	3.8E-05	*
50 mm				
HF40	HF40-7-1C	3.8E-05	3.7E-05	50
50 mm				
NF60	NF60-7-1C	4.6E-05	3.7E-05	*
50 mm				
HF60	HF60-7-1C	4.9E-05	3.2E-05	*
50 mm				

Legend: “-“ Data was not obtained for one inch disc, “*” The Correlation obtained is less than 0.98

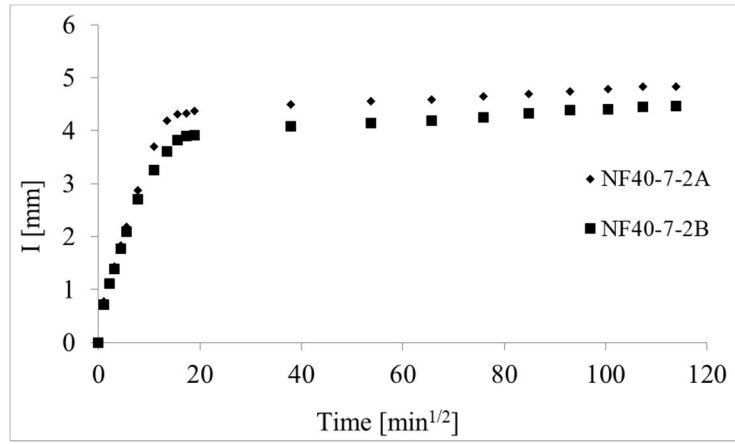


Figure 4.3: Initial and Secondary Water absorption of NF40 concrete mixture

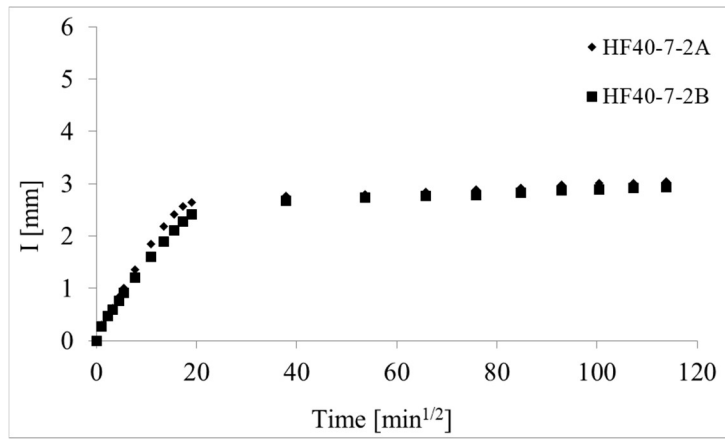


Figure 4.4: Initial and Secondary Water absorption of HF40 concrete mixture

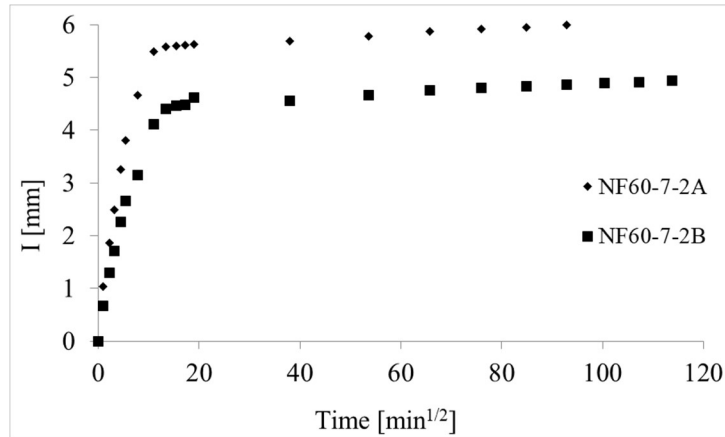


Figure 4.5: Initial and Secondary Water absorption of NF60 concrete mixture

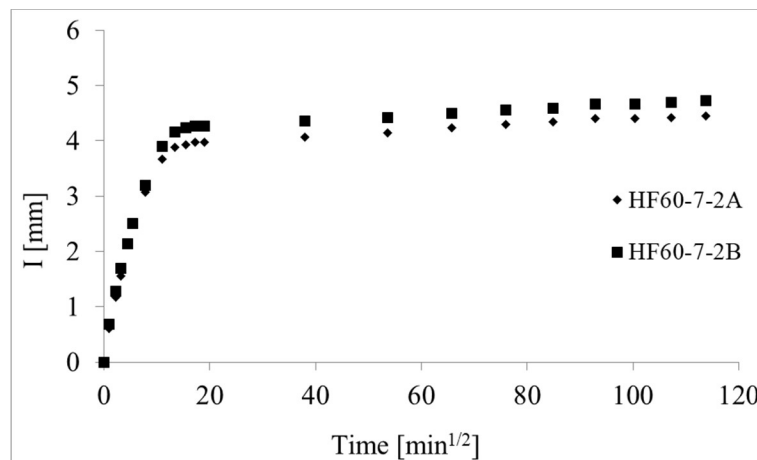
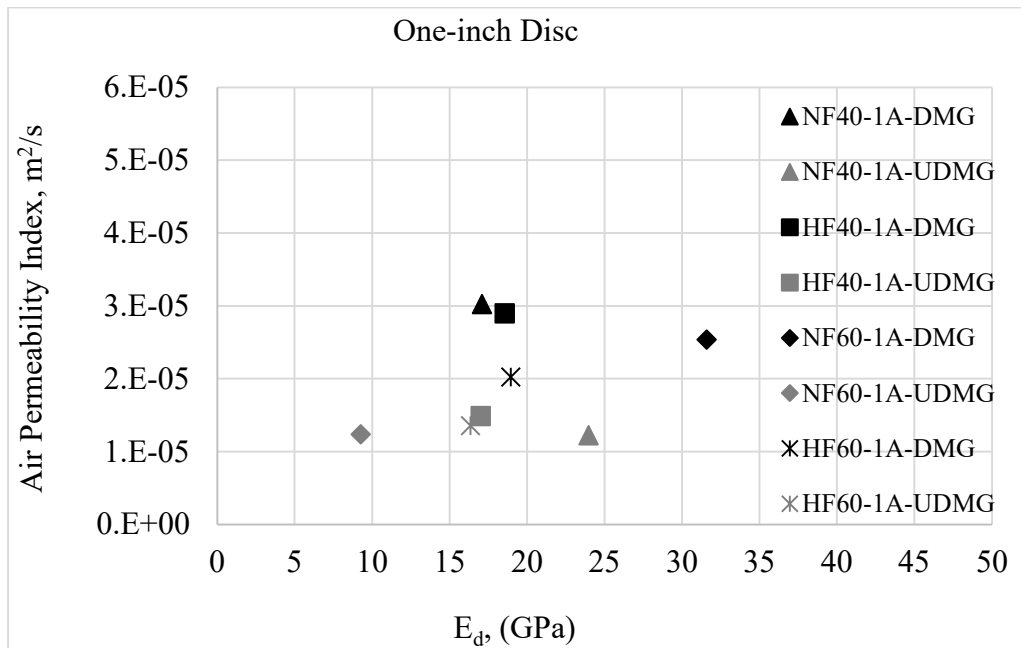


Figure 4.6: Initial and Secondary Water absorption of NF60 concrete mixture

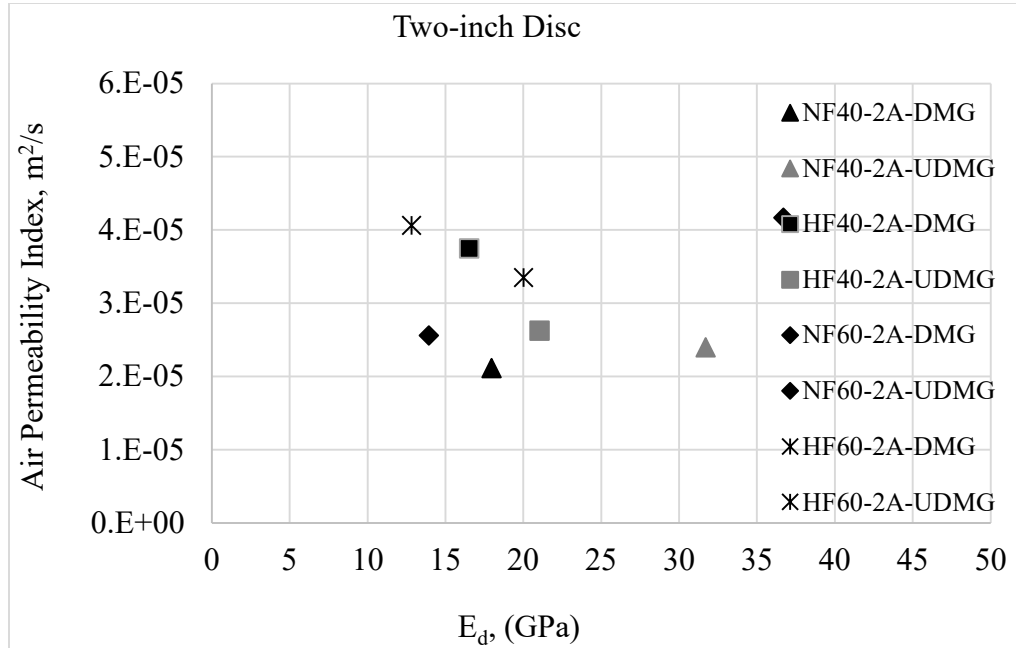
4.7 Relationship between the Measured Properties

Changes in the measured values of E_d and API after moisture conditioning are of interest since these parameters and the results have been effectively used in forensic investigations (Dilek and Leming 2007a; Dilek *et al.* 2003; Dilek 2008) and have been incorporated in the experiments carried out by (Recalde and Leming 2009; Recalde 2005;

Dilek and Leming 2007b). Figure 4.7 (a) shows E_d versus API for Normal and High strength mixture groups with different fly ash content for one-inch-thick discs. In the case of undamaged specimens, high E_d and low API are observed, however, for the damaged specimens low E_d and high API results were obtained. Similar measurements are also obtained in the case of two inches thick discs as shown in figure 4.7 (b).



(a)



(b)

Figure 4.7: Relationship Between E_d and API: (a) E_d versus API for Normal and High strength mixture groups with different fly ash content for one-inch-thick discs, (b) E_d versus API Relationship for two mixtures for two-inch thick discs.

The measured data is generally consistent with the previously reported results by Recalde and Leming (2009) where higher API resulted in lower E_d . In some cases, the proper results were not obtained which could be due to the possible errors in API due to the leaking of air during the testing procedure. The overall experimental results for the air permeability index obtained for undamaged specimens are presented in Table A1 and the measurements for damaged specimens are shown in Table A2.

4.8 Statistical Analysis Results

4.8.1 Effect of Fly Ash on Air Permeability Index (API)

Statistical analysis was carried out by considering the mean of all measured air permeability index results as presented in Table 4.7, however, the overall obtained experimental results for API before and after damage exposure are given in table 4.8.

Table 4.7: Means of Air Permeability Index for Undamaged and Damaged Disc Specimens

-	NF40-7-CA	HF40-7-CA	NF60-7-CA	HF60-7-CA
Undamaged Group	4.06E-05	6.72E-05	6.79E-05	6.66E-05
Damaged Group	6.22E-05	6.57E-05	6.61E-05	5.51E-05
Variance	2.31E-10	1.20E-12	1.71E-12	6.69E-11

The effect of high-temperature exposure of 300 °C was considered and differences between the damaged and undamaged groups of mixtures were determined. A single factor ANOVA procedure was carried out for all mixture groups. The sample means for mixtures NF40, HF40, NF60, and HF60 before damage were 4.06E-05, 6.72E-05, 6.79E-05, and 6.66E-05 respectively, however, means after damage for the same mixture groups were 2.31E-10, 1.20E-12, 1.71E-12, and 6.69E-11 respectively. Moreover, the effect of fly ash percentage on the Air Permeability Index was also determined and ANOVA analysis resulted in a p-value equal to 0.826 which is greater than the alpha value of 0.05. This result shows that there is a significant effect of fly ash percentage on the Air Permeability Index. In this case, we cannot reject the null hypothesis. Moreover, the ANOVA analysis results are shown in Appendix-B.

Table 4.8 shows the measured individual values of API and the average values of API₁ and API₂.

Table 4.8: Air Permeability Index for Different Concrete Mixture Groups before and after damage at 300 °C

Mixture Group	Average	STD. DEV.	Average	STD. DEV.
	API		API ₁ and API ₂	
	m ² /s		m ² /s	
Undamaged Condition				
NF40-7-CA	2.03E-05	3.36E-06	2.03E-05	5.42E-06
HF40-7-CA	3.36E-05	6.24E-06	3.36E-05	1.28E-05
NF60-7-CA	3.40E-05	1.75E-05	3.40E-05	1.74E-05
HF60-7-CA	3.33E-05	2.27E-05	3.33E-05	2.03E-05
Damaged Condition				
NF40-7-CB	3.11E-05	9.57E-06	3.11E-05	1.22E-05
HF40-7-CB	3.28E-05	5.81E-06	3.28E-05	1.24E-05
NF60-7-CB	3.30E-05	5.50E-06	3.30E-05	1.01E-05
HF60-7-CB	2.75E-05	6.11E-06	2.75E-05	6.90E-06

4.9 Summary

Chapter four of this dissertation (Phase-I) provided important results for concrete mixture with varying percentages of fly ash, the resonant frequency characteristics, and the effect of moisture content on the properties of different concrete mixtures. Moreover, a relationship between the dynamic Young's elastic modulus and the fluid penetrability

properties has also been part of the essence of this chapter. The following are the conclusions obtained from the first phase of this research study,

- Percentage replacement of cement with supplementary material such as fly ash showed a significant improvement in the compressive strength when compared to the traditional concrete. In the case of normal strength concrete, the compressive strength increased from 26.6 MPa to 30.1 MPa for concrete with 40% fly ash and 50.1 MPa for concrete with 60% fly ash.
- In the case of high strength cement concrete, the compressive strength increased significantly from 27.1 MPa to 32.5 MPa for mixture with 40% fly ash and 42.9 MPa for mixture with 60% fly ash. This presents that concrete with a higher fly ash percentage up to 60% could be used for structures exposed to a high temperature of about 300 °C.
- A higher value of E_d was observed for specimens soaked than the unsoaked or dry specimens. This is due to the water held in the large capillaries in the concrete solid resulting in the stiffening effect. This increase in the dynamic modulus of elasticity is due to the increase in the resonant frequency of disc specimens to a significant amount.
- Higher Initial water absorption rates (S_i) for damaged 50 mm thick disc specimens was observed than the undamaged specimens for all mixture groups. The Secondary Rates of water absorption (S_s) characteristics were different for specimens made from various mixtures with fly ash content.
- In most cases, water absorption rates were not obtained since the correlation coefficient (r) was less than 0.98.

- A relationship between E_d versus API for Normal and High strength mixture groups with different fly ash content was conducted which showed that, in the case of undamaged specimens, high E_d and low API was observed, however, for the damaged specimens low E_d and high API results were obtained. These results also behaved similarly in the case of two inches thick discs.

Statistical analysis results presented that there is a significant effect of fly ash percentage on the Air Permeability Index.

Chapter Five

Development of Analytical Technique for Characterization of Concrete and Microstructural Level (Phase II)

5.1 Introduction

This chapter presents the utilization of experimentally obtained results and identifying analytical model, to determine the modulus of elastic of thin concrete discs which is Phase II of this research study. The purpose of identifying the theoretical framework was to establish a practical tool to effectively characterize the effect of microcracking and damage on the elastic properties of dry and soaked concrete discs vibrating in free resonance. The idea behind the theoretical framework was to extend the model used in Rock mechanics and apply it to concrete materials of various types using thin concrete discs and which could easily estimate the material properties of concrete damaged when exposed to elevated temperatures. Additionally, the problem is defined in this chapter and the selected physical model is presented. The obtained model has been further modified and extended to be applicable to the resonant testing of thin concrete discs vibrating freely, the results of which have been compared using previously developed models. The experimental investigation carried out in Phase I, using various concrete mixtures with different fly ash proportions is further analyzed using the developed analytical model. A finite element analysis (FEA) was also performed to

compare the theoretical model behavior with that obtained using numerical models which is presented in Chapter Five of this dissertation.

5.2 Problem Setting

Thin concrete circular discs with inclusions such as absorbed or penetrated water undergoes the influence of many exerted forces and mechanisms acting upon them. Concrete is considered a heterogeneous material; however, it also depends on the scale of the analysis. If the concrete is analyzed at a macro-scale level, it could be assumed as homogeneous. From the morphological point of view or at a microstructural level, the concrete and its surface are considered as heterogeneous materials (Sadowski and Mathia, 2016). Due to the heterogeneous composition and phases of concrete, it becomes difficult to investigate the damage at the microscale level. Hence, an effective theoretical model could be used to estimate the deterioration that occurred in the concrete solid by considering thin circular discs. The formation of concrete with its constituents along with pores is shown in figure 5.1.

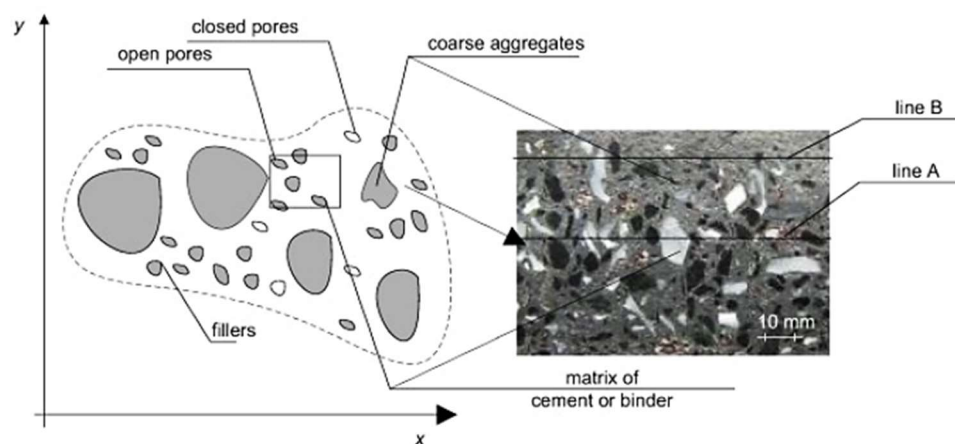


Figure 5.1: Concrete solid with different constituents (Sadowski and Mathia, 2016)

When determining the resonance characteristics of the thin concrete disc while performing experimental investigation, the difference observed in the resonant frequency between dry and soaked conditions of specimens is due to the presence of free water inside the pores. In soaked condition, the water entrapped in the interrelated void or microcracks system during the resonance is held by a combination of capillary adsorptive forces which results in pore fluid pressure being imposed on the outermost concrete walls at rest. When the circular discs undergo vibrations, shear strains and flexural strains of order around 10 kHz, generate a hydraulic relationship between the concrete matrix and the water through viscous flow. The random distribution of pores and the system of cracks in the solid, their size, and volumetric fractions of the constituents in various concrete mixtures with different damaging level, makes the modeling procedure complicated for the specimen. However, the variations in resonant behavior are generally due to the overall effect of the fluid entrapped inside the interconnected void system of the individual specimen. The variability and random distribution with the irregular orientation of the voids and cracks in the solid are due to the mixture proportions and the constituents, however, the mean characteristics between the mixtures provide a proper understanding of the primary differences in the micro-structural system (Recalde, 2009). When concrete mixtures are not properly mixed, it is likely to happen that the mixture could have a number of empty voids inside the solid specimen. Once the concrete gets hydrated, the water could penetrate and result in the overall changes of elastic properties. On the contrary, once cracks get generated at the later stage in concrete, the penetrated water could work initiate the hydration process again between the water and concrete resulting in self-healing of concrete and gaining more strength.

5.3 Identification of analytical Model

5.3.1 Areas Explored

To identify an effective analytical model to determine the changes occurring at the microstructural level of concrete, areas of fluid mechanics and rock physics were explored. Most of the analytical tools were presented in the 'Rock Physics Handbook' by (Mavko et al., 2009) and were studied. Several models from the rock mechanics that were considered, were not found to be a good representative of damaging behavior in concrete. Moreover, a few potential models, including a model developed by Cheng (1993) considering Padé approximation, were still found to be inapplicable for concrete after certain limitations of crack density parameter. The main idea was to estimate the crack density parameter and ultimately the elastic Young's modulus, but many potential models did not consider this parameter. Detailed examination of the models was carried out by solving numerical examples and checking their applicability for the thin concrete discs at resonance in free-free vibration. Successful models for the determination of elastic properties of the material were found in the area of stress wave propagation under the effective elastic media models. Stress wave propagation into the cracked media or the elastic continuum provides a deep understanding of the microstructural behavior and insight for the solid and fluid interaction with harmonic strains at relatively higher frequencies. The analytical models mostly consider the saturated and dry conditions separately for analysis purposes, as the dry voids are different from the fluid-filled cracks or voids. One of the most commonly used models to estimate the elastic moduli of mixtures with pores is Hashin-Shtrikman (1963) model. Theoretically, this model requires:

- (1) the volume proportions or fractions of different phases,
- (2) the elastic moduli of different phases, and
- (3) the geometric arrangement of the phases relative to each other.

For the model, if only the volume fraction and the inclusion moduli are specified, then the best way could be to prediction of the upper bounds and lower bounds as shown in figure 5.2.

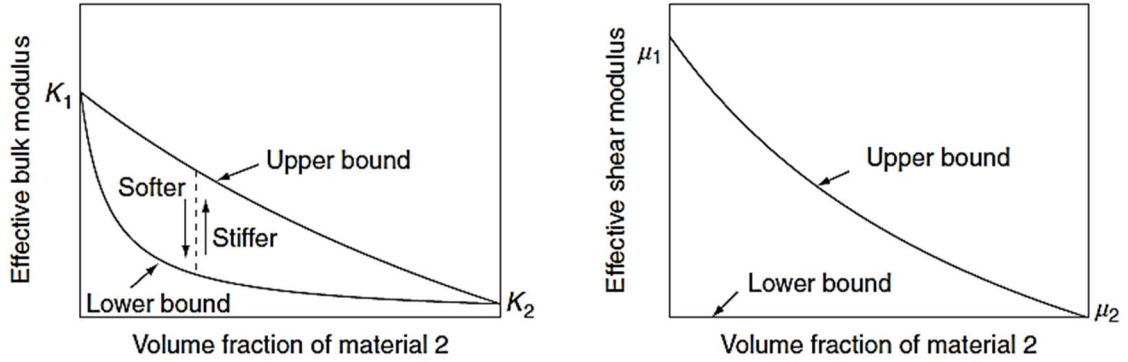


Figure 5.2: Diagram representing the upper and lower bounds on the elastic bulk and shear moduli (Mavko et al., 2009)

In the plot shown for bulk modulus, the effective modulus at any given volume fraction of the constituents in the solid could range between the bounds at any place along the dashed line shown vertically; however, the geometrical details play an important part in finding the precise value. The Hashin-Shtrikman bounds (Hashin-Shtrikman, 1963) have been observed to be ideal for specifying the best bounds for isotropic elastic composite for the cases where the geometrical details about constituents are not specified. In the situation where only two constituents exist, the bounds are presented as:

$$K^{HS\pm} = K_1 + \frac{f_2}{(K_2 - K_1)^{-1} + f_1 \left(K_1 + \frac{4}{3} \mu_1 \right)^{-1}} \quad (5.1)$$

$$\mu^{HS\pm} = \mu_1 + \frac{f_2}{(\mu_2 - \mu_1)^{-1} + 2f_1 (K_1 + 2\mu_1) / [5\mu_1 \left(K_1 + \frac{4}{3} \mu_1 \right)]} \quad (5.2)$$

where K_1 and K_2 are the bulk moduli of individual phases, μ_1 and μ_2 are the shear moduli of individual phases, and f_1 and f_2 are the volume fractions of the individual phases (Mavko et al., 2009).

5.3.2 Selection of Analytical Model

One of the most important challenges in the analysis of solids is predicting the shear wave velocities in solids saturated with liquid and those with dry-solid velocities and their effects on the elastic properties of the material. Hence, this section provides a brief overview of some of the physical models and theories that have been examined to explain why the estimated elastic moduli are higher when the specimen is saturated than when it is air dry. Since this phenomenon occurs due to the availability of free water in the interconnected system of voids and cracks, the goal was to identify a parameter that could describe the microstructure and its effect on the elastic properties which could easily be measurable from the simple quantities which are based on resonant frequencies presented in chapter three of this dissertation. Moreover, the relationship between stress wave propagation and free-free resonance of thin circular discs is described, followed by a brief overview of the various physical models and their applicability to the thin circular-shaped specimens' resonance test.

Specimens such as thin or thick discs, cylindrical elements, plates, and rods get excited at resonance by the inherent standing shear wave that coincides with their first vibration mode (Recalde, 2009). According to Hutchinson's (1979) hypothesis about the case of a thick circular plate, the first mode of vibration is generated by the presence of a standing shear wave. The formula to determine the dynamic shear modulus (G_d) of thin concrete discs is

presented by equation 5.7, followed by the combination of shear wave velocity and shear modulus expressions given in equations 3.4 and 3.6, respectively.

$$G_d = \rho v_s^2 \quad (5.5)$$

$$G_d = \rho \left(\frac{\omega r}{\Omega_0} \right)^2 \quad (5.6)$$

$$G_d = \rho \left(\frac{\pi f d}{\Omega_0} \right)^2 \quad (5.7)$$

To completely elaborate on the elastic body, more parameters such as Bulk modulus, Poisson's ratio, modulus of elasticity, or Lamé constants are required. To fulfill this criterion, the ultrasonic pulse velocity in accordance with ASTM-C597-16 was used.

In general, when a porous material is loaded under a considerable amount of compression, such as from a passing seismic wave, an increase in pore pressure occurs, which resists the compression and stiffens the material (Mavko et al., 2009). The low-frequency Gassmann–Biot (Gassmann, 1951; Biot, 1956) model predicts an increase in effective bulk modulus K_{sat} when a porous material is saturated, which is given by the expressions 5.8 and 5.9. Gassmann's model could be effective in determining the bulk modulus of a saturated porous material from the dry bulk modulus (Recalde, 2009).

$$\frac{K_{sat}}{K_0 - K_{sat}} = \frac{K_{dry}}{K_0 - K_{dry}} + \frac{K_{fl}}{\phi(K_0 - K_{fl})} \quad (5.8)$$

$$\mu_{sat} = \mu_{dry} \quad (5.9)$$

Or equation 4.9 could also be written as;

$$G_{sat} = G_{dry} \quad (5.10)$$

where K_{dry} = the effective bulk modulus of dry porous material, Pa; K_{sat} = the effective bulk modulus of the porous material saturated with pore fluid, Pa; K_0 = the bulk modulus of the solid material, Pa; K_{fl} = the effective bulk modulus of the pore fluid, Pa; ϕ = the porosity; μ_{dry} = the effective shear modulus of the dry porous material, Pa; and μ_{sat} = the effective shear modulus of the porous material saturated with pore fluid, Pa. Note that shear modulus could either be represented as μ or G .

Gassmann's relations make no assumptions on pore geometry and assume a homogeneous elastic material modulus. Most notably, these relations are only valid at “lower frequencies so that the induced pore pressures are evenly distributed over the pore space, such that there is ample time for the pore fluid to circulate and reduce wave-induced pore pressure”. The limitations for low frequency make these relations perform better for on-field stress wave data with very low frequencies. More details about the use and derived relations for Gassmann’s model are discussed thoroughly in Mavko et al. (2009). To calculate each of the four factors in the given relations, the other parameters need to be assumed or determined. Nondestructive determination of porosity would be ideal; however, it was not found to be feasible in the case of resonant testing of discs since concrete is considered a heterogeneous material with no K_0 . Since the parameter, K_{fl} is not the bulk modulus of the water, and it is not obvious that the vibration frequencies are within the lowest limits for which Gassmann’s relations are valid (Recalde, 2009). While Gassmann’s equations assume the same shear modulus both for dry and saturated materials, and the data obtained from the experimental work using resonant frequencies of discs, show that shear modulus for saturated material is higher than that of dry material (i.e., $\mu_{\text{sat}} > \mu_{\text{dry}}$), Gassmann’s relations were not seemed to be a suitable method.

O'Connell and Budiansky (1974; 1977) developed a series of relations for predicting the elastic moduli of solids incorporated with flat ellipsoidal cracks. They analyzed various conditions of dry and saturated circular penny-shaped cracks, dry and saturated elliptical cracks, isobaric saturated cracks, and viscoelastic properties across all frequencies. Their model is based on randomly distributed thin cracks in a homogenous, elastic solid material under constant stress, taking into account the 'self-consistent' approximation based on the variation in energy obtained by the inclusion of an isolated crack in an infinite medium (Recalde, 2009; O'Connell and Budiansky, 1977). This model predicts well how the effective elastic properties could change due to crack inclusions in material solids. Moreover, the O'Connell and Budiansky's model is efficient in determining the changes occurring in shear modulus, bulk modulus, Poisson's ratio, and modulus of elasticity due to the micro-cracks permeated in the solid, as calculated by the crack density parameter (ε) presented in equation 5.11 for circular penny-shaped cracks and equation 5.12 for flat elliptical cracks. The crack density parameter (ε) is defined as the function of crack numbers and their geometry, which is the radius for circular cracks and squared area to perimeter ratio for elliptical cracks (Recalde 2009).

$$\varepsilon_c = \frac{1}{V} \sum a^3 \quad (5.11)$$

$$\varepsilon_e = \frac{2N}{\pi V} \sum \frac{A_c^2}{P_c} \quad (5.12)$$

where, V = volume of the solid, m^3 ; a = long radius of the ellipse, m ; N = number of cracks; A_c = Area of the crack, m^2 ; P_c = crack perimeter, m ; ε_c = Crack density parameter for circular cracks; and ε_e = Crack density parameter for elliptical cracks

This investigation looked into two different scenarios which include, soft-fluid saturation and partial saturation conditions. The mathematical structure of the expressions describing the effective elastic moduli for a solid material permeated by thin cracks, for saturation with a soft fluid, and for partial saturation is given by the similar set of equations given in equations 5.13 to 5.16 as:

$$\frac{K}{K_0} = 1 - \frac{16}{9} \left[\frac{(1-\nu^2)}{1-2\nu} \right] D \varepsilon \quad (5.13)$$

$$\frac{E}{E_0} = 1 - \frac{16}{45} (1-\nu^2) \left[3D + \frac{4}{(2-\nu)} \right] \varepsilon \quad (5.14)$$

$$\frac{G}{G_0} = 1 - \frac{32}{45} (1-\nu) \left[D + \frac{3}{(2-\nu)} \right] \varepsilon \quad (5.15)$$

where,

$$\varepsilon = \frac{45 (\nu_0 - \nu)}{16 (1 - \nu^2)} \left[\frac{(2 - \nu)}{(1+3\nu_0)(2-\nu)-2(1-2\nu_0)} \right] \quad (5.16)$$

and K_0 = the bulk modulus of the uncracked solid, Pa; K = the effective bulk modulus, Pa; ν = the effective Poisson's ratio; ν_0 = Poisson's ratio of the un-cracked solid; G = the effective shear modulus of the solid, Pa; G_0 = the shear modulus for un-cracked concrete, Pa; a = the long elliptical radius, m; c = the crack thickness, m; and D depends on the degree of saturation and for cracks saturated with a soft fluid is given as:

$$D_{sf} = \left[1 + \frac{4 (1-\nu^2)}{3\pi (1-2\nu)} \frac{K_0}{K} \omega_{OB} \right]^{-1} \quad (5.17)$$

where

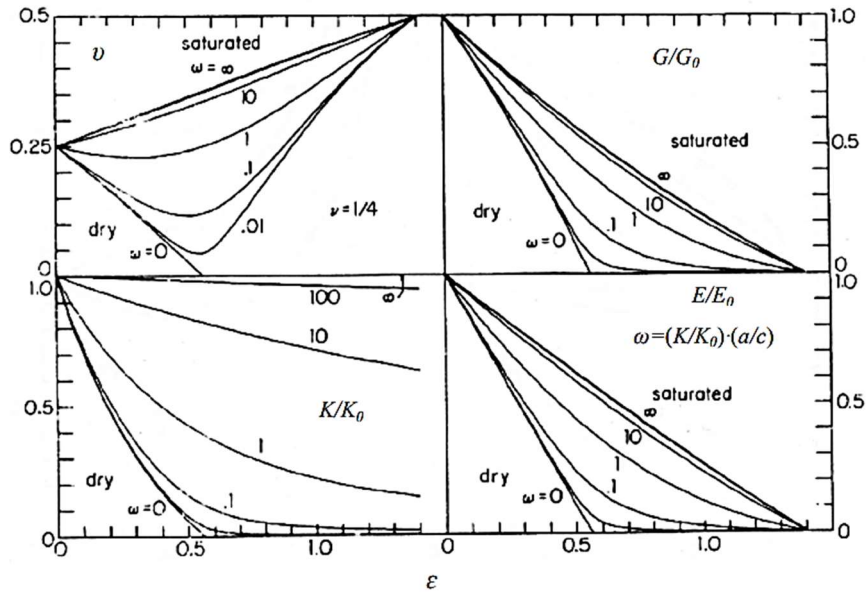
$$\omega_{OB} = \frac{a K_{fl}}{c K_0} \quad (5.18)$$

For the case of partial saturation, it is given as,

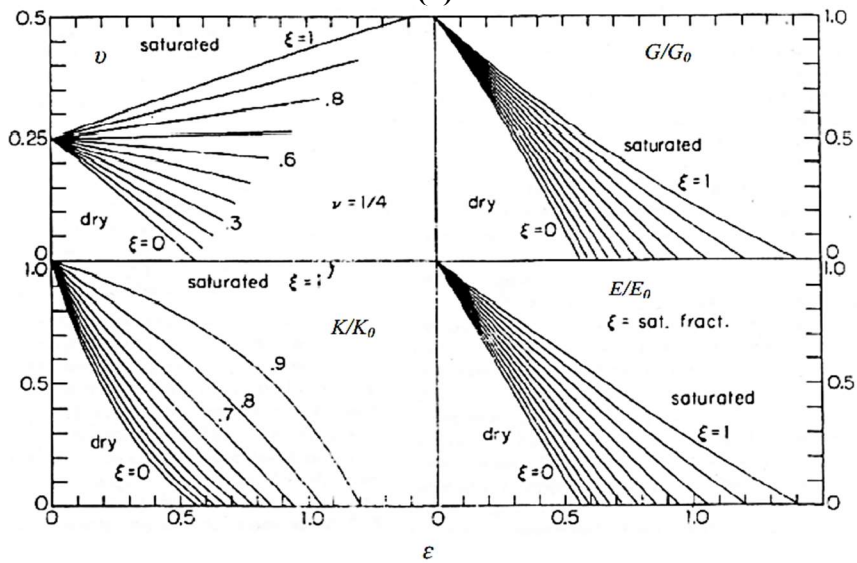
$$D_{ps} = 1 - \xi_{OB} \quad (5.19)$$

where, ξ_{OB} denotes the saturation level, and is expressed as the ratio of the saturated cracks to the overall crack numbers in the solid.

Figure 5.3 shows the effect of crack density parameter (ε) on the effective modulus due to the soft-fluid Saturation and the partial saturation for a solid with circular cracks and Poisson's ratio, (ν) equal to 0.25. For the $\varepsilon = 0.5$, the differences in the predicted moduli between circular and elliptical cracks were determined to be practically negligible (O'Connell and Budiansky, 1974). Mavko et al. (2009) presented that the partial saturation could be approximated using the Reuss average of the bulk modulus of water and air in the case of soft-fluid saturation. Figure 5.3 (a) and figure 5.3 (b) present the second quadrant which explains the higher shear modulus for a cracked solid when cracks are filled with a fluid compared to the cracks when empty are significant to some parts of this research investigation and to compare it with the other analytical model developed in this dissertation. This model shows the difference in the shear modulus of dry and soaked conditions and predicts higher shear modulus for the soaked condition when compared to the dry specimen shear modulus. Moreover, the model reveals higher differences in the elastic properties' values for the increased crack density. These models have been found applicable for high-frequency seismic investigations; however, these models may not be best suited for relaxed conditions if cracks are interconnected Mavko et al., (2009). The O'Connell and Budiansky model was found to be more appropriate in determining the elastic properties of soaked and dry solids in both and cracked conditions, however, this model has already been used and is presented in detail by Recalde (2009).



(a)



(b)

Figure 5.3: Diagram representing the Effective Elastic Properties of a Solid with Circular Cracks: (a) Effect of Soft Fluid Saturation (b) Effect of Partial Saturation (O'Connell and Budiansky, 1974)

After studying different models, a theoretical framework of Hudson was explored which described the changes in elastic Young's modulus due to the crack concentration in solid material. Moreover, this model was found to be predicting the behavior of soaked and dry

cracks in solids which was also serving purpose of conducting this research study, Hudson in his series of papers (1980, 1981) developed a second-order expansion in his model which is based on the “scattering theory of the average wave-field in an elastic solid with thin coin-shaped ellipsoidal cracks” (Mavko et al., 2009). Most importantly, this model is used to estimate the Young’s modulus of an elastic medium containing thin cracks by assuming very small aspect ratios. Hudson’s model is used to evaluate the elastic moduli in an isotropic medium with aligned penny-shaped cracks which are distributed evenly and individually. Hudson considered the medium as a transversely isotropic medium. If we consider the isotropic medium as our background medium, the elastic moduli of the transversely isotropic medium can be calculated from the elastic moduli of the background medium and crack parameters, and could be presented in the form as;

$$c_{ij}^{eff} = c_{ij}^0 + c_{ij}^1 + c_{ij}^2 \quad (5.20)$$

c_{ij}^{eff} are the effective elastic modulus, c_{ij}^0 are isotropic, and c_{ij}^1, c_{ij}^2 are the first and second-order corrections, respectively. The background medium can be represented in its general form as;

$$c_{ij}^0 = \begin{bmatrix} c_{11} & c_{12} & c_{12} & 0 & 0 & 0 \\ c_{12} & c_{11} & c_{12} & 0 & 0 & 0 \\ c_{12} & c_{12} & c_{11} & 0 & 0 & 0 \\ 0 & 0 & 0 & \mu & 0 & 0 \\ 0 & 0 & 0 & 0 & \mu & 0 \\ 0 & 0 & 0 & 0 & 0 & \mu \end{bmatrix}, c_{12} = c_{11} - 2c_{44} \quad (5.21)$$

“The relations between the elements c and those for Lamé parameters λ and μ of isotropic linear elasticity are given” as, $c_{11} = \lambda + 2\mu$, $c_{12} = \lambda$, $c_{44} = \mu$ (Mavko et al., 2009). Hence, the background medium can be presented in the form given below:

$$c_{ij}^0 = \begin{bmatrix} \lambda + 2\mu & \lambda & \lambda & 0 & 0 & 0 \\ \lambda & \lambda + 2\mu & \lambda & 0 & 0 & 0 \\ \lambda & 0 & \lambda + 2\mu & 0 & 0 & 0 \\ 0 & 0 & 0 & \mu & 0 & 0 \\ 0 & 0 & 0 & 0 & \mu & 0 \\ 0 & 0 & 0 & 0 & 0 & \mu \end{bmatrix} \quad (5.22)$$

where λ is the Lamé constant of the background medium (concrete in our case) and μ is the shear modulus (Note: The elements of the given matrix c_{ij}^0 , the background moduli, 1st order corrections, and 2nd order corrections are given by;

Table 5.1: The background moduli, 1st and 2nd order corrections used in Hudson Model

Background Moduli	1 st Order Corrections	2 nd Order Corrections
$c_{11}^0 = \lambda + 2\mu$	$c_{11}^1 = -\frac{\lambda^2}{\mu} \varepsilon U_3$	$c_{11}^2 = \frac{q}{15} \frac{\lambda^2}{\lambda + 2\mu} (\varepsilon U_3)^2$
$c_{13}^0 = \lambda$	$c_{13}^1 = -\frac{\lambda(\lambda + 2\mu)}{\mu} \varepsilon U_3$	$c_{13}^2 = \frac{q}{15} \lambda (\varepsilon U_3)^2$
$c_{33}^0 = \lambda + 2\mu$	$c_{33}^1 = -\frac{\lambda(\lambda + 2\mu)^2}{\mu} \varepsilon U_3$	$c_{33}^2 = \frac{q}{15} (\lambda + 2\mu) (\varepsilon U_3)^2$
$c_{44}^0 = \mu$	$c_{44}^1 = -\mu \varepsilon U_1$	$c_{44}^2 = \frac{2}{15} \frac{\mu(3\lambda + 8\mu)}{\lambda + 2\mu} (\varepsilon U_1)^2$

where ε is the crack density parameter and U_3 and U_1 are evaluated by the elastic parameters of the background medium and depend on crack conditions.

For dry cracks, U_1 and U_3 are given by the expressions,

$$U_1 = \frac{16(\lambda+2\mu)}{3(3\lambda+4\mu)} \quad (5.23)$$

$$U_3 = \frac{4(\lambda+2\mu)}{3(\lambda+\mu)} \quad (5.24)$$

In these equations for U_1 and U_3 , the aspect ratio of the crack does not appear, which is presumably due to vanishingly thin cracks with an aspect ratio nearly equal to zero.

In addition, “Hudson (1981) provided functions for “weak” inclusions specifically for materials with bulk and shear modulus to be smaller than the matrix or background moduli. Fluid-filled cracks could be considered a special case where the shear modulus of the inclusion vanishes”. And for fluid-filled cracks case, the expressions are given as,

$$U_1 = \frac{16(\lambda+2\mu)}{3(3\lambda+4\mu)} \frac{1}{(1+M)} \quad (5.25)$$

$$U_3 = \frac{4(\lambda+2\mu)}{3(\lambda+\mu)} \frac{1}{(1+\kappa)} \quad (5.26)$$

where M and κ are parameters related to the nature of the crack inclusions and background, which are determined by the following expressions,

$$M = \frac{4\mu'}{\pi\alpha\mu} \frac{(\lambda+2\mu)}{(3\lambda+4\mu)} \quad (5.27)$$

$$\kappa = \frac{\left(K' + \frac{4}{3}\mu'\right)(\lambda+2\mu)}{\pi\alpha\mu(\lambda+\mu)} \quad (5.28)$$

Where K' and μ' are the bulk and shear modulus of inclusion material (for fluid μ' is taken as zero).

“Dry cavities can be modeled by considering the inclusion moduli to zero, whereas fluid-saturated cavities are simulated by setting the inclusion shear modulus to zero” (Mavko *et.al.* 2009), where q is given by the expression:

$$q = 15 \frac{\lambda^2}{\mu^2} + 28 \frac{\lambda}{\mu} + 28 \quad (5.29)$$

and the crack density parameter can be estimated using below given equation:

$$\varepsilon = \frac{3\varphi}{4\pi} \quad (5.30)$$

where φ is the crack porosity and α is the aspect ratio calculated as minor/major axis of ellipsoid shown in figure 5.4(a) which is mathematically given as $\alpha = x/y$. In the case of circular penny-shaped cracks, the aspect ratio is calculated as $\alpha = c/a$, “where a is the radius of the circular crack and c as the half-length of the small axis” (Zhu et al. 2008) as shown in figure 5.4(b).

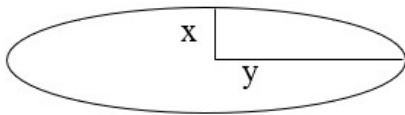


Figure 5.4(a): An ellipsoid crack

Aspect ratio is $\alpha = x/y$.

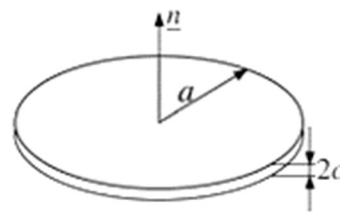


Figure 5.4(b) A penny-shaped

Aspect ratio is $\alpha = c/a$.

For the second phase and the main objective of this research study, Hudson’s model from the rock mechanics has been found to be suitable in expanding its applicability on thin concrete disc in determining the elastic properties. Hudson used the model for rock mechanics;

however, the use of this model has been extended to concrete using the data obtained through resonance frequency. The parameters of interest were to determine the crack density (ε) and the dynamic elastic modulus (E_d) of thin concrete discs using the experimental data obtained in Phase I. Hudson's model is applicable to estimate the effective elastic properties and attenuation of a porous material in terms of the inclusions and pore space (Mavko, 2009). In general, the application of such models for concrete solids has to encounter various geometries, voids, and pores since they are very small in shape and size. Such voids in concrete solid usually get entrapped with air and are thin with irregular shapes which are hard to locate in a way other than the microscope. Hence, measuring a crack density parameter ε for concrete material becomes an ideal approach to take into account the average effect of such voids at the microstructural level (Recalde, 2009). Moreover, estimation of ε would therefore give a better understanding of the thin and nearly flat cracks specifically those at the Interfacial transition zones around coarse aggregates assumed as penny-shaped cracks randomly oriented for modeling purposes.

5.4 Extension of Hudson's (1981) Model to Concrete Material

The analytical approach using Hudson's model has provided a practical approach to estimate the crack density parameter of concrete. This procedure was extended and applied on thin circular concrete discs to calculate ε by using dry and wet elastic moduli (E_{dry} and E_{wet}) of discs. As shown in equation 5.20, it is required to determine the effective elastic modulus and the first and second-order correction factors. These parameters were calculated using Lamé constants for the elastic properties. Considering the isotropic medium as our background medium, the uncracked shear and the elastic Young's moduli along with Lamé

coefficient were calculated using the equations from 5.31 to 5.33 by assuming Poisson's ratio ν equal to 0.25.

$$G_0 \text{ or } \mu_0 = \frac{E_0}{2(1+\nu_0)} \quad (5.31)$$

$$E_0 = 2G_0(1+\nu_0) \quad (5.32)$$

$$\lambda_0 = \frac{G_0(E_0 - 2G_0)}{3G_0 - E_0} \quad (5.33)$$

where, G_0 or μ_0 = the shear modulus of the background media (un-cracked solid), GPa; E_0 = the elastic Young's Modulus of the background media, GPa; ν_0 = the Poisson's ratio of the un-cracked media; and λ_0 = lamé coefficient depends on uncracked elastic properties, GPa. The background media in our case is concrete solid and the uncracked concrete elastic properties were incorporated in Hudson's model to estimate the crack density parameter. Moreover, c_{ij}^{eff} the effective elastic modulus was determined from the equation 5.34 and is given in the form,

$$C_{11}^{eff} = \frac{E(1-\nu)}{(1+\nu)(1-2\nu)} \quad (5.34)$$

The equation 5.34 was derived from the stiffness matrix based on Hook's law which is given in equation 5.38 as a constitutive matrix for isotropic material as;

$$\begin{bmatrix} \sigma_{xx} \\ \sigma_{yy} \\ \sigma_{zz} \\ \sigma_{yz} \\ \sigma_{zx} \\ \sigma_{xy} \end{bmatrix} = \frac{E}{(1+\nu)(1-2\nu)} \begin{bmatrix} 1-\nu & \nu & \nu & 0 & 0 & 0 \\ \nu & 1-\nu & \nu & 0 & 0 & 0 \\ \nu & \nu & 1-\nu & 0 & 0 & 0 \\ 0 & 0 & 0 & 1-2\nu & 0 & 0 \\ 0 & 0 & 0 & 0 & 1-2\nu & 0 \\ 0 & 0 & 0 & 0 & 0 & 1-2\nu \end{bmatrix} \begin{bmatrix} \varepsilon_{xx} \\ \varepsilon_{yy} \\ \varepsilon_{zz} \\ \varepsilon_{yz} \\ \varepsilon_{zx} \\ \varepsilon_{xy} \end{bmatrix} \quad (5.35)$$

The stiffness matrix for Voigt elastic for the linear elastic material is presented in structure and the expression shown below:

$$[C^{eff}] = \begin{bmatrix} C_{11} & C_{12} & C_{12} & 0 & 0 & 0 \\ C_{12} & C_{11} & C_{12} & 0 & 0 & 0 \\ C_{12} & C_{12} & C_{11} & 0 & 0 & 0 \\ 0 & 0 & 0 & C_{44} & 0 & 0 \\ 0 & 0 & 0 & 0 & C_{44} & 0 \\ 0 & 0 & 0 & 0 & 0 & C_{44} \end{bmatrix} \quad (5.36)$$

The parameters required to estimate the crack density parameter (ε) were either G_0 or E_0 which were obtained through the resonance frequency procedure presented in section 3.10 for the thin concrete disc. Other parameters that were measured include λ_0 , first, and second correction orders, c_{ij}^1, c_{ij}^2 respectively. The assumed parameters include the bulk modulus of the water and the Poisson's ratio. The equations 5.31 to 5.36 were incorporated in an excel program and an iterative procedure was developed to estimate a particular crack density parameter for damaged and undamaged concrete specimens. To determine the ε for two different conditions such as wet and dry, the equations 5.23 to 5.28 are incorporated into the correction factors given in Table 5.1 above. After developing these expressions an iterative procedure was run to optimize the function and ε was estimated for E_{dry} and E_{wet} in both conditions. Since the analysis was conducted for damaged and undamaged concrete specimens, there was a need to determine two crack densities for the same specimen, such as before and after the high-temperature exposure. For this, a new set of equations is introduced, and a system for determining four unknowns such as $\varepsilon_1, \varepsilon_2, \nu_0$, and E_0 is introduced. At this point, the drawback was that a non-destructive nature of testing was denied which required to

determine the crack density of the specimen after inducing damage and to characterize the concrete solid adequately at two different conditions i.e., prior damage and after damage. The detailed application of this model is presented in section 4.5 with a detailed numerical example.

Hudson's model showed that the crack density parameter of thin concrete discs could be determined easily and effectively using the non-destructive measuring approach for dynamic Young's modulus of elasticity and dynamic Poisson's ratio of concrete specimens both in dry and wet conditions using the same specimen. The advantage of using Hudson's model is that changes in ε for deteriorated concrete could be estimated on small specimens rather than using concrete cylinders and the reduction in elastic Young's modulus due to damage can be estimated once the change in crack density parameter from a damaging event is known. Developing the above-mentioned procedure using the fundamentals formed by Hudson's (1981) and calculating the damage levels in concrete discs at elevated temperatures, it could therefore be postulated that the equations from Hudson's (1981) model could be applicable for analyzing and determining elastic properties for thin concrete discs correctly. The comparison of the parameters used in Hudson's model for rock mechanics and the extension to concrete material is presented in Table 5.2.

Table 5.2: Comparison between Hudson's Model for Rock Mechanics and Concrete Material

Hudson's Model for Rock Mechanics	Hudson's Extended Model for Concrete Material	
Input Parameters (Uncracked Solid)		
μ λ	G_{dry} and G_{wet} $\lambda_0 = \mu_0 = G_0$	
$\nu_0 = 0.25$ (Poisson Solid)		
G_{dry} and G_{wet} converted into E_{dry} and E_{wet}		
Dry Crack Condition		
$U_1 = [16 (\lambda + 2\mu)] / [3 (3\lambda + 4\mu)]$	$U_1 = [16 (\lambda_0 + 2G_0)] / [3 (3\lambda_0 + 4G_0)]$	5.37
$U_3 = [4 (\lambda + 2\mu)] / [3 (\lambda + \mu)]$	$U_3 = [4 (\lambda_0 + 2G_0)] / [3 (\lambda_0 + G_0)]$	5.38
$C^1_{11} = - (\lambda^2/\mu) \varepsilon U_3$	$C^1_{11} (dry) = - (\lambda^2_0/G_0) \varepsilon_{dry} U_3_{dry}$	5.39
Saturated Crack Condition		
$U_1 = [16 (\lambda + 2\mu)] / [3 (3\lambda + 4\mu)] * 1/(1+M)$	$U_1 = [16 (\lambda_0 + 2G_0)] / [3 (3\lambda_0 + 4G_0)] * 1/(1+M)$	5.40
$U_3 = [4 (\lambda + 2\mu)] / [3 (\lambda + \mu)] * 1/(1+\kappa)$	$U_3 = [4 (\lambda_0 + 2G_0)] / [3 (\lambda_0 + G_0)] * 1/(1+\kappa)$	5.41
$C^1_{11} = - (\lambda^2/\mu) \varepsilon U_3$	$C^1_{11} (wet) = - (\lambda^2_0/G_0) \varepsilon_{wet} U_3_{wet}$	5.42
G_0 or $\mu_0 = E_0 / 2 (1+\nu_0)$		5.43
$E_0 = 2G_0 (1+\nu_0)$		5.44
$\lambda_0 = G_0 (E_0 - 2G_0) / (3G_0 - E_0)$		5.45
$C^{eff}_{11} = C^0_{11} + C^1_{11}$		5.46
$C^0_{11} = \lambda + 2\mu$	$C^0_{11} = \lambda + 2G_0$	5.47
$C^{eff}_{11} = E (1 - \nu_0) / (1 + \nu_0) (1 - 2\nu_0)$		5.48
$E_{model} = C^{eff}_{11} (1 + \nu_0) (1 - 2\nu_0) / (1 - \nu_0)$		5.49
$E_{model} = E_{measured}$		
Output: E_0 and ε		

The input parameters are shown in table 5.2 of uncracked solids for shear modulus in both dry and soaked conditions, G_{dry} and G_{wet} calculated experimentally have been introduced and

were converted to E_{dry} and E_{wet} by assuming a Poisson solid having Poisson's ratio (ν_0) equal to 0.25 for both conditions. To calculate effective moduli shown in the equation. 5.46, correction factors were required which are calculated using the isotropic background moduli c_{11}^0 and the first order correction c_{11}^1 factor as shown in Table 5.1. The factor U_3 which depends on the crack condition was calculated separately for dry and wet conditions using the equation. 5.38 and equation. 5.39 respectively. The uncracked shear modulus (G_0) and (E_0) were calculated using equation 5.43 and equation 5.44, The parameters M and κ in equation 5.40 and equation. 5.45 were calculated using the equations shown in Table 5.1. An aspect ratio of 0.2 was used during the calculations where it was needed. Once C^{eff} was calculated, E_{model} was determined using the iterative procedure and the function was optimized when E_{model} was found equal to be $E_{measured}$ and E_0 and crack density parameter (ϵ) was determined by the model.

5.5 Numerical Example on Hudson's Model

Hudson's model to determine the elastic properties of concrete from the estimated crack density parameter has provided an effective practical procedure for thin concrete discs. In this section, a detailed numerical example to understand the behavior of Hudson's first and second orders is presented with the input values given in Table 5.3 below. The purpose of the development of Hudson's second order was to expand the application of the model to perform well for rocks or solid materials with higher crack densities (Cheng 1993). Examples below present the performance of Hudson's model using first and second order for thin concrete discs in both soaked and dry conditions.

Table 5.3: Input values for Numerical example

Parameter	Value	Unit
$\lambda_0 = \mu_0$	12.974	GPa
ν_0	0.25	-
ϵ	0.500	-
U_3	2.00	-
U_1	2.500	-
q	53.333	-
K'	2.100	GPa
α	0.010	-

Note: The parameters shown in this table have been explained in detail in section 5.4.

5.5.1 Hudson's Model with First Order Correction Only

Hudson's first order correction was used at the beginning of the calculations and the second-order was neglected as shown in equation 5.50, which was later added by Hudson as an extension for higher crack density parameters. The background material properties were used, and the obtained results are presented in figures 5.4 and 5.5.

$$c_{ij}^{eff} = c_{ij}^0 + c_{ij}^1 \quad (5.50)$$

The Normalized elastic moduli using only the first order have been plotted for dry and soaked conditions shown in figure 5.4. It could be seen in the figure that the results of the two conditions are significant. A downward trend was observed, which appears to be monotonically decreasing as crack density increases. Similar behavior has also been

witnessed for plots generated for effective moduli and Young's modulus for dry as well as fluid-filled cracks in figure 5.5 (a) and figure 5.5 (b) for the thin concrete discs and the plot follows descending order and does not diverge or intersect with each other.

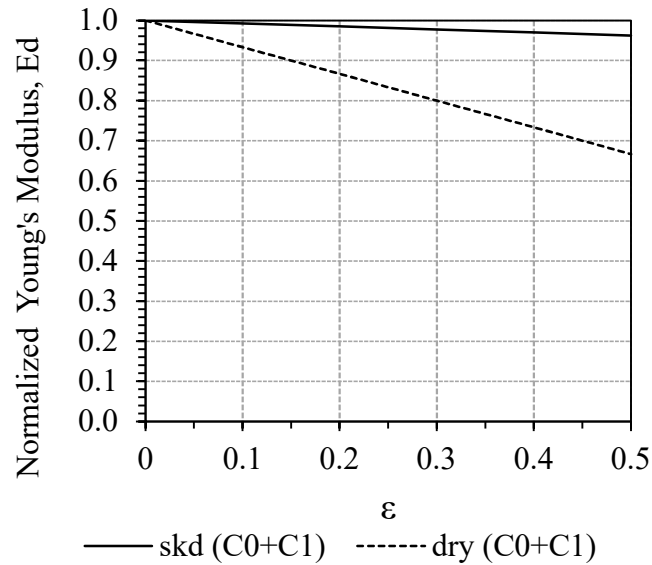


Figure 5.5: Normalized elastic modulus for Hudson's first order correction

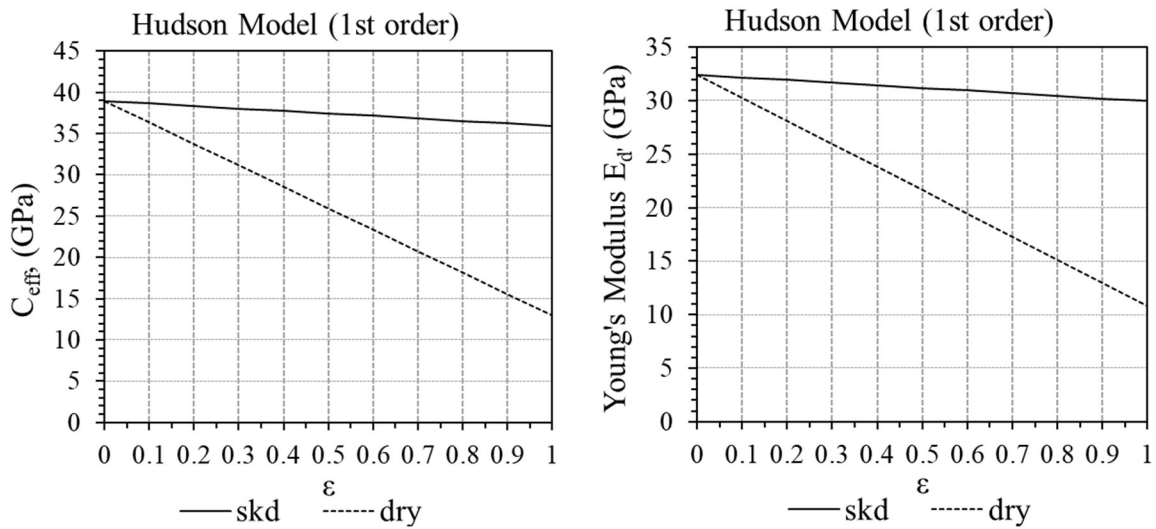


Figure 5.6: (a) Effective moduli vs CDP (b) Young's modulus vs CDP plots in soaked and dry conditions.

5.5.2 Hudson's Model with First and Second Order Corrections

Figure 5.7 presents a graph for normalized elastic modulus in both soaked and dry conditions for first and second-order corrections as a function of crack density for concrete. The effective elastic moduli were normalized with respect to the background moduli. It can be observed in figure 5.8 that the second-order expansion is diverging rather than converging, which is due to the fact that the expansion is approaching the true solution rapidly for the second order correction, compared to the first-order correction, and is asymptotic in nature (Cheng 1993).

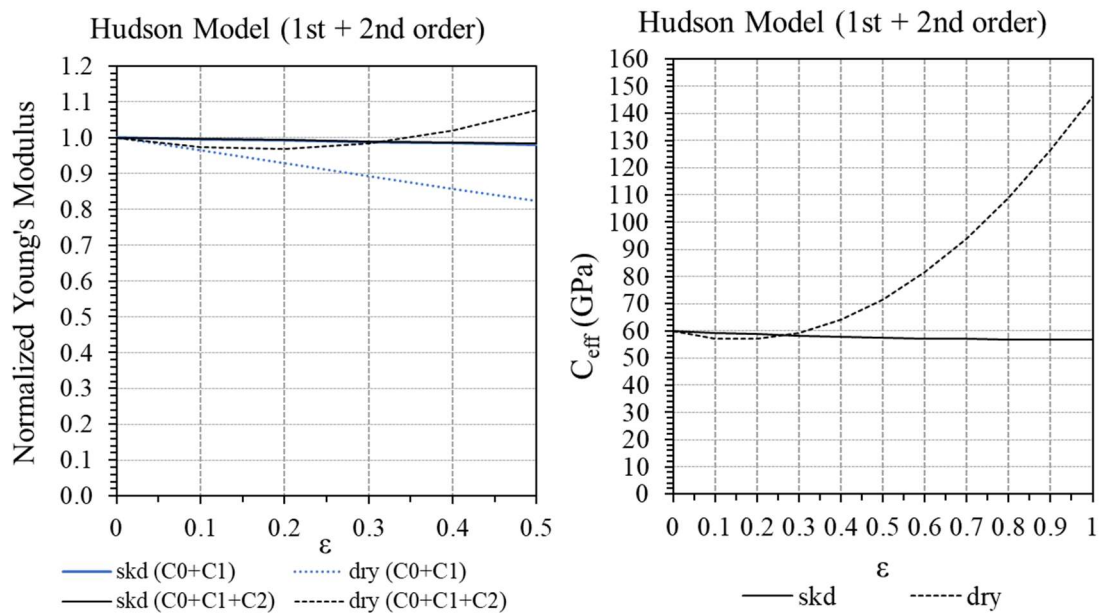


Figure 5.7: (a) Normalized elastic Young's modulus vs ϵ (b) Effective moduli vs ϵ for Hudson's first and second order expansion for dry and soaked conditions.

Moreover, the plot for effective moduli of the background material (concrete in this case) can be observed clearly in figure 5.7, where Hudson’s second-order expansion diverges in the case of dry crack condition after some limit of crack density parameter. This expansion by Hudson (1981) was introduced for the purpose of extending the model for higher crack densities of solid materials; however, it was observed that this purpose has not been achieved for the case of dry cracks and the model behaves differently than what it was expected by following the descending trend.

5.5.3 Proposed Padé Approximation for Second Order by Cheng (1993)

To avoid the problem of diverging series in Hudson’s model, an alternative expansion was proposed by (Cheng 1993) for the effective moduli. This approximation was proposed to get along with Hudson’s model and eliminate the divergence issue up to some extent of crack densities. This proposed expansion is based on the exact solution form for inclusions having spherical shapes and expands in a Padé approximation (Bender and Orszag 1978) and is presented in the following form;

$$c_{ij}^{eff} = c_{ij}^0 \frac{1-a_{ij}\varepsilon}{1+b_{ij}\varepsilon} \quad (5.51)$$

“Padé approximation is a rational function of two polynomials, which is frequently used to model the behavior of functions, which are divergent if expressed in power series” (Cheng 1993). This approximation has been developed to be similar to the second-order crack densities by establishing the Padé coefficients as:

$$b_{ij} = -\frac{c_{ij}^2}{c_{ij\varepsilon}^1} \quad (5.52)$$

and

$$a_{ij} = -\frac{c_{ij}^1}{c_{ij\varepsilon}^0} - b_{ij} \quad (5.53)$$

Cheng (1993) presented this proposed model using Padé approximation which falls between Hudson's corrections for first and second-order. According to Cheng, it was found that the proposed new expansion appeared to be decreasing monotonically with increasing crack densities, which was found applicable and prevented the difficulties encountered with Hudson's second-order expansion of divergence in the case of dry cracks. Perhaps mathematically it is valid since the coefficients proposed have been set to be identical with those of Hudson's second-order expansion (Cheng, 1993).

However, there is again an issue encountered by using the Padé approximation proposed in (Cheng, 1993) for thin concrete discs. The developed plots using the coefficients given in 5.52 and 5.53 do not demonstrate the desired downward trend for higher crack density parameters for the concrete disc. By using Cheng's (1993) proposed formulation, the plots in figure 5.7 (a) and figure 5.7 (b) was generated for effective moduli (C_{eff}) and Young's Modulus (E_d) which demonstrates a smaller change in Elastic modulus with an increase in the crack density parameter.

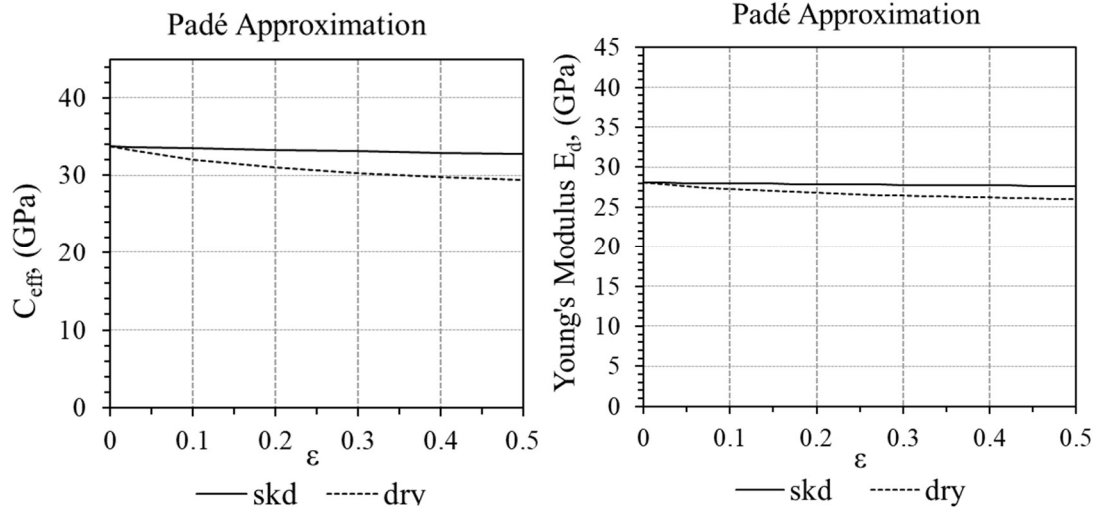


Figure 5.8: (a) Effective moduli vs ϵ (b) Young's modulus vs ϵ plots generated using Padé approximation.

The trend for dry and soaked cracks shown in plots 5.7 (a) and 5.7 (b) move nearly parallel to each other and a proper solution is not achieved. This new expansion was expected to perform well in avoiding the divergence issue; however, it is clear that avoidance of the divergence issue was not achieved in the present form for thin concrete discs as the model does not lead towards an appropriate solution. The trend followed for dry and soaked concrete specimens shown in figure 5.7 (b) using Padé approximation shows a minimum difference in Young's modulus, which is expected to be higher with increasing crack densities and has not been observed using the expansion proposed by (Cheng 1993).

5.6 Validating Hudson's Extended Model with Cheng (1973) Model

In order to validate the developed model used in this dissertation using Hudson's model for the thin concrete disc, the results from Cheng (1993) study were incorporated to guarantee that the equations and relations used to conduct the investigation is correct and match with

the plots developed by Cheng (1993). This was carried out to check and support the investigation of the new proposed Padé expansion which was found to be not feasible for thin concrete discs. The plots and the trend followed as shown in figure 5.10 (a) and figure 5.10 (b) using Hudson's first and second-order expansion for dry and soaked crack condition are very identical to those obtained by Cheng (1993). The second-order correction from Hudson's model always shows an issue of divergence which has also been validated in the given plot for dry cracks condition. Moreover, figures from 5.8 to 5.11 show further comparisons for Hudson's first and second-order corrections along with the proposed new Padé expansion. Additionally, the results were validated and exactly match the results and graphs of Cheng's (1993) model.

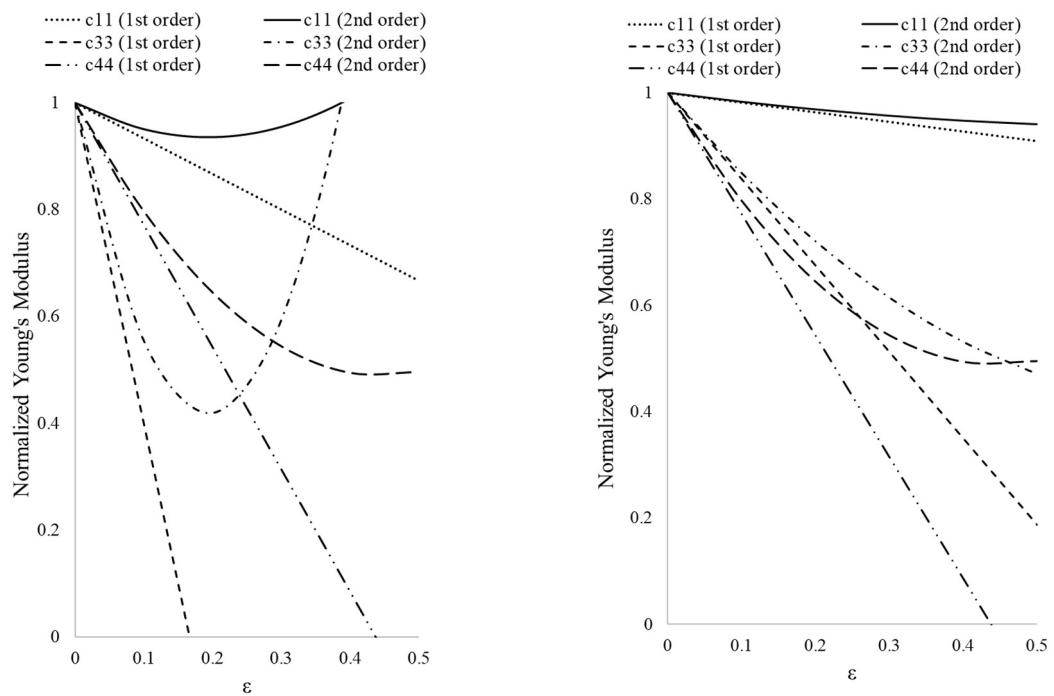


Figure 5.9: (a) Normalized Young's Modulus vs ϵ for dry (b) Normalized Young's Modulus vs ϵ for soaked cracks using Hudson's first and second order expansion.

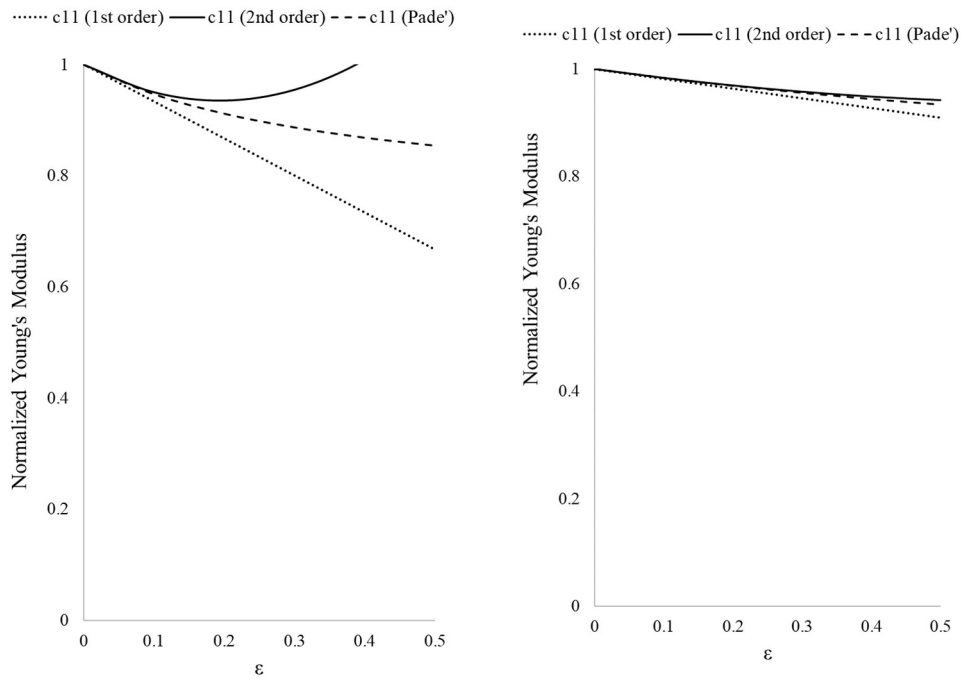


Figure 5.10: Comparison of 1st, 2nd and new Padé expansion for Normalized Young's Modulus c_{11} for (a) Dry cracks condition and (b) Soaked cracks condition

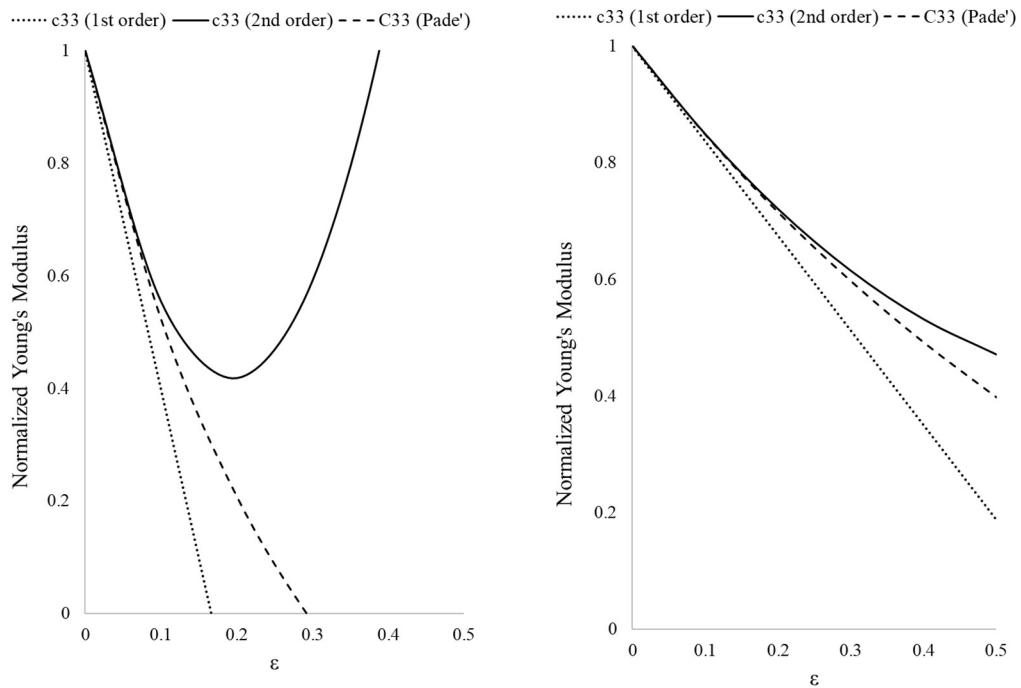


Figure 5.11: Comparison of 1st, 2nd and new Padé expansion for Normalized Young's Modulus c_{33} for (a) Dry cracks condition and (b) Soaked cracks condition

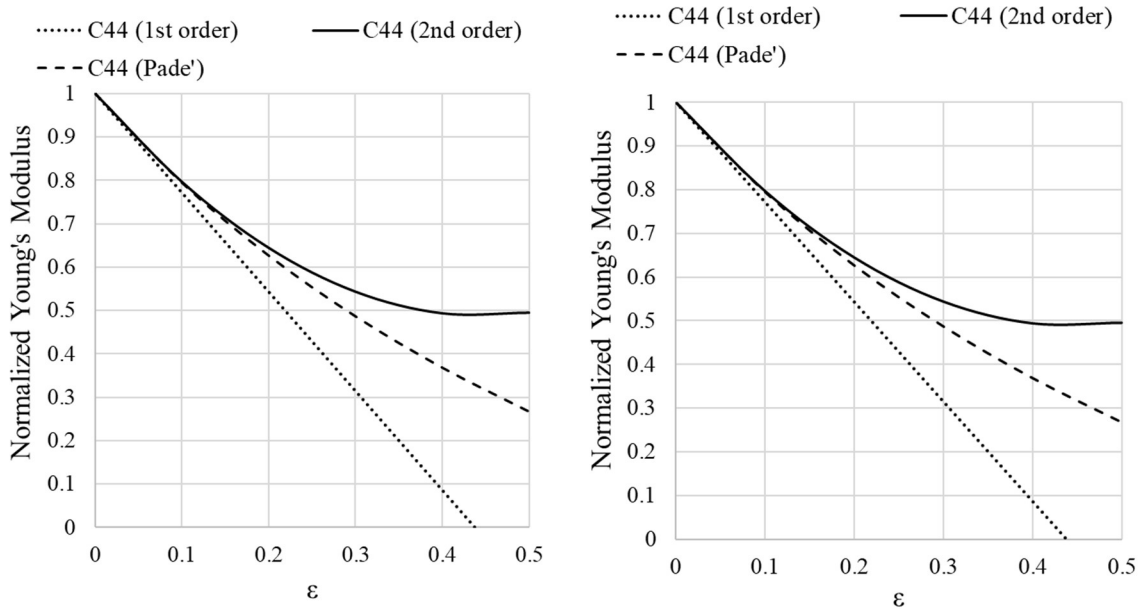


Figure 5.12: Comparison of 1st, 2nd and new Padé expansion for Normalized Young's Modulus c_{44} for (a) Dry cracks condition and (b) Soaked cracks condition

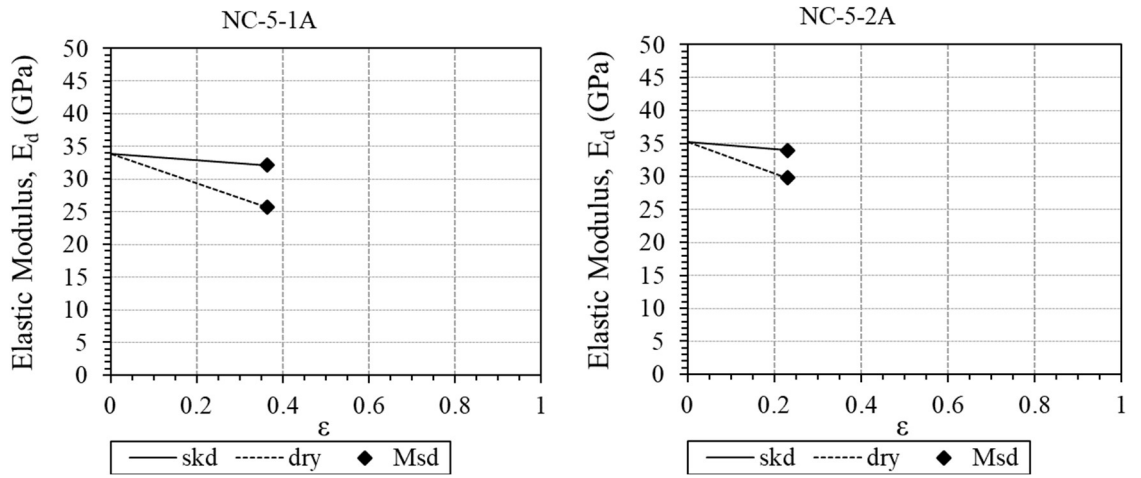
Note: Plots for Normalized c_{44} in figures 5.11(a) and (b) are identical because we have similar U_1 values during calculation for both soaked and dry cases.

5.7 Determination of CDP and Young's Modulus using Hudson Extended Model

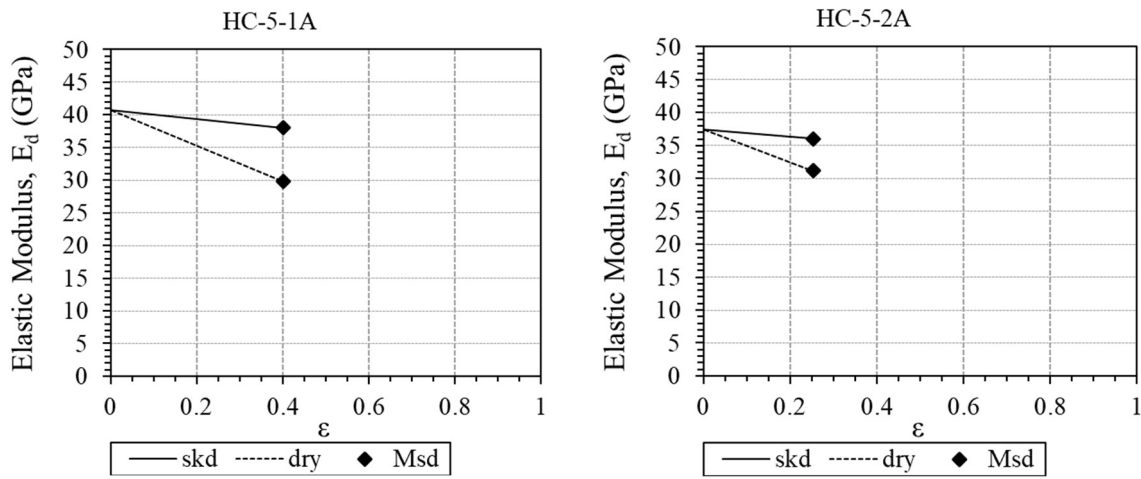
After thoroughly exploring different models explained above and finding that the second-order expansion in Hudson's model diverges rather than converges at a certain crack density limit as well as concluding that Cheng (1993) proposed a new formulation with Padé approximation not feasible for thin concrete discs, Hudson's first order was decided to be used to obtain suitable results. This issue has also been explained in a handbook by Mavko et al. (2009), who have suggested that using just the first-order correction would reveal better results than using the second-order correction factor. The obtained results were based on the data collected experimentally where shear modulus (G_d) was calculated from shear wave

speed using the formulation developed by Hutchinson (1979). The dynamic shear modulus was used in Hudson's model along with assumed Poisson's ratio ν equal to 0.25 to determine dynamic Young's modulus (E_d) and crack density parameter for thin concrete discs shown in figures 5.13 to 5.18.

An improvement in the dynamic Young's modulus E_d after exposing specimens to elevated temperatures was observed after soaking and drying thin discs, showing that autogenous healing had occurred in specimens after water absorption. Therefore, ε was preferred to determine at two different conditions that are E_{skd} to E^* for ε_1 and E_{sat} to E' for ε_2 for specimens exposed to 300 °C temperature followed by saturating and drying conditions. The increase in E_d after damage and after saturation and drying cycle could be due to the water penetrating through cracks and contacting with the concrete constituents and activating the hydration process again. It sometimes happens while during the curing process water does not reach the whole concrete constituents to take place in the process for concrete to gain strength and remains in-active which might be the case in our research work and resulted in autogenous healing after the concrete is exposed to elevated temperature and inducing damage.

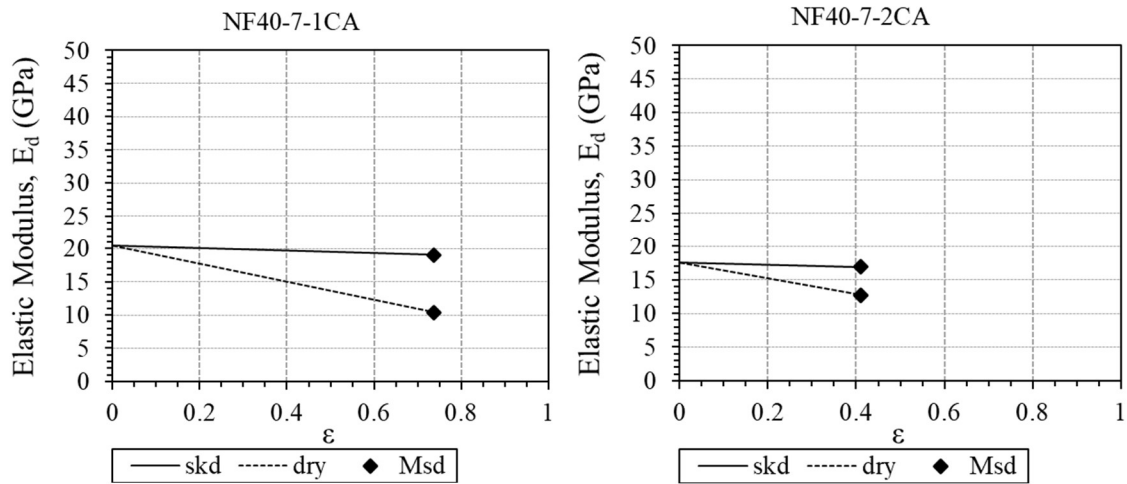


(a)

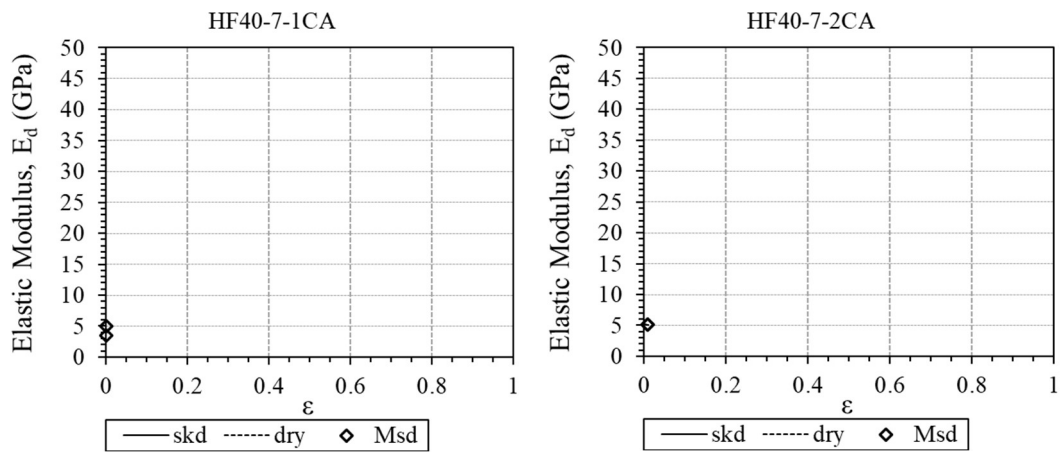


(b)

Figure 5.13: Application of Hudson's model on dry and soaked control specimens for (a) Normal and (b) High Strength concrete mixtures 'NC and HC'

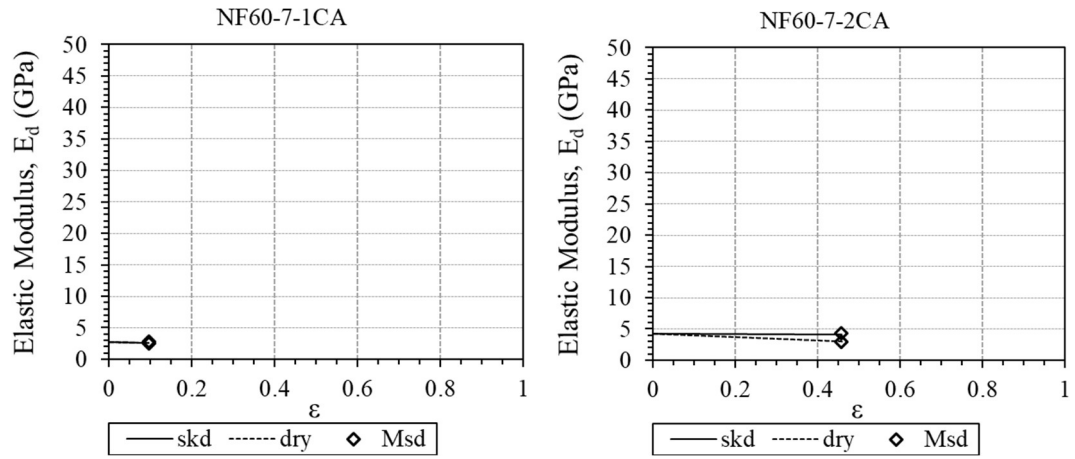


(a)

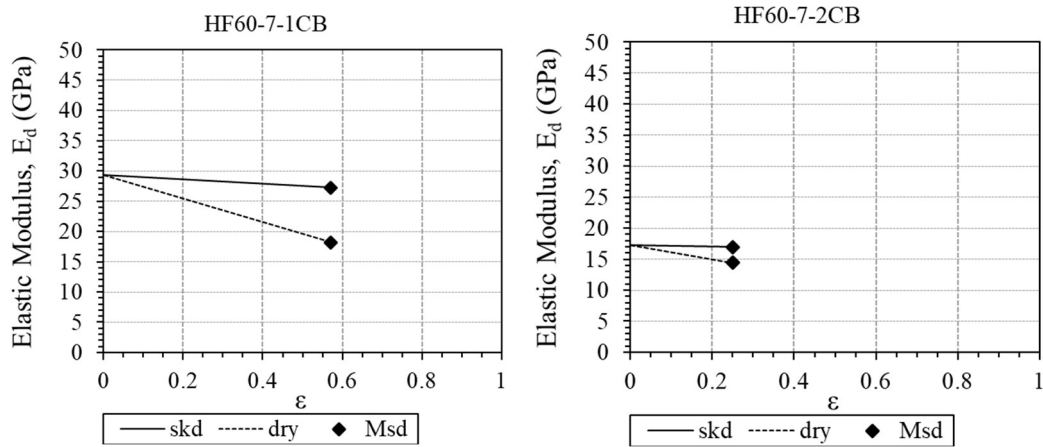


(b)

Figure 5.14: Application of Hudson’s model on dry and soaked control specimens for (a) Normal and (b) High Strength concrete mixture with 40% fly ash ‘NFHC’

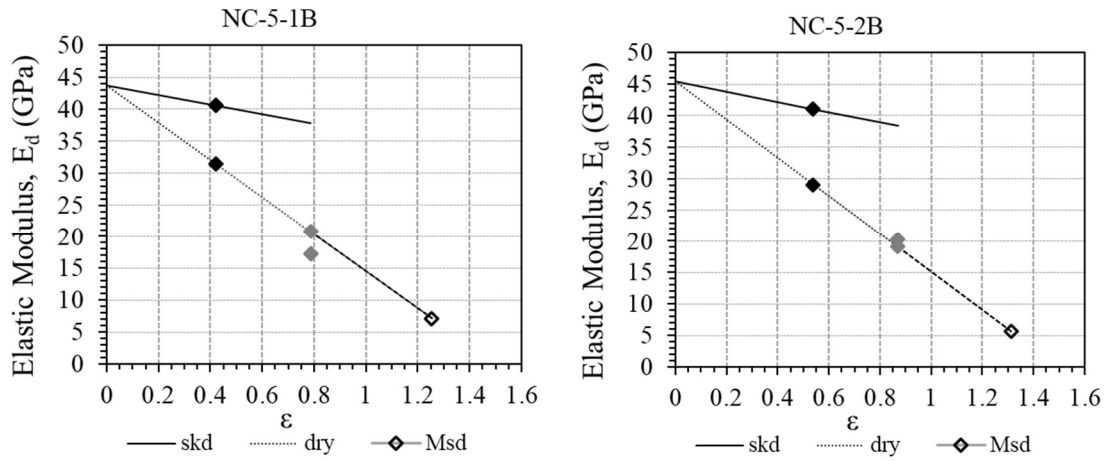


(a)

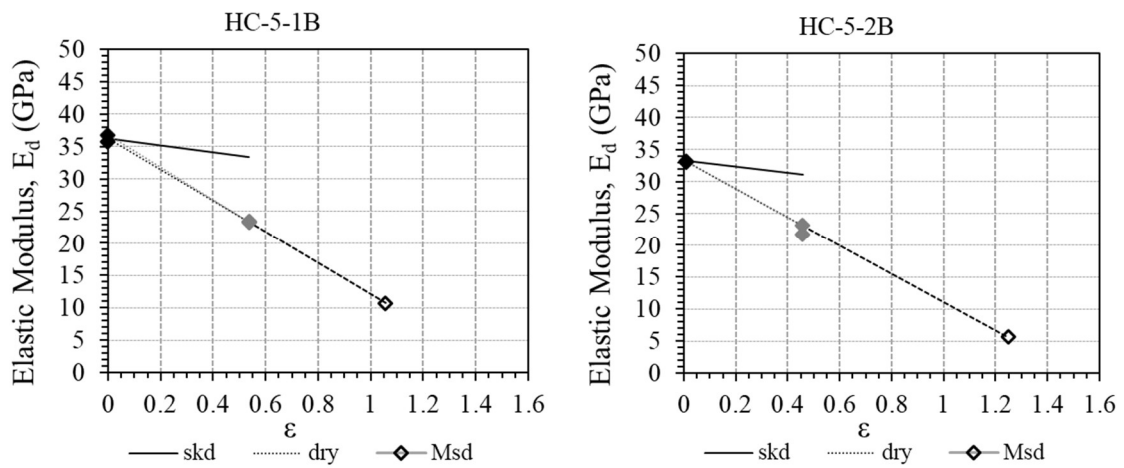


(b)

Figure 5.15: Application of Hudson's model on dry and soaked specimens for (a) Normal and (b) High Strength concrete mixtures with 60% fly ash 'NF60 and HF60'

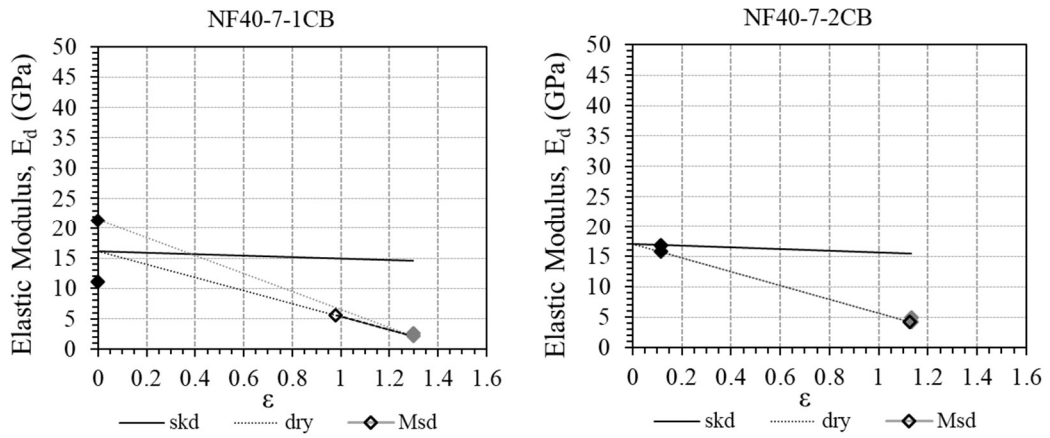


(a)

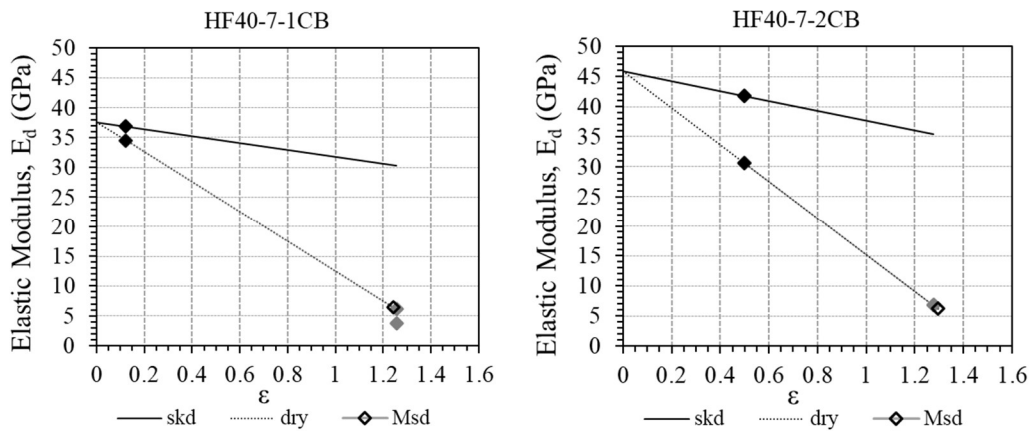


(b)

Figure 5.16: Application of Hudson's model on dry and soaked control specimens for (a) Normal and (b) High Strength concrete mixture 'NC and HC'

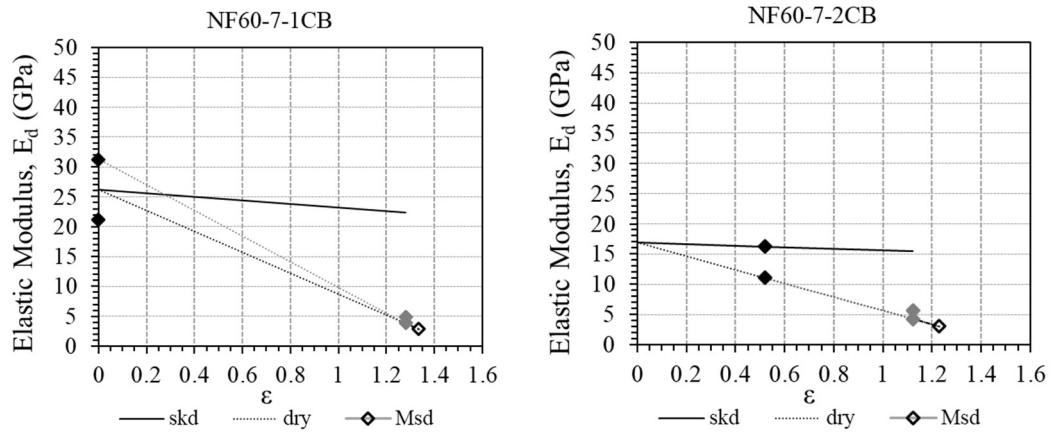


(a)

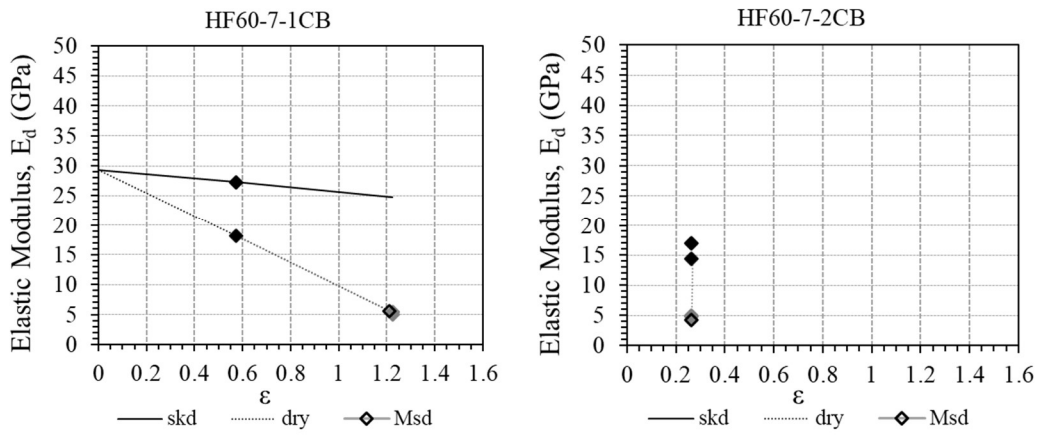


(b)

Figure 5.17: Application of Hudson's model on dry and soaked damaged specimens at 300 °C (570 °F) with 40% fly ash content (a) Normal Strength (NF40) and High Strength (HF40) concrete mixtures



(a)



(b)

Figure 5.18: Application of Hudson’s model on dry and soaked damaged specimens at 300 °C (570 °F) with 60% fly ash content NF60 and HF60 (a) Normal Strength (NF60) and (b) High Strength (HF60) concrete mixtures

5.8 Comparing Hudson's Extended Model Results with O'Connell and Budiansky Model

Going through extensive analysis of numerous concrete disc specimens for various concrete mixtures under different conditions, the results for crack density parameter and Young's modulus were obtained using both Hudson's and O'Connell and Budiansky's models, which were subsequently compared. A similarity in crack density parameters was observed for the control specimens (Labeled as A) using Hudson's and O'Connell and Budiansky models. Both models almost behave similarly and have nearly equal CDP and E_d values which are in good agreement. This agreement for both models was found to be in the control specimens which were kept undamaged. However, higher CDP values were observed in Hudson's model when the concrete specimens are exposed to high temperatures of 300 °C (570 °F). The crack density parameter obtained using Hudson's model is higher than one, whereas with the O'Connell and Budiansky model, the CDP was found to be less than one.

The obtained results using both models have been presented in table 5.4 to table 5.7, whereas the comparison of crack density parameter (ϵ) and Young's Modulus (E) for different mixture groups have been shown graphically in figure 4.18. It could be observed in the plots that, both models behave differently, and the results obtained using Hudson's model for damaged specimens resulted in a higher value of ϵ when compared to those obtained using O'Connell and Budiansky's model. The detailed results obtained for elastic properties at different damage levels are presented in Appendix-C.

Table 5.4: Results for (ϵ) and Young's modulus for Control Normal and High Strength Undamaged Specimens using Hudson and O'Connell & Budiansky Models

Specimen ID	Input – G_d (GPa)		Hudson's Model		O'Connell & Budiansky Model	
	skd	dry	ϵ	E_0 (GPa)	ϵ	E_0 (GPa)
NC-4-1A	13.97	14.72	0	35.86	0	30.93
NC-4-2A	12.89	9.25	0.46	33.44	0.29	43
NC-5-1A	12.85	10.26	0.33	32.97	0.23	40.32
NC-5-2A	13.6	11.91	0.21	34.59	0.16	39.83
NC-6-1A	13.14	10.18	0.37	33.84	0.25	41.99
NC-6-2A	11.21	9.55	0.24	28.49	0.19	33.56
HC-4-1A	14.26	12.01	0.27	36.47	0.2	43.1
HC-4-2A	15.06	12.67	0.27	38.57	0.2	45.55
HC-5-1A	15.22	11.92	0.36	39.34	0.24	48.34
HC-5-2A	14.42	12.47	0.23	36.77	0.17	42.69
HC-6-1A	15.83	11.2	0.49	41.49	0.29	53.19
HC-6-2A	14.75	12.46	0.26	37.75	0.19	44.48

Table 5.5: Results for (ϵ) and Young's modulus for Mixtures with 40% and 60% fly ash damaged at 300 °C using Hudson's Model

Specimen ID	Before Damage				After Damage				EXP-SKD-DRY			
	Input – G_d (GPa)		Output		Input – G_d		Output		Input – G_d		Output	
	skd	dry	ϵ	E_0 (GPa)	skd*	dry*	ϵ	E_0 (GPa)	skd'	dry'	ϵ	E_0 (GPa)
NF40-7-1CA	7.62	4.16	0.71	19.74	0.80	0.77	0.05	2.00	0.80	0.68	0.22	2.00
NF40-7-2CA	6.76	5.08	0.39	17.20	0.71	1.25	0.00	2.45	0.71	1.34	0.00	2.56
NF40-7-2CB	6.77	6.31	0.11	16.99	2.00	1.69	0.24	5.02	2.00	1.67	0.25	5.02
NF40-7-1CB	4.42	8.53	0.00	16.18	1.02	2.25	0.00	4.09	1.02	0.87	0.22	2.55
NF60-7-1CA	4.35	4.10	0.09	10.91	1.10	1.03	0.10	2.75	1.10	1.14	0.00	2.80
NF60-7-2CA	6.50	5.16	0.33	16.48	1.70	1.19	0.45	4.27	1.70	1.43	0.24	4.26
NF60-7-2CB	6.49	4.43	0.50	16.58	2.24	1.22	0.69	5.65	2.24	1.70	0.36	5.62
NF60-7-1CB	8.47	12.52	0.00	26.23	1.96	1.15	0.63	4.93	1.96	1.54	0.33	4.91
HF40-7-1CA	10.22	8.70	0.24	25.93	1.38	2.02	0.00	4.26	1.38	2.01	0.00	4.24
HF40-7-2CA	11.49	8.44	0.43	29.64	2.06	2.05	0.01	5.15	2.06	2.01	0.04	5.15
HF40-7-2CB	16.71	12.23	0.45	43.74	2.72	2.49	0.13	6.82	2.72	2.72	0.00	6.80
HF40-7-1CB	14.75	13.81	0.11	37.23	1.47	2.57	0.00	5.05	1.47	2.45	0.00	4.90
HF60-7-1CA	3.71	4.01	0.00	9.65	1.43	0.55	0.93	3.60	1.43	0.93	0.53	3.58
HF60-7-2CA	1.14	5.67	0.00	8.51	1.27	1.01	0.31	3.18	1.27	1.21	0.07	3.17
HF60-7-2CB	6.79	5.78	0.24	17.15	1.93	1.69	0.19	4.84	1.93	2.01	0.00	4.92
HF40-7-1CB	10.90	7.27	0.54	28.26	1.98	2.25	0.00	5.29	1.98	2.16	0.00	5.17

Table 5.6: Results for (ϵ) and Young's modulus for Mixtures with 40% and 60% fly ash damaged at 300 °C using O'Connell and

Budiansky Model

-	Before Damage				After Damage				EXP-SKD-DRY			
	Input – G_d (GPa)		Output		Input – G_d		Output		Input – G_d		Output	
ID	skd	dry	ϵ	E_0 (GPa)	skd*	dry*	ϵ	E_0 (GPa)	skd'	dry'	ϵ	E_0 (GPa)
NF40-7-1CA	7.62	4.16	0.38	28.30	0.80	0.77	0.06	2.11	0.80	0.68	0.18	2.38
NF40-7-2CA	6.76	5.08	0.27	22.02	0.71	1.25	-0.38	1.74	0.71	1.34	-0.37	1.83
NF40-7-2CB	6.77	6.31	0.10	18.61	2.00	1.69	0.19	6.03	2.00	1.67	0.20	6.09
NF40-7-1CB	4.42	8.53	-0.37	11.55	1.02	2.25	-0.37	2.93	1.02	0.87	0.18	3.04
NF60-7-1CA	4.35	4.10	0.09	11.82	1.10	1.03	0.10	3.01	1.10	1.14	-0.08	2.55
NF60-7-2CA	6.50	5.16	0.23	20.48	1.70	1.19	0.30	5.73	1.70	1.43	0.19	5.14
NF60-7-2CB	6.49	4.43	0.31	22.20	2.24	1.22	0.38	8.31	2.24	1.70	0.26	7.23
NF60-7-1CB	8.47	12.52	-0.37	18.64	1.96	1.15	0.36	7.09	1.96	1.54	0.24	6.20
HF40-7-1CA	10.22	8.70	0.19	30.61	1.38	2.02	-0.37	3.02	1.38	2.01	-0.37	3.02
HF40-7-2CA	11.49	8.44	0.28	37.91	2.06	2.05	0.01	5.20	2.06	2.01	0.04	5.35
HF40-7-2CB	16.71	12.23	0.28	55.21	2.72	2.49	0.12	7.65	2.72	2.72	0.00	6.82
HF40-7-1CB	14.75	13.81	0.10	40.42	1.47	2.57	-0.37	3.60	1.47	2.45	-0.37	3.49
HF60-7-1CA	3.71	4.01	-0.30	7.22	1.43	0.55	0.45	5.74	1.43	0.93	0.33	4.97
HF60-7-2CA	1.14	5.67	-0.37	6.16	1.27	1.01	0.23	3.99	1.27	1.21	0.07	3.38
HF60-7-2CB	6.79	5.78	0.19	20.35	1.93	1.69	0.16	5.64	1.93	2.01	-0.09	4.45
HF40-7-1CB	10.90	7.27	0.32	37.61	1.98	2.25	-0.37	3.74	1.98	2.16	-0.37	3.66

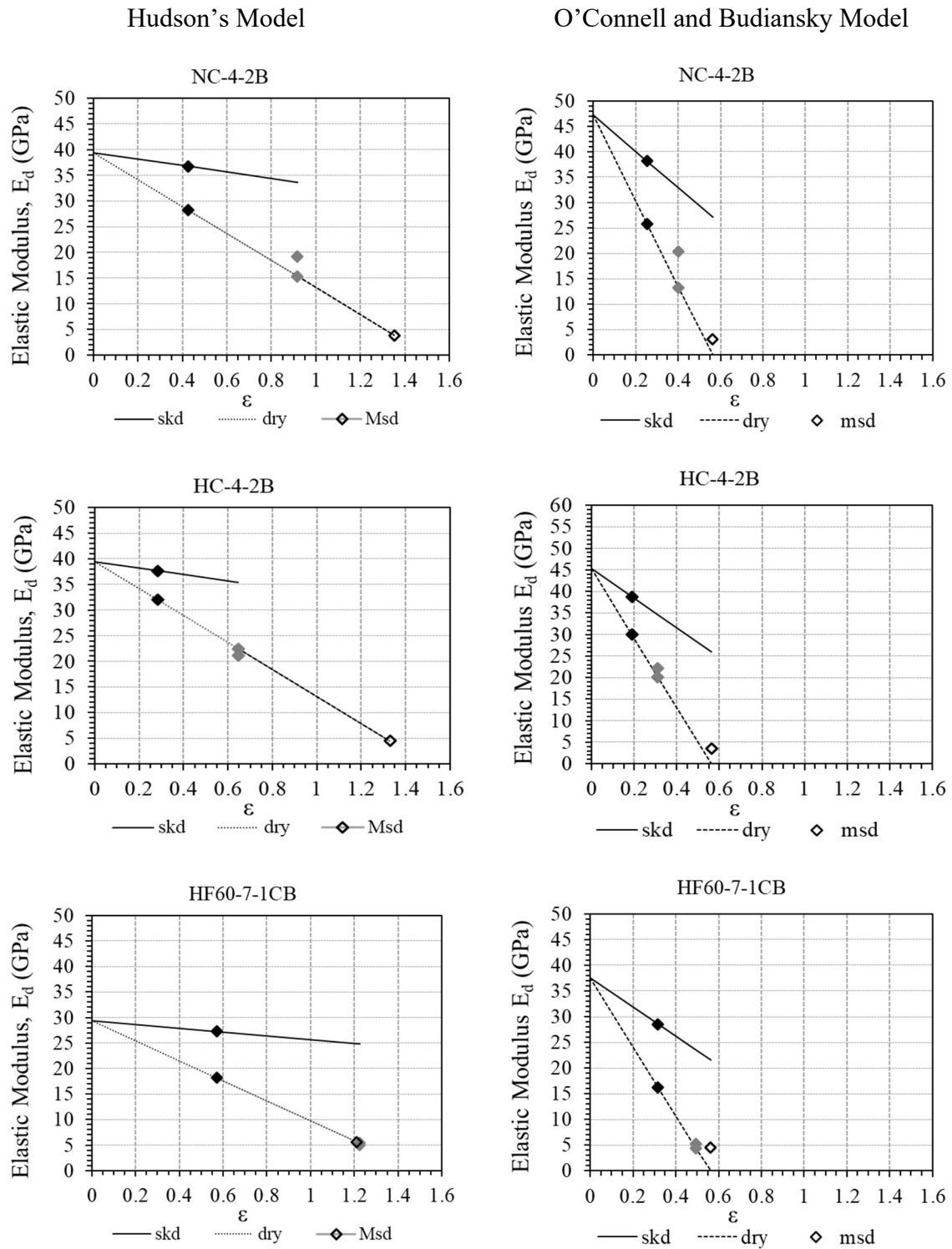


Figure 5.19: Comparison of Hudson's model and O'Connell and Budiansky Model for Normal and High Strength Control mixture groups for one and two-inch thick discs..

Moreover, the two mixtures of normal and high strength with different fly ash percentages are plotted in figure 5.18 shows an increase in Crack density values with Hudson's model when compared to those obtained using O'Connell and Budiansky. In the case of the O'Connell and Budiansky model, a higher Young's modulus is obtained when compared to Hudson's model. The increase in elastic modulus for different specimens with the two models has been presented in Table 5.7. The lowest value of the percentage increase using the average values of mixture groups for the one-inch disc is 6.71 and the highest percentage increase is about 31.5. On the contrary, when using two-inch thick disc specimens, the lowest and highest percentages obtained are 3.34 and 31.49 respectively.

Table 5.7: Difference in percentage shown using two models for one and two-inch thick disc

ID	Hudson	O&B	% Increase	ID	Hudson	O&B	% Increase
	E ₀ (GPa)	E ₀ (GPa)			E ₀ (GPa)	E ₀ (GPa)	
NC-4-1A	35.86	30.93	-13.75	NC-4-2A	33.44	43	28.59
NC-5-1A	32.97	40.32	22.29	NC-5-2A	34.59	39.83	15.15
NC-6-1A	33.84	41.99	24.08	NC-6-2A	28.49	33.56	17.8
Mean NC-1	34.22	37.75	10.3	Mean NC-2	32.17	38.8	20.59
HC-4-1A	36.47	43.1	18.18	HC-4-2A	38.57	45.55	18.1
HC-5-1A	39.34	48.34	22.88	HC-5-2A	36.77	42.69	16.1
HC-6-1A	41.49	53.19	28.2	HC-6-2A	37.75	44.48	17.83
Mean HC-1	39.1	48.21	23.3	Mean HC-2	37.7	44.24	17.36
Before Damage							
HF40-7-1CA	25.93	30.61	18.03	HF40-7-2CA	29.64	37.91	27.9
HF40-7-1CB	37.23	40.42	8.57	HF40-7-2CB	43.74	55.21	26.23
Mean HF40-1	31.58	35.515	12.46	Mean HF40-2	36.69	46.56	26.91
HF60-7-1CA	9.65	7.22	-25.18	HF60-7-2CA	8.51	6.16	-27.61
HF60-7-1CB	28.26	37.61	33.07	HF60-7-2CB	17.14	20.35	18.69
Mean HF60-1	18.96	22.415	18.24	Mean HF60-2	12.83	13.26	3.34
NF40-7-1CA	19.74	28.3	43.37	NF40-7-2CA	17.2	22.02	28.06
NF40-7-1CB	16.18	11.55	-28.61	NF40-7-2CB	16.99	18.61	9.52
Mean NF40-1	17.96	19.925	10.95	Mean NF40-2	17.09	20.32	18.85
NF60-7-1CA	10.91	11.82	8.38	NF60-7-2CA	16.47	20.48	24.31
NF60-7-1CB	26.23	18.64	-28.93	NF60-7-2CB	16.58	22.2	33.93
Mean NF60-1	18.57	15.23	-17.97	Mean NF60-2	16.53	21.34	29.14
After Damage							
HF40-7-1CA	4.26	3.02	-29.04	HF40-7-2CA	5.14	5.2	1.08
HF40-7-1CB	5.05	3.6	-28.67	HF40-7-2CB	6.82	7.65	12.18
Mean HF40-1	4.65	3.31	-28.84	Mean HF40-2	5.98	6.43	7.41
HF60-7-1CA	3.6	5.74	59.66	HF60-7-2CA	3.18	3.99	25.57
HF60-7-1CB	5.29	3.74	-29.29	HF60-7-2CB	4.84	5.64	16.62
Mean HF60-1	4.44	4.74	6.71	Mean HF60-2	4.01	4.82	20.17
NF40-7-1CA	2	2.11	5.61	NF40-7-2CA	2.45	1.74	-28.92
NF40-7-1CB	4.09	2.93	-28.36	NF40-7-2CB	5.02	6.03	20.14
Mean NF40-1	3.04	2.52	-17.22	Mean NF40-2	3.73	3.89	4.06
NF60-7-1CA	2.75	3.01	9.5	NF60-7-2CA	4.27	5.73	34.13
NF60-7-1CB	4.93	7.09	43.75	NF60-7-2CB	5.65	8.31	47.05
Mean NF60-1	3.84	5.05	31.49	Mean NF60-2	4.96	7.02	41.49

The percentage increase in Young’s modulus using Hudson’s model and O’Connell and Budiansky’s model is presented in table 5.8 for one- and two-inches thick discs. The results shown are the averages of Young’s modulus for all different groups.

Table 5.8: Percentage difference in mean Young’s modulus for one-inch-thick disc

Specimen ID	Hudson	O&B	% Increase	Specimen ID	Hudson	O&B	% Increase
	E ₀ (GPa)	E ₀ (GPa)			E ₀ (GPa)	E ₀ (GPa)	
NC-1	34.2	37.7	10.3	NC-2	32.2	38.8	20.6
HC-1	39.1	48.2	23.3	HC-2	37.7	44.2	17.4
Before Damage							
HF40-1	31.6	35.5	12.5	HF40-2	36.7	46.6	26.9
HF60-1	19	22.4	18.2	HF60-2	12.8	13.3	3.3
NF40-1	18	19.9	11	NF40-2	17.1	20.3	18.8
NF60-1	18.6	15.2	-17.9	NF60-2	16.5	21.3	29.1
After Damage							
HF40-1	4.7	3.3	-28.8	HF40-2	6	6.4	7.4
HF60-1	4.4	4.7	6.7	HF60-2	4	4.8	20.2
NF40-1	3	2.5	-17.2	NF40-2	3.7	3.9	4.1
NF60-1	3.8	5.1	31.5	NF60-2	5	7	41.5

Tables 5.9 and 5.10 shows the results obtained using Hudson’s model for one-inch-thick discs where uncracked dynamic Young’s modulus and the differences in the crack density at different levels are presented.

Table 5.9: Hudson Model for one-inch

Mixture Group	Specimen ID	E_0	Crack Density Parameter			$\Delta\epsilon$	
		(GPa)	ϵ_1	ϵ_2	ϵ_3	$\epsilon_2 - \epsilon_1$	$\epsilon_3 - \epsilon_1$
NCUD	NC-4-1A	35.860	0.000	-	0.976	-	0.976
	NC-5-1A	32.970	0.364	-	0.788	-	0.424
	NC-6-1A	33.840	0.407	-	0.892	-	0.485
NCD	NC-4-1B	50.370	0.665	1.161	1.161	0.496	0.496
	NC-5-1B	43.761	0.422	1.255	1.255	0.832	0.832
	NC-6-1B	42.729	0.421	1.193	1.193	0.772	0.772
HCUD	HC-4-1A	37.325	0.293	-	0.789	-	0.496
	HC-5-1A	40.731	0.403	-	0.536	-	0.134
	HC-6-1A	43.602	0.537	-	0.892	-	0.355
HCD	HC-4-1B	42.369	0.000	1.222	0.789	1.222	0.789
	HC-5-1B	36.246	0.000	1.057	0.536	1.057	0.536
	HC-6-1B	37.715	0.179	0.923	0.669	0.744	0.491

‘UD’ is undamaged group, ‘D’ is the damaged group at 300 °C temperature ‘ E_0 ’ is the Young’s modulus of uncracked solid, ‘ ϵ_1 ’ is the crack density parameter before damage using shear modulus values for SKD and Dry conditions, ‘ ϵ_2 ’ is the crack density parameter after 300 °C exposure to specimens, ‘ ϵ_3 ’ is the cack density obtained after damaging specimens using soaked and dry conditions SKD’ and Dry’

Table 5.10: O’Connell and Budiansky Model for one-inch

Mixture Group	Specimen ID	E_0	Crack Density Parameter			$\Delta\epsilon$	
		(GPa)	ϵ_1	ϵ_2	ϵ_3	$\epsilon_2 - \epsilon_1$	$\epsilon_3 - \epsilon_1$
NCUD	NC-4-1A	30.930	0.000	-	0.473	-	0.473
	NC-5-1A	40.320	0.230	-	0.496	-	0.266
	NC-6-1A	41.990	0.250	-	0.479	-	0.229
NCD	NC-4-1B	61.863	0.333	0.422	0.473	0.089	0.140
	NC-5-1B	51.895	0.248	0.362	0.496	0.114	0.248
	NC-6-1B	50.763	0.248	0.393	0.479	0.145	0.231
HCUD	HC-4-1A	43.100	0.200	-	0.469	-	0.269
	HC-5-1A	48.340	0.240	-	0.405	-	0.165
	HC-6-1A	53.190	0.290	-	0.389	-	0.000
HCD	HC-4-1B	40.933	0.000	0.313	0.469	0.313	0.469
	HC-5-1B	33.579	0.000	0.196	0.405	0.196	0.405
	HC-6-1B	41.625	0.133	0.307	0.389	0.174	0.256

‘NC’ is normal strength concrete, ‘HC’ is high strength concrete, ‘UD’ is undamaged group, ‘D’ is the damaged group at 300 °C temperature ‘ E_0 ’ is the elastic Young’s modulus of uncracked solid, ‘ ϵ_1 ’ is the crack density parameter before damage using shear modulus values for SKD and Dry conditions, ‘ ϵ_2 ’ is the crack density parameter after 300 °C exposure to specimens, ‘ ϵ_3 ’ is the cack density obtained after damaging specimens using soaked and dry conditions SKD’ and Dry’

The equivalent E_0 for normal and high strength mixture groups have a mean of 39.9 and 39.6 GPa, a standard deviation of 6.8 and 2.9 GPa and a range of 17.4, and 7.3 GPa respectively. The change in crack density parameter (ϵ) shows an expected increase in the measured values due to the high-temperature exposure damage. Autogenous healing was also observed in damaged specimens as well as an increase in the value of ϵ after DRY' and SKD' cycles and is pronounced in the normal and high strength mixture groups.

The undamaged crack density parameter for normal strength concrete, $\epsilon_{1, NC}$ has a mean value of 0.380, with a standard deviation of 0.214 and a range of 0.665, whereas the coefficient of variation is about 56% which is a higher value and is due to the low value for the mean. In the case of high strength concrete mixture, $\epsilon_{1, HC}$ had a mean value of 0.235, with a standard deviation of 0.217 and a range of 0.537, similarly in this case a higher value for the coefficient of variation of about 92% was obtained. A comparison of statistics to the results obtained using Hudson's model with those calculated using the O'Connell and Budiansky model is presented in Table 5.11.

For the damaged crack density parameter ' ϵ_3 ' the crack density obtained after damaging specimens using soaked (SKD') and dry (DRY') conditions, the mean of the NCD mixture group was 0.885 and 0.665 for mixture HCD.

Table 5.11: Comparison of the Two Model Results

Property	Hudson's Model				O'Connell and Budiansky Model			
	mean	std. dev.	Range	c.v. (%)	mean	std. dev.	Range	c.v. (%)
$E_{0, NC}$ (GPa)	39.922	6.835	17.400	17.122	41.683	6.300	19.134	15.114
$E_{0, HC}$ (GPa)	39.665	2.997	7.355	7.556	43.493	6.401	16.944	14.716
$\epsilon_{1, NC}$	0.380	0.214	0.665	56.458	0.218	0.113	0.333	51.743
$\epsilon_{1, HC}$	0.235	0.217	0.537	92.372	43.493	0.123	0.290	0.282
$\epsilon_{2, NC}$	1.203	0.048	0.094	3.956	0.392	0.030	0.060	7.648
$\epsilon_{2, HC}$	1.067	0.150	0.299	14.019	0.272	0.066	0.117	24.223
$\epsilon_{3, NCUD}$	0.885	0.094	0.188	10.664	0.483	0.012	0.023	2.472
$\epsilon_{3, NCD}$	0.885	0.094	0.188	10.664	0.483	0.012	0.188	2.472
$\epsilon_{3, HCUD}$	0.739	0.183	0.356	24.786	0.421	0.042	0.080	10.055
$\epsilon_{3, HCD}$	0.665	0.127	0.253	19.060	0.421	0.042	0.253	10.055
$(\epsilon_2 - \epsilon_1)_{NCD}$	0.700	0.179	0.336	25.567	0.116	0.028	0.336	24.184
$(\epsilon_2 - \epsilon_1)_{HCD}$	1.008	0.043	0.478	4.231	0.228	0.075	0.478	32.818
$(\epsilon_3 - \epsilon_1)_{NCUD}$	0.628	0.303	0.553	48.184	0.323	0.132	0.401	40.754
$(\epsilon_3 - \epsilon_1)_{NCD}$	0.383	0.081	0.160	21.230	0.206	0.058	0.160	28.145
$(\epsilon_3 - \epsilon_1)_{HCUD}$	0.328	0.183	0.363	55.677	0.145	0.136	0.323	93.766
$(\epsilon_3 - \epsilon_1)_{HCD}$	0.605	0.161	0.299	26.601	0.377	0.109	0.299	29.015

'NC' is normal strength concrete, 'HC' is high strength concrete, 'UD' is undamaged group, 'D' is the damaged group at 300 °C temperature 'E₀' is the Young's modulus of uncracked solid, 'ε₁' is the crack density parameter before damage using shear modulus values for SKD and Dry conditions, 'ε₂' is the crack density parameter after 300 °C exposure to specimens, 'ε₃' is the cack density obtained after damaging specimens using soaked and dry conditions SKD' and Dry'

In the case of two-inch thick concrete disc specimens, the equivalent E₀ for normal and high strength mixture groups E_{0, NC} and E_{0, HC} had a mean of 35.3 and 39.8 GPa, a standard deviation of 6.1 and 5.3 GPa, and a range of 16.9 and 12.2 GPa respectively. The measured values of both mixture groups are presented in Table 5.12 and Table 5.13, however, the statistical results are presented in Table 5.14. The crack density parameter (ε) values increased when measured after the damage induced due to high-temperature exposure. In the case of two-inch thick discs, the Autogenous healing was also observed in damaged specimens as

well as an increase in the value of ϵ after DRY' and SKD' cycles for normal and high strength mixture groups. The undamaged crack density parameter for normal strength concrete, $\epsilon_{1, NC}$ has a mean value of 0.343, with a standard deviation of 0.150 and a range of 0.356, although the coefficient of variation was found to be higher i.e., about 44% which is due to the low value for the mean. In the case of high strength concrete mixture, $\epsilon_{1, HC}$ had a mean value of 0.180, with a standard deviation of 0.127 and a range of 0.275, a higher value for the coefficient of variation of about 70% was obtained, however. A comparison of statistics to the results obtained using Hudson's model with those calculated using the O'Connell and Budiansky model is presented in Table 4.18. For the damaged crack density parameter ' ϵ_3 ' the crack density obtained after damaging specimens using soaked (SKD') and dry (DRY') conditions, the mean of the NCD mixture group was 0.737 and 0.539 for mixture HCD.

Table 5.12: Hudson Model for two-inch

Mixture Group	Specimen ID	E_0	Crack Density Parameter			$\Delta\epsilon$	
		(GPa)	ϵ_1	ϵ_2	ϵ_3	$\epsilon_2 - \epsilon_1$	$\epsilon_3 - \epsilon_1$
NCUD	NC-4-2A	33.440	0.460	-	1.353	-	0.893
	NC-5-2A	34.590	0.210	-	1.314	-	1.104
	NC-6-2A	28.490	0.240	-	1.250	-	1.010
NCD	NC-4-2B	39.434	0.427	1.353	0.917	0.926	0.490
	NC-5-2B	45.396	0.539	1.314	0.870	0.775	0.330
	NC-6-2B	30.642	0.183	1.250	0.426	1.067	0.243
HCUD	HC-4-2B	45.550	0.270	-	0.647	-	0.377
	HC-5-2B	42.690	0.230	-	0.458	-	0.228
	HC-6-2B	44.480	0.260	-	0.512	-	0.252
HCD	HC-4-2B	39.468	0.285	1.331	0.647	1.046	0.362
	HC-5-2B	33.263	0.010	1.248	0.458	1.238	0.448
	HC-6-2B	33.563	0.027	1.249	0.512	1.222	0.485

Table 5.13: O’Connell and Budiansky Model for two-inch

Mixture Group	Specimen ID	E_0	Crack Density Parameter			$\Delta\epsilon$	
		(GPa)	ϵ_1	ϵ_2	ϵ_3	$\epsilon_2 - \epsilon_1$	$\epsilon_3 - \epsilon_1$
NCUD	NC-4-2A	43.000	0.290	-	0.523	-	0.233
	NC-5-2A	39.830	0.160	-	0.513	-	0.353
	NC-6-2A	33.560	0.190	-	0.490	-	0.300
NCD	NC-4-2B	47.270	0.253	0.402	0.523	0.149	0.270
	NC-5-2B	55.159	0.292	0.390	0.513	0.098	0.221
	NC-6-2B	34.172	0.139	0.227	0.490	0.088	0.351
HCUD	HC-4-2A	45.550	0.200	-	0.515	-	0.315
	HC-5-2A	42.690	0.170	-	0.482	-	0.312
	HC-6-2A	44.480	0.190	-	0.483	-	0.293
HCD	HC-4-2B	45.262	0.189	0.310	0.515	0.121	0.326
	HC-5-2B	33.510	0.009	0.199	0.482	0.190	0.473
	HC-6-2B	34.224	0.025	0.225	0.483	0.200	0.458

Table 5.14: O’Connell and Budiansky Model for two-inch

Property	Hudson’s Model				O’Connell and Budiansky Model			
	mean	std. dev.	Range	c.v. (%)	mean	std. dev.	Range	c.v. (%)
E_0, NC (GPa)	35.332	6.181	16.906	17.495	42.165	6.712	21.599	15.917
E_0, HC (GPa)	39.836	5.386	12.287	13.521	40.953	11.011	12.040	26.888
ϵ_1, NC	0.343	0.150	0.356	43.837	0.221	0.051	0.153	23.319
ϵ_1, HC	0.180	0.127	0.275	70.324	0.131	0.229	0.191	175.708
ϵ_2, NC	1.306	0.052	0.103	3.972	0.340	0.098	0.175	28.780
ϵ_2, HC	1.276	0.047	0.083	3.716	0.245	0.087	0.111	35.553
$\epsilon_3, NCUD$	1.306	0.052	0.491	3.972	0.340	0.014	0.033	4.090
ϵ_3, NCD	0.737	0.271	0.491	36.749	0.509	0.019	0.033	3.690
$\epsilon_3, HCUD$	0.539	0.097	0.189	18.017	0.493	0.422	0.033	85.563
ϵ_3, HCD	0.539	0.033	0.189	6.124	0.493	0.078	0.033	15.729
$(\epsilon_2 - \epsilon_1)_{NCD}$	0.923	0.146	0.292	15.848	0.112	0.033	0.061	29.298
$(\epsilon_2 - \epsilon_1)_{HCD}$	1.169	0.107	0.192	9.121	0.170	0.130	0.079	76.407
$(\epsilon_3 - \epsilon_1)_{NCUD}$	1.002	0.106	0.474	10.564	0.126	0.067	0.120	53.131
$(\epsilon_3 - \epsilon_1)_{NCD}$	0.354	0.125	0.247	35.387	0.281	0.017	0.130	5.901
$(\epsilon_3 - \epsilon_1)_{HCUD}$	0.286	0.080	0.149	27.927	0.307	0.195	0.022	63.484
$(\epsilon_3 - \epsilon_1)_{HCD}$	0.432	0.063	0.123	14.618	0.419	0.137	0.147	32.727

The graphical representation of all mixtures from normal strength and high strength concrete and their performance under different level conditions are presented in figures from 5.19 to figure 5.26 where one-inch and two-inch thick concrete discs are shown. It could be observed from the figures that at testing condition number '4' which is Skd' (specimens exposed to high temperature and soaked in water) a gain in strength is achieved which is due to the which could be due to the autogenous healing of concrete happening after water penetration in the cracks resulting in re-activating the hydration process.

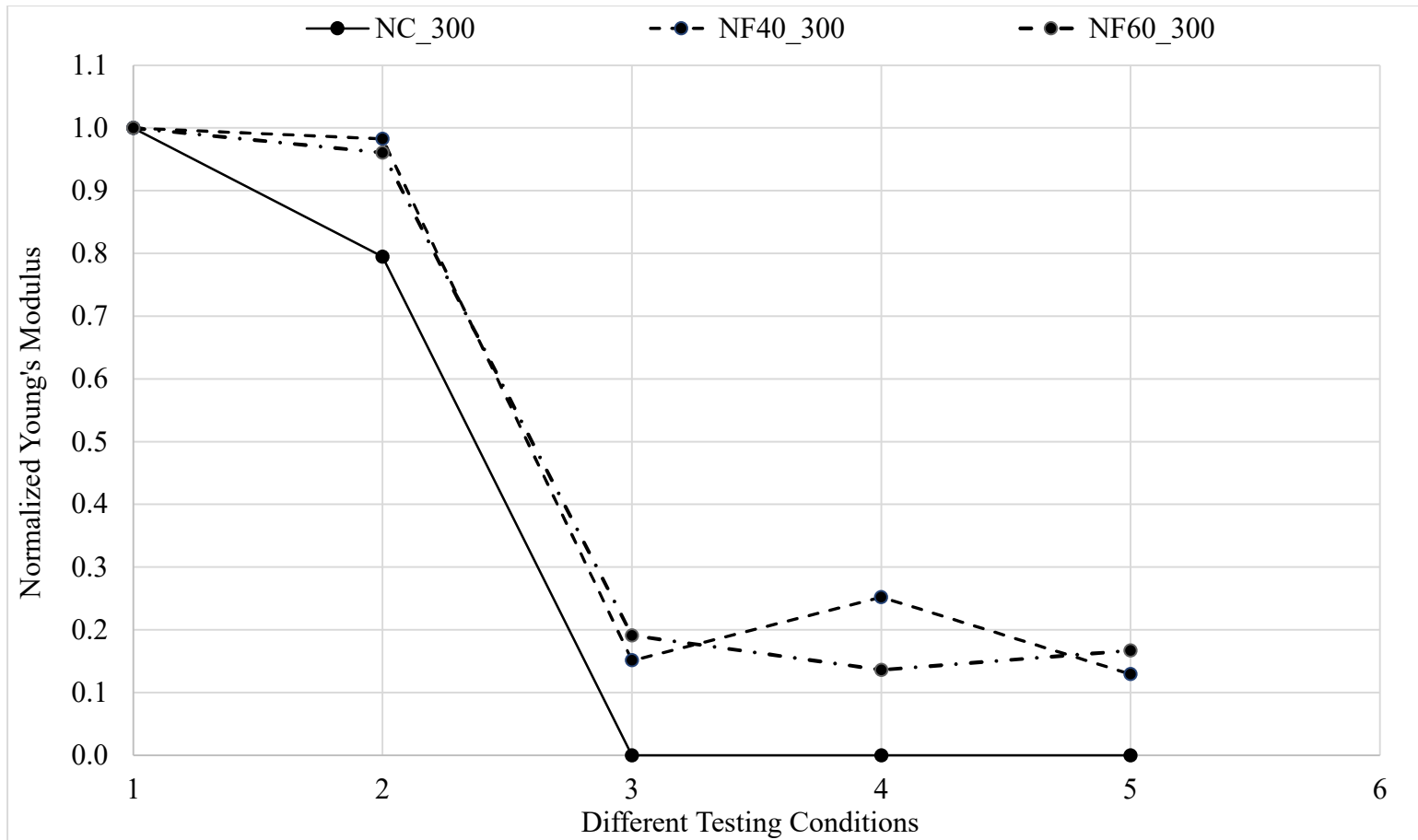


Figure 5.20: Comparison of Normalized Young's Modulus for Normal Strength Concrete Mixtures damaged at 300 °C for one-inch thick disc specimens

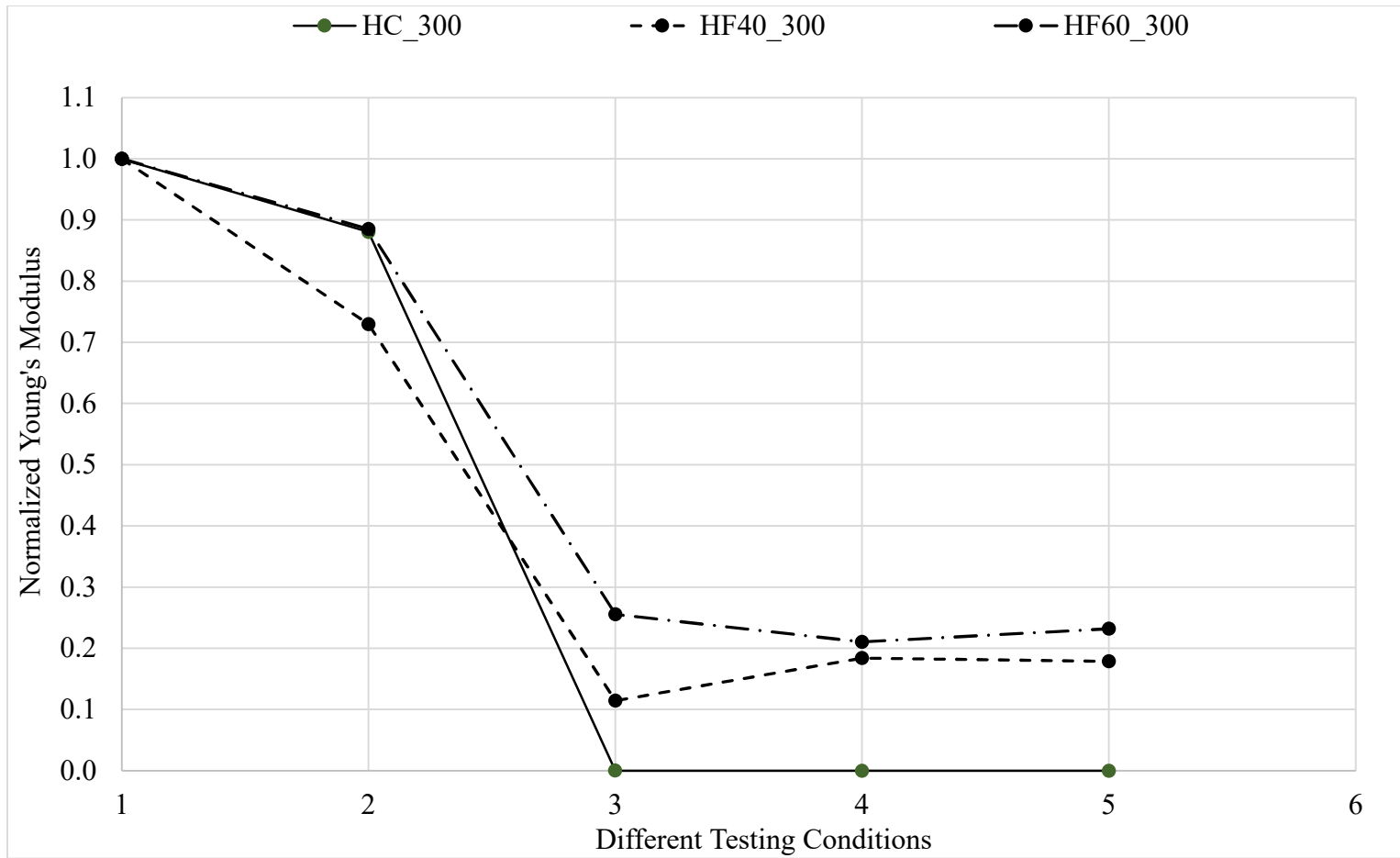


Figure 5.21: Comparison of Normalized Young's modulus for High Strength Concrete Mixtures damaged at 300 °C for one-inch thick disc specimens

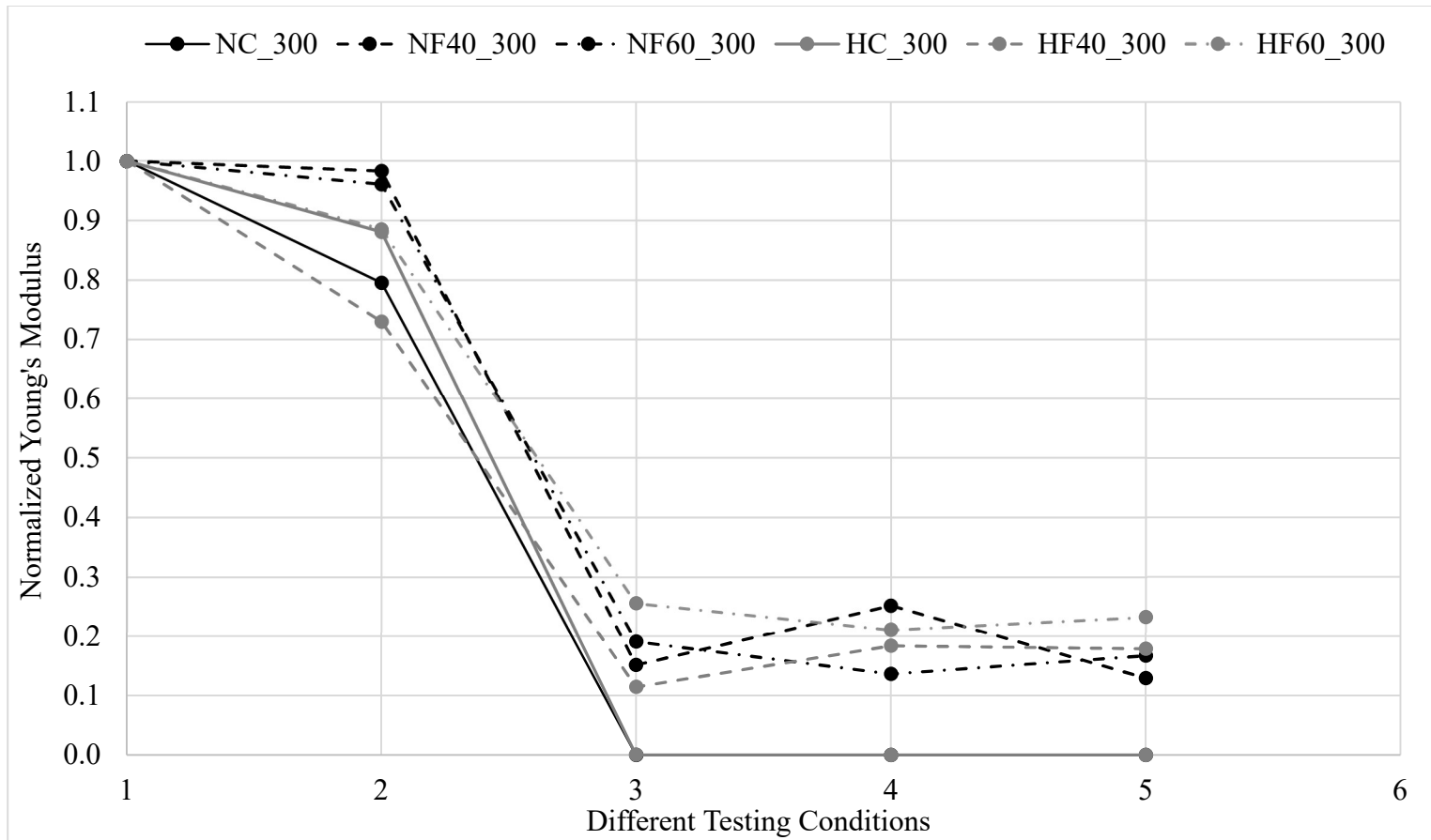


Figure 5.22: Comparison of Normalized Young's modulus for Normal and High Strength Concrete Mixtures damaged at 300 °C for one-inch thick disc specimens

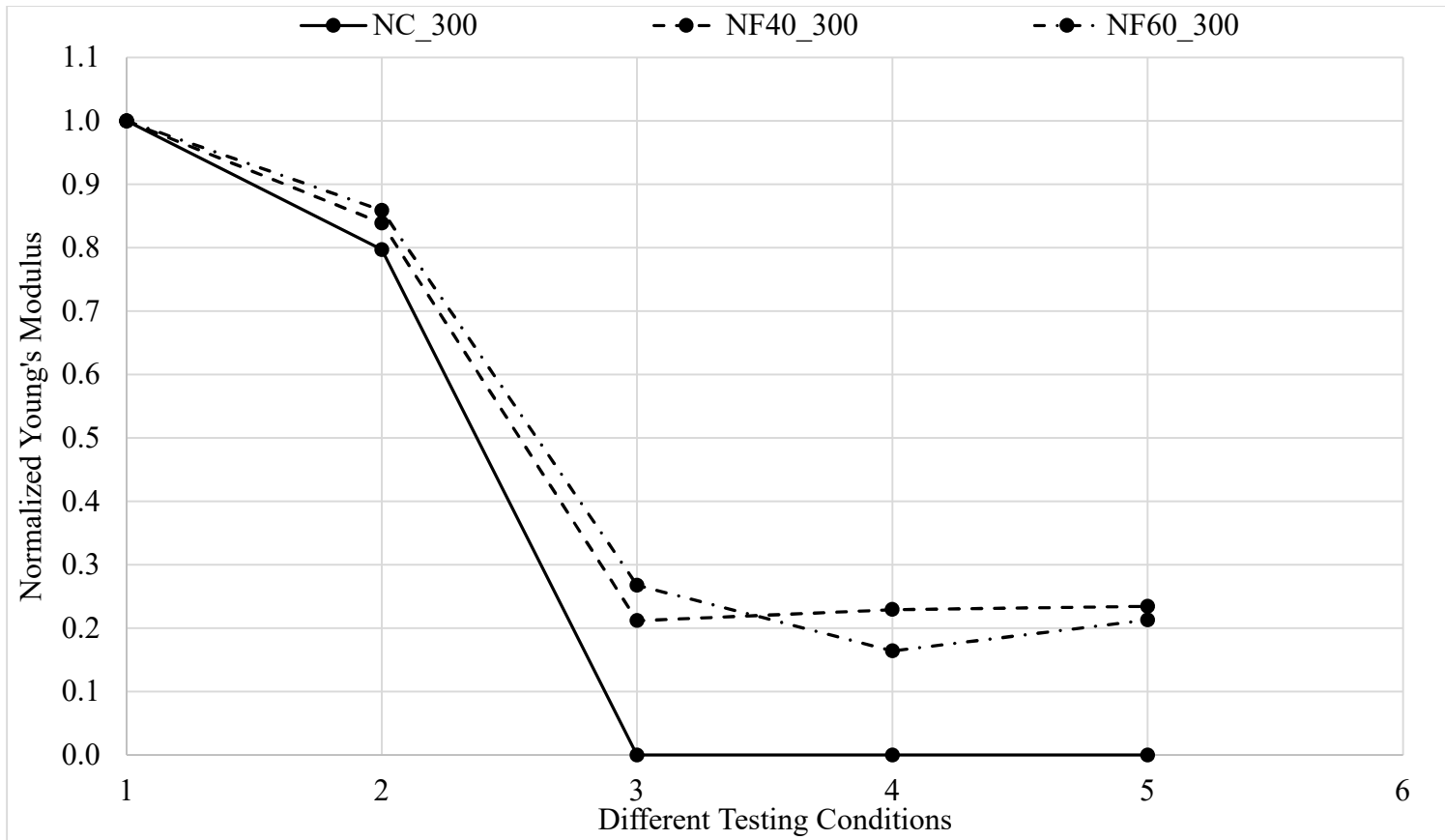


Figure 5.23: Comparison of Normalized Young's Modulus for Normal Strength Concrete Mixtures damaged at 300 °C for two-inch thick disc Specimens

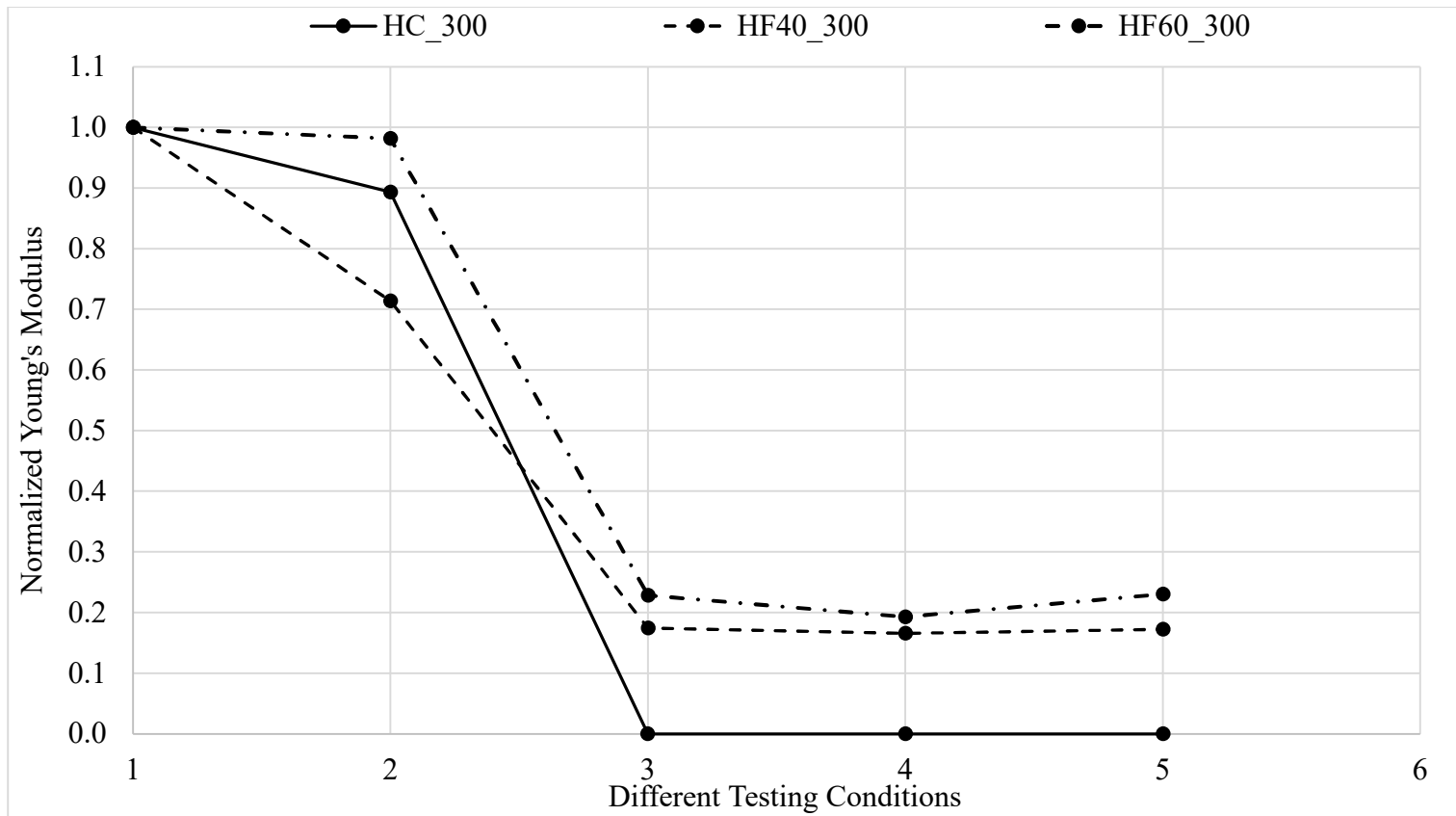


Figure 5.24: Comparison of Normalized Young's Modulus for High Strength Concrete Mixtures damaged at 300 °C for two-inch thick disc Specimens

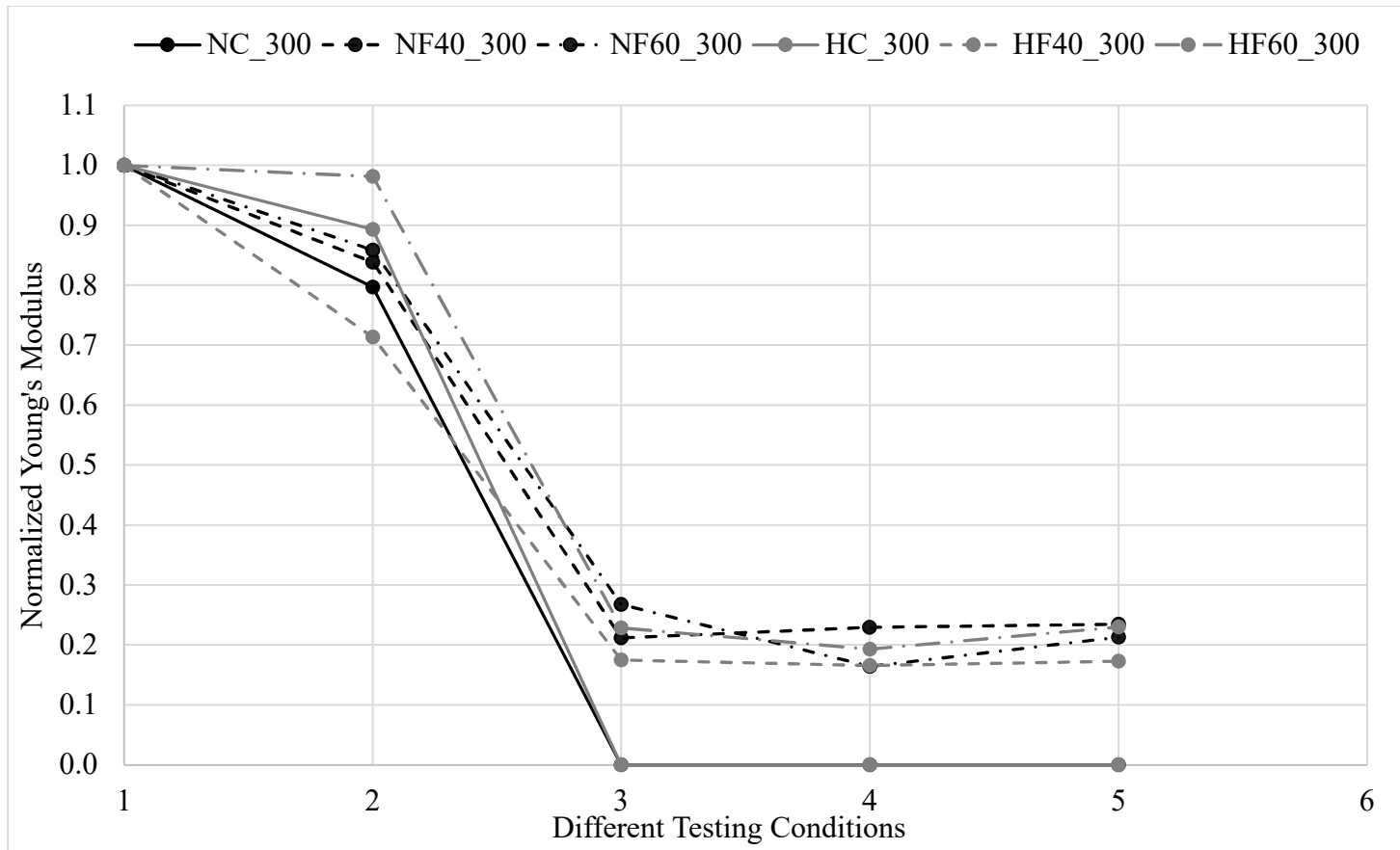


Figure 5.25: Comparison of Normalized Young's Modulus for Normal and High Strength Concrete Mixtures damaged at 300 °C for two-inch thick disc Specimens

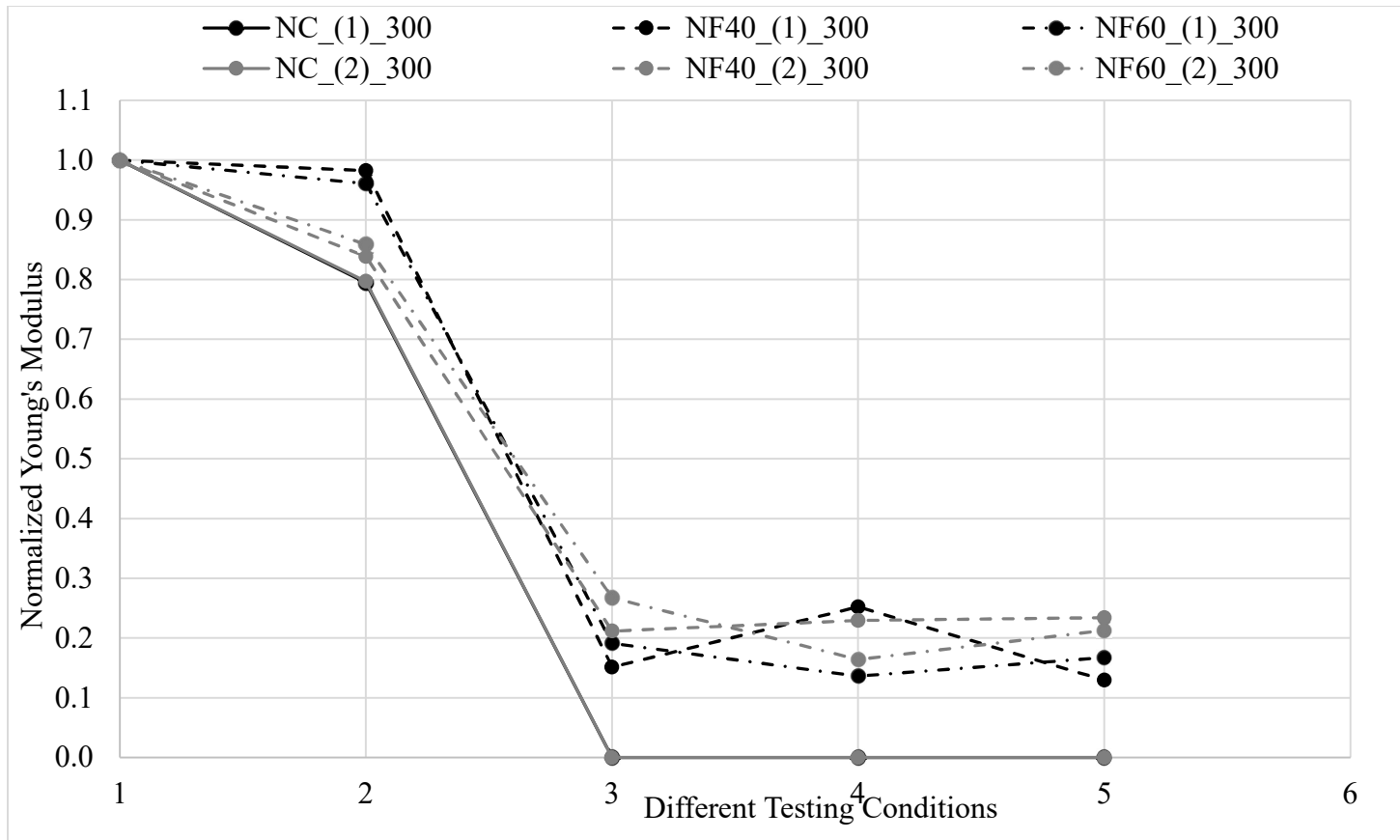


Figure 5.26: Comparison of Normalized Young's Modulus for Normal Strength Concrete Mixtures damaged at 300 °C for one-inch and two-inch thick disc Specimens

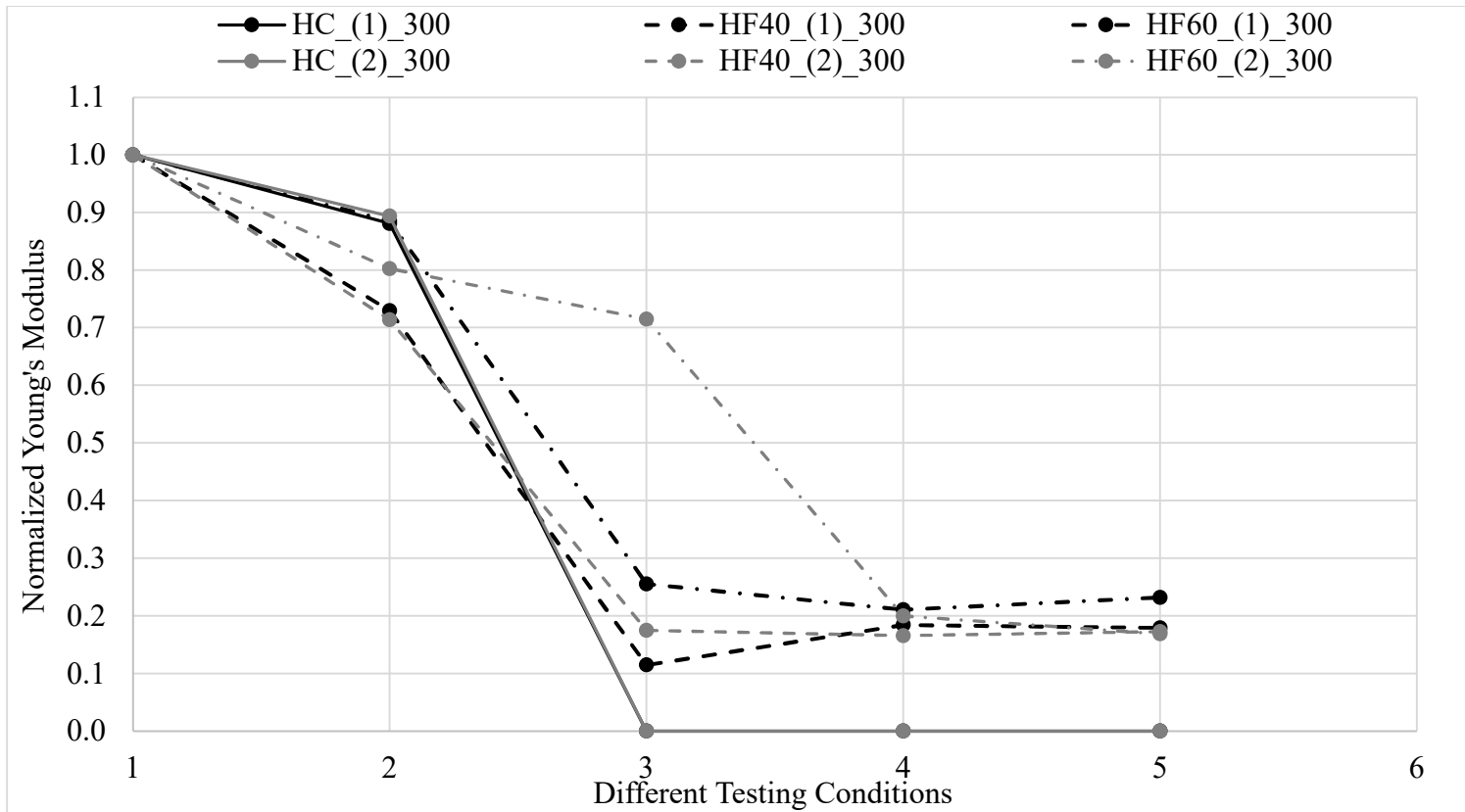
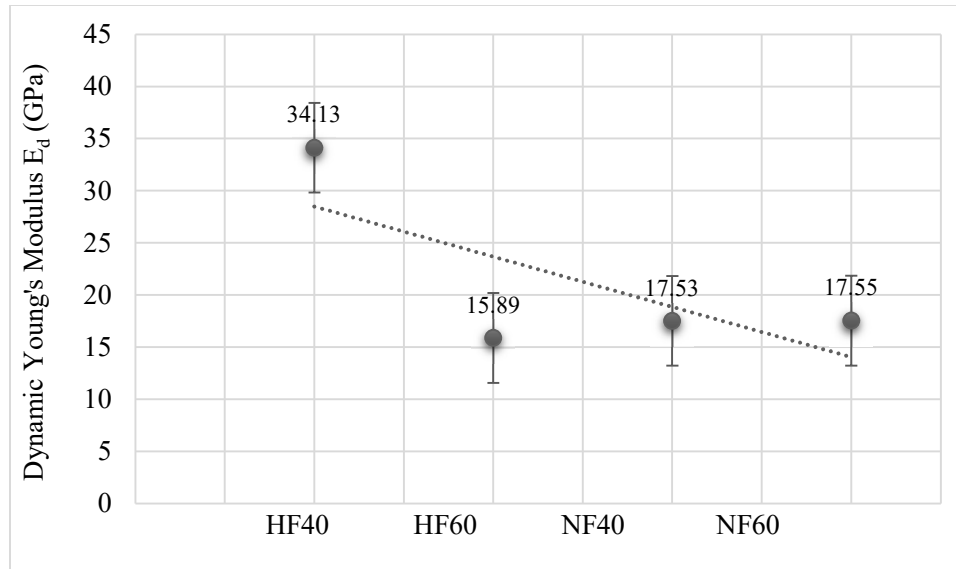


Figure 5.27: Comparison of Normalized Young's Modulus for High Strength Concrete mixtures damaged at 300 °C for one-inch and two-inch thick disc Specimens

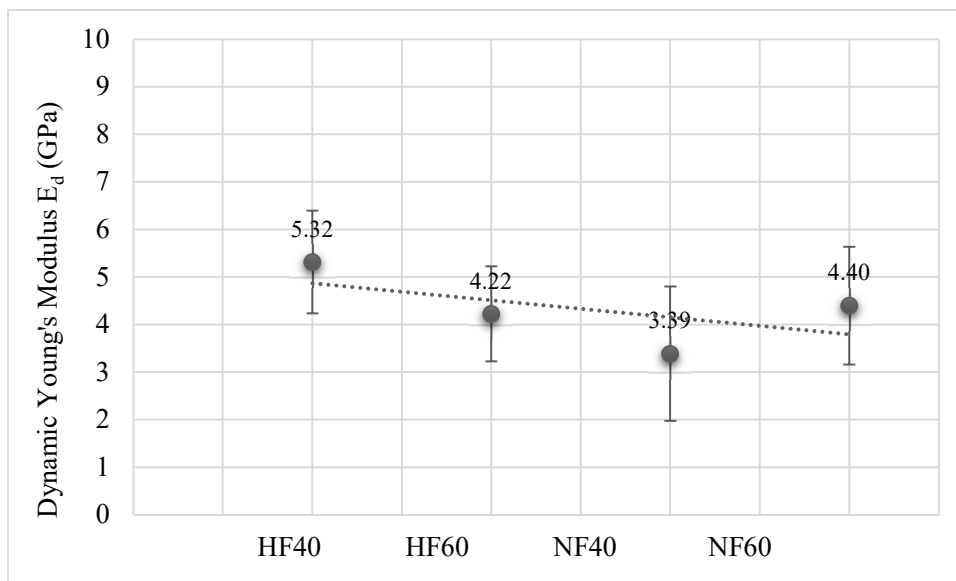
5.9 Difference in Elastic Modulus due to Temperature Exposure

Analysis of the temperature effects on the dynamic Young's modulus of elasticity (E_d) was carried out using a single-factor analysis of variance (ANOVA) with a 95% confidence level. Single-factor ANOVA is defined as a comparison of the differences within a single group to the variation among multiple groups (NIST 2010). The difference between undamaged and damaged elastic modulus with exposure to 300 °C (570 °F) was observed. For group C-specimens undamaged, the P -value is (0.0083), which is less than the alpha value of 0.05; however, the F value is greater than F critical, indicating that the mean of the samples is varying, and hence, the null hypothesis could be rejected. In the case of C-specimens after damaging to 300 °C (570 °F), the obtained P -value is (0.2082) and is greater than alpha value of 0.05 showing that mean of the samples are in good agreement and the mean of mixtures is similar; hence, we cannot reject the null hypothesis.

The detailed ANOVA analysis results for each mixture are provided in Appendix-B. Figure 4.74 (a) and figure 4.74 (b) below shows the difference in Young's modulus for all mixtures comprised of enhanced sustainable concrete materials damaged at 300 °C (570 °F).



(a)



(b)

Figure 5.28: Difference in Young's modulus for all mixtures damaged at high temperatures

(a) Specimens before damage (b) Specimens after damage

5.10 Statistical Analysis Results

5.10.1 Effect of Elevated Temperature on the Dynamic Shear Modulus

Statistical analysis on the effects of elevated temperature of 300 °C (570 °F) on the elastic properties of concrete i.e., Shear modulus (G_d) was carried out using single-factor analysis of variance (ANOVA) with a 95% confidence level. The change in the shear modulus between mixture groups with different fly ash content was observed when the discs were exposed to the high temperature of 300 °C. Statistical analysis was carried out for the specimens labeled as ‘C’ cracked and damaged due to relatively short exposure of two hours. ANOVA analysis resulted in a P-value (0.194) that is greater than the alpha value of 0.05, which presents that there is no significant difference in the change of the G_d for the temperature exposure of 300 °C for all concrete mixtures with different percentages of fly ash and we can reject the null hypothesis. The detailed ANOVA analysis results for the effect of high temperature on different mixtures is presented in Appendix-B, however, table 5.15 shows the mean values for change in G_d for different mixtures.

5.10.2 Effect of Elevated Temperature on Crack Density Parameter

The effect of elevated temperature of 300 °C on the crack density parameter (ϵ) was determined using single-factor ANOVA considering a 95% confidence level. The change in ϵ was observed by analyzing the mean values for all mixture types used in this research work with relatively short temperature exposure of two hours. Statistical analysis results revealed a P-value (0.0069) which is less than the alpha value of 0.05 which shows that there is a significant difference in the change of the crack density parameter ϵ for the

temperature exposure of 300 °C for all concrete mixtures with different percentages of fly ash. The detailed ANOVA analysis results for the effect of elevated temperature on the crack density for different mixtures is presented in Appendix-B, however, table 5.15 shows the mean values for change in ϵ values for different mixtures groups.

5.10.3 Relationship between the Decrease in G_d and increase of CDP for Damaged Specimens

The relationship between the change in dynamic shear modulus (G_d) with the change in crack density parameter is inversely proportional. When G_d decreases, the crack density parameter increases and vice versa which happens due to the temperature induced to specimens and high temperatures. However, the change in these parameters is different for concrete mixtures with normal and high strengths. Table 5.15 shows the mean value of dynamic shear modulus and the crack density parameter and the changes in parameters for each of the mixture groups with different fly ash content.

Table 5.15: Mean values for change in ϵ and G_d values for different concrete Mixtures

Specimens	Initial ϵ	Initial G_d	Change in ϵ	Change in G_d
NF40-7-1C_Mean	0.355	5.893	-0.328	6.344
NF60-7-1C_Mean	0.045	7.682	-0.316	8.310
NF40-7-2C_Mean	0.250	5.374	-0.132	5.696
NF60-7-2C_Mean	0.412	6.321	-0.159	4.796

5.11 Summary

This chapter presented the extension of Hudson's model from rock mechanics to concrete material which has been utilized to analyze the changes occurring in dynamic elastic modulus (E_d) and crack density parameter of the concrete disc in soaked and dry conditions before and after damage. For the purpose of comparison, the extension of Hudson's model was compared with the model developed by Recalde (2009) which is similarly an extension of the O'Connell and Budiansky's (1974) model to concrete. A significant difference was observed in the results of both models and the accuracy of both methods could be obtained using microscopic analysis. Moreover, a proposed new method based on the Padé approximation developed by Cheng (1993) was also used for comparison purposes. Six different concrete mixtures comprised of normal strength and high strength concrete with 0, 40 and, 60% of fly ash content in addition to the control mixture were used as a sustainable material with high-temperature exposure. The purpose of heating the specimen at high temperature was to induce microstructural damage and to quantify the changes at micro-cracking level using the crack density parameter (ε), as estimated using the analytical technique presented at the beginning of this chapter. Moreover, the relationships among estimated concrete properties were analyzed and the differences in fundamental behavior of various sustainable concrete mixtures under different conditions were identified and compared.

The following is a list of conclusions obtained from this part of the research study:

- Comparing the two models used—Hudson's model and O'Connell and Budiansky models—almost similar crack density parameters were observed for the control

specimens (Labeled as A). Both models behaved nearly identical and have nearly equal CDP and E_d values which shows that the results are promising.

- A good agreement for the estimated elastic values of concrete using both models was found to be in the control specimens which were kept undamaged. However, higher CDP values were observed in Hudson's model than in the O'Connell and Budiansky's model when the concrete specimens were exposed to 300 °C (570 °F). The obtained (ε) using Hudson's extended model was higher than that obtained using O'Connell and Budiansky model.
- A new technique known as Padé approximation introduced by Cheng (1993) to solve the issue with the second-order expansion in Hudson's model of diverging at a certain limit of crack density rather than converging, was found to be not suitable for thin concrete discs, hence, Hudson's first order was used to obtain appropriate results.
- The two concrete mixtures analyzed with sustainable cement materials made with 40, and 60% fly ash content increased in strength for normal and high strength concrete when compared to the control mixture.
- Autogenous healing in all damaged concrete mixtures happened to a lesser extent after soaking them in water for 24 hours. Since concrete was damaged and cracked severely it did not exhibit a higher value of autogenous. However, in mixtures containing 40% fly ash such as (Mixture NF40) and (Mixture HF40), the autogenous healing occurred at a considerable level where mixtures tried to reach their un-damaged condition which happened to less extent.

- The water penetrated through cracks and held in capillaries produced a stiffening effect in the concrete discs which was observed while conducting the resonant testing, resulting in higher Young's modulus E_d for soaked concrete discs than for the dry concrete specimens.
- Statistical analysis showed that there is no significant difference in the change of the G_d for the temperature exposure of 300 °C for all concrete mixtures with different percentages of fly ash.
- Statistical analysis revealed that there is a significant difference in the change of the crack density parameter ϵ for the temperature exposure of 300 °C for all concrete mixtures with different percentages of fly ash.
- The analytical method presented in this research study to estimate crack density parameter and elastic Young's modulus has potential as an easy-to-use analytical tool for many researchers in the field of concrete materials and for forensic investigations on different concrete mixtures either with or without supplementary cementitious materials used.

The list below presents some future recommendations:

- The application of Hudson's (1981) Model could be extended to specimens thicker than two inches (50 mm) and for cylinders made with different SCMs such as, blast furnace slag, Silica fume and sugarcane bagasse ash.
- More analytical procedures could be developed using different rock mechanics models and to compare the obtained results with Hudson's (1981) in estimating the elastic properties of concrete.

- The analytical models presented in this research study could be applied on thin concrete disc specimens made using seawater which could cause sulfate attack on concrete due to the Potassium and magnesium sulfates reaction with calcium hydroxide, and to compare with the elastic properties for those specimens made using fresh water.
- In most cases, a significant difference was observed in the results of both O'Connell and Budiansky and Hudson's extended models and the accuracy of these methods could be done using microscopic analysis.

Chapter Six

Development of Numerical Models (Phase III)

6.1 Introduction

6.1.1 Finite Element Modeling Approach in Abaqus Program

In general, the Abaqus computer program offers two main techniques to develop models and to run the simulation which include Abaqus/Standard and Abaqus/Explicit. The procedure of Abaqus/Explicit is largely applicable for the explicit dynamic analysis and is preferred to develop larger and complex models. It has been found to be computationally useful for the dynamic responses of comparatively short times and permits for the classification of general contact conditions (Simulia 2011). The Abaqus/standard method is used to provide accurate stress solutions in static and low-speed dynamics. It is an ideal approach for lower dynamic events such as sealing pressure in a gasket joint, steady-state rolling of a wheel, or crack propagation in composites (Simulia 2020). Moreover, in Abaqus/Standard, the actual concrete properties or results obtained from experimental testing could be used as input values providing an opportunity to the user by defining the desired elastic properties (Diane 2013).

Hence, following the Abaqus/Standard approach, different commands and techniques adopted in developing a finite element model for concrete RVE with randomly oriented

cracks in dry and soaked conditions are presented. The mechanism of each command used and the properties as an input value into Abaqus to analyze the concrete RVE in estimating the effective elastic properties is also discussed. Moreover, various modeling approaches available within Abaqus that are utilized for carrying out this research study (mainly for the purposes of modeling randomly oriented cracks in dry and saturated conditions) are also presented. Specifically, this includes the modeling of cracks in RVE with different directions, co-ordinates, and various material properties of the inclusions in the concrete solid as a three-dimensional model. The material along with its elastic properties and the boundary conditions applied to the RVE models are discussed in the preceding sections.

6.1.2 Material Elastic Properties

The Abaqus software offers the opportunity to develop models with user defined elastic properties as the input values ultimately making the modeling process much easier. For modeling purposes, modulus of elasticity for concrete (E_0) is defined along with Poisson's ratio (ν_0). In the case of dry/void cracks in the RVE, the application of elastic properties was straightforward, however, for saturated cracks, Young's modulus was calculated using the equation 6.1 and 6.2. The bulk modulus of water at 20°C is 2.2 GPa (Fine and Millero, 1973) and was used in the equation 6.2 (Gurtin, 1972) along with water's Poisson's ratio of 0.49 to calculate the elastic Young's modulus of water which resulted to be equal to 132 MPa.

$$K = \frac{E}{3(1-2\nu)} \quad (6.1)$$

$$E = 3K(1 - 2\nu) \quad (6.2)$$

Once elastic properties were determined from the above used formulae, they were defined using the elastic tab under the mechanical properties command in Abaqus. For the analysis purposes of RVEs, the concrete material was assumed to be isotropic, and this option falls under the edit material command in the Abaqus program. In addition to the elastic properties, the density of concrete was also defined using the density command within the Abaqus program (Wurst, 2013).

6.1.3 RVE Geometry and Material Properties

A cubical geometry of RVE for the purpose of the numerical analysis was selected providing an easy application of boundary conditions. Two different RVE sizes with dimensions $100 \times 100 \times 100 \text{ micron}^3$ and $200 \times 200 \times 200 \text{ micron}^3$ were selected for the modeling purpose as shown in figures 6.1 (a) and 6.1 (b) respectively.

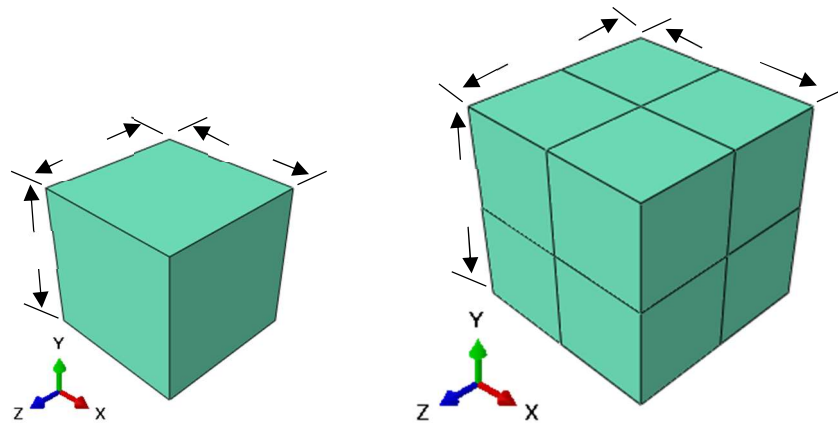


Figure 6.1: (a) smaller RVE (b) Larger RVE size to develop numerical models

For the analysis purpose, two RVEs from the same specimen with and without predefined cracks were developed using the Abaqus computer program. Two different types of the thin concrete disc (25 mm thick with 100 mm diameter) and thicker disc (50 mm thick with 100 mm diameter) with and without damage were behind the idea of analyzing RVE instead of the entire specimen as shown in figure 6.2 below. Analyzing the overall discs permeated with very small cracks were found to be a cost-effective approach as the analysis took a long time to generate the results and even sometimes the program crashed to generate results. Hence, RVE was found to be a promising way of analyzing the discs and obtaining elastic properties of the concrete material.

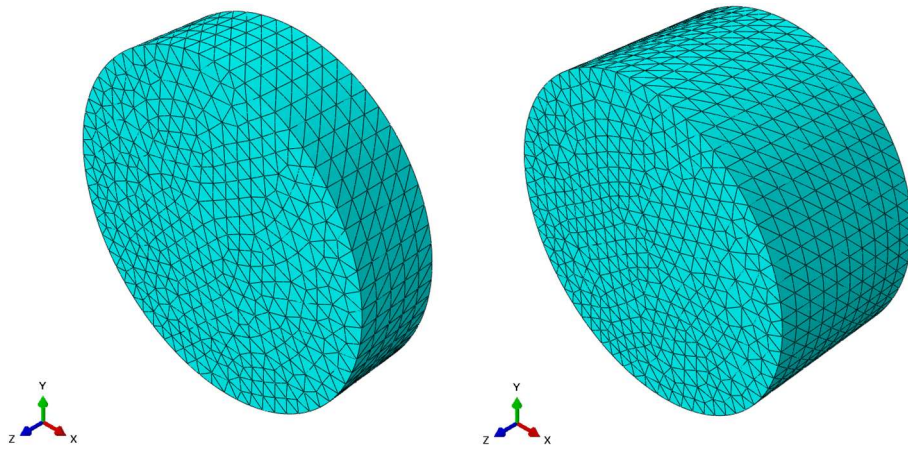


Figure 6.2: FE model of one and two-inches thick concrete disc

The purpose of doing this is to make the simulation computationally efficient and economical. Since the cracks are very small in concrete discs, a representation of a smaller volume was necessary to identify cracks and make them visible. Material properties shown in table 6.1 were specified for the concrete specimen.

Table 6.1: Concrete Material Properties

Density, ρ	Young's Modulus	Poisson's Ratio
kg/m^3	Ed (GPa)	ν
2400	40	0.25

6.1.4 Modelling of Cracks

An example of cracked RVE is shown in figure 6.3 where penny-shaped cracks were identified with random orientation using the Abaqus program. The damage comprises were thin randomly oriented cracks in different directions throughout the RVE. In reality, the cracks are very small, hence an RVE is modeled at a small scale to make the cracks visible in the concrete volume. To make the modeling procedure easier, circular penny-shaped cracks were chosen which have also been observed in previous analytical models developed by O'Connell and Budiansky (1974). Each crack has been placed in a different orientation and with different coordinates, ensuring random distribution of cracks along the RVE. The dimensions of the cracks were selected depending on the required crack density. To make the RVE appropriate for FE discretization, the cracks permeated were spaced at enough distance from the neighboring cracks to avoid any distortion in finite elements. Prior to modeling RVEs with multiple cracks, a single crack was placed by defining the x, y, and z coordinate in the RVE (coordinates for various cracks in RVEs are presented in Appendix-D). At certain points where multiple cracks intersected each other, the computer program resulted in errors while meshing, which were avoided by changing the coordinates of the

cracks and defining different locations in the RVE ensuring sufficient distance for the cracks.

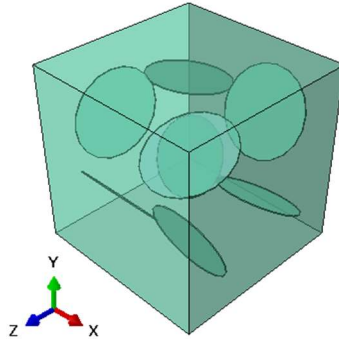


Figure 6.3: Damaged RVE with dry cracks in concrete

6.2 Python Scripting in Abaqus Software

Python scripting plays a vital role and makes the procedure simpler when it comes to generating different geometrical entities and different RVE dimensions in Abaqus software. When a model is created using Abaqus graphical user interface (GUI), each command or function is scripted internally by Abaqus after every operation is performed. The commands include the geometry of the model, defining material properties, assembly, loads, boundary conditions, meshing as well as job operation. Abaqus GUI generates these commands in an object-oriented programming language known as Python (python.org). While working on GUI, the command operations are sent internally to the Abaqus kernel (which is the core of the program working as a brain internally in Abaqus). The kernel interprets the command operations and uses the settings and options to generate an internal representation of the model creating a script (Mandar Kulkarni, 2012). The generated script could further be interpreted and modified according to the need of the model in Python.

6.2.1 Mesh Sensitivity Analysis in Abaqus

In this research work, three different mesh sizes (coarse, normal, and fine as shown in figure 5.11) were selected. Models were run and the appropriate mesh size considering the obtained results and the time taken by the CPU while running the simulation was considered prior to conducting further modeling procedures. A three-dimensional RVE for the concrete solid was created with different crack orientations such as vertical, horizontal, and inclined 45-degree crack. The creation of the 3D geometry of concrete solid with a single crack was relatively straightforward for the concrete RVE with equally sized square solid. The orientation of the single crack in RVE was kept changed to determine computationally the most cost-effective and correct mesh size. A mesh sensitivity analysis was conducted on three different RVEs with varied mesh sizes of 20, 15, and 10 microns. For all the specified mesh sized RVEs, orthotropic elastic properties such as elastic Young's modulus, Poisson's value, and shear modulus were determined. The assumed elastic modulus value of 40 GPa for concrete and Poisson's ratio of 0.25 was used as input in Abaqus for the purpose of analysis. The details of the initial RVE developed for sensitivity analysis had a volume of $100 \times 100 \times 100$ micron³ with penny-shaped crack having a radius of 25 microns and depth equal to one micron. A minimal difference was observed in the elastic properties results for the sensitivity analysis which is presented in table 6.2. These results indicate that, except for the 10-micron mesh, the results begin to converge and are relatively similar as the mesh size decreases. Figure 6.4 below shows RVE with different mesh sizes, and the results are compared in table 6.2 below. The representative volume elements (RVEs) shown were modeled using dimensions equal to $100 \times 100 \times 100$

micron³ with single penny-shaped cracks having a radius of 25 microns and a depth of one micron.

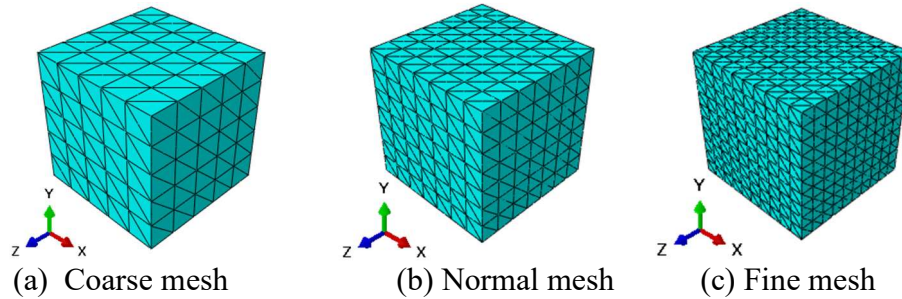


Figure 6.4: Three different mesh sizes selected during simulation.

Table 6.2: Comparison of obtained results using three different mesh sizes.

Mesh Size	Young's Modulus, E	Elements	CPU time
(microns)	(GPa)	-	(sec)
Coarse – 20	39.076	1286	131
Normal – 15	39.045	2911	156
Fine – 10	38.989	8333	319

6.3 Analysis for Different Concrete Conditions

Analysis was conducted in two different conditions for the purpose of observing the behavior and changes in the effective elastic properties of concrete. The two different conditions and the process of modeling with user input details are explained as under;

1. Soaked Condition

In soaked condition, concrete was assumed to be submerged in water and the cracks were filled with water. The user input defined values for conducting numerical analysis was

Young's modulus (E_0) and Poisson's ratio (ν_0) which were equal to 132 MPa and 0.49 respectively. Young's modulus for water was calculated using equation 5.2. Different RVE models with varying crack densities of different RVE sections are presented in figure 6.5.

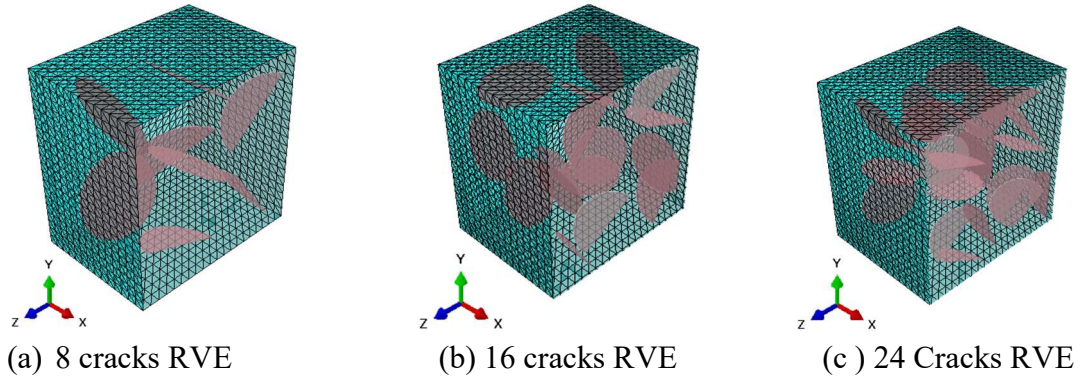


Figure 6.5: Section of different RVEs for soaked concrete condition.

2. Dry Condition

In the case of dry condition, the cracks in concrete were assumed to be empty and void. For the analysis purpose in Abaqus, the user input values for modulus of elasticity (E_0) and Poisson's ratio (ν_0) were used as 40 MPa and 0.25, respectively. The RVE sections with dry crack conditions for different crack densities are shown in figure 6.6.

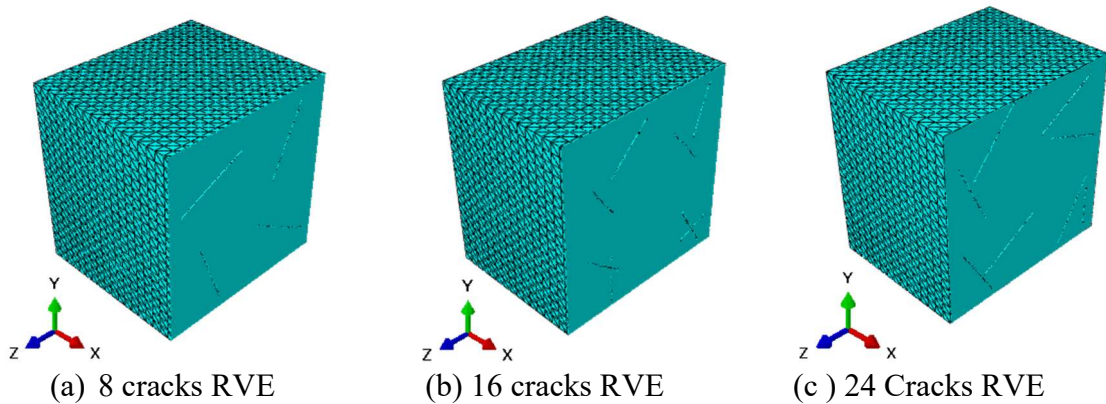


Figure 6.6: Section of different RVEs for dry concrete condition

6.4 Generation of RVE

Numerical estimation of effective elastic properties of solid with cracks was computed by FE simulation of periodic representative volume elements (RVEs) with randomly oriented penny-shaped circular cracks. Different RVEs were modeled for the desired crack density parameter (CDP) ranging from 0.1 to 1.0 with randomly distributed pores along the RVE with a crack thickness equal to one micron. The effective elastic properties were determined using the EasyPBC plugin developed by (Omeiry et al., 2019) and are shown in figure 6.7 and is explained in the preceding section.

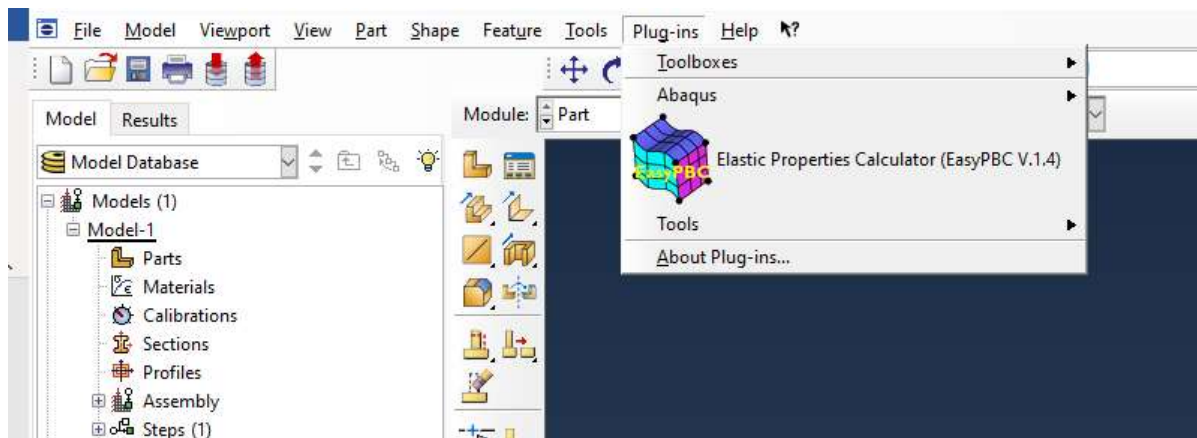


Figure 6.7: EasyPBC plugin installed in Abaqus program

Different RVEs were developed and analyzed in the increasing order of dimensions and to compare if the obtained results are in correlation. Two different conditions, dry and saturated were used for modeling RVEs. In the case of dry conditions, the cracks were left empty as voids and for saturated conditions, the cracks were filled with water by specifying different material properties.

During this numerical study, the below given requirements for RVEs had to be satisfied prior to proceeding with the modeling part (Vasylevskiy et. al, 2018).

- the RVE must be appropriate for finite element discretization,
- the RVE must be periodic (where opposite faces of the represented cell to be identical).
- the cracks in the RVE must be randomly distributed and oriented.

For the finite element analysis, the RVE was assumed to be of a cubical shape in order to satisfy one of the requirements for RVE generation. The radius of the penny-shaped cracks was chosen based on the desired crack density and was obtained using the equations 6.3 and 6.4 below.

$$\varepsilon = \frac{1}{V} \Sigma a^3 \quad (6.3)$$

$$a^3 = \varepsilon \frac{V}{n} \quad (6.4)$$

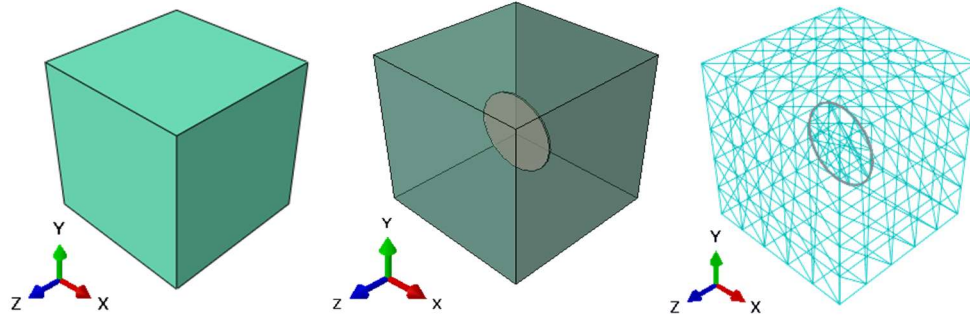
where, ε = crack density parameter; a = radius of the crack; V = volume of the RVE; and n = number of cracks in the RVE.

An example of the calculated crack radius using equation 6.4 in RVE with the desired crack density parameter and 8 cracks in a single RVE is presented in Table 6.3. However, the detail for crack radius and cracks up to 16 and 24 in a single RVE is presented in Appendix-E.

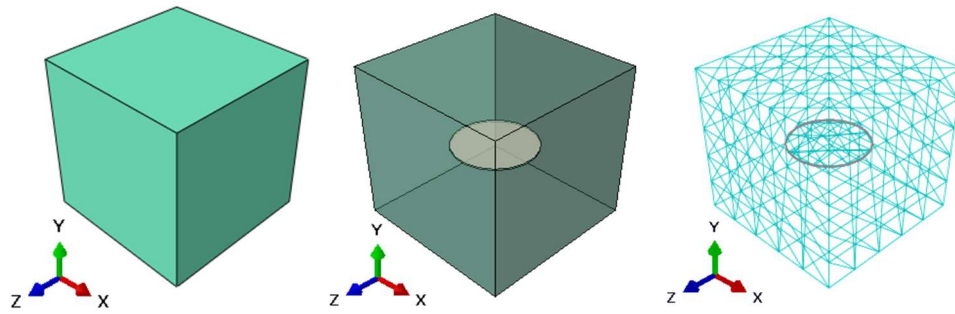
Table 6.3: Details for crack radius and number of cracks in 200x200x200 micron³ RVE

S.No.	CDP	Volume (V)	No. of Cracks (n)	Crack radius (a)
-	-	(200) ³ micron ³	-	micron
1	0.1	8000000	8	46.4
2	0.2	8000000	8	58.4
3	0.3	8000000	8	66.9
4	0.4	8000000	8	73.6
5	0.5	8000000	8	79.3
6	0.6	8000000	8	84.3
7	0.7	8000000	8	88.7
8	0.8	8000000	8	92.8
9	0.9	8000000	8	96.5
10	1	8000000	8	100

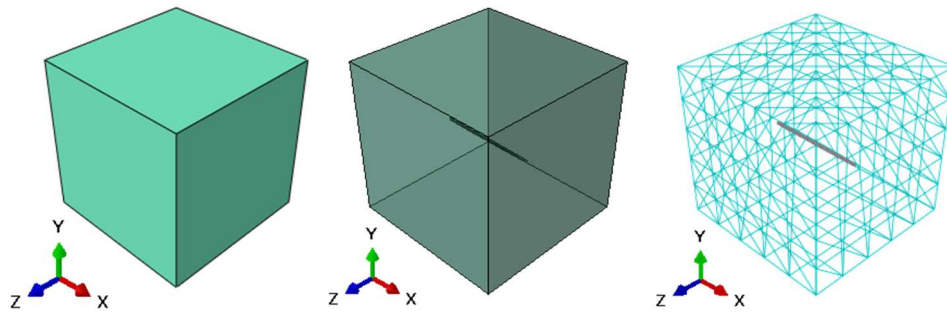
To avoid distortion or errors in meshing, the distance between the adjacent cracks had to be enough (Vasylevskyi et al., 2018). In some cases, when there was much overlapping among cracks or cracks were going out of the RVE boundary, the finite element discretization showed errors that were avoided by changing the orientation of the cracks. Initially smaller RVEs with single vertical, horizontal, and inclined cracks were modeled to check the accuracy of the obtained elastic response before proceeding to the larger RVEs. Four RVEs with dimensions 100x100x100 micron³ were generated with single and multiple crack orientations as shown in figure 6.8. The single crack in each RVE was oriented vertically, horizontally and inclined at 45 degrees along with the x-axis of the RVE. The crack numbers in RVE along with the coordinates in x, y, and z directions for each RVE is presented in Appendix-D.



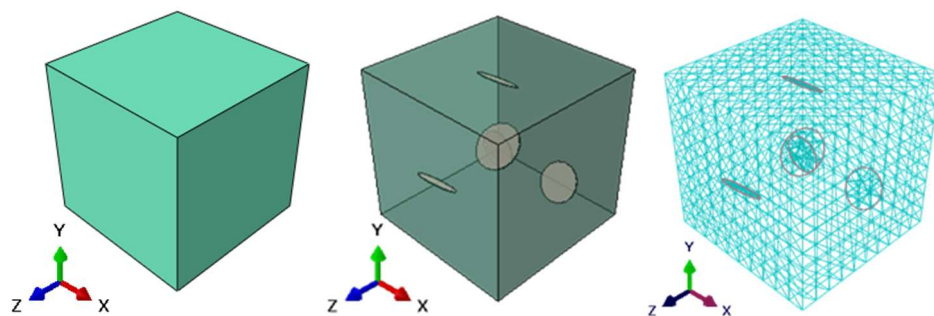
(a) RVE with vertical parallel to x-axis crack



(b) RVE with horizontal parallel to z-axis crack



(c) RVE with horizontal inclined crack



(d) RVE with multiple random cracks

Figure 6.8: RVE with different number of cracks and their orientations

In the beginning, a one-micron deep crack of 25-micron radius was used for the analysis purpose. This process of generation of geometry was carried out using Abaqus software. Once the geometry was generated with the required number of cracks and their orientations, the RVE was meshed with Quadratic Tet elements (C3D10) with a 10-micron element size. Note that the mesh pattern must be identical on the opposite sides of the RVEs to avoid errors while running simulation and for this purpose, the tetrahedral shape of elements was selected for the finite element discretization. When the meshing using tetrahedral element shape was generated, an EasyPBC plugin developed by (Omeiry et al., 2019) was run and the elastic properties were determined. An example of mesh generation using tetrahedral element shape for RVE with 24 randomly oriented cracks and with CDP equal to 0.2 is shown in figure 6.9.

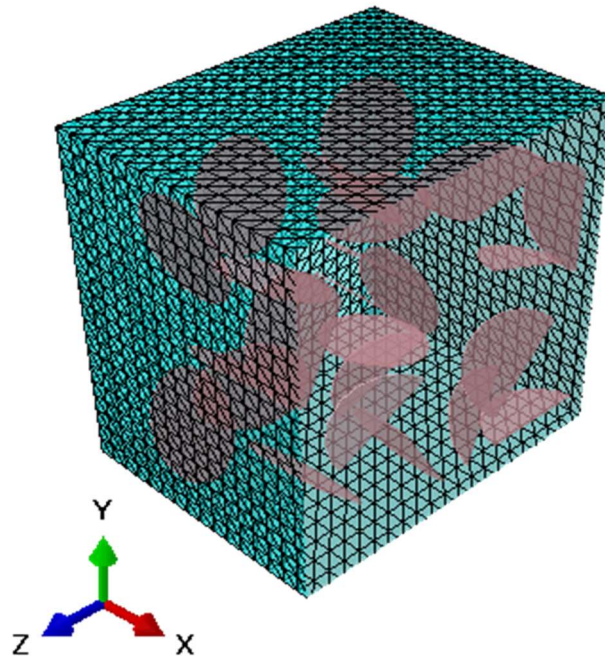


Figure 6.9: RVE containing 24 randomly oriented cracks meshed with quadratic Tet elements (C3D10), with a crack density as defined by equation 1.2 is, $\epsilon = 0.2$

Comparisons of modulus of elasticity are presented in figure 6.10 for single and eight RVEs (stacking eight 100x100x100 micron³ RVEs to make a bigger RVE as 2 to the power 3). The dry condition results are presented in blue and soaked condition with orange showing similar results between 100x100x100 micron³ RVE and RVE with dimensions equal to 200x200x200 micron³. This proves that no matter what size the RVE is, it will represent the same result. Based on this approach, and making sure the RVE modeling presents promising results, further simulation was performed using 200x200x200 micron³ RVE with different numbers of cracks and radius using desired crack density ranging from 0.1 to 1.0. Table 6.4 also shows the comparison of modulus of elasticity for one and eight RVEs.

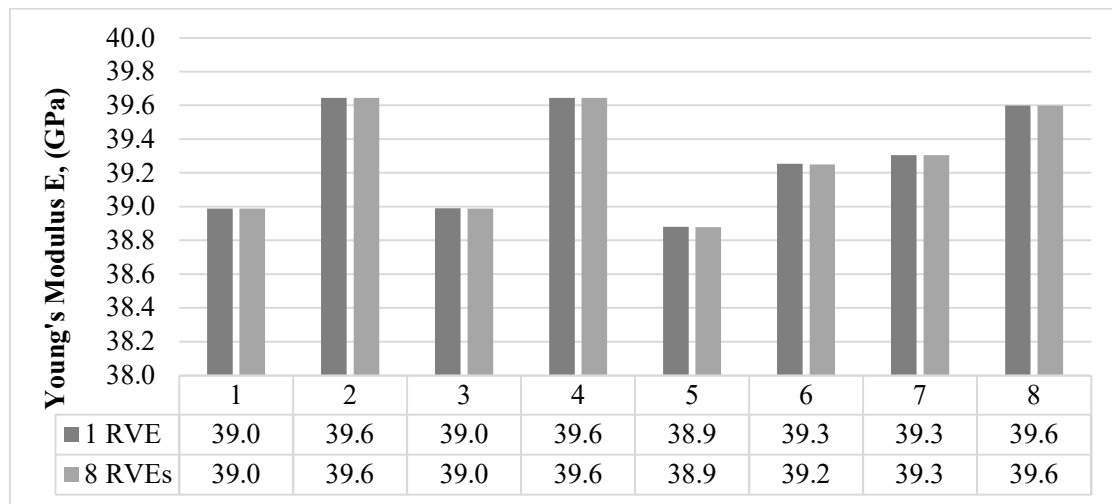


Figure 6.10: Comparison of elastic Young's modulus using single and eight RVEs for dry and soaked conditions.

Table 6.4: Comparing dry (blue) and soaked (orange) results between one and Eight RVEs.

Description	1 RVE	8 RVEs
	E (GPa)	
-		
1-Vertical crack with 10-micron mesh size – Dry	38.9	38.9
2-Vertical crack with 10-micron mesh size – Skd	39.6	39.6
3-Horizontal crack with 10-micron mesh size – Dry	38.9	38.9
4-Horizontal crack with 10-micron mesh size -Skd	39.6	39.6
5-Inclined crack with 10-micron mesh size – Dry	38.8	38.8
6-Inclined crack with 10-micron mesh size – Skd	39.2	39.2
7-Random cracks with 10-micron mesh size – Dry	39.3	39.3
8-Random cracks with 10-micron mesh size – Skd	39.5	39.5

Results for dry and soaked RVEs were determined differently by defining different material properties for each specimen. RVEs shown in figure 6.10 below exhibit cracks in dry condition which clearly show an empty void providing cuts in the concrete solid. However, in the case of saturated RVE shown in figure 6.11, the cracks are filled with water and could be seen in the figure below with different material properties distinguished with purple color. Since cracks in saturated conditions are filled with water, cuts in the solid cannot be seen. Moreover, the finite element numbers during meshing were different for the same size RVE in dry and saturated condition due to the different material properties. The analysis time also varied for both conditions no matter if the mesh and RVE size were the same. Similar to the single crack RVE, the larger RVE bundled with eight smaller RVEs with different numbers of cracks and orientations is presented in figure 6.12.

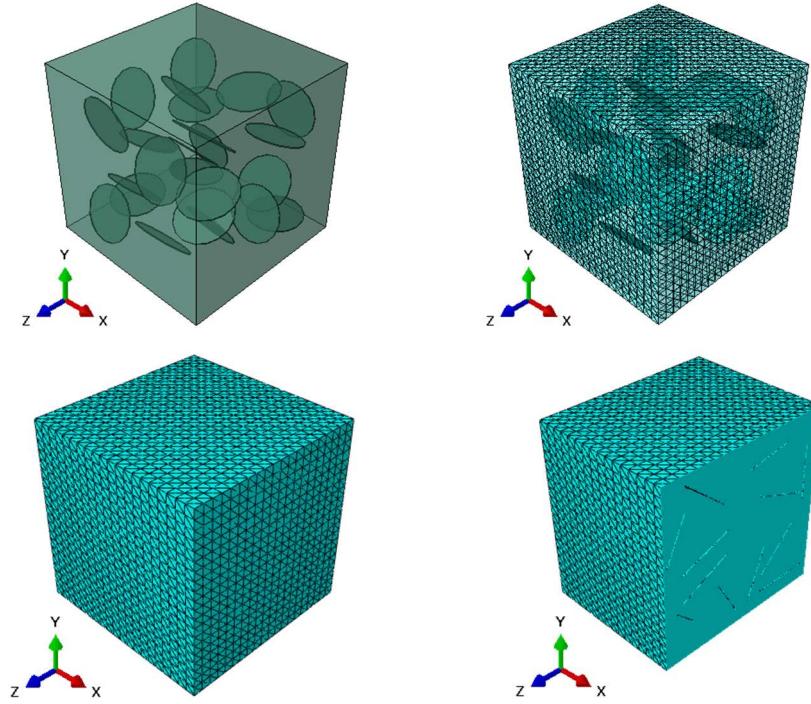


Figure 6.11: RVE in case of dry condition with cracks shown as empty voids.

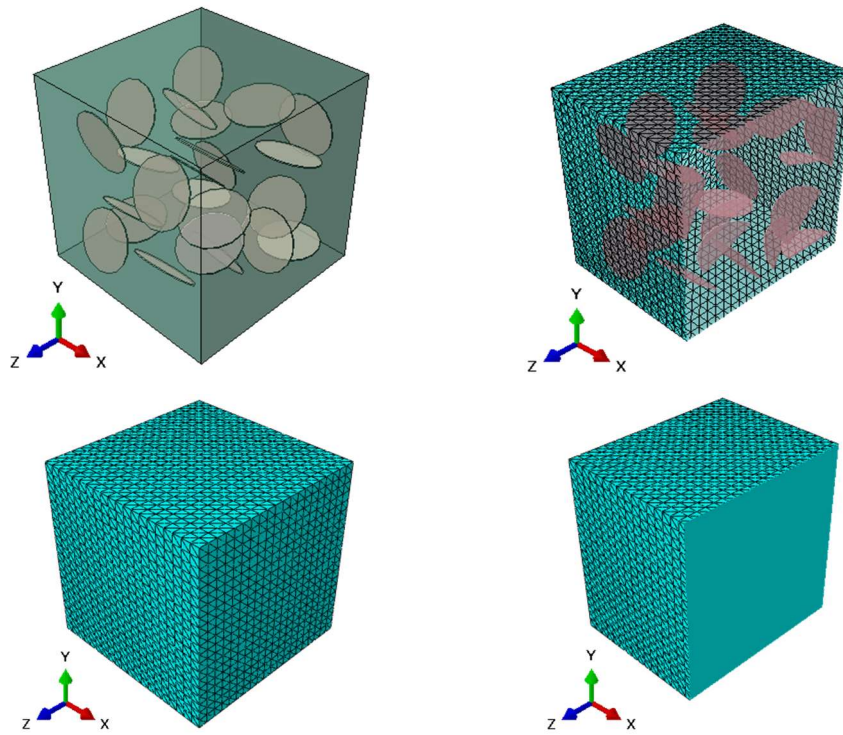


Figure 6.12: RVE in case of saturated condition with cracks shown in purple color.

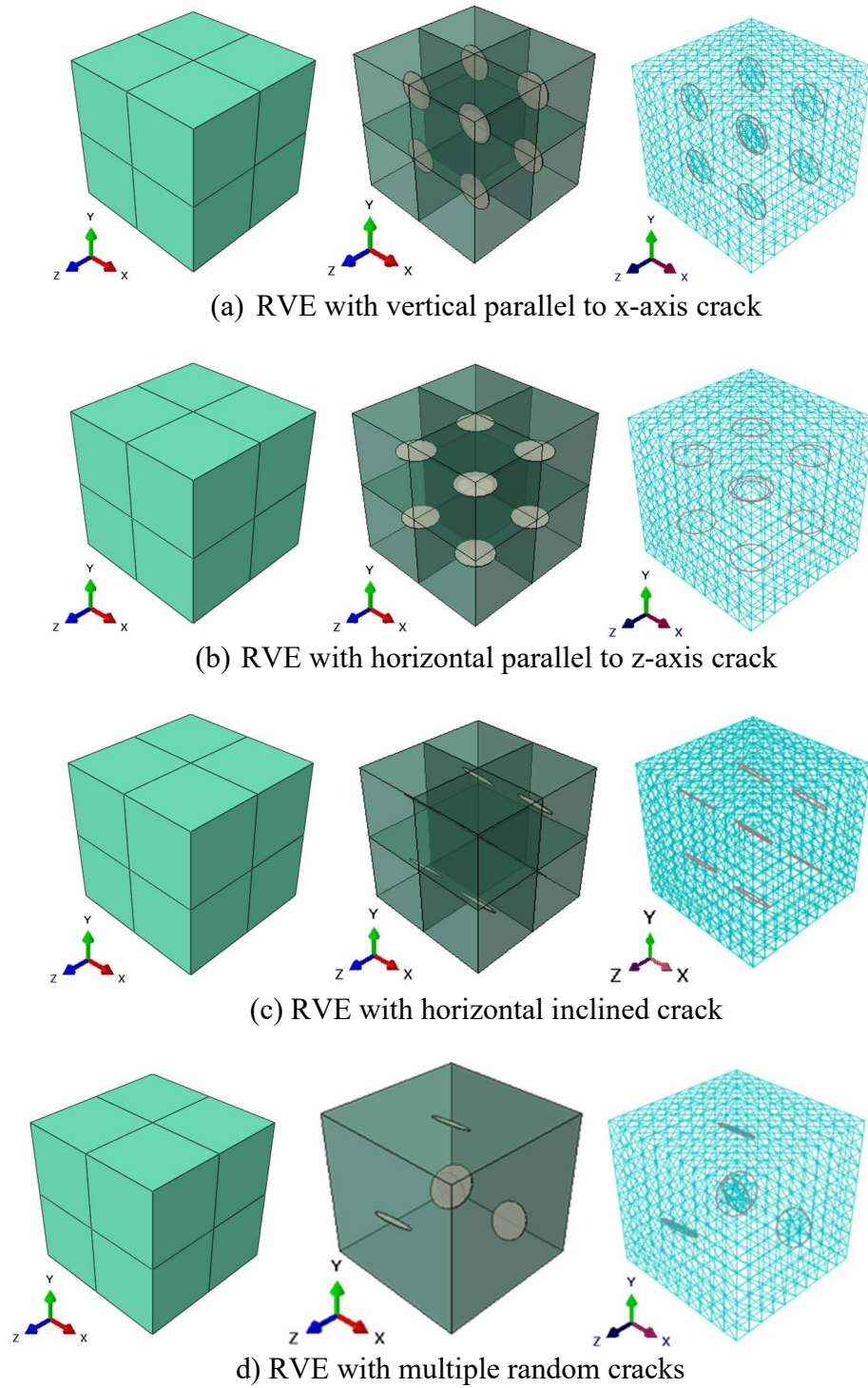


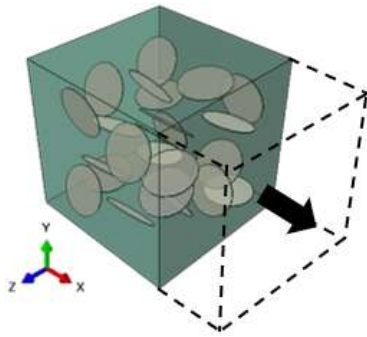
Figure 6.13: RVE with different number of cracks and their orientations

6.5 Homogenization of RVE

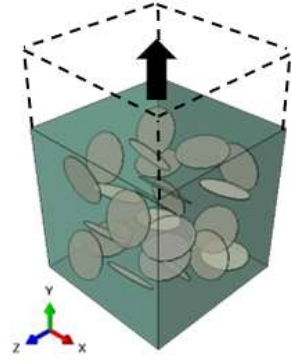
The homogenization of the smallest volume of a heterogeneous material and analysis of computing its effective elastic properties are traditional challenges in the micromechanics of heterogeneous material. In past, research have developed multiple models of homogenization which include the direct averaging method, the inclusion model based on Eshelby's solution, and the two-scale expansion method Cailleaud (1994) and Andrievski (2001). The inclusion model can estimate the effective elastic properties of the heterogeneous material depending on the geometrical size, the orientation of the inclusion, the number of inclusions, and their inherent properties. The Hashin-Shtrikman model Hashin (1963) and Ostoja-Starzewski and Jeulin (2001) models have been developed which are extensively used to estimate the effective elastic properties of numerous smallest volumes of the corresponding inhomogeneous materials. Another approach to solve the problems of homogenization is to utilize mathematical approaches and finite element simulations on the unit cells or the represented volumes of the overall composite material. These techniques have been found to be efficient in estimating the effective elastic properties of various heterogeneous materials by applying the constitutive law and the spatial distribution of various microstructural elements (Bouttani et al., 2016; Mumtaz et al., 2022). Selection of the proper size RVE and the effective properties of the material have been studied widely by many researchers using numerical techniques and statistical tools (Ghosein, 2014), and (Kanit et al., 2003). The obtained effective properties depend in fact on the selection of the proper boundary conditions utilized to impose uniform strains or stresses. Traditionally, there are three types of boundary conditions which are extensively used in numerical homogenization of RVE such as and Periodic boundary

conditions (PBCs), stress uniform boundary conditions (SUBC) and kinematic uniform boundary conditions (KUBC) (Bouittani et. al., 2016).

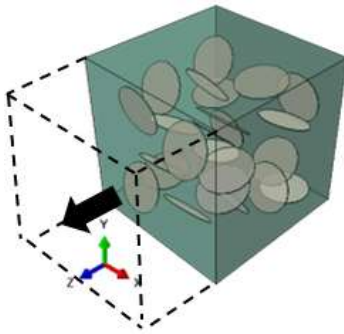
During this research study, periodic boundary conditions are imposed using the numerical homogenization technique presented in (Omeiry et al., 2019) on the unit cells of concrete composite with randomly distributed penny-shaped cracks in dry and saturated conditions. Periodic boundary conditions (PBCs) are a group of boundary conditions that is found to be efficient in simulating larger solid material specimens simply by modeling a finite Representative Volume Element (RVE) (Weidong et. al., 2014). The main idea of homogenization of RVE is to numerically apply uniform strains and to determine the effective elastic properties of the material model (Omeiry et al., 2019) which are presented in figure 6.14 below. “These strains are generally applied in numerous independent sets, where each set determines specific elastic properties of the represented element. Since the representative volume element is presumed to be a part of a periodic material, it becomes necessary to perform a simulation of the periodicity of the RVE with the adjoining material prior to and after being strained in a finite element program” (Omeiry et al., 2019).



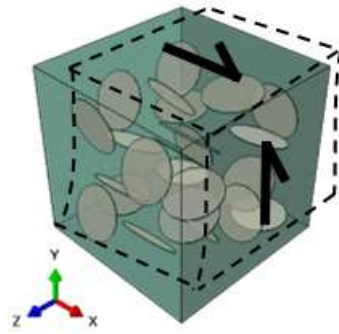
(a) E_{11} Young's modulus
 ν_{12} and ν_{13} Poisson's ratio



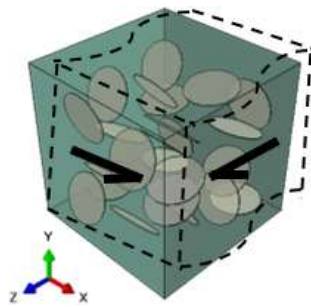
(b) E_{22} Young's modulus
 ν_{21} and ν_{23} Poisson's ratio



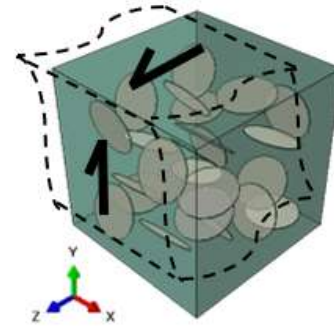
(c) E_{33} Young's modulus
 ν_{31} and ν_{32} Poisson's ratio



(d) G_{12} Shear modulus



(e) G_{13} Shear modulus



(f) G_{23} Shear modulus

Figure 6.14: Diagrams representing displacement boundary conditions required to estimate the effective elastic properties.

6.6 Abaqus EasyPBC Plugin

An Abaqus computer program plugin developed by (Omeiry et al., 2019) using Python programming language known as EasyPBC was used to calculate the effective elastic properties of RVE. This plugin is helpful in estimating the homogenized elastic properties by applying the concepts of unified periodic RVE homogenized method in preprocessing and post-processing phases (Omeiry et al., 2019). The EasyPBC plugin window in the Abaqus program is shown below in figure 6.15.

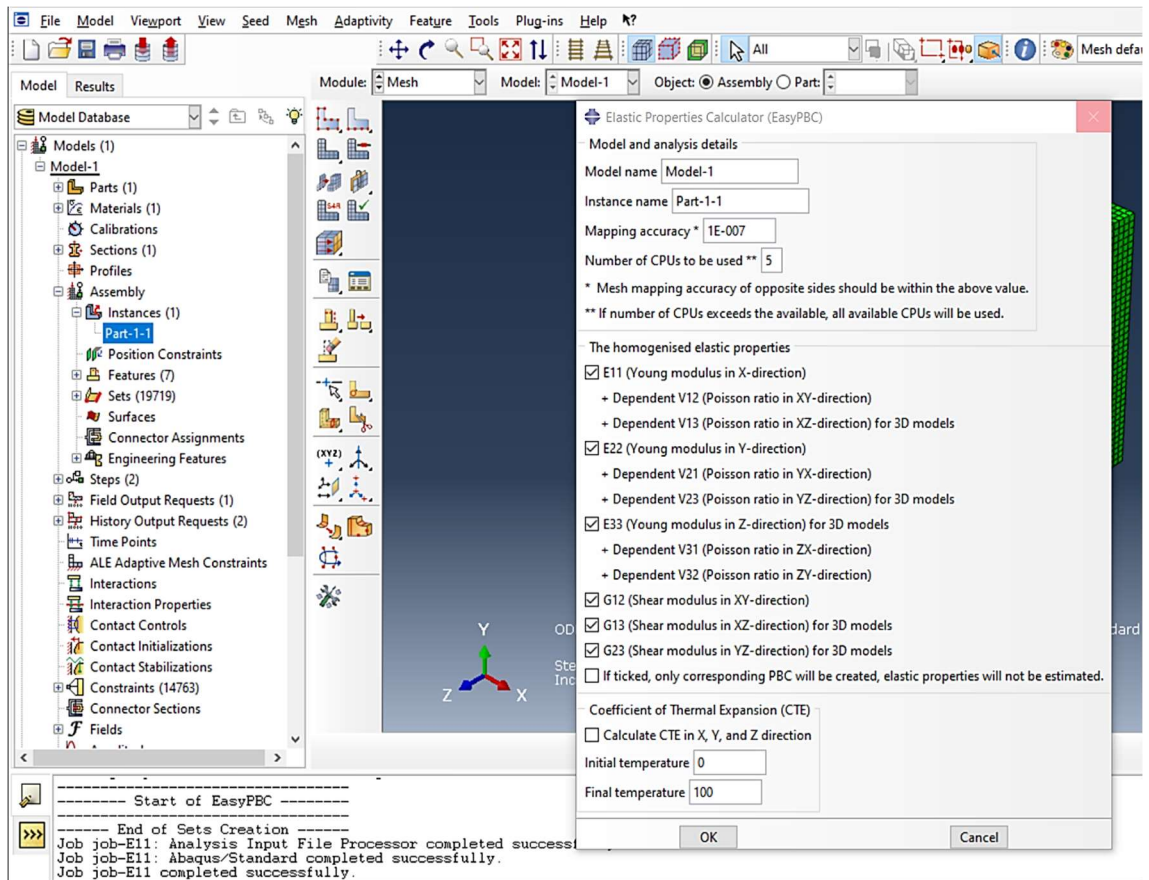


Figure 6.15: EasyPBC plugin main window in Abaqus program

In the first phase, the plugin determines the geometrical dimensions for the modeled representative volume element, categorizes boundary surfaces, generates nodal sets, creates constraint equations for each node, and imposes the required displacement boundary conditions. In contrast, the post-processing phase computes stress–strain values and other procedures associated to estimate the effective elastic properties of RVE, such as modulus of elasticity and shear modulus. The details of the main operations of the EasyPBC plugin and its working process is thoroughly explained in (Omeiry et al., 2019). EasyPBC plugin requires the user to specify the instance name and the number of CPUs to run the model. If not, the plugin itself runs and simulates based on the available CPUs in the computer. It is necessary to correct the modal and instance name before running the plugin. Moreover, the homogenized elastic properties along with the Poisson’s ratios in all directions could easily be estimated after checking all the boxes for the modulus of elasticity and Bulk modulus as shown in the plugin window in figure 6.15. The detailed operations of the EasyPBC plugin are shown in the flowchart in figure 6.16.

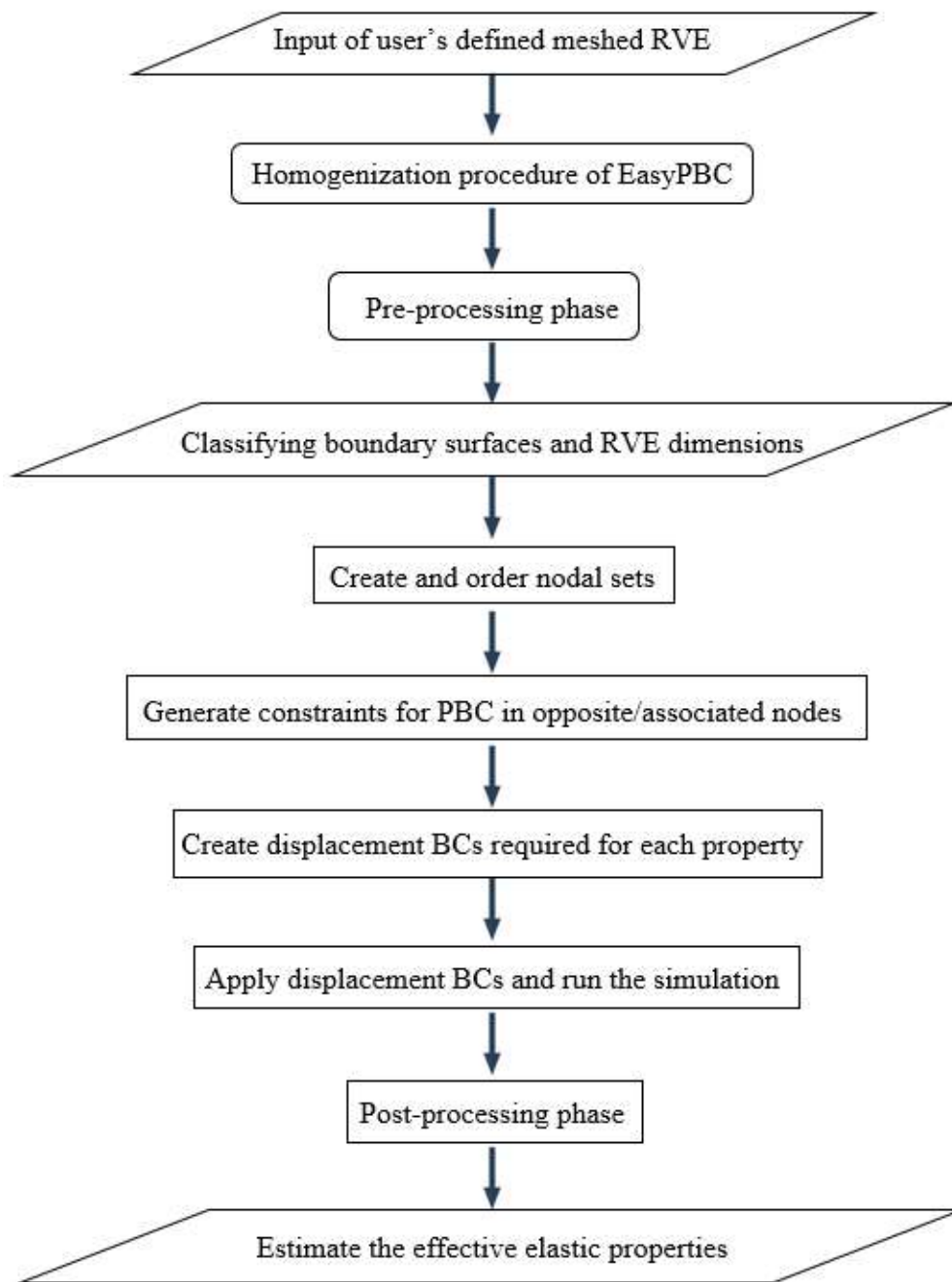
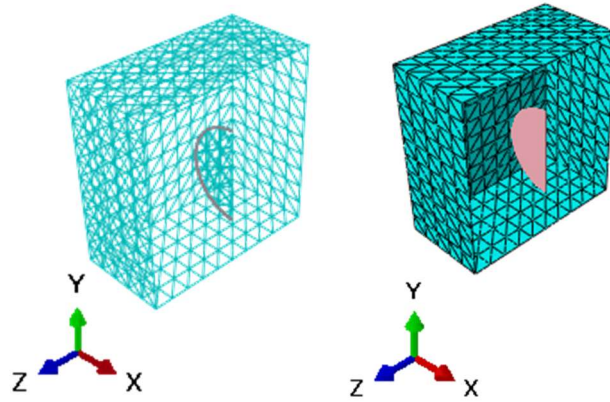
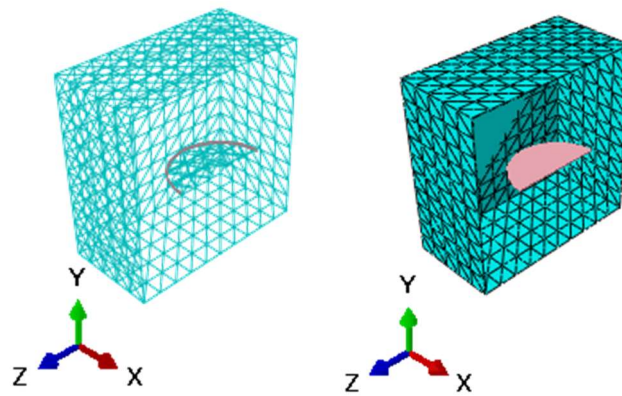


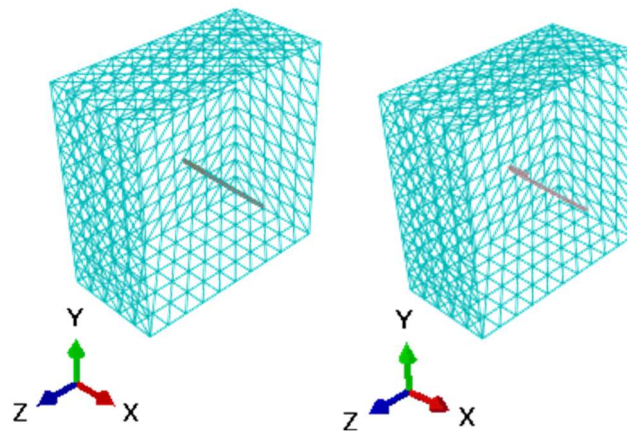
Figure 6.16: EasyPBC plugin processing flowchart (Omeiry et al. 2019).



(a) Vertical crack position in single RVE in dry and skd conditions respectively

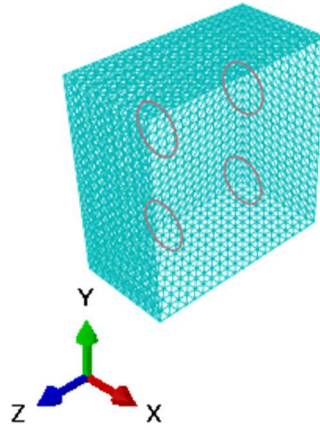


(b) Horizontal crack position in single RVE in dry and skd conditions respectively

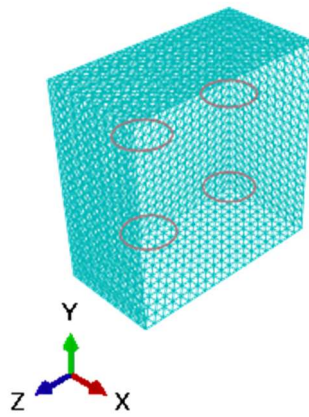


(c) Inclined crack position in single RVE in dry and skd conditions respectively

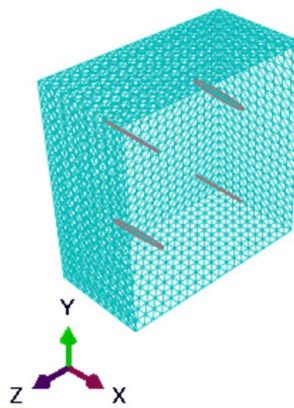
Figure 6.17: Position of cracks in $100 \times 100 \times 100$ micron³ RVE in dry and soaked conditions



(a) Vertical crack position in bundle of eight RVEs in dry and skd conditions



(b) Horizontal crack position in bundle of eight RVEs in dry and skd conditions



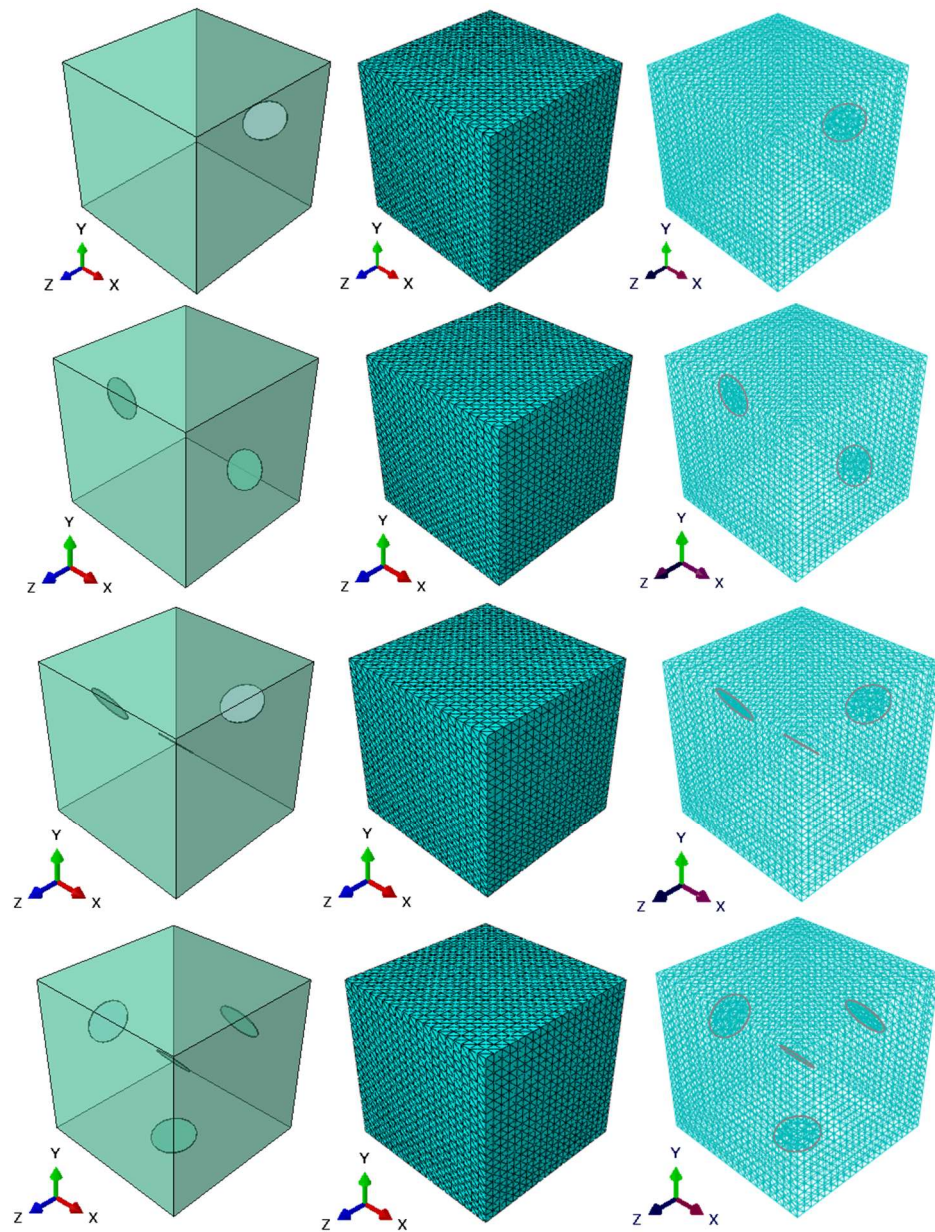
(a) Inclined crack position in bundle of eight RVEs in dry and skd conditions

Figure 6.18: Position of cracks in $200 \times 200 \times 200$ micron³ RVE in dry condition

6.7 RVEs with one to eight cracks both in dry and soaked conditions

6.7.1 RVEs with Dry Permeated Cracks

Different RVEs were modeled for the analysis purpose with desired crack density in dry condition starting from one crack in RVE and gradually increasing until eight cracks which are shown in figure 6.19.



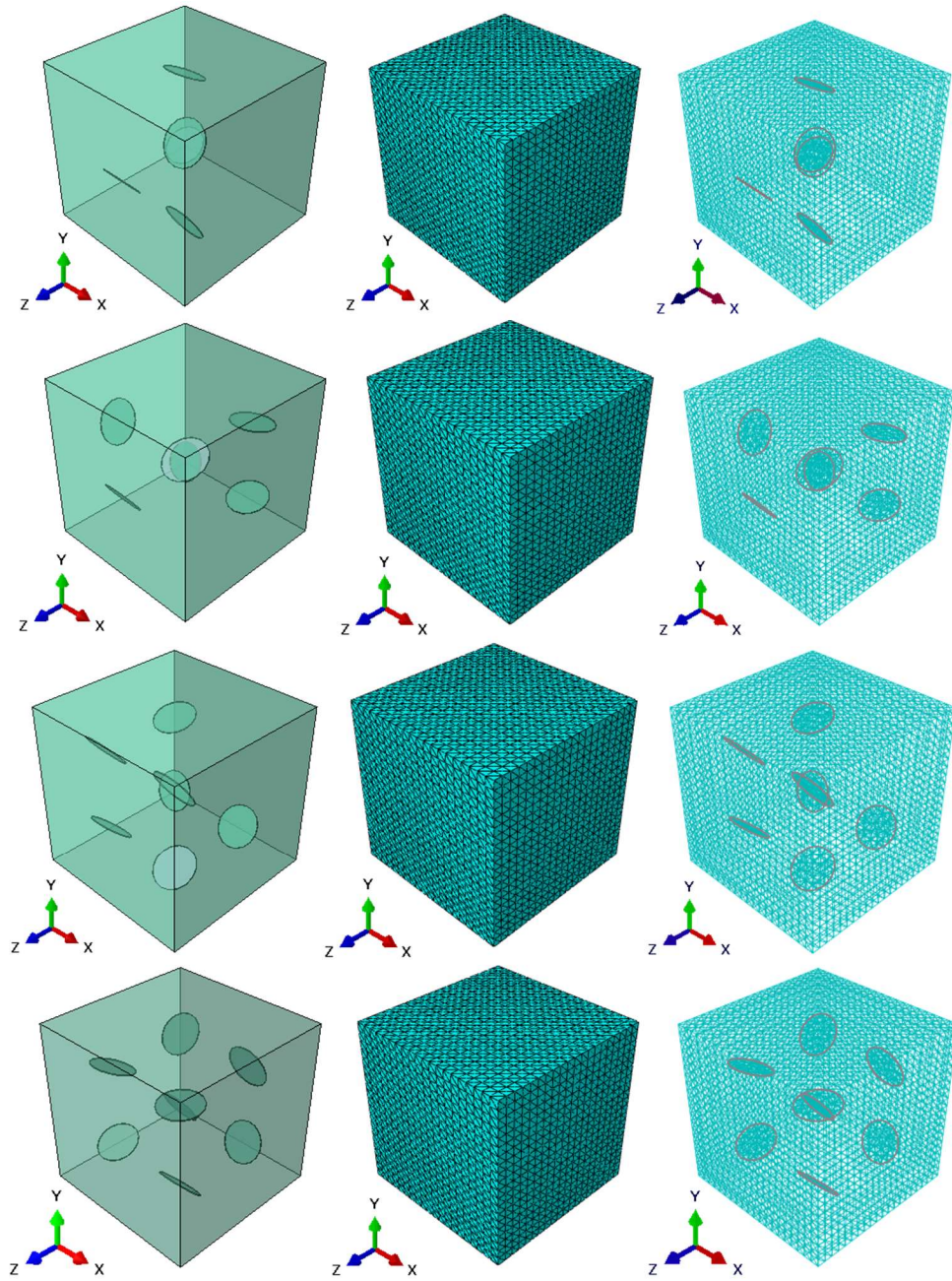
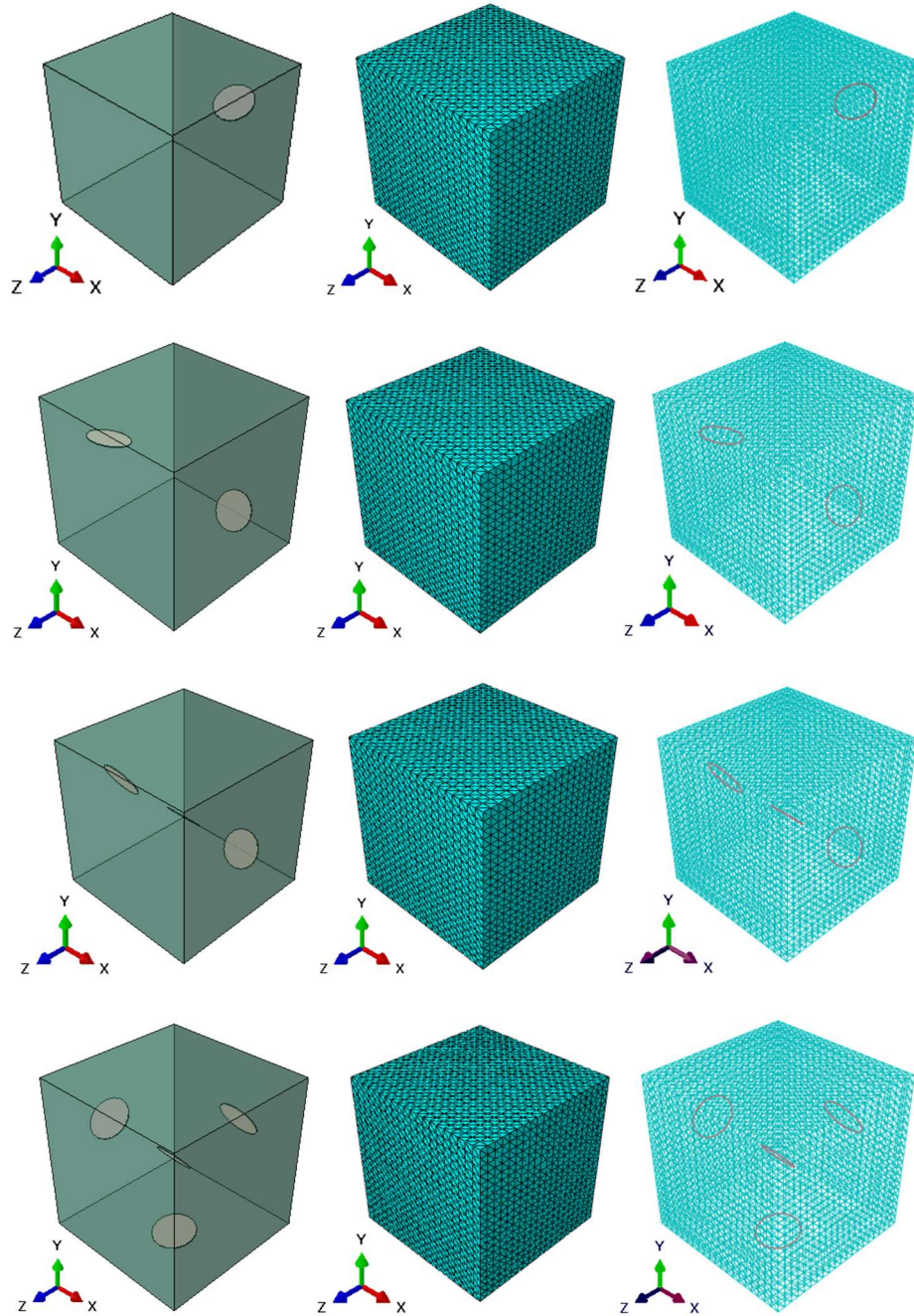


Figure 6.19: Position of dry cracks in 200x200x200 micron³ RVE starting from single crack to eight cracks

6.7.2 RVEs with Wet Permeated Cracks

Similar to the dry condition, wet cracks were permeated in RVEs starting with a single crack and gradually increasing the number of cracks up to eight cracks in a single RVE as shown in figure 6.20.



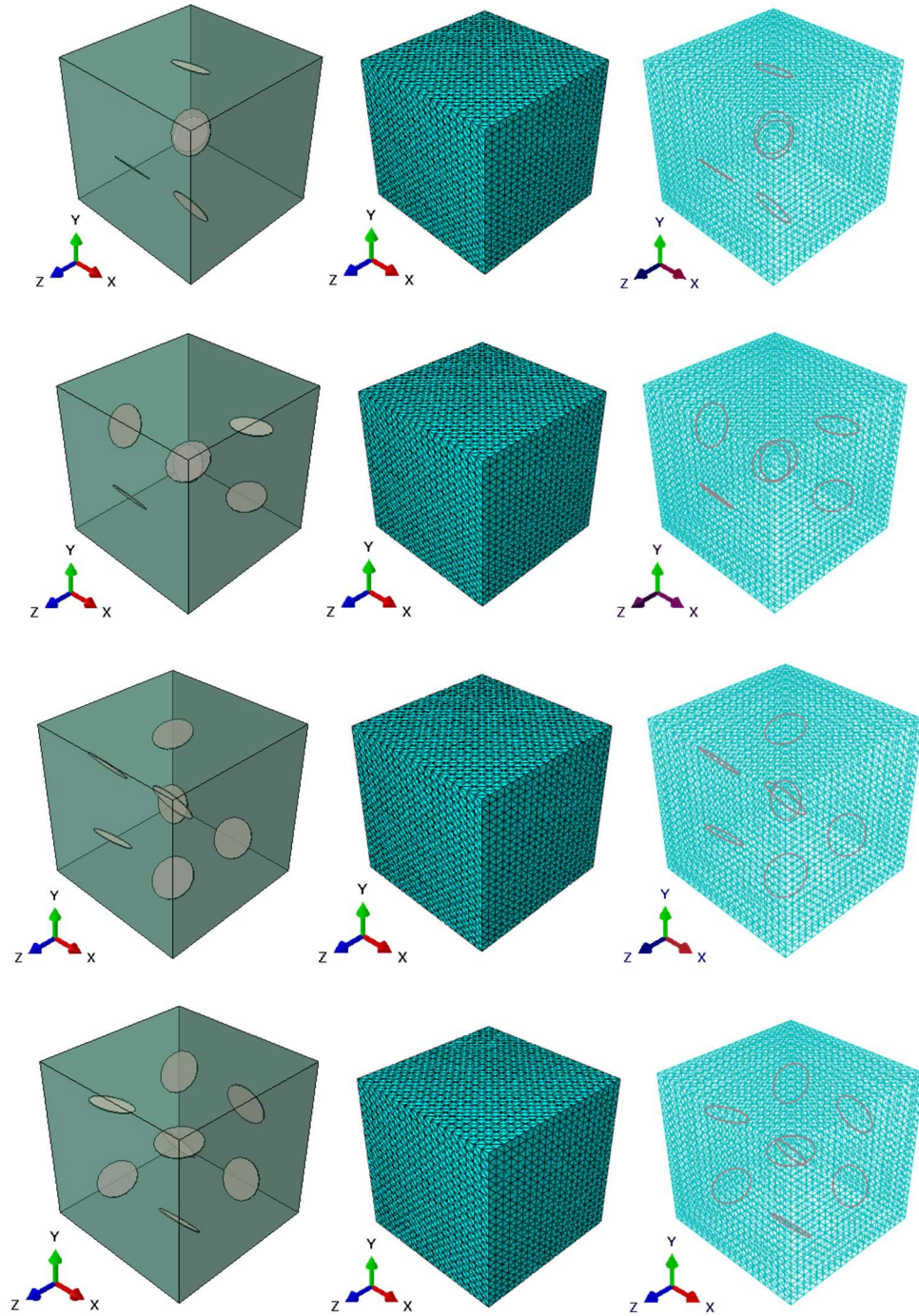


Figure 6.20: Position of wet cracks in $200 \times 200 \times 200$ micron³ RVE starting from single crack to eight cracks

6.8 Numerical Analysis Results and Discussion

6.8.1 Case with Twenty-Four Cracks in RVE

To compare the results of analytical models presented in this dissertation, numerical analysis was conducted on a single RVE with a different number of cracks permeated in the representative volume element. A numerical model of RVE with 24 cracks was developed and the elastic Young's modulus values for dry and soaked conditions were obtained after conducting simulation as presented in table 6.5. The number of cracks was decided to compare with other RVE cracks and determine if the desired crack density exhibits similar elastic properties of concrete. The estimated results shown in table 6.5 are also graphically presented in figures 6.21 and figure 6.22. In the cases with crack density parameters of 0.9 and 1.0 for soaked condition, the results were not generated by the numerical model which was due to the availability of larger cracks overlapping each other and due to the different material properties for the fluid and concrete which resulted in error while meshing and the models were not able to run in Abaqus program.

Table 6.5: Young's Modulus results Obtained Numerically with 24 cracks RVE

No. of Cracks	CDP	E, GPa		Normalized	
		Dry	Skd	Dry	Skd
0	0	40	40	1	1
24	0.1	33.8	37.3	0.846	0.935
24	0.2	29.1	34.7	0.729	0.870
24	0.3	27.1	32.9	0.678	0.823
24	0.4	25.5	31.7	0.638	0.794
24	0.5	24.8	30.8	0.621	0.772
24	0.6	23.7	29.9	0.593	0.748
24	0.7	23.3	29.1	0.583	0.729
24	0.8	23.6	29.0	0.591	0.727
24	0.9	23.0	0.000	0.575	0.000
24	1	23.1	0.000	0.579	0.000

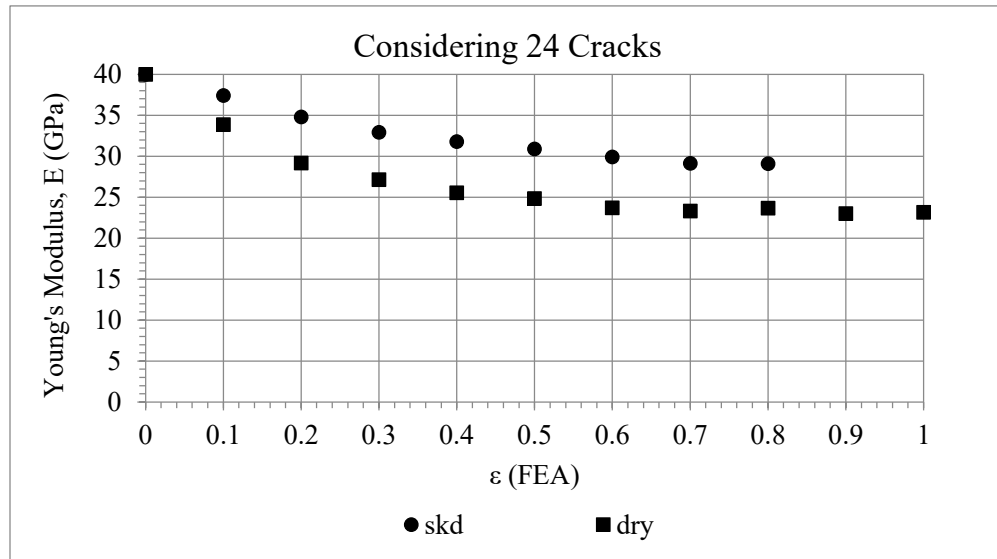


Figure 6.21: Young's Modulus Results of RVE with 24 Cracks for Dry and Soaked Cracks Condition

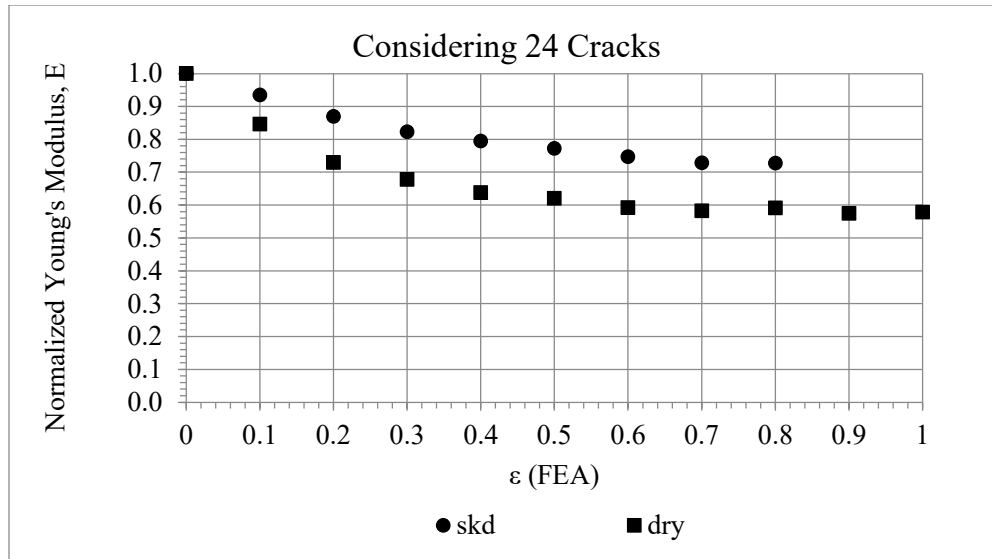


Figure 6.22: Normalized Young's Modulus Results of RVE with 24 Cracks for Dry and Soaked Cracks Condition

The results shown in figure 6.21 and figure 6.22 reveal a similar pattern obtained using the analytical Hudson (1981) model with a decrease in Young's modulus as CDP increases. The values for soaked conditions are always higher than those obtained with dry cracks which is due to the penetrated water through cracks held in capillaries producing a stiffening effect in the concrete specimens. The plots show a little variation as it does not follow a smooth trend line, however, to make the plots look smoother with a clear downward trend, the average of many RVEs could be taken.

6.8.2 Case with Sixteen Cracks in RVE

Similarly, a numerical model for RVE with 16 cracks was generated to compare the elastic Young's modulus properties are in good agreement or are different from those obtained using RVE with 24 cracks. The numerical results obtained presented in table 6.6 provide a slight difference in the elastic modulus results which could be due to the different crack

orientations. The difference in Young's modulus for 24 cracks and 16 cracks is nearly 0.1% which could be neglected and considering the results as similar and are graphically presented in figures 6.23 and 6.24.

Table 6.6: Young's Modulus results Obtained Numerically with 16 cracks RVE

No. of Cracks	CDP	E, GPa		Normalized	
		Dry	Skd	Dry	Skd
0	0	40	40	1	1
16	0.1	33.9	37.2	0.850	0.932
16	0.2	30.3	35.5	0.760	0.888
16	0.3	26.8	34.0	0.672	0.852
16	0.4	25.8	33.9	0.646	0.848
16	0.5	25.0	31.9	0.625	0.800
16	0.6	25.0	31.7	0.626	0.793
16	0.7	25.2	31.2	0.630	0.782
16	0.8	23.0	29.6	0.576	0.742
16	0.9	23.3	29.1	0.584	0.730
16	1	23.0	28.9	0.577	0.724

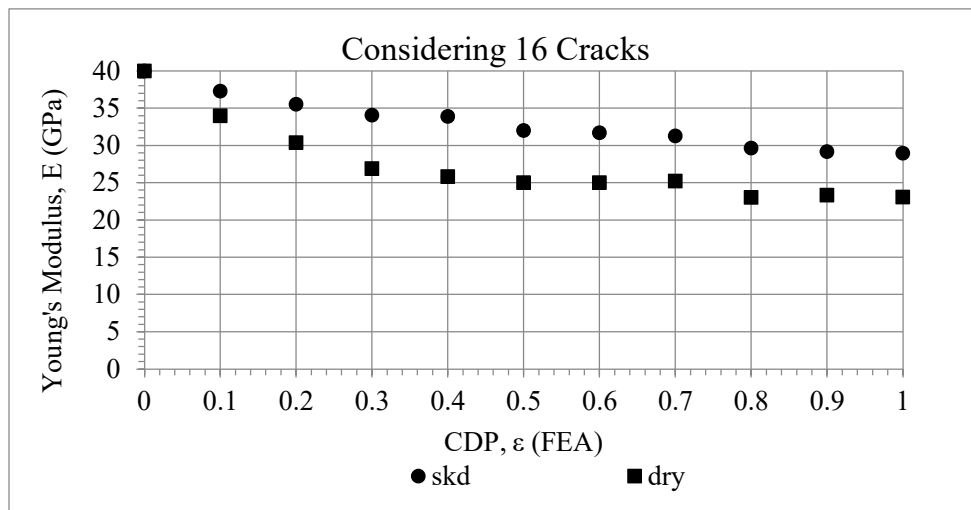


Figure 6.23: Young's Modulus Results of RVE with 16 Cracks for Dry and Soaked Cracks Condition

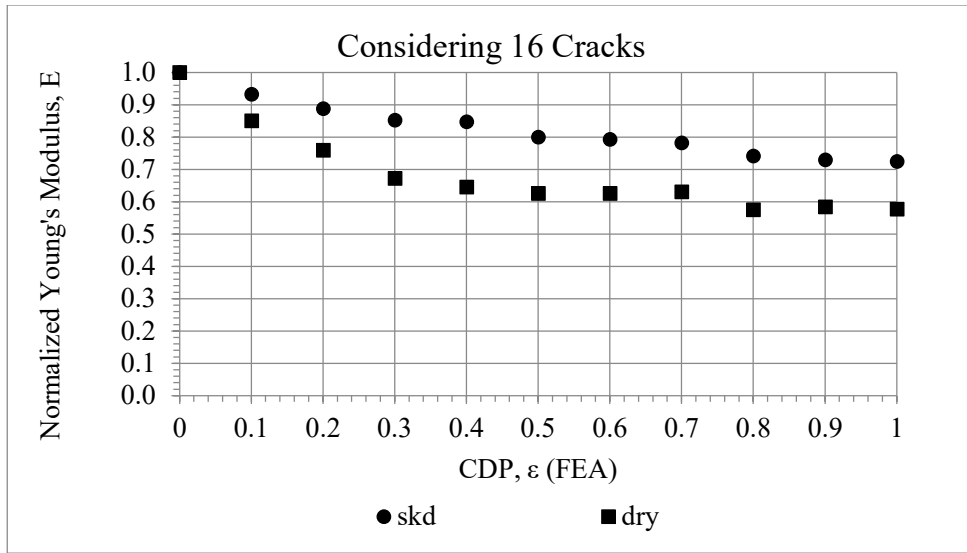


Figure 6.24: Normalized Young's Modulus Results of RVE with 24 Cracks for Dry and Soaked Cracks Condition.

6.8.3 Case with Eight Cracks in RVE

Modeling eight cracks in RVE was straightforward as the cracks were placed at a distance where cracks did not overlap each other resulting in proper meshing and assigning material properties. The simulation in this case, was quite faster as compared to the RVEs with twenty-four and sixteen cracks. Table 6.7 below shows the numerically obtained Young's modulus values for dry and soaked crack conditions which showed a slight difference in results when compared to RVEs with higher cracks. Figures 6.25 and 6.26 graphically present the plotted results where trend lines show a bumpy pattern which is due to the different crack orientations and could be avoided by modeling multiple RVEs and taking the average values. Since RVE with eight cracks takes less simulation time and presents comparable results with RVEs with more cracks, it was decided to be the best modeling solution to determine the elastic properties of concrete. The plots in figure 6.25

and figure 6.26 were generated in the first case, however, the three cases along with the average values are plotted in figures 6.27 and 6.28 for dry case and figures 6.29 and 6.30 for soaked cracks condition.

Table 5.7: Young's Modulus results Obtained Numerically with 8 cracks RVE

No. of Cracks	CDP	E, GPa		Normalized	
		Dry	Skd	Dry	Skd
0	0	40	40	1	1
8	0.1	32.3	35.7	0.809	0.895
8	0.2	23.4	33.3	0.587	0.833
8	0.3	21.7	32.2	0.543	0.807
8	0.4	20.9	33.9	0.524	0.848
8	0.5	19.6	31.9	0.492	0.800
8	0.6	18.0	27.9	0.452	0.698
8	0.7	19.4	28.2	0.487	0.707
8	0.8	17.6	27.2	0.440	0.680
8	0.9	15.6	26.6	0.392	0.666
8	1	15.2	25.7	0.382	0.644

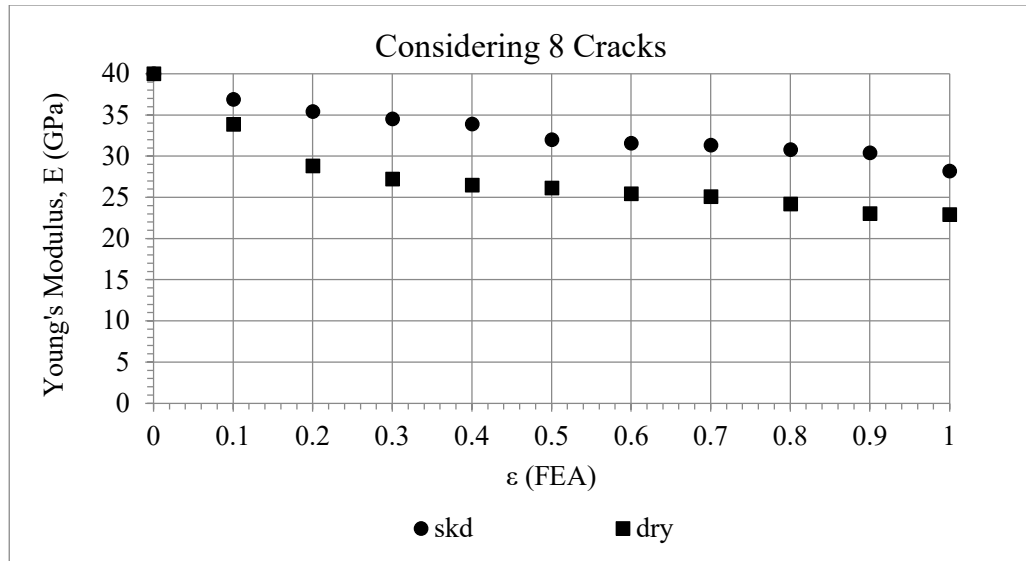


Figure 6.25: Young's Modulus Results of RVE with 8 Cracks for Dry and Soaked Cracks Condition

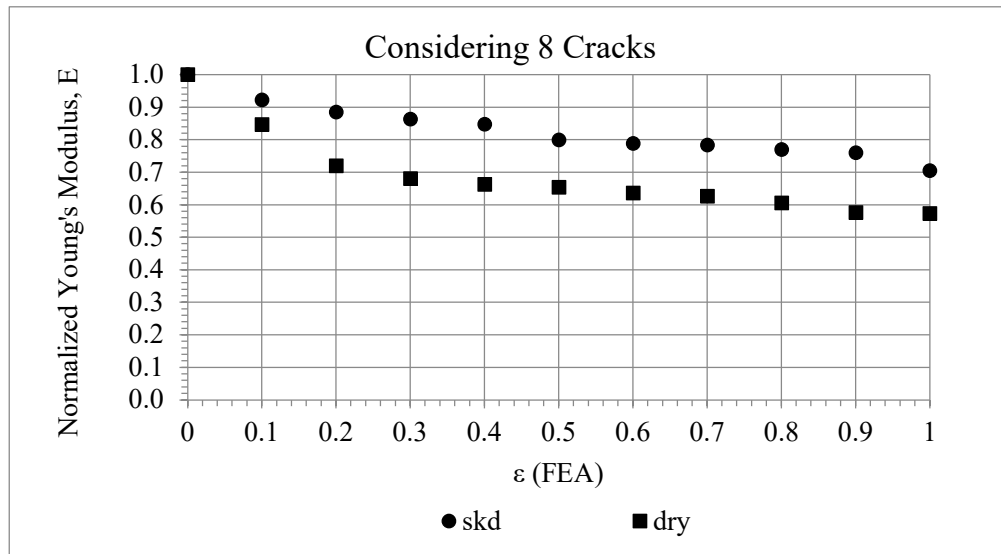


Figure 6.26: Normalized Young's Modulus Results of RVE with 8 Cracks for Dry and Soaked Cracks Condition

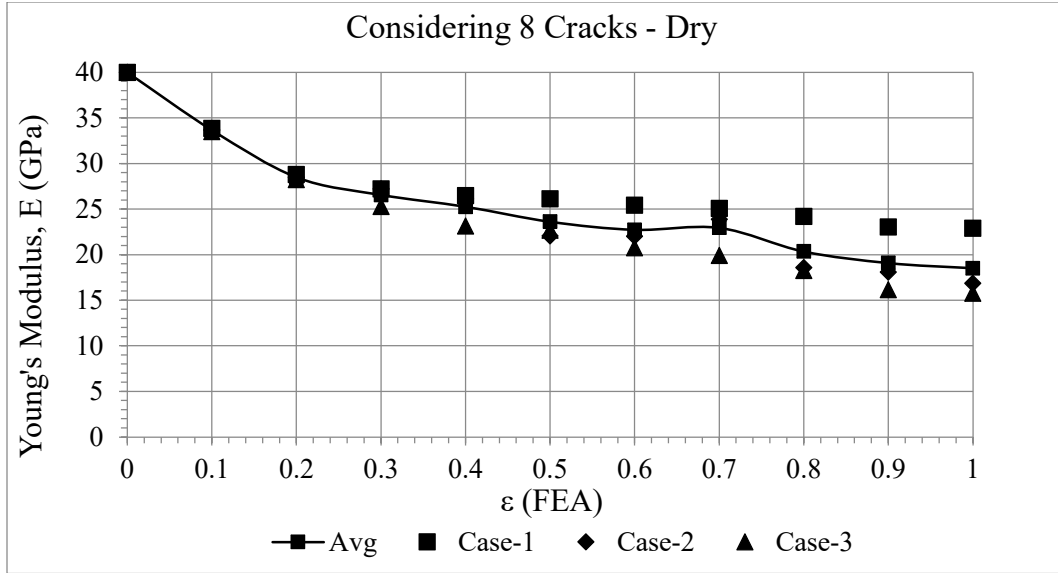


Figure 6.27: Comparison of Young's Modulus with three Cases of 8 different crack orientations in RVE and average values of all three Cases for dry condition

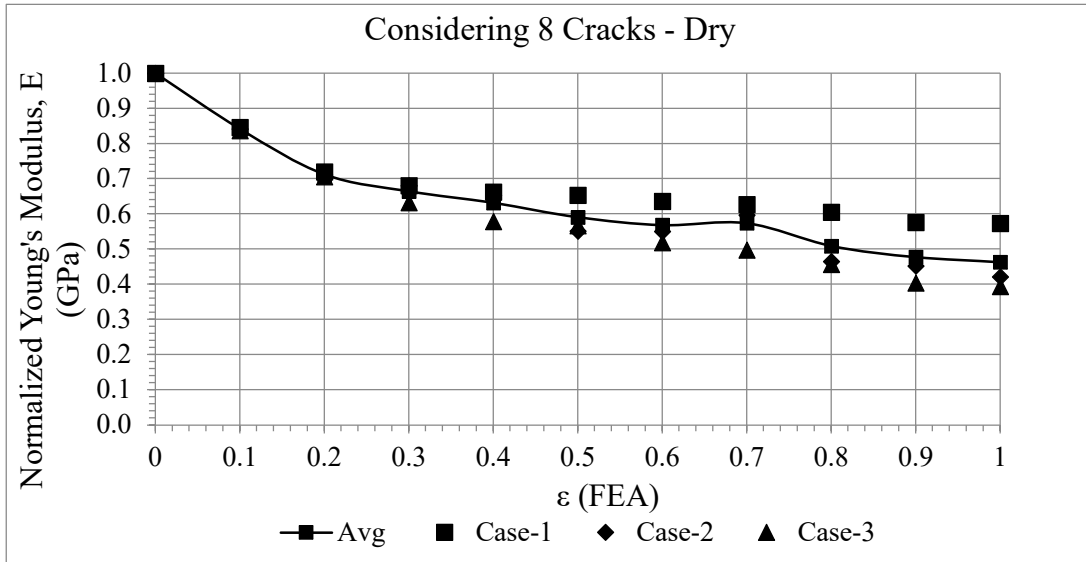


Figure 6.28 Comparison of Normalized Young's Modulus with three Cases of 8 different crack orientations in RVE and average values of three Cases for dry condition

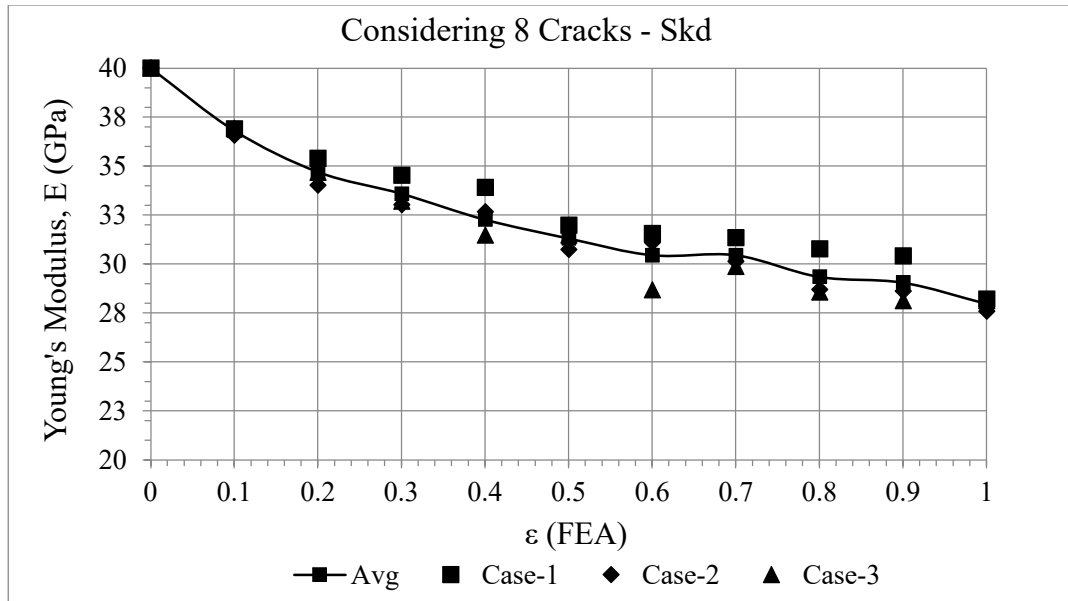


Figure 6.29: Comparison of Young's Modulus with three Cases of 8 different crack orientations in RVE and average values of all three Cases for soaked condition

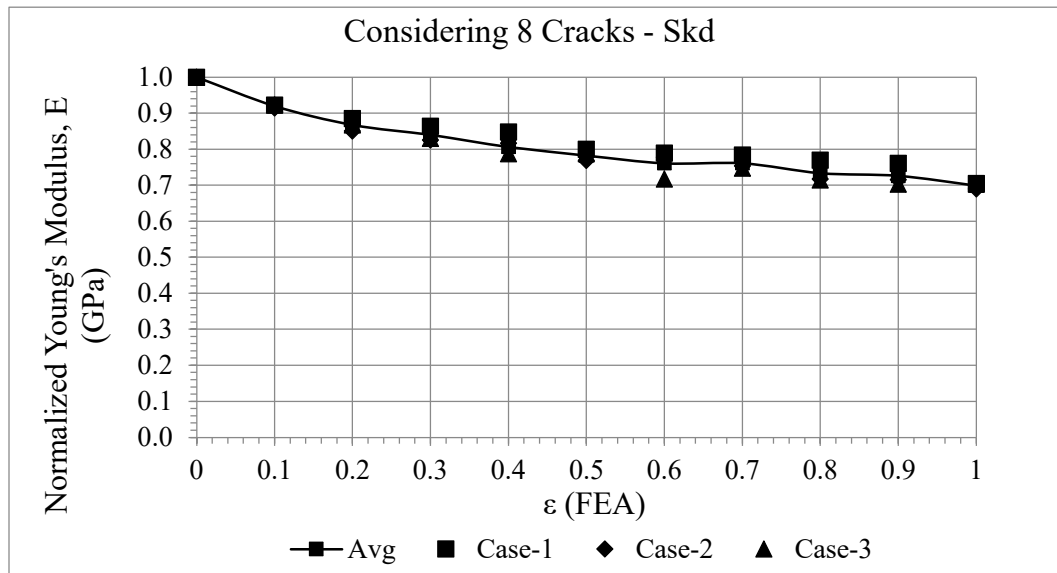


Figure 6.30: Comparison of Normalized Young's Modulus with three Cases of 8 different crack orientations in RVE and average values of all three Cases for soaked condition

It could be observed from the results presented in figures 6.29 and 6.30 for the case of fluid-filled cracks conditions considering three different cases, the results show decrease in Young's modulus until the crack density parameter of 0.2 and is identical. The variation in the results beyond CDP of 0.2 is again due to the overlapping of cracks and their different orientation.

Moreover, in the case of dry cracks, shown in figures 6.27 and 6.28, the results are identical until the crack density parameter is equal to 0.1. The further variation could be avoided by modeling multiple RVEs and taking their average values for similarity. The more the RVEs are modeled, the smoother and identical decrease in Young's modulus could be achieved for the desired crack density.

Young's modulus results were compared for 24, 16, and 8 cracks RVEs in figures 6.31 and 6.32 for dry cracks conditions. The plots show an almost similar pattern of strength reduction as the crack density parameter increases. It concludes that either option from RVEs with 24, 16, and 8 cracks could be chosen for analysis purposes since the difference in the results is very small. Hence, RVE with 8 cracks was chosen as a suitable modeling solution in determining the elastic properties of concrete more economically in a shorter time.

A similar pattern could also be observed in figures 6.33 and 6.34 for the case of dry cracks where Young's modulus results are decreasing with an increase in CDP with nearly equal values. The most precise values we could observe are obtained until the crack density parameter was equal to 0.2 and the results start to deviate slightly for other cases with a higher number of cracks.

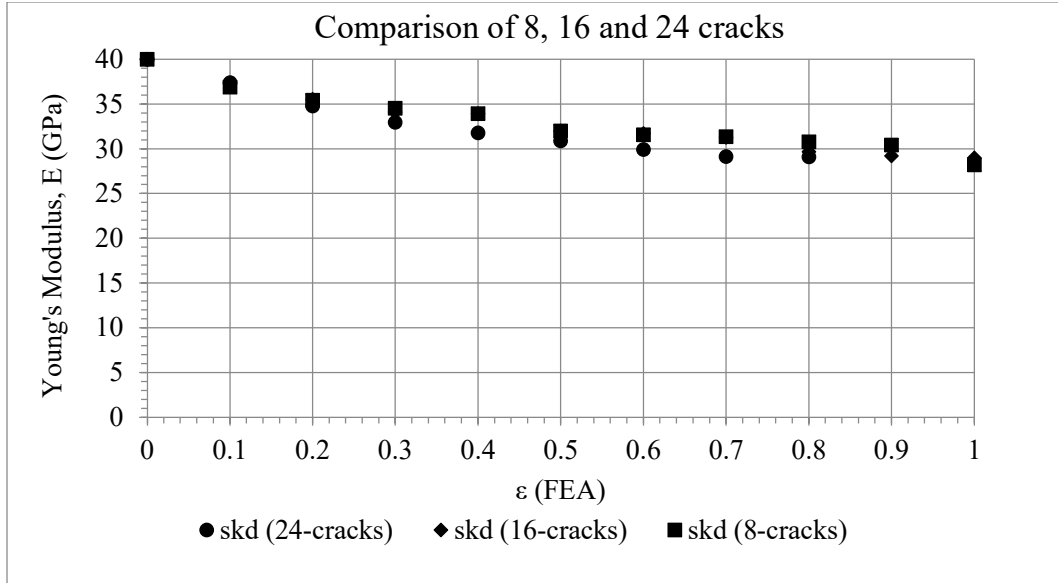


Figure 6.31: Comparison of Young's Modulus results obtained from RVEs with 8, 16 and 24 cracks for soaked cracks condition

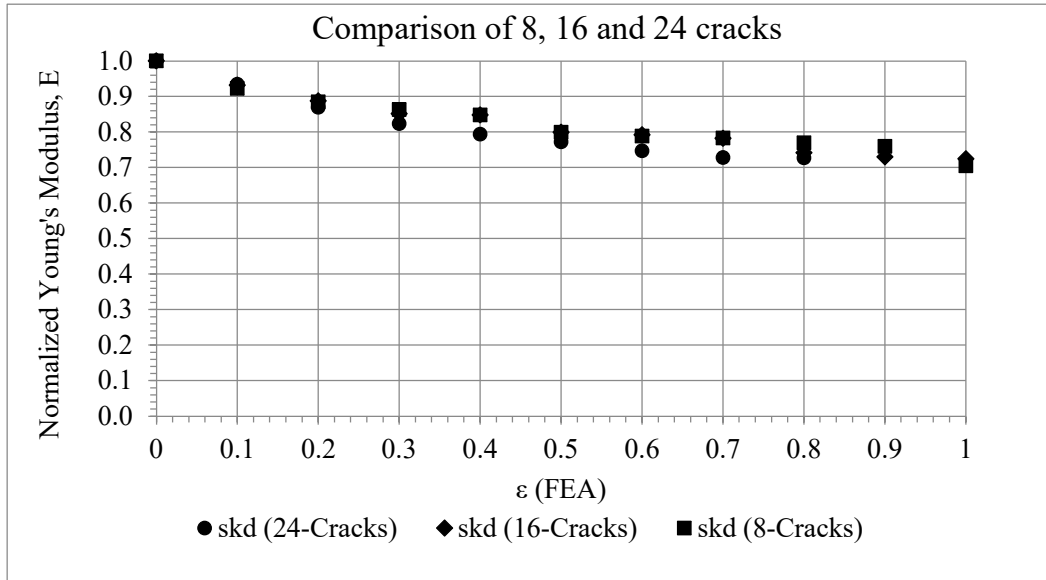


Figure 6.32: Comparison of Normalized Young's Modulus results obtained from RVEs with 8, 16 and 24 cracks for soaked cracks condition

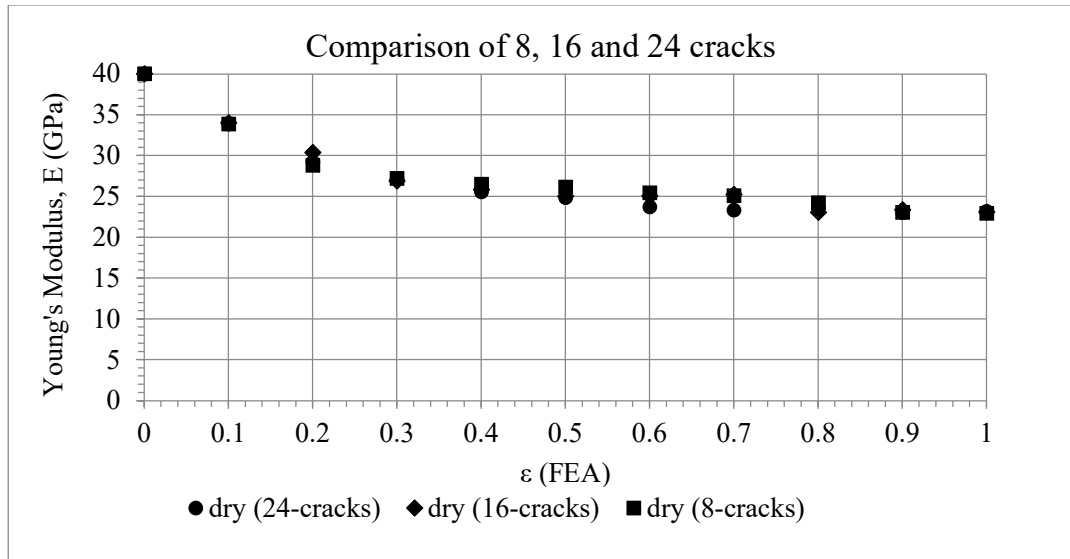


Figure 6.33: Comparison of Young's Modulus results obtained from RVEs with 8, 16 and 24 cracks for dry cracks condition

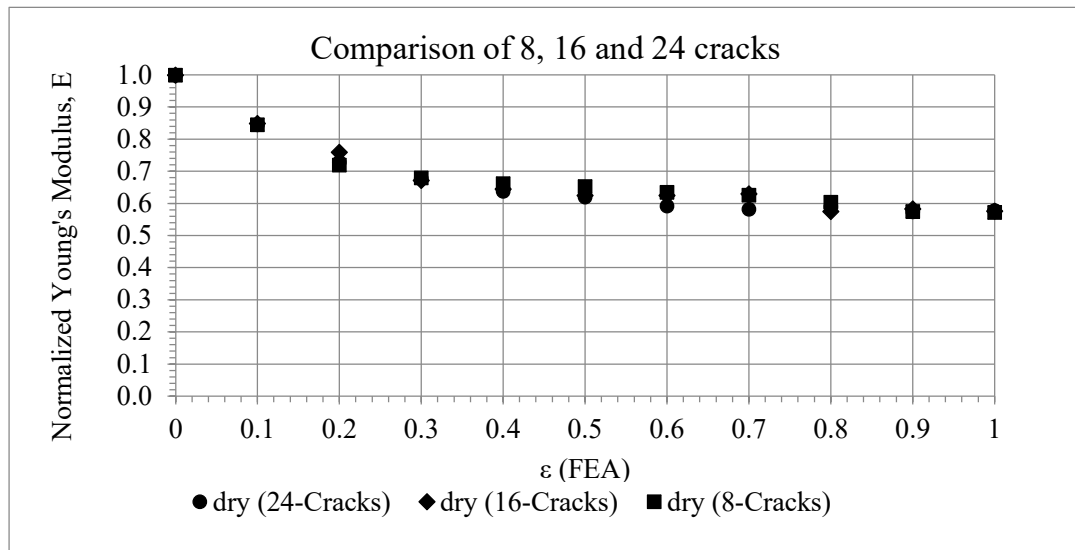


Figure 6.34: Comparison of Normalized Young's Modulus results obtained from RVEs with 8, 16, and 24 cracks for dry cracks condition

6.9 Comparing Numerical Analysis Results with Developed Analytical Models

The purpose of performing finite element analysis (FEA) using representative volume elements (RVEs) was to compare and results obtained using the extended models of Hudson’s (1981) used in this research study and the O’Connell and Budiansky models developed by Recalde (2009). Moreover, the proposed analytical model developed by Cheng (1993) based on Padé expansion has also been brought into the picture for comparing the numerically obtained Young’s modulus results with those estimated using mathematical relations. Figure 6.35 shows the plots developed for soaked cracks conditions where the numerically obtained FEA results were compared with different analytical models including the extension of the Hudson’s (1981) model developed in this research study.

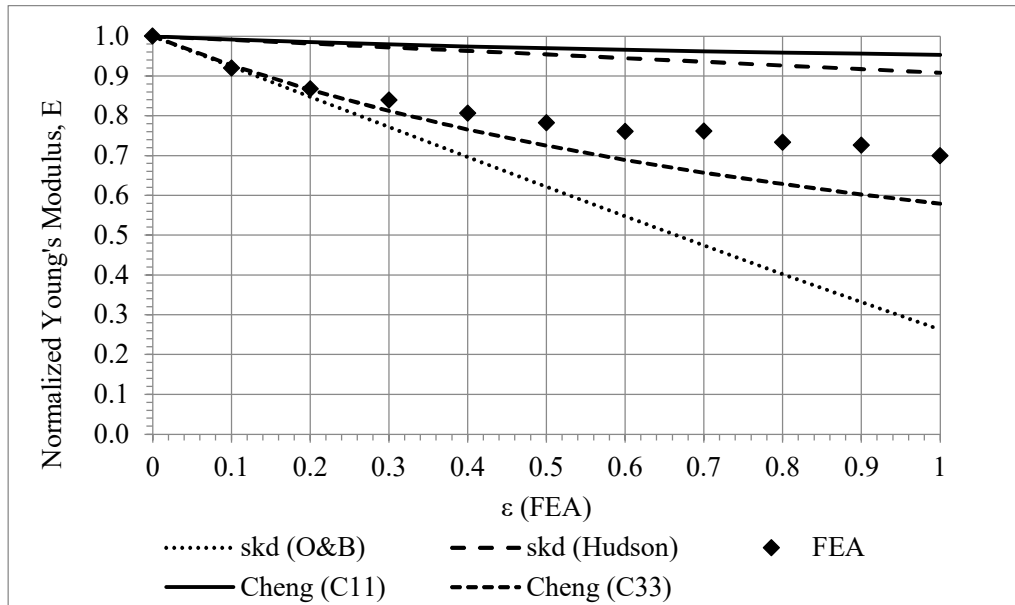


Figure 6.35: Comparison of Numerically obtained Normalized Young’s Modulus results with different analytical models for soaked cracks condition

It could be observed that the numerically obtained results are consistent until the crack density parameter is equal to 0.2 when compared to O’Connell and Budainsky’s (1981) model and with the third-order correction of Cheng’s (1993) model. Within this limit, the normalized Young’s modulus results behave well and beyond the 0.2 value of CDP, the results begin to diverge. Moreover, in the case of dry cracks condition shown in figure 6.36 where the plots indicate the numerical model results are consistent until the CDP limit of 0.1. This diversion of results beyond the specified limit of CDP could be due to the reason that the numerical analysis results begin to dominate over the other results obtained using different analytical models causing Young’s modulus to deviate rather than decrease in a similar fashion of trend with other analytical models. However, this statement could not yet be generalized about the deviating results observed with finite element analysis.

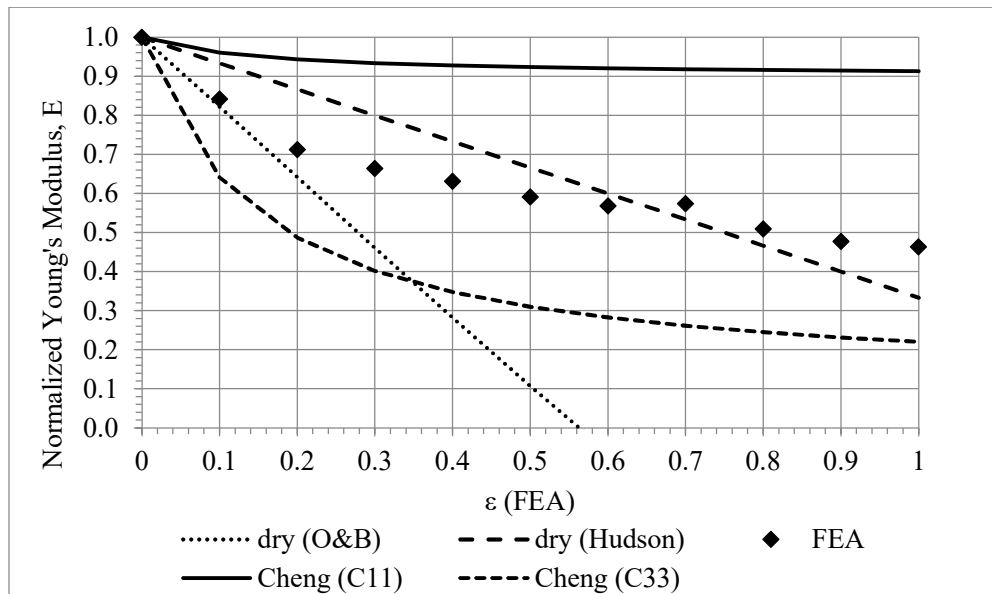


Figure 6.36: Comparison of Numerically obtained Normalized Young’s Modulus results with different analytical models for dry cracks condition

Statistical analysis was conducted to calculate the standard deviations and to present error bars for the elastic modulus obtained from different cases of RVEs with 8 cracks for both soaked and dry conditions. Average values of all cases were considered for both soaked and dry conditions which are presented in table 6.8 and table 6.9, and the data points are graphically presented in figures 6.37 and 6.38. The reduction from the uncracked concrete Young's modulus of 40 GPa was presented for cracked densities of 0.1 to 1.0 calculated using 8 cracks in the RVE. It could be observed in table 5.8 that the results determined numerically for three cases in dry and soaked condition have a slight change in the results which shows that the model creation was performed without posing errors. The results show a significant decrease in concrete strength which could be observed from the plots shown in figure 5.44.

Table 6.8: Young’s Modulus results obtained Numerically with 8 cracks RVE for both soaked and dry crack conditions

CDP	Numerically obtained Young’s Modulus E, GPa						Avg	Avg	STD	STD
	Dry- Case 1	Dry- Case 2	Dry- Case 3	Skd- Case 1	Skd- Case 2	Skd- Case 3	Dry	Skd	Dry	Skd
0	40	40	40	40	40	40	40	40	0	0
0.1	33.8	33.6	33.4	36.9	36.5	36.9	33.6	36.8	0.175	0.195
0.2	28.7	28.4	28.2	35.4	34.0	34.6	28.4	34.7	0.287	0.687
0.3	27.2	27.2	25.2	34.5	33.0	33.2	26.5	33.5	1.113	0.824
0.4	26.4	26.1	23.1	33.9	32.6	31.4	25.2	32.6	1.831	1.218
0.5	26.1	22.0	22.6	31.9	30.7	31.4	23.6	31.4	2.195	0.624
0.6	25.4	22.0	20.7	31.5	31.0	28.6	22.7	30.4	2.419	1.539
0.7	25.0	23.8	19.9	31.3	30.1	29.8	22.9	30.4	2.706	0.780
0.8	24.1	18.5	18.2	30.7	28.6	28.5	20.3	29.3	3.335	1.242
0.9	23.0	18.0	16.1	30.4	28.6	28.1	19.0	29.0	3.543	1.203
1	22.9	16.8	15.7	28.2	27.5	28.1	18.5	27.9	3.847	0.329

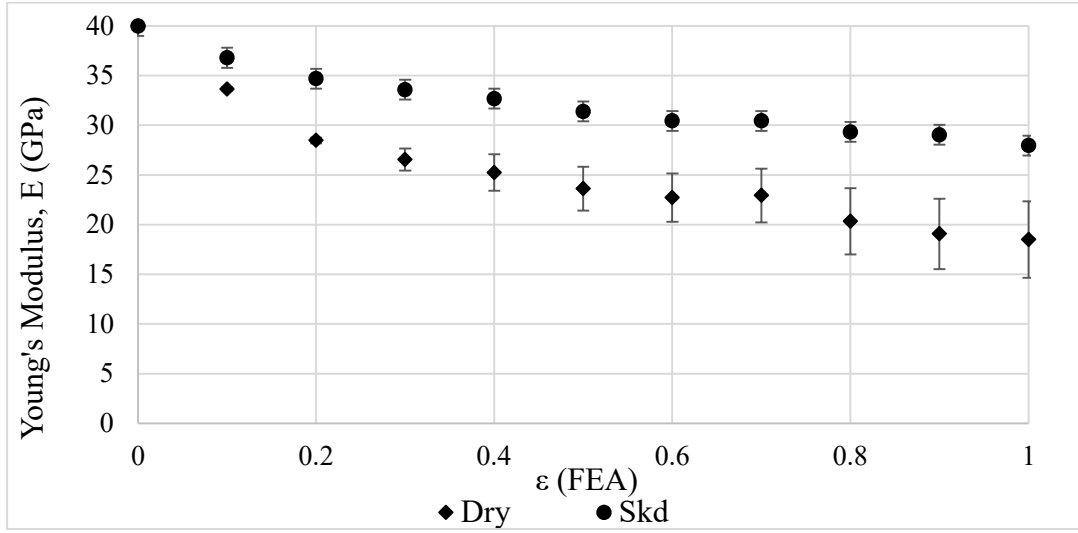


Figure 6.37: Error bars for Young's modulus using FEA results for dry and soaked crack conditions

Table 6.9: Normalized Young's Modulus Results obtained Numerically with 8 cracks RVE for both soaked and dry crack conditions

CDP	Normalized Young's Modulus E, GPa						Avg	Avg	STD	STD
	Dry-	Dry-	Dry-	Skd-	Skd-	Skd-	Dry	Skd	Dry	Skd
	Case 1	Case 2	Case 3	Case 1	Case 2	Case 3				
0	1	1	1	1	1	1	1	1	0	0
0.1	0.846	0.842	0.837	0.923	0.914	0.923	0.842	0.920	0.004	0.005
0.2	0.720	0.712	0.705	0.885	0.851	0.867	0.712	0.868	0.007	0.017
0.3	0.680	0.680	0.632	0.863	0.826	0.830	0.664	0.840	0.028	0.021
0.4	0.662	0.653	0.579	0.848	0.817	0.787	0.631	0.817	0.046	0.030
0.5	0.653	0.552	0.567	0.800	0.769	0.787	0.591	0.785	0.055	0.016
0.6	0.636	0.550	0.519	0.789	0.777	0.717	0.568	0.761	0.060	0.038
0.7	0.627	0.597	0.498	0.783	0.753	0.747	0.574	0.761	0.068	0.020
0.8	0.605	0.465	0.457	0.769	0.717	0.714	0.509	0.734	0.083	0.031
0.9	0.576	0.452	0.404	0.760	0.716	0.703	0.477	0.726	0.089	0.030
1	0.573	0.421	0.394	0.705	0.690	0.703	0.463	0.699	0.096	0.008

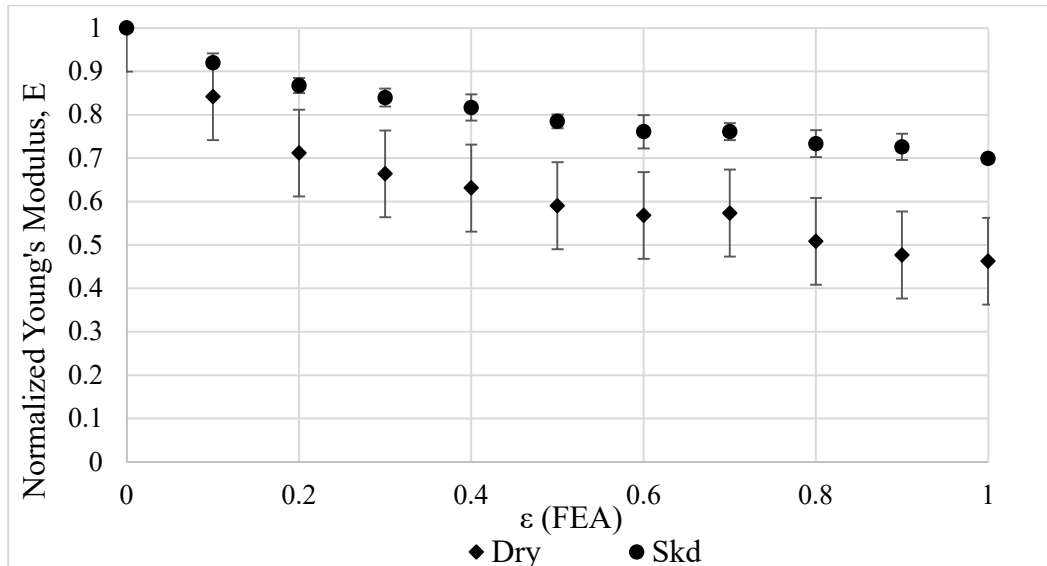


Figure 6.38: Error bars for Normalized Young's modulus using FEA results for dry and soaked crack conditions

It could be observed in figure 6.37 and figure 6.38 that for the case of soaked crack condition results, there is not much range in the data points, and the results are concise throughout each case and show smaller differences between the ranges. In contrast, in the case of dry conditions, a larger range was observed in the data which could be seen in the plots presented in blue color. The larger range for dry condition is observed at the last data set of crack density parameter equal to 1.0 ranging from 57.3% to all the way down to 39.4%. This observation also presents a clear idea that due to the smaller range in the data points plotted for the soaked condition, the numerical model behaved better for higher crack densities when compared to the dry crack case condition.

6.10 Summary

Chapter six of this research study presented the finite element analysis of representative volume elements which was set as a basis to numerically analyze models to determine the Young's modulus of elasticity (E_d) for soaked and dry conditions. The aim was to perform numerical analysis and to compare the elastic properties of concrete obtained using analytical models. A representative volume element was chosen as a proper solution to analyze a part of the disc specimen which resulted in lowering the computational cost and a quick solution. Mesh sensitivity analysis, determination of a proper RVE size, and the most suitable RVE in terms of crack numbers, economy, and time was considered for conducting further analysis using the Abaqus computer program. A comparative study considering numerical analysis results and those with mathematical relations was conducted along with the statistical analysis to determine the crack density parameter limit the FEA model could be applied for.

Below is a list of conclusions obtained from the last part of this research investigation using finite element analysis:

- A cubical geometry of the representative volume element for conducting finite element analysis was selected providing an easy application of boundary conditions. Two different RVE sizes with dimensions $100 \times 100 \times 100 \text{ micron}^3$ and $200 \times 200 \times 200 \text{ micron}^3$ were selected for the modeling purpose and to determine the elastic Young's modulus.

- Similar results for Young's modulus were achieved numerically either using a smaller or higher number of cracks in the RVE provided that the crack density was kept the same.
- This provided a clear idea that using a smaller number of cracks in RVE would yield similar results obtained with higher cracks and found to be the most suitable solution avoiding the crack overlaps creating issues in meshing and generating good results and was also an economical method in reducing the computational costs.
- Numerical analysis results when plotted, exhibited a similar trend in reducing Young's modulus values with the increase of crack densities when compared to the analytical models.
- Finite element analysis of RVE also presented higher Young's modulus values for soaked conditions which were observed in experimental investigations and were due to the water held in capillaries producing a stiffening effect in the concrete specimens.
- The difference in Young's modulus for 24, 16, and 8 cracks in RVE were found to have nearly 0.1% difference which could be neglected, and results could be considered almost similar.
- Numerical modeling procedure using 8 cracks in RVE was straightforward provided that the cracks were equally spaced without overlapping or interfering with each other resulting in easily assigning material properties, proper meshing, and generating suitable results with quicker simulation.

- Numerically obtained results for Young's modulus in the case of soaked cracks were similar to those obtained using the O'Connell and Budiansky model until the crack density parameter value of 0.2 and were in good agreement with the third-order correction of Cheng (1993) model.
- In the case of water-filled cracks, the results were identical until the crack density parameter was equal to 0.1 and was consistent with the O'Connell and Budiansky model.
- It was found that the results obtained using numerical models were valid for smaller crack densities for the case of dry cracks condition. The further diversion of the elastic modulus results beyond the 0.1 limit of CDP could be due to the reason that the numerical analysis results begin to dominate over the other results obtained using different analytical models causing Young's modulus to deviate when compared to the analytical models. However, this statement for the deviation in results occurring with numerical modeling with finite element analysis could not be generalized.
- The statistical analysis conducted on the results obtained from cracked concrete using three cases for dry and soaked conditions showed a slight change in Young's modulus values which confirms that the model creation was performed without producing errors.
- For the case of soaked crack condition results obtained after conducting statistical analysis, it was observed that there is no significant range in the data points and the results were found to be more concise throughout each case and showed little differences between the ranges.

- In the case of dry condition, a larger range in the data set of crack density parameters equal to 1.0 was observed which ranged from 57.3% to 39.4%.
- This observation also presented a clear idea that due to the smaller range in the data points plotted for the soaked condition, the numerical model behaved better for higher crack densities when compared to the dry crack case condition.

The following is the list of future recommendations:

- The variation shown in the plots of Young's modulus obtained with different cracks in RVE and not following a smooth trend line, could be avoided if an average result of many RVEs with different crack orientations is considered.
- The more the RVEs are modeled, the smoother and identical decrease in Young's modulus could be achieved for the desired crack density.
- The best way could be by using Python language, creating many loops, and assigning crack angles both positive and negative from 0 to 90 degrees in generating quick RVEs and getting smoother trend lines resulting in suitable results.
- The numerical analysis results could be compared with other rock mechanics models and the use of multiple models could be beneficial to researchers involved in conducting a forensic investigation of damaged structures.

Chapter Seven

Conclusions and Future Recommendations

7.1 Conclusions

The research study presented in this dissertation is comprised of three main parts which include;

- (1) Experimental investigations (Phase I)
- (2) Developing an analytical model (Phase II) and
- (3) Conducting numerical finite element modeling (Phase III)

Each of the above-mentioned parts is presented thoroughly in this dissertation, however, the conclusions are summarized below.

7.1.1 Experimental Investigation (Phase I) Conclusions

From the experimental study (Phase I), the following was concluded:

- A fundamental was set by using different concrete mixtures using SCM such as fly ash with cement replacement by 40 and 60 percent and to use the obtained data for later parts such as analytical models to estimate dynamic Young's modulus (E_d) and crack density parameter.

- The specimens were damaged at an elevated temperature of 300 °C in the oven for consecutive two hours which were then soaked and dried for the resonant characteristics and measuring frequency and to calculate elastic properties of concrete using mathematical relations.
- The first part provided the overall experimental data which was further utilized to estimate the changes in dynamic modulus of elasticity and played a major part in completing this research investigation presented in this dissertation.
- Percentage replacement of cement with supplementary material such as fly ash presented a significant increase in the compressive strength when compared to the traditional concrete. In the case of normal strength concrete, the compressive strength increased from 26.6 MPa to 30.1 MPa for concrete with 40% fly ash and 50.1 MPa for concrete with 60% fly ash.
- In the case of high-strength cement concrete, the compressive strength increased significantly from 27.1 MPa to 32.5 MPa for mixture with 40% fly ash and 42.9 MPa for mixture with 60% fly ash. This shows that concrete with a higher percentage of fly ash content up to 60% could be used for structures exposed to a high temperature of about 300 °C.
- A higher value of E_d was observed for specimens soaked than the unsoaked or dry specimens. This is due to the water held in the large capillaries in the concrete solid resulting in the stiffening effect. This increase in the dynamic modulus of elasticity is due to the increase in the resonant frequency of concrete disc specimens to a significant amount.

- Higher Initial Rates of Absorption of Water (S_i) for damaged 50 mm thick disc specimens was observed than the undamaged specimens for all mixture groups. The Secondary Rates of water absorption (S_s) characteristics were different for specimens made from various mixtures with fly ash content.
- In most cases, water absorption rates were not obtained since the correlation coefficient (r) was less than 0.98.
- A relationship between E_d versus API for Normal and High strength mixture groups with different fly ash content was conducted which showed that, in the case of undamaged specimens, high E_d and low API was observed, however, for the damaged specimens low E_d and high API results were obtained. These results also behaved similarly in the case of two inches thick discs.
- Statistical analysis results showed that there is a significant effect of fly ash percentage on the Air Permeability Index.

7.1.2 Extension of Hudson's model (Phase II)

Phase II of this research work is comprised of the extension of Hudson's model to concrete material. The following were concluded from this part of the dissertation:

- The obtained crack density parameter using Hudson's extended model was used to analyze the changes occurring in dynamic modulus of elasticity (E_d) of thin disc specimens in soaked and dry conditions for damaged and undamaged conditions.
- The extension of Hudson's model presented in this research study was compared with the model developed by Recalde (2009) which is an extension of O'Connell

and Budiansky (1974) model and was found to be in good agreement for control specimens at certain limited crack density parameters where both models behaved almost identical.

- Higher ε values were observed in Hudson's extended model rather than the O'Connell and Budiansky model when the concrete samples were exposed to high temperatures of 300 °C (570 °F). The obtained (ε) using Hudson's extended model was higher than one, whereas, with the O'Connell and Budiansky model, the (ε) was found to be always less than one.
- A new technique known as Padé approximation, which was introduced by Cheng (1993) to solve the issue with the second-order expansion in Hudson's extended model of diverging rather than converging at a certain crack density limit, did not behave well in the case of thin concrete discs. Hence, it was decided that Hudson's first order would best be used to obtain appropriate results.
- The two concrete mixtures analyzed with sustainable cement materials made with 40, and 60% fly ash content improved the overall strength for normal strength and high strength concrete when compared to the control mixture.
- Autogenous healing in all damaged concrete mixtures happened at a lesser extent after soaking them in water for 24 hours, however, the concrete damaged and cracked severely did not exhibit a higher value of autogenous.
- Mixtures containing 40% fly ash such as (Mixture NF40) and (Mixture HF40), the autogenous healing occurred at a considerable level where mixtures tried to reach their un-damaged condition which happened to less extent.

- The water penetrated through cracks and held in capillaries produced a stiffening effect in the concrete discs which was observed while conducting the resonant testing, resulting in higher Young's modulus E_d for soaked concrete discs than for the dry concrete specimens.
- Statistical analysis showed that there is no significant difference in the change of the E_d for the temperature exposure of 300 °C for all concrete mixtures with different percentages of fly ash.
- Statistical analysis revealed that there is a significant difference in the change of the crack density parameter ϵ for the temperature exposure of 300 °C for all concrete mixtures with different percentages of fly ash.
- The analytical method presented in this research study to estimate crack density parameter and elastic Young's modulus has potential as an easy-to-use analytical tool for many researchers in the field of concrete materials and for forensic investigations on different concrete mixtures either with or without supplementary cementitious materials used.
- This study revealed an interesting finding of both methods which behaved differently. Since different results are obtained from Hudson's extended model and the existing O'Connell and Budiansky model used for over one decade, a research work could be extended to check which method reveals accurate results. This could be done using microscopic analysis, which is quite expensive, however, it could prove the accuracy of both analytical models.

The list below presents some future recommendations:

- The application of Hudson's model could be extended to specimens thicker than two inches (50 mm) and for cylinders made with different SCMs such as blast furnace slag, silica fume, and sugarcane bagasse ash.
- More analytical procedures could be developed using different rock mechanics models and to compare the obtained results with Hudson's (1981) in estimating the elastic properties of concrete.
- The analytical models presented in this research study could be applied on thin concrete disc specimens made using seawater which could cause sulfate attack on concrete due to the Potassium and magnesium sulfates reaction with calcium hydroxide, and to compare with the elastic properties for those specimens made using freshwater.
- In most cases, a significant difference was observed in the results of both O'Connell and Budiansky and Hudson's extended models and the accuracy of these methods could be done using microscopic analysis.

7.1.3 Finite Element Modeling

From the last part of numerical analysis, the following were concluded:

- A procedure using cubical geometry of RVE was found to be a suitable solution for conducting finite element analysis in determining the elastic Young's modulus of concrete easily and efficiently.
- Similar results for Young's modulus were obtained numerically either with a smaller or higher number of cracks in the RVE provided that the crack density was kept the same.

- It concludes that either option from RVEs with 24, 16, and 8 cracks could be chosen for analysis purposes since the difference in the results is minimal.
- RVE with the least number of cracks was chosen to conduct finite element analysis and determine suitable results for the elastic properties of concrete more economically in a shorter time.
- Using a smaller number of cracks in RVE yielded similar results obtained with higher cracks and was found to be the most appropriate solution which avoided the crack overlapping creating issues in meshing and resulted in generating good results and reducing the computational costs.
- Numerical analysis results when plotted, exhibited a similar trend in reducing Young's modulus values with the increase of crack densities when compared to the analytical models.
- Finite element analysis of RVE also presented higher Young's modulus values for soaked conditions which were observed in experimental investigations and were due to the water held in capillaries producing a stiffening effect in the concrete specimens.
- Numerically obtained results for Young's modulus in the case of soaked cracks were similar to those obtained using the O'Connell and Budiansky model until crack density parameter value of 0.2 and with the third-order correction of Cheng (1993) model were in good agreement.

- In the case of water-filled cracks, the results were identical until the crack density parameter was equal to 0.1 and was consistent with the O'Connell and Budiansky model.
- It was found that the developed numerical model behaved well for smaller crack densities in case of dry cracks condition. The further diversion of the elastic modulus results beyond the 0.1 limit of CDP could be due to the reason that the numerical analysis results begin to dominate over the other results obtained using different analytical models causing Young's modulus to deviate when compared to the analytical models.
- However, this statement for the deviation in results occurring with numerical modeling could not yet be generalized.

7.2 Future Recommendations

The following is the list of future recommendations observed while conducting this research study:

- Microscopic investigation is required to be carried out in determining the damage in thin concrete discs and to compare the results with the analytical models presented in this research work.
- The application of Hudson (1981) should be extended to specimens thicker than two inches (50 mm) and for cylinders made with different SCMs such as blast furnace slag, silica fume, sugarcane bagasse ash, and other available materials with pozzolanic properties.

- More analytical procedures should be developed using different rock mechanics models to compare the elastic properties of concrete obtained using Hudson's extended model.
- In the case of numerical modeling, the variation in the plots of Young's modulus obtained with different cracks in RVE, could be avoided if an average result of several RVEs with different crack orientations is considered.
- Use of Python language should be carried out in assigning crack orientations by defining crack angles in generating quick RVEs and several iterations in obtaining smoother trend lines resulting in suitable results.
- The numerical analysis results should be compared with other rock mechanics models and the use of multiple models should be introduced to researchers involved in conducting a forensic investigation of damaged structures.

REFERENCES:

“EN, 1992-1-2: design of concrete structures. Part 1-2: general rules—structural fire design,” *Eurocode 2, European Committee for Standardization, Brussels, Belgium*, 2004.

[Abaqus 2020 \(3ds.com\)](#) accessed on May 20th 2021.

Aboudi, J., “Mechanics of Composite Materials, A Unified Micromechanical Approach”, *Elsevier Science Publishers, Amsterdam*, 1991.

ACI 318-08 Building Code Requirements for Structural Concrete and Commentary

Aldea, C.M., Shah, S.P., Karr, A., “Effect of Microcracking on Durability of High-Strength Concrete”, *Transportation Research Record*, 1999;1668 (1), pp. 86-90.
doi:10.3141/1668-13

Al Kassem, Ghayath, “Micromechanical Material Models for Polymer Composites through Advanced Numerical Simulation Techniques”, *Diese Dissertation ist auf den Internetseiten der Hochschulbibliothek online verfügbar*. 2019

Anupama, K.D., Priyadarsini, R.S., and Narayanan, S., “Effect of Elevated Temperatures on the Mechanical Properties of Concrete” *2nd International Conference on*

Structural Integrity and Exhibition 2018, Procedia Structural Integrity, 2019, 14, 384-394.

ASCE, "2021 Report Card for America's Infrastructure," *American Society of Civil Engineers*, Reston, VA, <https://infrastructurereportcard.org/>

ASTM C 469/C469M-14, American society for testing and materials “Standard Test Method for Static Modulus of Elasticity and Poisson’s Ratio of Concrete in Compression.”

ASTM C138-14, American society for testing and materials – “Standard Test Method for Density (Unit Weight), Yield, and Air Content (Gravimetric) of Concrete.”

ASTM C143-16, American society for testing and materials – “Standard Test Method for Slump of Hydraulic-Cement Concrete.”

ASTM C150 / C150M – 16, American Society for testing and materials – “Standard Specification for Portland Cement”

ASTM C192-14, American Society for testing and materials – “Standard Practice for Making and Curing Concrete Test Specimens in the Laboratory.”

ASTM C206-14, American Society for testing and materials – “Standard Specification for Finishing Hydrated Lime.”

ASTM C231-14, American society for testing and materials – “Standard Test Method for Air Content of Freshly Mixed Concrete by the Pressure Method.”

ASTM C39/ C39M-16, American society for testing and materials – “Standard Test Method for Compressive Strength of Cylindrical Concrete Specimens.”

ASTM Standard C597-16 American society for testing and materials “Standard Test method for Pulse Velocity through Concrete.”

ASTM Standard Test C1585-16, American society for testing and materials – Standard Test Method for Measurement of Rate of Absorption of Water by Hydraulic Cement Concretes.”

Burgarella, B., Aurelien Maurel-Pantel, Lahellec, N., Hochard, C., “Micromechanical modelling of matrix cracks effect on shear and transverse response for unidirectional composites with a full field approach” *Composite Structures, Elsevier*, 2019, 208, 338-345.

Babalola, O.E., Awoyera, P.O., Le, D.H., and Romero, L.M.B., “A Review of Residual Strength Properties of Normal and High Strength Concrete Exposed to elevated temperatures: Impact of materials Modification on behaviour of Concrete Composite,” *Elsevier Journal of Construction and Building Materials*, 2021, 296, 123448.

Behnood. A., and Ziari, H., “Effects of Silica Fume Addition and Water to Cement Ratio on the Properties of High-Strength Concrete after Exposure to High Temperatures”, *Cement and Concrete Composites*, 2008, 30, 106-112.

- Bender, C.M., and S.A. Orszag, “Advanced Mathematical Methods for scientists and Engineers, *McGraw-Hill, New York*, 1978.
- Biot, M.A., “Theory of propagation of elastic waves in a fluid saturated porous solid.I. Low frequency range and II. Higher-frequency range”, *J. Acoust. Soc. Am.*, 1956, 28, 168–191.
- CIB W14 Report“, "Repairability of Fire Damaged Structures", *Fire Safety Journal*, Volume 16, No. 4, 1990, pp. 251-336.
- Cailletaud, G., “Size effects on elastic properties of random composites,” *Engineering Computations*, 1994, 11, 99–110.
- Chen, B., and Liu, J., “Residual Strength of Hybrid-Fiber-reinforced High-Strength Concrete after Exposure to High Temperatures,” *Journal of Cement and Concrete Research*, June 2004, 34(6), 1065-1069.
- Chen, G.M., He, Y.H., Yang, H., Chen, J.F., and Guo, Y.C., “Compressive behavior of Steel Fiber Reinforced Recycled Aggregate Concrete After Exposure to Elevated Temperatures,” *Journal of Construction and Building Materials*, November 2014, 71(30), 1-15.
- Cheng, C.H., “Crack Models for a Transversely Isotropic Medium” *Journal of Geophysical Research*, 1993, 98(B1), 675-684.
- Choe, G., Kim, G., Gucunski, N., and Lee, S., “Evaluation of the mechanical properties of 200 MPa Ultra-High Strength Concrete at Elevated Temperatures and residual

- Strength of Column,” *Journal of Construction and Building Materials*, 2015, 86, 159-168.
- Chowdhury, S., “Effects of Elevated Temperature on Mechanical Properties of High-Strength Concrete”, *23rd Australasian Conference on Mechanics of Structures and Materials (ACMSM-23)*, at Byron Bay, NSW, Australia, 2.
- Cook, R.D., “Finite Element Modeling for Stress Analysis”, *University of Wisconsin, Madison*, 1995.
- Cooper, R.C., Bruno, G., Wheeler, M.R., Pandey, A., Watkins, T.R., Shyam, A., “Effect of microcracking on the uniaxial tensile response of β -eucryptite ceramics: Experiments and constitutive model” *Acta Materialia*, Volume 135, 2017, pp. 361-371.
- Cruz, C.R., “Elastic properties of concrete at high temperatures,” *Journal of the PCA Research and Development Laboratories*, 1966, 8, 37–45.
- Dascalua, C., Bilbiea, G., and Agiasofitou, E.K., “Damage and size effects in elastic solids:A homogenization approach” *International Journal of Solids and Structures*, 2008, 45 (2008), 409–430.
- David N. Bilow, and Mahmoud E. Kamara, “Fire and Concrete Structures” ASCE Structures (2008): Crossing Borders
- Diane, W., “Finite Element Analysis to Simulate Reinforced Concrete Corrosion in Beams and Bridge Decks,” *Master’s thesis the University of Delaware*, 2013.

- Dias, W.P.S., Khoury, G.A., and Sullivan, P.J.E., "Mechanical Properties of Hardened cement Paste Exposed to temperatures up to 700 °C (1292 °F)," *ACI Materials Journal*, 1990, 87(2), 160-166.
- Dilek U., "Assessment of Damage Gradients Using Dynamic Modulus of Thin Concrete Disks," *ACI Materials Journal*, 2008, 105(5), 429-437.
- Dilek, U., and Leming, M. L., "Mechanistic Evaluation of Dicer Salt Scaling Damage using Dynamic Elastic Young's Modulus of Concrete Disks," Presented in *Transportation Research Board (TRB) 84th Annual Meeting Compendium of Papers*, 2005.
- Dilek, U., and Leming, M. L., "Elastic Dynamic Young's Modulus and Permeability of Concrete in Fire Damaged Structural Members," *ASCE Journal of Materials in Civil Engineering*, V. 20, No.2, 2008, pp. 102-110.
- Dilek, U., and Leming, M. L., "Comparison of Pulse Velocity and Impact-Echo Findings to Properties of Thin Disks from a Fire Damaged Slab," *ASCE Journal of Performance of Constructed Facilities*, V. 21, No. 1, 2007a, pp. 13-21.
- Dilek, U., Leming, M. L., and Guth, D., "Relationship Between Elastic Modulus and Permeability of Damaged Concrete," *Journal of the Transportation Research Board, Concrete TRB(1893)*, 2004, pp. 53-60. 187

- Dilek, U., Leming, M. L., and Sharpe, E. F., "Assessment of Cryogenic Fluid Spill Damage to Concrete," *Forensic Engineering: Proceedings of the Third Congress*, P.A. Bosela et al., eds., American Society of Civil Engineers, Reston, VA, 2003, pp. 269-279.
- Dilek, U., "Nondestructive and Laboratory Evaluation of Damage Gradients in Concrete Structure Exposed to Cryogenic Temperatures," *ASCE Journal of Performance of Constructed Facilities*, V. 20, No. 1, 2006, pp. 37-44.
- Dilek, U., "Evaluation of Fire Damage to a Precast Concrete Structure Nondestructive, Laboratory, and Load Testing," *Journal of Performance of Constructed Facilities*, V. 19 No.1, 2005, pp. 42-48.
- Dilek, U., Caldwell, T., Sharpe, E. F., and Leming, M. L., "Fire Damage Assessment, Prestressed Concrete Double-Tees at Parking Deck," *Forensic Engineering: Proceedings of the Third Congress*, P.A. Bosela et al., eds., American Society of Civil Engineers, Reston, VA, 2003, pp. 247-258.
- Drugan, W., and Willis, J., "A micromechanics-based nonlocal constitutive equation and estimates of representative volume element size for elastic composites," *Journal of the Mechanics and Physics of Solids*, 1996, 44, 497–524.
- Fine, R. A. and Millero, F. J., "Compressibility of water as a function of temperature and pressure," *Journal of Chemical Physics*, 1973, 59(10):5529-5536. Doi: 10.1063/1.1679903.

Garside, M., “U.S. Domestic Production of Cement Clinker from 2007 to 2020”, *Statistica, Chemicals & Resources: Mining, Metals & Minerals*, <https://www.statista.com/statistics/219330/us-clinker-production/> (Accessed on July 17, 2021)

Gassmann, F., “Über die Elastizität poröser Medien. Vier. der Natur,” *Gesellschaft Zurich*, 1951, 96, 1–23.

Gurtin, M.E. “The linear theory of elasticity. A Handbook for Physics, bd. 6a/2,” *Springer*, 1972.

Helal, J., and Mendis, S., P., “Non-destructive Testing of Concrete: A Review of Methods,” *Special Issue: Electronic Journal of Structural Engineering*, 2015, 14(1).

Hosseini, R., Azadi M., Sadeghi Hegar, M., and Pournaghi, M. Shariyat, Y., “Free and forced vibration analysis on finite element model of an off-road vehicle”, *International Journal of Automotive Engineering*, 2015, Vol. 5, Number 4, Dec 2015, 2028-2033.

<http://www.itl.nist.gov/div898/handbook/>, National Institute of Standards and Technology, Gaithersburg, MD.

https://www.concreteconstruction.net/how-to/materials/what-is-fly-ash_o Accessed on March 2020.

Hudson, J. A., “Overall Properties of a Cracked Solid,” *Math. Proc. Cambridge, Phil. Soc.*, 1980, 88, 371-384.

- Hudson, J. A., "Wave Speeds and Attenuation of Elastic Waves in Material Containing Cracks," *Geophysical Journal of Astronomy. Soc.*, 1981, 64, 133-150.
- Husem, M., "The effects of high temperature on compressive and flexural strengths of ordinary and high-performance concrete," *Fire Safety Journal*, 2006, 41(2), 155-163.
- Hutchinson, J. R., "Axisymmetric Flexural Vibrations of a Thick Free Circular Plate," *Journal of Applied Mechanics*, 1979, 46, 139-144.
- Hsu, T. T. C., Slate, F. O., Sturman, G. M., and Winter, G, "Microcracking of Plain Concrete and the Shape of the Stress-Strain Curve," *ACI Journal Proceedings*, Vol. 60, No. 2, 1963, pp. 209-224.
- Jornet, A., Guidali, E., and Muhlethaler, U., "Microcracking in High Performance Concrete," *Swedish National Testing and Research Institute: 1993, Building Technology*.
- Kanit, T., Forest, S., Galliet, I., Mounoury, V., and Jeulin, D., "Determination of the size of the representative volume element for random composites: statistical and numerical approach," *Methods in applied mechanics and engineering*, 2003, 195, 3960–3982.
- Kassir, M.K., Bandyopadhyay, K.K., and Reich, M., "Thermal Degradation of Concrete in the Temperature Range from Ambient to 315 °C (600 °F)," *Report prepared for*

Office of Environmental Restoration and Waste Management US Department of Energy, Washington, D.C., 1996.

Khoso S, Raad J, and Parvin A (2019) Experimental investigation on the properties of recycled concrete using hybrid fibers. *Open Journal of Composite Materials*, 9, 183-196.

Kodur, V., “Properties of Concrete at Elevated Temperatures,” *Hindawi International Scholarly Research Notices*, Article ID 468510, 2014, 15.

Leming, M. L., Nau, M. J., and Fukuda, J., “Nondestructive Determination of the Dynamic Modulus of Concrete Disks,” *ACI Materials Journal*, 1998, 95(1), 50-57.

Lubineau, G., and Ladeveze, P. “Construction of a micromechanics-based intralaminar mesomodel, and illustrations in ABAQUS/Standard,” *Computational Materials Science*, 2008, 43(1), 137-145.

Malhotra, H.L., “The Effect of Temperatures on the Compressive Strength of Concrete,” *Magazine of Concrete Research*, 1956, 8(3), 85-94.

Malhotra, V.M. “High-Performance, High-Volume Fly Ash Concrete.” *Concrete International* 24(7), 2002, pp. 30-34

Mavko, G., and Jizba, D., “Estimating grain-scale fluid effects on velocity dispersion in rocks”, *Geophysics*, 1991, 56, 1940–1949.

- Mavko, G., Mukerji, T., and Dvorkin, J., “The Rock Physics Handbook: Tools for seismic Analysis in Porous Media,” *Cambridge University Press, Second edition*, Cambridge, NY, 2009.
- McCoy, B. C., Leming, M. L., and Seracino, R., “Crack Density and Elastic Properties of Sustainable Concretes,” *ACI Materials Journal*, 2014, 111(1), 13-21.
- Mehta, P.K., and Monteiro, P.J.M., “Concrete: Microstructure, Properties and Materials,” *McGraw-Hill, New, York*, 2017.
- Mehta, P.K., and Monteiro, P.J.M., Microstructure of Concrete | McGraw-Hill Education, 2014, *Access Engineering (accessengineeringlibrary.com)*, Accessed on June 7th, 2021.
- Michel, J. C., Moulinec, H., and Suquet, P., “Effective properties of composite materials with periodic microstructure: a computational approach. Computer methods in applied mechanics and engineering, 1999, 172(1), 109-143.
- Mumtaz, M., Zafarparandeh, I., Erbulut, D. U., “Investigation into Cervical Spine Biomechanics Following Single, Multilevel and Hybrid Disc Replacement Surgery with Dynamic Cervical Implant and Fusion: A Finite Element Study” - *Bioengineering*, 2022
- NIST, 2010, “*NIST/SEMATECH e-Handbook of Statistical Methods*,
- O’Connell, R. J., and Budiansky, B., “Seismic Velocities in Dry and Saturated Cracked Solids,” *Journal of Geophysical Research*, 1974, 79(36), 4626-4627.

O’Connell, R. J., and Budiansky, B., “Viscoelastic Properties of Fluid Saturated Cracked Solids,” *Journal of Geophysical Research*, 1977, 82(35), 5719-5735.

Omairey, S., P., Dunning, and S., Sriramula, “Development of an Abaqus Plugin Tool for Periodic RVE Homogenization,” *Engineering with Computers*, 2018, <https://doi.org/10.1007/s00366-018-0616-4>.

Ostoya-Starzewski, M., and Jeulin, D. (2001), “Mechanics of Random and Multiscale Microstructures,” *Springer*, 2001.

Phan, L. T., and Carino, N. J., “Review of Mechanical Properties of HSC at Elevated Temperature,” *ASCE Journal of Materials in Civil Engineering*, 1998, 10(1), 58-656.

Phan, L.T., “Fire Performance of High-Strength Concrete: A Report of the State of the Art,” 1996.

Philleo, R., “Some Physical Properties of Concrete at High Temperatures,” *ACI Journal Proceedings*, 1958, 54(10), 1-6.

Python.org, <http://www.python.org/>

Rajib, “Concrete Microcracking Basics”, *Civil Engineering World, A Learning Platform for Civil Engineers*, February, 2020, [Concrete Microcracking Basics - Civil Engineering World \(civil-engg-world.com\)](#) Accessed on June 20, 2021.

- Ravindrarajah, R.S., Swamy, R.N., "Load effects on fracture of concrete", *Materials and Structures*, 22, 15–22 (1989), <https://doi.org/10.1007/BF02472690>
- Recalde, J. J., "Vibration Characteristics and Use in Concrete Damage Assessment," M.S. Thesis, Department of Civil, Construction, and Environmental Engineering, North Carolina State University, Raleigh, NC, 2005, 254 p.
- Recalde, J.J., "Estimating Crack Growth in Temperature Damaged Concrete," *PhD dissertation*, North Carolina State University, Raleigh, NC, 2009, 211p.
- Recalde, J.J., and Leming, M.L., "Changes in Fluid Penetrability and Mechanical Properties of Concrete Due to High Temperature Exposure," *Journal of ASTM International*, 2009, 6(6), 13.
- Rekha, K., and Potharaju, M., "Residual Compressive Strength of Recycled Brick Aggregate Concrete at High temperatures," *International Journal of Emerging Technology and Advanced Engineering*, January 2015, 5(1), 159-164.
- [Representative elementary volume – Wikipedia](#), assessed on September 15th 2020.
- Reuss, A., "Berechnung der Fließgrenzen von Mischkristallen auf Grund der Plastizitätsbedingung für Einkristalle" *Z. Ang. Math. Mech.*, 1929, 9, 49–58.
- Sadowski, L., and Mathia, T.G., "Multi-scale metrology of concrete surface morphology: Fundamentals and specificity," *Journal of Construction and Building Materials*, 2016, 113, 613-621.

- Sakir, S., Raman, N. S., Safiuddin, M.D., Kaish, A. B. M. A. and Mutalib, A. A.,
“Utilization of By-Products and Wastes as Supplementary Cementitious Materials
in Structural Mortar for Sustainable Construction,” *Journal of Sustainability MDPI*,
2020, 12(3888), 1 – 35.
- Schneider, U., “Concrete at high temperatures – A general Review,” *Fire Safety Journal*,
1988, 13(1), 55-68.
- Slate, F.O., Hover K.C., “Microcracking in concrete. In: Carpinteri A., Ingraffea A.R. (eds)
Fracture mechanics of concrete: Material characterization and testing”,
Engineering Application of Fracture Mechanics, vol 3. Springer, 1984, Dordrecht.
https://doi.org/10.1007/978-94-009-6149-4_5
- Slate, F. O., and Olsefski, S., "X-Rays for Study of Internal Structure and Microcracking
of Concrete," *ACI Journal Proceedings*, V. 60, No. 5, 1963, pp. 575-588
- Soltani, A., Khoso, S., Keerio, M.A., and Formisano, A., “Assessment of Physical and
Mechanical Properties of Concrete Produced from Various Portland Cement
Brands,” *Open J. Compos. Mater.*, 2019, doi: 10.4236/ojcm.2019.94020.
- Tomasz, D., Wioletta, J.R., Mariusz, T., Artur, K., Jerzy, G., and Ritoldas, S., “Effects of
High Temperatures on the Properties of High-Performance Concrete (HPC),”
Procedia Engineering, 2017, 172, 256-263.

- Tvergaard, V., Hutchinson, J.W., “Microcracking in Ceramics Induced by Thermal Expansion or Elastic Anisotropy”, *Journal of the American Ceramic Society*, First published: March 1988, <https://doi.org/10.1111/j.1151-2916.1988.tb05022.x>
- U. S. Green Building Council, 2008, "LEED 2009 for New Construction and Major Renovations Rating System." U.S. Green Building Council.
- Khoso, S., Raad, J., and Parvin, A., “Experimental Investigation on the Properties of Recycled Concrete Using Hybrid Fibers,” *Open J. Compos. Mater.*, 2019, doi: 10.4236/ojcm.2019.92009.
- Khoso, S., Khan, J.S., Ansari, A.A., Khaskheli, Z.A., “Experimental Investigation on the Properties of Cement Concrete Partially Replaced by Silica Fume and Fly Ash,” *Int. J. Appl. Eng. Sci.*, vol. 14, no. 3, pp. 345–350, 2016.
- Kodur, V. R., and Harmathy, T. Z., “Properties of building materials,” in *SFPE Handbook of Fire Protection Engineering*, P. J. DiNenno, Ed., National Fire Protection Association, Quincy, Mass, USA, 2008.
- Vasylevskyi, K., Drach, B., and Tsukrov, I., “On micromechanical modeling of orthotropic solids with parallel cracks” *International Journal of Solids and Structures*, 2018, 144–145, 46–58.
- Vu, G., Timothy, J.J., Iskhakov, T., Meschke, G., “Multiscale modeling of distributed microcracking in concrete” *Proceedings in Applied Mathematics and Mechanics : PAMM* Volume: 20 Issue 1 (2021) ISSN: 1617-7061 Online ISSN: 1617-7061

- Tang, W. C., and Lo, T. Y., “Mechanical and fracture properties of normal-and high-strength concretes with fly ash after exposure to high temperatures,” *Magazine of Concrete Research*, 2009, 61(5), 323–330.
- Walsh, J. B., “The Effect of Cracks on the Compressibility of Rocks,” *Journal of Geophysical Research*, 1965, 70(2), 381-389.
- Workman, G. Moore, O. P., “Nondestructive Testing Handbook 10. Overview: Columbus,” *American Society of Nondestructive Testing*, 2012.
- Xia, Z., Zhou, C., Yong, Q., and Wang, X., On selection of repeated unit cell model and application of unified periodic boundary conditions in micro-mechanical analysis of composites,” *International Journal of Solids and Structures*, (2006) 43(2), 266-278.
- Xia, Zihui, Zhang, Yunfa, and Ellyin, Fernand. “A unified boundary conditions for representative volume elements of Composites and Applications” *International Journal of Solids and Structures*, 2013, 40 (2003), 1907-1921.
- Ye, Fan, and Wang, Hu, “A simple Python Code for Computing Effective Properties of 2D and 3D Representative Volume Element under Periodic Boundary Conditions,” *State Key Laboratory of Advanced Design and Manufacturing for Vehicle Body, Hunan University, Changsha 410082, P.R. China*, 2015.
- Yucel, Adil, and Arpaci, Alaeddin, “Free and forced vibration analyses of ship structures using the finite element method”, *J Mar Sci Technol*, 2013. 18:324–338, DOI 10.1007/s00773-012-0210-1.

- Zega, C.J., and Maio, A.A.D., “Recycled Concrete Exposed to High Temperatures,” *Magazine of Concrete Research*, December 2006, 58(10), 675-682.
- Zhao, H., Liu, F., and yang, H., (2020), “Residual Compressive Response of Concrete produced with Both Coarse and Fine Recycled Concrete Aggregates after Thermal Exposure,” *Journal of Construction and Building materials*, 244(2020),
- Zhou, X. Y., Gosling, P. D., Pearce, C. J., Ullah, Z., & Kaczmarczyk, L. (2015). Perturbation-based stochastic multi-scale computational homogenization method for woven textile composites. *International Journal of Solids & Structures*, 80, 368-380.
- Zhu, Qizhi, Kondo, Djimedo, Shao, Jianfu, and Pensee, Vincent, “Micromechanical modelling of anisotropic damage in brittle rocks and application,” *International Journal of Rock Mechanics and Mining Sciences*, 2008, 45(4), 467–477.

Appendix A

Experimentally Obtained Air Permeability Index (API) Results

Tables A1 and A2 below show the experimental results obtained for Air Permeability Index for undamaged specimens and specimens damaged at 300 °C respectively. The results shown are for all the specimens with different percentages of fly ash used i.e., 40 percent and 60 percent for both normal strength and higher strength concrete mixtures.

Table A1: Air Permeability Index Calculations for Undamaged Specimens

Specimen	P ₀	P ₁	Δt ₁		P ₀	P ₁	Δt ₂		D	H	Area	P ₀	P ₁	Δt ₁	API ₁	P ₀	P ₁	Δt ₂	API ₂	API
	inHg vac	inHg vac	min	sec	inHg vac	inHg vac	min	sec	mm	mm	cm ²	kPa	kPa	s	m ² /s	kPa	kPa	s	m ² /s	m ² /s
NF40-41A	23	20	1	9	23	20	1	24	102.27	24.10	82.1	23.438	33.597	69.0	2.58E-06	23.4	33.6	84.0	2.12E-06	2.35E-06
NF40-42A	23	20	0	16.00	23	20	0	51.00	101.77	48.93	81.3	23.438	33.597	16.0	2.28E-05	23.4	33.6	51.0	7.16E-06	1.50E-05
NF40-51A	23	20	0	5.00	23	20	0	15.00	102.07	22.37	81.8	23.438	33.597	5.0	3.32E-05	23.4	33.6	15.0	1.11E-05	2.21E-05
NF40-52A	23	20	0	7.00	23	20	0	31.00	101.87	50.47	81.5	23.438	33.597	7.0	5.37E-05	23.4	33.6	31.0	1.21E-05	3.29E-05
HF40-41A	23	20	0	8.00	23	20	0	23.00	102.70	24.90	82.8	23.438	33.597	8.0	2.28E-05	23.4	33.6	23.0	7.93E-06	1.54E-05
HF40-42A	23	20	0	8.00	23	20	0	48.00	101.40	50.17	80.8	23.438	33.597	8.0	4.71E-05	23.4	33.6	48.0	7.86E-06	2.75E-05
HF40-51A	23	20	0	8.00	23	20	0	35.00	102.60	25.60	82.7	23.438	33.597	8.0	2.35E-05	23.4	33.6	35.0	5.37E-06	1.44E-05
HF40-52A	23	20	0	8.00	23	20	1	0.00	101.40	47.00	80.8	23.438	33.597	8.0	4.42E-05	23.4	33.6	60.0	5.89E-06	2.50E-05
NF60-41A	23	20	0	10.00	23	20	0	32.00	102.50	23.40	82.5	23.438	33.597	10.0	1.72E-05	23.4	33.6	32.0	5.38E-06	1.13E-05
NF60-42A	23	20	0	8.00	23	20	0	50.00	102.17	48.20	82.0	23.438	33.597	8.0	4.46E-05	23.4	33.6	50.0	7.14E-06	2.59E-05
NF60-51A	23	20	0	9.00	23	20	0	23.00	102.87	23.80	83.1	23.438	33.597	9.0	1.93E-05	23.4	33.6	23.0	7.56E-06	1.34E-05
NF60-52A	23	20	0	8.00	23	20	0	58.00	102.47	48.33	82.5	23.438	33.597	8.0	4.45E-05	23.4	33.6	58.0	6.13E-06	2.53E-05
HF60-41A	23	20	0	8.00	23	20	0	24.00	101.30	23.60	80.6	23.438	33.597	8.0	2.22E-05	23.4	33.6	24.0	7.41E-06	1.48E-05
HF60-42A	23	20	0	6.00	23	20	0	24.00	102.00	44.87	81.7	23.438	33.597	6.0	5.55E-05	23.4	33.6	24.0	1.39E-05	3.47E-05
HF60-51A	23	20	0	8.00	23	20	0	35.00	103.60	22.33	84.3	23.438	33.597	8.0	2.01E-05	23.4	33.6	35.0	4.59E-06	1.23E-05
HF60-52A	23	20	0	6.00	23	20	0	41.00	102.70	46.13	82.8	23.438	33.597	6.0	5.63E-05	23.4	33.6	41.0	8.24E-06	3.23E-05

Table A2: Air Permeability Index Calculations for Specimens Damaged at 300 °C

Specimen	P ₀	P ₁	Δt ₁		P ₀	P ₁	Δt ₂		D	H	Area	P ₀	P ₁	Δt ₁	API_1	P ₀	P ₁	Δt ₂	API_2	API
	inHg vac	inHg vac	min	sec	inHg vac	inHg vac	min	sec	mm	mm	cm ²	kPa	kPa	s	m ² /s	kPa	kPa	s	m ² /s	m ² /s
NF40-7(1Ca)	23	20	0	9.00	23	20	0	12.00	102.30	25.00	82.2	23.438	33.597	9.0	2.05E-05	23.4	33.6	12.00	1.54E-05	1.79E-05
NF40-7(2Ca)	23	20	0	12.00	23	20	0	19.00	102.07	45.00	81.8	23.438	33.597	12.0	2.78E-05	23.4	33.6	19.00	1.76E-05	2.27E-05
NF40-7(2Cb)	23	20	0	8.00	23	20	0	13.00	101.50	49.97	80.9	23.438	33.597	8.0	4.69E-05	23.4	33.6	13.00	2.88E-05	3.78E-05
NF40-7(1Cb)	23	20	0	6.00	23	20	0	11.00	101.10	24.97	80.3	23.438	33.597	6.0	3.15E-05	23.4	33.6	11.00	1.72E-05	2.43E-05
HF40-7(1Ca)	23	20	0	5.00	23	20	0	8.00	101.60	24.00	81.1	23.438	33.597	5.0	3.59E-05	23.4	33.6	8.00	2.25E-05	2.92E-05
HF40-7(2Ca)	23	20	0	7.00	23	20	0	14.00	101.50	47.30	80.9	23.438	33.597	7.0	5.07E-05	23.4	33.6	14.00	2.53E-05	3.80E-05
HF40-7(2Cb)	23	20	0	7.00	23	20	0	14.00	101.40	45.87	80.8	23.438	33.597	7.0	4.92E-05	23.4	33.6	14.00	2.46E-05	3.69E-05
HF40-7(1Cb)	23	20	0	5.00	23	20	0	8.00	101.00	23.33	80.1	23.438	33.597	5.0	3.54E-05	23.4	33.6	8.00	2.21E-05	2.87E-05
NF60-7(1Ca)	23	20	0	8.00	23	20	0	11.00	100.90	26.33	80.0	23.438	33.597	8.0	2.50E-05	23.4	33.6	11.00	1.82E-05	2.16E-05
NF60-7(2Ca)	23	20	0	6.00	23	20	0	10.00	101.20	46.07	80.4	23.438	33.597	6.0	5.79E-05	23.4	33.6	10.00	3.48E-05	4.63E-05
NF60-7(2Cb)	23	20	0	8.00	23	20	0	13.00	102.23	49.47	82.1	23.438	33.597	8.0	4.57E-05	23.4	33.6	13.00	2.81E-05	3.69E-05
NF60-7(1Cb)	23	20	0	5.00	23	20	0	8.00	102.67	24.47	82.8	23.438	33.597	5.0	3.59E-05	23.4	33.6	8.00	2.24E-05	2.92E-05
HF60-7(1Ca)	23	20	0	9.00	23	20	0	12.00	103.00	24.40	83.3	23.438	33.597	9.0	1.97E-05	23.4	33.6	12.00	1.48E-05	1.73E-05
HF60-7(2Ca)	23	20	0	6.00	23	20	0	9.00	102.10	47.93	81.9	23.438	33.597	6.0	5.92E-05	23.4	33.6	9.00	3.95E-05	4.94E-05
HF60-7(2Cb)	23	20	0	10.00	23	20	0	13.00	101.70	48.20	81.2	23.438	33.597	10.0	3.60E-05	23.4	33.6	13.00	2.77E-05	3.19E-05
HF60-7(1Cb)	23	20	0	7.00	23	20	0	10.00	101.00	25.23	80.1	23.438	33.597	7.0	2.73E-05	23.4	33.6	10.00	1.91E-05	2.32E-05

Appendix B

Statistical Analysis Results

The following section presents the statistical analysis results conducted using ANOVA single factor of the undamaged and damaged groups of specimens at elevated temperature of 300 °C.

**Anova: Single Factor
for 300 °C
Temperature**

SUMMARY

<i>Groups</i>	<i>Count</i>	<i>Sum</i>	<i>Average</i>	<i>Variance</i>
Undamaged Group	4	0.000242	6.06E-05	1.77E-10
Damaged Group	4	0.000249	6.22E-05	2.59E-11

ANOVA

<i>Source of Variation</i>	<i>SS</i>	<i>df</i>	<i>MS</i>	<i>F</i>	<i>P-value</i>	<i>F crit</i>
Between Groups	5.36E-12	1	5.36E-12	0.053	0.826	5.987
Within Groups	6.10E-10	6	1.02E-10			
Total	6.15E-10	7				

SINGLE FACTOR ANOVA RESULTS

ANOVA: Single Factor

Dynamic Elastic Young's Modulus E_d

C-Specimens Before Damage

SUMMARY

Groups	Count	Sum	Average	Variance
HF40	4	136.539	34.135	63.084
HF60	4	63.567	15.892	82.691
NF40	4	70.104	17.526	2.369
NF60	4	70.184	17.546	40.516

ANOVA

Source of Variation	SS	df	MS	F	P-value	F crit
Between Groups	889.260	3	296.4200	6.2847	0.0083	3.4903
Within Groups	565.982	12	47.1651			
Total	1455.242	15				

C-Specimens After Damage at 300 °C

SUMMARY

Groups	Count	Sum	Average	Variance
HF40	4	21.266	5.317	1.162
HF60	4	16.898	4.224	1.000
NF40	4	13.555	3.389	1.990
NF60	4	17.604	4.401	1.531

ANOVA

Source of Variation	SS	df	MS	F	P-value	F crit
Between Groups	7.501	3	2.5004	1.7601	0.2082	3.4903
Within Groups	17.047	12	1.4206			
Total	24.5484	15				

Single Factor ANOVA, considering 300 °C temperature exposure

Effect of Temperature on Shear Modulus

SUMMARY

<i>Groups</i>	<i>Count</i>	<i>Sum</i>	<i>Average</i>	<i>Variance</i>
Change in Gd_ 300 C (1C)	2	14.653	7.326	1.93
Change in Gd 300 C (2C)	2	10.491	5.245	0.405

ANOVA

<i>Source of Variation</i>	<i>SS</i>	<i>df</i>	<i>MS</i>	<i>F</i>	<i>P-value</i>	<i>F crit</i>
Between Groups	4.330	1	4.33	3.705	0.194	18.512
Within Groups	2.337	2	1.168			
Total	6.66	3				

Single Factor ANOVA, considering 300 °C temperature exposure

Effect of Temperature on Crack Density Parameter

SUMMARY

<i>Groups</i>	<i>Count</i>	<i>Sum</i>	<i>Average</i>	<i>Variance</i>
Change in ϵ _ 300 C (1C)	2	-0.643	-0.321	7.5645E-05
Change in ϵ 300 C (2C)	2	-0.291	-0.145	0.000355

ANOVA

<i>Source of Variation</i>	<i>SS</i>	<i>df</i>	<i>MS</i>	<i>F</i>	<i>P-value</i>	<i>F crit</i>
Between Groups	0.031	1	0.031	144.025	0.0068	18.512
Within Groups	0.0004	2	0.0002			
Total	0.031	3				

Appendix C

Results for Crack Density Parameter and Young's Modulus obtained using Hudson's Extended Model and O'Connell and Budiansky Model

This section presents the results of crack density parameter and Young's modulus for normal strength and high strength concrete using Hudson's Model and O'Connell and Budiansky Model for two points as well as five points which could be seen in the tables below. Both models were used to compare the results obtained using different fly ash proportions for undamaged and damaged specimens at 300 °C.

Table C1: Results of CDP and Young's modulus for Control Normal and High Strength Concrete using Hudson's Model for two points

Control Specimens Undamaged with No-Fly Ash				
-	Input - G_d (GPa)		Output	
Specimen - ID	skd	dry	ϵ	E_0 (GPa)
NC-4-1A	13.967	14.721	0	35.860
NC-4-2A	12.890	9.2531	0.462	33.439
NC-5-1A	12.849	10.261	0.333	32.972
NC-5-2A	13.602	11.907	0.209	34.589
NC-6-1A	13.135	10.184	0.371	33.835
NC-6-2A	11.207	9.551	0.243	28.489
HC-4-1A	14.260	12.010	0.265	36.467
HC-4-2A	15.060	12.670	0.268	38.569
HC-5-1A	15.219	11.924	0.363	39.340
HC-5-2A	14.423	12.469	0.228	36.774
HC-6-1A	15.829	11.197	0.488	41.488
HC-6-2A	14.754	12.464	0.262	37.747

Table C2: Results of CDP and Young's modulus for Normal and High Strength Concrete using Hudson's Model for two points

-	Before Damage				After Damage				EXP-SKD-DRY			
	Input - G_d (GPa)		Output		Input - G_d		Output		Input - G_d		Output	
	ID	skd	dry	ϵ	E_0 (GPa)	skd*	dry*	ϵ	E_0 (GPa)	skd'	dry'	ϵ
NF40-7-1CA	7.623	4.162	0.709	19.739	0.799	0.771	0.054	1.998	0.799	0.684	0.217	2.000
NF40-7-2CA	6.763	5.079	0.392	17.195	0.712	1.246	0.000	2.448	0.712	1.336	0.000	2.560
NF40-7-2CB	6.766	6.312	0.107	16.992	2.002	1.693	0.235	5.019	2.002	1.669	0.253	5.021
NF40-7-1CB	4.417	8.525	0.000	16.178	1.018	2.254	0.000	4.090	1.018	0.870	0.220	2.550
NF60-7-1CA	4.352	4.102	0.089	10.906	1.099	1.030	0.096	2.749	1.099	1.139	0.000	2.798
NF60-7-2CA	6.502	5.161	0.325	16.475	1.700	1.194	0.452	4.272	1.700	1.432	0.240	4.262
NF60-7-2CB	6.494	4.430	0.498	16.576	2.238	1.223	0.689	5.651	2.238	1.703	0.364	5.624
NF60-7-1CB	8.465	12.517	0.000	26.228	1.957	1.151	0.625	4.932	1.957	1.538	0.326	4.913
HF40-7-1CA	10.217	8.700	0.242	25.934	1.383	2.022	0.000	4.256	1.383	2.012	0.000	4.243
HF40-7-2CA	11.494	8.435	0.433	29.639	2.058	2.045	0.009	5.145	2.058	2.006	0.038	5.147
HF40-7-2CB	16.713	12.228	0.452	43.738	2.721	2.489	0.131	6.819	2.721	2.717	0.000	6.797
HF40-7-1CB	14.751	13.805	0.109	37.229	1.471	2.566	0.000	5.047	1.471	2.447	0.000	4.898
HF60-7-1CA	3.713	4.007	0.000	9.650	1.426	0.551	0.925	3.595	1.426	0.930	0.527	3.582
HF60-7-2CA	1.135	5.673	0.000	8.509	1.268	1.008	0.311	3.178	1.268	1.214	0.065	3.171
HF60-7-2CB	6.789	5.777	0.236	17.145	1.930	1.693	0.187	4.836	1.930	2.007	0.000	4.922
HF60-7-1CB	10.896	7.272	0.535	28.263	1.977	2.254	0.000	5.289	1.977	2.161	0.000	5.173

Table C3: Results of CDP and Young's modulus for Control specimens using Hudson's

Model for two points

-	Input - G_d (GPa)		Output		
	ID	skd	dry	ϵ	E_0 (GPa)
	HF40-4-1A	8.464	7.364	0.2094	21.3952
	HF40-4-2A	12.068	10.069	0.2734	30.7848
	HF40-5-1A	10.274	7.096	0.4968	26.5253
	HF40-5-2A	12.481	8.075	0.5722	32.6372
	HF40-6-1A	9.242	7.154	0.3631	23.5976
	HF40-6-2A	13.738	10.540	0.3859	35.4760
	HF60-4-1A	8.085	7.575	0.1019	20.3167
	HF60-4-2A	8.119	5.266	0.5547	20.8914
	HF60-5-1A	5.455	4.899	0.1603	13.7140
	HF60-5-2A	8.371	8.570	0.0000	21.1753
	HF60-6-1A	6.791	5.669	0.2619	17.1695
	HF60-6-2A	7.124	7.496	0.0000	18.2749
	NF40-4-1A	4.318	3.198	0.4013	10.9161
	NF40-4-2A	4.982	6.272	0.0000	14.0670
	NF40-5-1A	2.893	3.195	0.0000	7.6102
	NF40-5-2A	5.511	5.297	0.0612	13.8065
	NF40-6-1A	4.191	4.382	0.0000	10.7155
	NF40-6-2A	4.299	5.078	0.0000	11.7221
	NF60-4-1A	5.094	4.547	0.1683	12.8046
	NF60-4-2A	7.681	6.678	0.2090	19.3973
	NF60-5-1A	6.660	9.241	0.0000	19.8761
	NF60-5-2A	8.106	6.440	0.3281	20.6077
	NF60-6-1A	4.923	4.641	0.0896	12.3409
	NF60-6-2A	7.144	5.707	0.3188	18.1189

Table C4: Results of CDP and Young's modulus for damaged specimens using Hudson's

Model for five points

ID	Input - G_d (GPa)					Output			
	skd	dry	dry*	skd'	dry'	ϵ_1	ϵ_2	ϵ_3	E_0 (GPa)
NF40-7-1CA	7.623	4.162	0.771	0.799	0.684	0.709	1.354	1.370	19.739
NF40-7-2CA	6.763	5.079	1.246	0.712	1.336	0.392	1.228	1.209	17.195
NF40-7-2CB	6.766	6.312	1.693	2.002	1.669	0.107	1.126	1.132	16.992
NF40-7-1CB	4.417	8.525	2.254	1.018	0.870	0.000	0.978	1.298	16.178
NF60-7-1CA	4.352	4.102	1.030	1.099	1.139	0.089	1.146	1.108	10.906
NF60-7-2CA	6.502	5.161	1.194	1.700	1.432	0.325	1.228	1.174	16.475
NF60-7-2CB	6.494	4.430	1.223	2.238	1.703	0.498	1.223	1.115	16.576
NF60-7-1CB	8.465	12.517	1.151	1.957	1.538	0.000	1.335	1.280	26.228
HF40-7-1CA	10.217	8.700	2.022	1.383	2.012	0.242	1.208	1.209	25.934
HF40-7-2CA	11.494	8.435	2.045	2.058	2.006	0.433	1.241	1.246	29.639
HF40-7-2CB	16.713	12.228	2.489	2.721	2.717	0.452	1.287	1.267	43.738
HF40-7-1CB	14.751	13.805	2.566	1.471	2.447	0.109	1.242	1.254	37.229
HF60-7-1CA	3.713	4.007	0.551	1.426	0.930	0.000	1.286	1.139	9.650
HF60-7-2CA	1.135	5.673	1.008	1.268	1.214	0.000	1.056	0.965	8.509
HF60-7-2CB	6.789	5.777	1.693	1.930	2.007	0.236	1.130	1.061	17.145
HF60-7-1CB	10.896	7.272	2.254	1.977	2.161	0.535	1.201	1.213	28.263

Table C5: Results of CDP and Young's modulus for Control, Normal and High Strength Concrete using O'Connell and Budiansky Model for two points

Control Specimens Undamaged No Fly Ash				
-	Input - G_d		Output	
ID	skd	dry	ϵ	E_0 (GPa)
NC-4-1A	13.967	14.721	0	30.930
NC-4-2A	12.890	9.2531	0.286	43.003
NC-5-1A	12.849	10.261	0.230	40.316
NC-5-2A	13.602	11.907	0.164	39.830
NC-6-1A	13.135	10.184	0.248	41.993
NC-6-2A	11.207	9.551	0.186	33.555
HC-4-1A	14.260	12.010	0.195	43.095
HC-4-2A	15.060	12.670	0.195	45.549
HC-5-1A	15.219	11.924	0.242	48.340
HC-5-2A	14.423	12.469	0.174	42.688
HC-6-1A	15.829	11.197	0.293	53.194
HC-6-2A	14.754	12.464	0.192	44.480

Table C6: Results of CDP and Young's modulus for damaged specimens using O'Connell and Budiansky Model for five points

-	Input - G_d					Output				
	ID	skd	dry	dry*	skd'	dry'	ϵ_1	ϵ_2	ϵ_3	G_0 (GPa)
NC-4-2B	14.699	11.284	1.548	7.698	6.134	0.253	0.402	0.523	18.908	47.270
NC-4-1B	17.589	11.221	4.552	7.713	7.036	0.333	0.422	0.473	24.745	61.863
NC-5-2B	16.422	11.628	2.250	8.087	7.631	0.292	0.390	0.513	22.064	55.159
NC-5-1B	16.229	12.576	2.863	6.904	8.312	0.248	0.362	0.496	20.758	51.895
NC-6-2B	11.963	10.761	2.042	8.040	8.779	0.139	0.227	0.490	13.669	34.172
NC-6-1B	15.873	12.298	3.501	7.058	6.928	0.248	0.393	0.479	20.305	50.763
HC-4-2B	15.070	12.792	1.783	8.458	8.982	0.189	0.310	0.515	18.105	45.262
HC-4-1B	16.822	17.073	3.145	8.854	8.028	-0.030	0.313	0.469	16.373	40.933
HC-5-2B	13.289	13.221	2.237	8.674	9.241	0.009	0.199	0.482	13.404	33.510
HC-5-1B	14.276	14.721	4.280	9.345	9.317	-0.068	0.196	0.405	13.432	33.579
HC-6-2B	13.374	13.183	2.246	9.614	8.843	0.025	0.225	0.483	13.690	34.224
HC-6-1B	14.670	13.287	5.804	9.249	8.353	0.133	0.307	0.389	16.650	41.625

Table C7: Results of CDP and Young's modulus for damaged specimens using
O'Connell and Budiansky Model for five points

Specimen		Input - G_d (GPa)					Output			
ID	skd	dry	dry*	skd'	dry'	ϵ_1	ϵ_2	ϵ_3	E_0 (GPa)	
NF40-7-1CA	7.623	4.162	0.771	0.799	0.684	0.379	0.534	0.530	28.301	
NF40-7-2CA	6.763	5.079	1.246	0.712	1.336	0.265	0.489	0.494	22.022	
NF40-7-2CB	6.766	6.312	1.693	2.002	1.669	0.101	0.453	0.451	18.609	
NF40-7-1CB	4.417	8.525	2.254	1.018	0.870	-0.374	0.471	0.314	11.554	
NF60-7-1CA	4.352	4.102	1.030	1.099	1.139	0.089	0.444	0.456	11.824	
NF60-7-2CA	6.502	5.161	1.194	1.700	1.432	0.234	0.478	0.492	20.481	
NF60-7-2CB	6.494	4.430	1.223	2.238	1.703	0.308	0.469	0.496	22.199	
NF60-7-1CB	8.465	12.517	1.151	1.957	1.538	-0.374	0.462	0.488	18.641	
HF40-7-1CA	10.217	8.700	2.022	1.383	2.012	0.186	0.483	0.482	30.610	
HF40-7-2CA	11.494	8.435	2.045	2.058	2.006	0.276	0.499	0.497	37.909	
HF40-7-2CB	16.713	12.228	2.489	2.721	2.717	0.277	0.503	0.508	55.207	
HF40-7-1CB	14.751	13.805	2.566	1.471	2.447	0.097	0.489	0.486	40.421	
HF60-7-1CA	3.713	4.007	0.551	1.426	0.930	-0.299	0.403	0.470	7.224	
HF60-7-2CA	1.135	5.673	1.008	1.268	1.214	-0.374	0.312	0.357	6.160	
HF60-7-2CB	6.789	5.777	1.693	1.930	2.007	0.187	0.442	0.461	20.351	
HF60-7-1CB	10.896	7.272	2.254	1.977	2.161	0.317	0.493	0.490	37.614	

Table C8: Results of CDP and Young's modulus using O'Connell and Budiansky's Model for two points

-	Before Damage				After Damage				EXP-SKD-DRY			
	Input - G_d (GPa)		Output		Input - G_d		Output		Input - G_d		Output	
	ID	skd	dry	ϵ	E_0 (GPa)	skd*	dry*	ϵ	E_0 (GPa)	skd'	dry'	ϵ
NF40-7-1CA	7.623	4.162	0.379	28.301	0.799	0.771	0.059	2.110	0.799	0.684	0.182	2.383
NF40-7-2CA	6.763	5.079	0.265	22.023	0.712	1.246	-0.375	1.744	0.712	1.336	-0.374	1.827
NF40-7-2CB	6.766	6.312	0.101	18.609	2.002	1.693	0.191	6.028	2.002	1.669	0.202	6.093
NF40-7-1CB	4.417	8.525	-0.374	11.554	1.018	2.254	-0.374	2.928	1.018	0.870	0.183	3.042
NF60-7-1CA	4.352	4.102	0.089	11.824	1.099	1.030	0.096	3.007	1.099	1.139	-0.083	2.550
NF60-7-2CA	6.502	5.161	0.234	20.481	1.700	1.194	0.296	5.734	1.700	1.432	0.194	5.136
NF60-7-2CB	6.494	4.430	0.308	22.199	2.238	1.223	0.379	8.305	2.238	1.703	0.258	7.231
NF60-7-1CB	8.465	12.517	-0.374	18.641	1.957	1.151	0.359	7.093	1.957	1.538	0.240	6.203
HF40-7-1CA	10.217	8.700	0.186	30.610	1.383	2.022	-0.374	3.024	1.383	2.012	-0.374	3.015
HF40-7-2CA	11.494	8.435	0.276	37.908	2.058	2.045	0.011	5.195	2.058	2.006	0.043	5.351
HF40-7-2CB	16.713	12.228	0.278	55.207	2.721	2.489	0.123	7.646	2.721	2.717	0.003	6.824
HF40-7-1CB	14.751	13.805	0.097	40.421	1.471	2.566	-0.374	3.598	1.471	2.447	-0.374	3.489
HF60-7-1CA	3.713	4.007	-0.299	7.224	1.426	0.551	0.445	5.741	1.426	0.930	0.325	4.969
HF60-7-2CA	1.135	5.673	-0.374	6.161	1.268	1.008	0.233	3.991	1.268	1.214	0.069	3.380
HF60-7-2CB	6.789	5.777	0.187	20.351	1.930	1.693	0.162	5.640	1.930	2.007	-0.092	4.445
HF60-7-1CB	10.896	7.272	0.317	37.614	1.977	2.254	-0.374	3.741	1.977	2.161	-0.374	3.655

Table C9: Results of CDP and Young's modulus for Control specimens using O'Connell and Budiansky's Model for two points

-	Input - G_d (GPa)		Output	
	ID	skd	dry	ϵ
HF40-4-1A	8.464	7.364	0.1692	24.9180
HF40-4-2A	12.068	10.069	0.2013	36.7285
HF40-5-1A	10.274	7.096	0.3031	34.9214
HF40-5-2A	12.481	8.075	0.3281	43.6507
HF40-6-1A	9.242	7.154	0.2485	29.5763
HF40-6-2A	13.738	10.540	0.2533	44.1941
HF60-4-1A	8.085	7.575	0.0961	22.1294
HF60-4-2A	8.119	5.266	0.3271	28.3636
HF60-5-1A	5.455	4.899	0.1408	15.6057
HF60-5-2A	8.371	8.570	-0.0498	20.0094
HF60-6-1A	6.791	5.669	0.2009	20.6598
HF60-6-2A	7.124	7.496	-0.1313	15.8696
NF40-4-1A	4.318	3.198	0.2715	14.1687
NF40-4-2A	4.982	6.272	-0.3742	9.9675
NF40-5-1A	2.893	3.195	-0.3742	5.3787
NF40-5-2A	5.511	5.297	0.0633	14.6154
NF40-6-1A	4.191	4.382	-0.1089	9.5152
NF40-6-2A	4.299	5.078	-0.3747	8.2929
NF60-4-1A	5.094	4.547	0.1465	14.6556
NF60-4-2A	7.681	6.678	0.1698	22.6269
NF60-5-1A	6.660	9.241	-0.3742	14.1099
NF60-5-2A	8.106	6.440	0.2333	25.5208
NF60-6-1A	4.923	4.641	0.0884	13.3727
NF60-6-2A	7.144	5.707	0.2300	22.4101

Appendix D

Detail of RVEs with Number of Cracks and their Co-ordinates using ABAQUS Computer Program

The following section presents the Geometry of RVE along with cracks modeled inside the selected RVEs with different orientations. The RVEs have been modeled starting with one crack and gradually increased till eight cracks. The details of crack co-ordinates have also been presented in the figures shown below. The modeling was carried out using ABAQUS computer program.

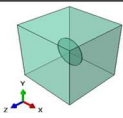
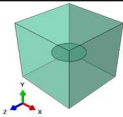
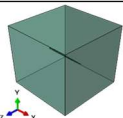
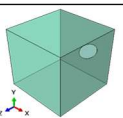
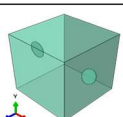
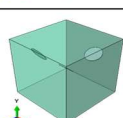
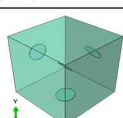
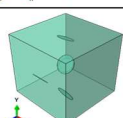
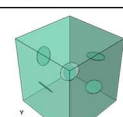
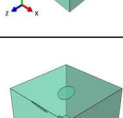
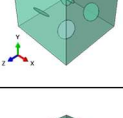
RVE Geometry	Cracks	Rotation	Co-ordinates
	-	(Degrees)	(x,y,z)
	1	0	50,50,50
	1	90	50,50,49.6
	1	45	50,50,49.5
	1	-60	150,150,50
	1	-30	150,150,50
	2	75	50,150,150
	1	45	50,50,50
	2	-60	150,150,50
	3	30	50,150,150
	1	30	150,150,50
	2	-50	50,150,150
	3	40	50,50,50
	4	-80	150,50,150
	1	25	150,50,150
	2	-35	150,150,150
	3	-55	50,50,50
	4	65	50,150,50
	5	40	50,50,150
	1	-25	50,50,50
	2	35	50,50,150
	3	-75	150,50,50
	4	80	150,150,50
	5	-30	50,150,150
	6	-60	150,150,150
	1	-20	50,50,50
	2	50	50,50,150
	3	-70	50,150,50
	4	40	50,150,150
	5	-40	150,50,50
	6	-55	150,50,150
	7	30	150,150,150
	1	30	50,50,50
	2	-65	50,50,150
	3	-40	50,150,50
	4	70	50,150,150
	5	-25	150,50,50
	6	45	150,50,150
	7	-85	150,150,150
	8	15	150,150,50

Figure D1: Crack position and orientation in multiple RVEs

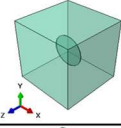
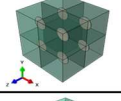
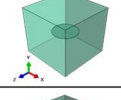
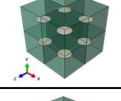
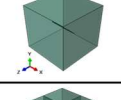
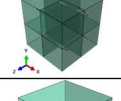
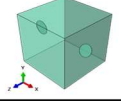
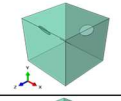
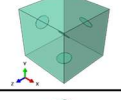
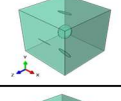
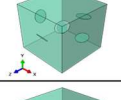
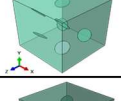
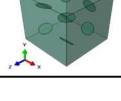
RVE Geometry	No. of Cracks in RVE	Dry condition			Soaked condition
		Mesh size	Elements	Simulation time	Elements
		microns	-	sec	-
	1	20	1286	131	1328
		15	2911	157	2984
		10	8333	319	8457
		5	54772	2349	54634
	8	20	10263	412	10649
		15	23395	745	23977
		10	66919	2932	67599
		20	1303	118	1350
	1	15	2911	162	2984
		10	8283	336	8523
		20	10646	254	10703
	8	15	23331	699	23756
		10	66725	2878	67531
		20	1306	140	1333
	1	15	2914	152	2961
		10	8086	304	8169
		20	10153	246	10433
	8	15	23044	689	23503
		10	64175	3582	65323
		10	45966	3552	46560
	2	10	51303	1510	50753
	3	10	55587	2180	54666
	4	10	58166	2574	58788
	5	10	58279	2396	59956
	6	10	61255	1991	62151
	7	10	63989	2459	65481
	8	10	66877	2816	67839

Figure D2: Crack position and orientation in bundled multiple RVEs

Appendix E

Detail of Elastic Properties of Different RVEs

This section presents elastic properties obtained for RVEs both in dry and saturated conditions. The results are obtained by modeling RVE with single crack up to eight cracks and the results have been presented in the tables given below.

Details of 100*100*100 micron³ RVE with single vertical crack

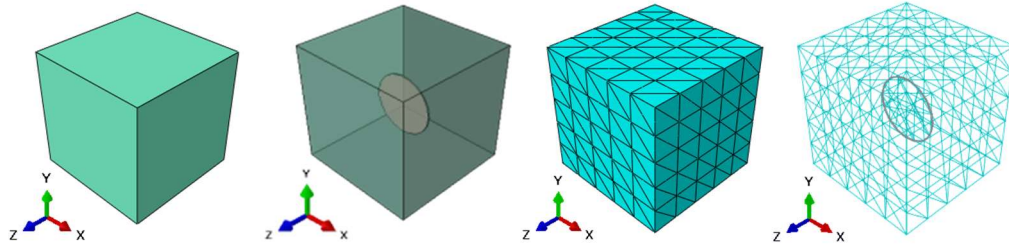


Table E1: Elastic properties for single vertical crack RVE obtained using EasyPBC plugin in Abaqus for dry crack condition.

DRY CRACKS

ONE RVE with Single Crack (Vertical crack parallel to x-axis)										
Case 1: One micron deep dry crack with 20-micron mesh size - 1286 elements - Process time 131 sec										
E_{11}	ν_{12}	ν_{13}	E_{22}	ν_{21}	ν_{23}	E_{33}	ν_{31}	ν_{32}	E_{avg}	E_{avg}
(MPa)	-	-	(MPa)	-	-	(MPa)	-	-	(MPa)	(GPa)
39918.56	0.250	0.250	39918.56	0.250	0.250	37389.42	0.234	0.234	39075.51	39.08
Case 2: One micron deep dry crack with 15-micron mesh size - 2911 elements - Process time 156 sec										
39918.28	0.250	0.250	39918.29	0.250	0.250	37298.08	0.234	0.234	39044.88	39.04
Case 3: One micron deep dry crack with 10-micron mesh size - 8333 elements - Process time 319 sec										
39917.08	0.250	0.250	39917.84	0.250	0.250	37132.09	0.233	0.233	38989.01	38.99

Table E2: Elastic properties for single vertical crack RVE obtained using EasyPBC plugin in Abaqus for soaked crack condition.

SATURATEDCRACKS										
ONE RVE with Single Crack (Vertical crack parallel to x-axis)										
Case 1: One micron deep Wet crack with 20-micron mesh size - 1328 elements - Process time 112 sec										
E₁₁ (MPa)	v₁₂	v₁₃	E₂₂ (MPa)	v₂₁	v₂₃	E₃₃ (MPa)	v₃₁	v₃₂	E_{avg} (MPa)	E_{avg} (GPa)
39919.17	0.250	0.251	39919.19	0.250	0.251	39160.12	0.246	0.246	39666.16	39.67
Case 2: One micron deep Wet crack with 15-micron mesh size - 2984 elements - Process time 739 sec										
39918.82	0.250	0.251	39918.81	0.250	0.251	39135.97	0.246	0.246	39657.87	39.66
Case 3: One micron deep Wet crack with 10-micron mesh size - 8457 elements - Process time 706 sec										
39918.36	0.250	0.251	39918.34	0.250	0.251	39097.08	0.246	0.246	39644.60	39.64

Table E3: Shear modulus results for single vertical crack RVE obtained using EasyPBC plugin in Abaqus for dry crack condition.

DRY CRACKS				
RVE with Single Crack (Vertical crack parallel to x-axis)				
G₁₂	G₁₃ (MPa)	G₂₃	E_{avg} (MPa)	E_{avg} (GPa)
20-micron mesh				
15967.498	15453.206	15453.792	15624.832	15.625
15-micron mesh				
15967.413	15429.343	15430.322	15609.026	15.609
10-micron mesh				
15967.245	15393.952	15394.370	15585.189	15.585

Table E4: Shear modulus results for single vertical crack RVE obtained using EasyPBC plugin in Abaqus for dry crack condition.

SATURATED CRACKS				
RVE with Single Crack (Vertical crack parallel to x-axis)				
G₁₂	G₁₃ (MPa)	G₂₃	E_{avg} (MPa)	E_{avg} (GPa)
20-micron mesh				
15967.601	15485.741	15487.403	15646.915	15.647
15-micron mesh				
15967.484	15457.868	15458.967	15628.106	15.628
10-micron mesh				
15967.335	15428.791	15428.100	15608.075	15.608

Details of 100*100*100 micron³ RVE with single Horizontal crack

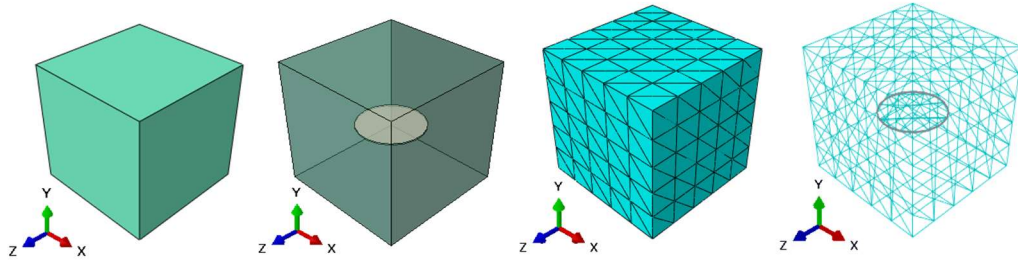


Table E5: Elastic properties for single horizontal crack RVE obtained using EasyPBC plugin in Abaqus for dry crack condition.

DRY CRACKS										
ONE RVE with Single Crack (Horizontal crack parallel to z-axis)										
Case 1: One micron deep dry crack with 20-micron mesh size - 1303 elements - Process time 118 sec										
E₁₁ (MPa)	v₁₂	v₁₃	E₂₂ (MPa)	v₂₁	v₂₃	E₃₃ (MPa)	v₃₁	v₃₂	E_{avg} (MPa)	E_{avg} (GPa)
39918.54	0.250	0.250	37381.92	0.234	0.234	39918.54	0.250	0.250	39073.00	39.073
Case 2: One micron deep dry crack with 15-micron mesh size - 2911 elements - Process time 163 sec										
39918.26	0.250	0.250	37286.35	0.234	0.234	39918.26	0.250	0.250	39040.96	39.041
Case 3: One micron deep dry crack with 10-micron mesh size - 8283 elements - Process time 336 sec										
39917.81	0.250	0.250	37136.56	0.233	0.233	39917.80	0.250	0.250	38990.72	38.991

Table E6: Elastic properties for single horizontal crack RVE obtained using EasyPBC plugin in Abaqus for saturated crack condition.

SATURATEDCRACKS										
ONE RVE with Single Crack (Horizontal crack parallel to z-axis)										
Case 1: One micron deep Wet crack with 20-micron mesh size - 1350 elements - Process time 114 sec										
E₁₁ (MPa)	v₁₂	v₁₃	E₂₂ (MPa)	v₂₁	v₂₃	E₃₃ (MPa)	v₃₁	v₃₂	E_{avg} (MPa)	E_{avg} (GPa)
39919.16	0.251	0.250	39158.36	0.246	0.246	39919.12	0.250	0.251	39665.54	39.666
Case 2: One micron deep Wet crack with 15-micron mesh size - 2984 elements - Process time 150 sec										
39918.87	0.251	0.250	39142.36	0.246	0.246	39918.88	0.250	0.251	39660.04	39.660
Case 3: One micron deep Wet crack with 10-micron mesh size - 8523 elements - Process time 295 sec										
39918.34	0.251	0.250	39097.04	0.246	0.246	39918.36	0.250	0.251	39644.58	39.645

Table E7: Shear modulus results for single horizontal crack RVE obtained using EasyPBC plugin in Abaqus for dry crack condition.

DRY CRACKS				
RVE with Single Crack (Horizontal crack parallel to z-axis)				
G₁₂	G₁₃	G₂₃	E_{avg}	E_{avg}
	(MPa)		(MPa)	(GPa)
20-micron mesh				
15453.95	15967.494	15454.119	15625.188	15.625
15-micron mesh				
15429.996	15967.396	15429.85	15609.081	15.609
10-micron mesh				
15394.315	15967.236	15394.135	15585.229	15.585

Table E8: Shear modulus results for single horizontal crack RVE obtained using EasyPBC plugin in Abaqus for saturated crack condition.

SATURATED CRACKS				
RVE with Single Crack (Horizontal crack parallel to z-axis)				
G₁₂	G₁₃	G₂₃	E_{avg}	E_{avg}
	(MPa)		(MPa)	(GPa)
20-micron mesh				
15483.79	15967.584	15484.454	15645.276	15.645
15-micron mesh				
15462.864	15967.504	15464.384	15631.584	15.632
10-micron mesh				
15427.202	15967.336	15428.171	15607.570	15.608

Details of 100*100*100 micron³ RVE with single Inclined 45-degree crack

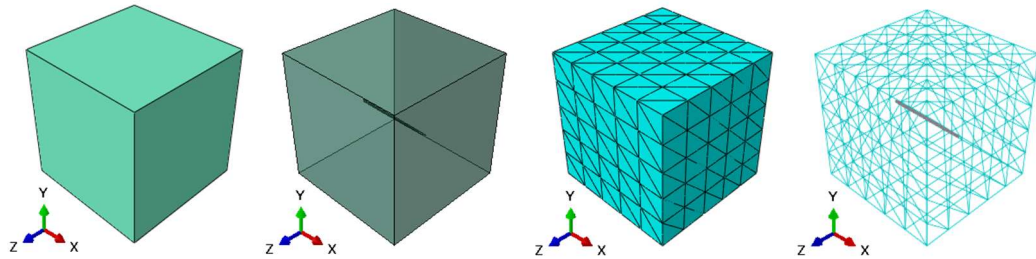


Table E9: Elastic properties for single horizontal crack RVE obtained using EasyPBC plugin in Abaqus for dry crack condition.

DRY CRACKS										
ONE RVE with Single Crack (Inclined 45-degree crack)										
Case 1: One micron deep dry crack with 20-micron mesh size - 1306 elements - Process time 140 sec										
E₁₁ (MPa)	v₁₂	v₁₃	E₂₂ (MPa)	v₂₁	v₂₃	E₃₃ (MPa)	v₃₁	v₃₂	E_{avg} (MPa)	E_{avg} (GPa)
39918.49	0.250	0.250	38506.53	0.241	0.244	38497.83	0.241	0.244	38974.29	38.97
Case 2: One micron deep dry crack with 15-micron mesh size - 2914 elements - Process time 152 sec										
39918.33	0.250	0.250	38449.13	0.241	0.254	38459.44	0.241	0.244	38942.30	38.94
Case 3: One micron deep dry crack with 10-micron mesh size - 8086 elements - Process time 304 sec										
39917.83	0.250	0.250	38363.38	0.240	0.244	38360.66	0.240	0.244	38880.62	38.88

Table E10: Elastic properties for single horizontal crack RVE obtained using EasyPBC plugin in Abaqus for saturated crack condition.

SATURATED CRACKS										
ONE RVE with Single Crack (Inclined 45-degree crack)										
Case 1: One micron deep wet crack with 20-micron mesh size - 1333 elements - Process time 110 sec										
E₁₁ (MPa)	v₁₂	v₁₃	E₂₂ (MPa)	v₂₁	v₂₃	E₃₃ (MPa)	v₃₁	v₃₂	E_{avg} (MPa)	E_{avg} (GPa)
39919.15	0.250	0.250	39003.99	0.245	0.258	39008.48	0.245	0.258	39310.53	39.31
Case 2: One micron deep wet crack with 15-micron mesh size - 2961 elements - Process time 150 sec										
39918.85	0.250	0.250	38973.42	0.244	0.259	38973.82	0.244	0.259	39288.70	39.29
Case 3: One micron deep wet crack with 10-micron mesh size - 8169 elements - Process time 303 sec										
39918.40	0.250	0.250	38919.69	0.244	0.259	38920.48	0.244	0.259	39252.86	39.25

Table E11: Shear modulus results for single inclined 45-degree crack RVE obtained using EasyPBC plugin in Abaqus for dry crack condition.

DRY CRACKS				
RVE with Single Crack (Inclined 45-degree crack)				
G₁₂	G₁₃	G₂₃	E_{avg}	E_{avg}
	(MPa)		(MPa)	(GPa)
20-micron mesh				
15709.828	15709.782	15531.200	15650.270	15.650
15-micron mesh				
15700.59	15700.671	15513.512	15638.258	15.638
10-micron mesh				
15682.179	15682.143	15485.795	15616.706	15.617

Table E12: Shear modulus results for single inclined 45-degree crack RVE obtained using EasyPBC plugin in Abaqus for saturated crack condition.

SATURATED CRACKS				
RVE with Single Crack (Inclined 45-degree crack)				
G₁₂	G₁₃	G₂₃	E_{avg}	E_{avg}
	(MPa)		(MPa)	(GPa)
20-micron mesh				
15725.096	15724.979	15834.544	15761.540	15.762
15-micron mesh				
15714.272	15714.176	15831.299	15753.249	15.753
10-micron mesh				
15699.65	15699.671	15823.914	15741.078	15.741

Details of 200*200*200 micron³ RVE with eight vertical cracks

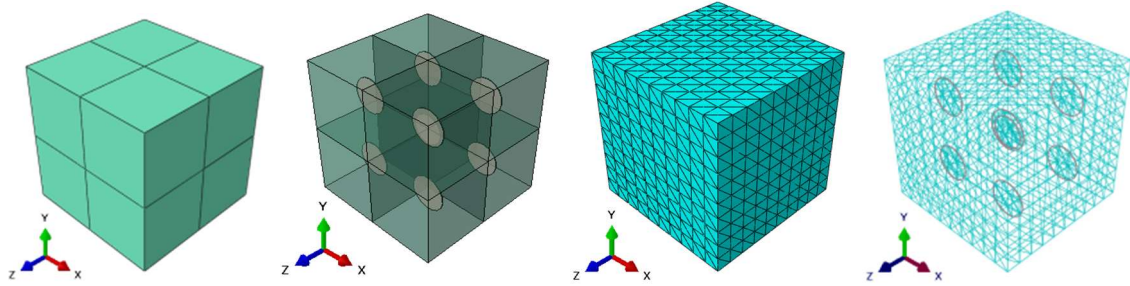


Table E13: Elastic properties for eight vertical crack RVE obtained using EasyPBC plugin in Abaqus for dry crack condition.

DRY CRACKS

Eight RVEs with 8 Cracks (Vertical parallel to x-axis) - One crack in each single RVE										
Case 1: One micron deep dry crack with 20-micron mesh - 10263 elements - Process time 412 sec										
E₁₁ (MPa)	v₁₂	v₁₃	E₂₂ (MPa)	v₂₁	v₂₃	E₃₃ (MPa)	v₃₁	v₃₂	E_{avg} (MPa)	E_{avg} (GPa)
39918.56	0.250	0.250	39918.56	0.250	0.250	37398.29	0.234	0.234	39078.47	39.08
Case 2: One micron deep dry crack with 15-micron mesh - 23395 elements - Process time 745 sec										
39918.24	0.250	0.250	39918.28	0.250	0.250	37295.67	0.234	0.234	39044.06	39.04
Case 3: One micron deep dry crack with 10-micron mesh - 66919 elements - Process time 2933 sec										
39917.79	0.250	0.250	39917.80	0.250	0.250	37128.21	0.233	0.233	38987.93	38.99

Table E14: Elastic properties for eight vertical crack RVE obtained using EasyPBC plugin in Abaqus for saturated crack condition.

SATURATEDCRACKS

Eight RVEs with 8 Cracks (Vertical parallel to x-axis) - One crack in each single RVE										
Case 1: One micron deep dry crack with 20-micron mesh - elements 10649 - Process time 263 sec										
E₁₁ (MPa)	v₁₂	v₁₃	E₂₂ (MPa)	v₂₁	v₂₃	E₃₃ (MPa)	v₃₁	v₃₂	E_{avg} (MPa)	E_{avg} (GPa)
39919.18	0.250	0.251	39919.19	0.250	0.251	39162.96	0.246	0.246	39667.10	39.67
Case 2: One micron deep dry crack with 15-micron mesh - 23977 elements - Process time 10005 sec										
39918.83	0.250	0.251	39918.86	0.250	0.251	39139.68	0.246	0.246	39659.12	39.66
Case 3: One micron deep dry crack with 10-micron mesh - elements 67599 - Process time 8543 sec										
39918.37	0.250	0.251	39918.34	0.250	0.251	39097.36	0.246	0.246	39644.69	39.64

Table E15: Shear modulus results for eight vertical cracks RVE obtained using EasyPBC plugin in Abaqus for dry crack condition.

DRY CRACKS				
RVE with Single Crack (Vertical crack parallel to x-axis)				
G₁₂	G₁₃	G₂₃	E_{avg}	E_{avg}
	(MPa)		(MPa)	(GPa)
20-micron mesh				
15967.5	15456.87	15457.97	15627.447	15.627
15-micron mesh				
15967.4	15429.29	15430.88	15609.189	15.609
10-micron mesh				
15967.24	15392.5	15392.8	15584.180	15.584

Table E16: Shear modulus results for eight vertical cracks RVE obtained using EasyPBC plugin in Abaqus for saturated crack condition.

SATURATED CRACKS				
RVE with Single Crack (Vertical crack parallel to x-axis)				
G₁₂	G₁₃	G₂₃	E_{avg}	E_{avg}
	(MPa)		(MPa)	(GPa)
20-micron mesh				
15967.598	15486.836	15487.053	15647.162	15.647
15-micron mesh				
15967.49	15460.481	15461.646	15629.872	15.630
10-micron mesh				
15967.339	15428.91	15428.294	15608.181	15.608

Details of 200*200*200 micron³ RVE with eight horizontal cracks

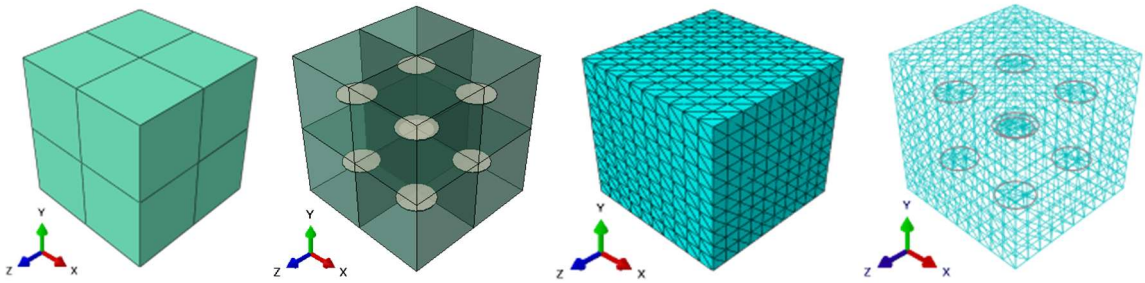


Table E17: Elastic properties for eight horizontal crack RVE obtained using EasyPBC plugin in Abaqus for dry crack condition.

DRY CRACKS										
Eight RVEs with 8 Cracks (Horizontal parallel to z-axis) - One crack in each RVE										
Case 1: One micron deep dry crack with 20-micron mesh - 10646 elements - Process time 254 sec										
E₁₁	v₁₂	v₁₃	E₂₂	v₂₁	v₂₃	E₃₃	v₃₁	v₃₂	E_{avg}	E_{avg}
(MPa)	-	-	(MPa)	-	-	(MPa)	-	-	(MPa)	(GPa)
39918.56	0.250	0.250	37392.06	0.234	0.234	39918.55	0.250	0.250	39076.39	39.08
Case 2: One micron deep dry crack with 15-micron mesh - 23331 elements - Process time 699 sec										
39918.24	0.250	0.250	37292.04	0.234	0.234	39918.28	0.250	0.250	39042.86	39.04
Case 3: One micron deep dry crack with 10-micron mesh - 66725 elements - Process time 2878 sec										
39917.81	0.250	0.250	37131.74	0.233	0.233	39917.81	0.250	0.250	38989.12	38.99

Table E18: Elastic properties for eight horizontal crack RVE obtained using EasyPBC plugin in Abaqus for saturated crack condition.

SATURATED CRACKS										
Eight RVEs with 8 Cracks (Horizontal parallel to z-axis) - One crack in each RVE										
Case 1: One micron deep wet crack with 20-micron mesh - 10703 elements - Process time 262 sec										
E₁₁	v₁₂	v₁₃	E₂₂	v₂₁	v₂₃	E₃₃	v₃₁	v₃₂	E_{avg}	E_{avg}
(MPa)	-	-	(MPa)	-	-	(MPa)	-	-	(MPa)	(GPa)
39919.18	0.251	0.250	39161.14	0.246	0.246	39919.19	0.250	0.251	39666.50	39.67
Case 2: One micron deep wet crack with 15-micron mesh - 23756 elements - Process time 692 sec										
39918.83	0.251	0.250	39139.63	0.246	0.246	39918.87	0.250	0.251	39659.11	39.66
Case 3: One micron deep wet crack with 10-micron mesh - 67531 elements - Process time 2906 sec										
39918.35	0.251	0.250	39096.44	0.246	0.246	39918.36	0.250	0.251	39644.39	39.64

Table E19: Shear modulus results for eight horizontal cracks RVE obtained using EasyPBC plugin in Abaqus for dry crack condition.

DRY CRACKS				
RVE with Single Crack (Horizontal crack parallel to z-axis)				
G₁₂	G₁₃	G₂₃	E_{avg}	E_{avg}
(MPa)			(MPa)	(GPa)
20-micron mesh				
15454.785	15967.496	15454.887	15625.723	15.626
15-micron mesh				
15428.931	15967.394	15430.545	15608.957	15.609
10-micron mesh				
15393.342	15967.241	15393.33	15584.638	15.585

Table E20: Shear modulus results for eight horizontal cracks RVE obtained using EasyPBC plugin in Abaqus for saturated crack condition.

SATURATED CRACKS				
RVE with Single Crack (Horizontal crack parallel to z-axis)				
G₁₂	G₁₃	G₂₃	E_{avg}	E_{avg}
(MPa)			(MPa)	(GPa)
20-micron mesh				
5487.105	15967.602	15487.515	12314.074	12.314
15-micron mesh				
15460.668	15967.492	15461.848	15630.003	15.630
10-micron mesh				
15428.132	15967.336	15428.23	15607.899	15.608

Details of 200*200*200 micron³ RVE with eight inclined 45-degree cracks

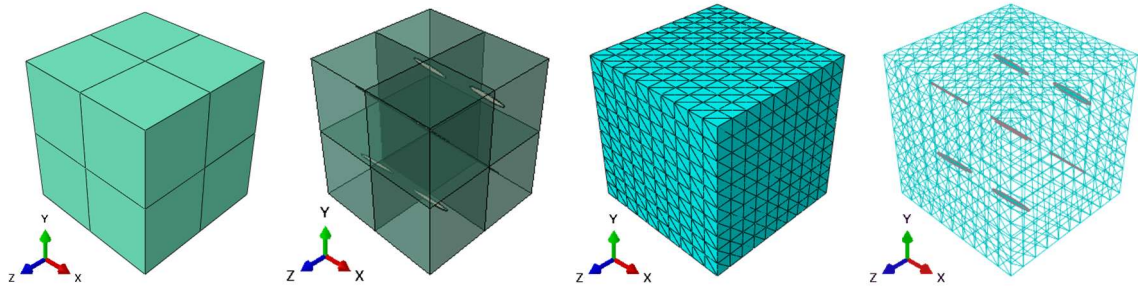


Table E21: Elastic properties for eight inclined 45-degree cracks RVE obtained using EasyPBC plugin in Abaqus for dry crack condition.

DRY CRACKS										
Eight RVEs with 8 Cracks (Inclined 45-degree cracks) - One crack in each single RVE										
Case 1: One micron deep dry crack with 20-micron mesh size - 10153 elements - Process time 246 sec										
E₁₁	v₁₂	v₁₃	E₂₂	v₂₁	v₂₃	E₃₃	v₃₁	v₃₂	E_{avg}	E_{avg}
(MPa)	-	-	(MPa)	-	-	(MPa)	-	-	(MPa)	(GPa)
39918.56	0.250	0.250	38520.44	0.241	0.244	38515.94	0.241	0.244	38984.98	38.99
Case 2: One micron deep dry crack with 15-micron mesh size - 23044 elements - Process time 689 sec										
39918.26	0.250	0.250	38447.30	0.241	0.244	38449.53	0.241	0.244	38938.37	38.93
Case 3: One micron deep dry crack with 10-micron mesh size - 64175 elements - Process time 3582 sec										
39917.83	0.250	0.250	38360.97	0.240	0.244	38357.76	0.240	0.244	38878.86	38.88

Table E21: Elastic properties for eight inclined 45-degree cracks RVE obtained using EasyPBC plugin in Abaqus for saturated crack condition.

SATURATED CRACKS										
Eight RVEs with 8 Cracks (Inclined 45-degree cracks) - One crack in each single RVE										
Case 1: One micron deep wet crack with 20-micron mesh size - 10433 elements - Process time 282 sec										
E₁₁	v₁₂	v₁₃	E₂₂	v₂₁	v₂₃	E₃₃	v₃₁	v₃₂	E_{avg}	E_{avg}
(MPa)	-	-	(MPa)	-	-	(MPa)	-	-	(MPa)	(GPa)
39919.18	0.250	0.250	39017.44	0.245	0.258	39020.06	0.245	0.258	39318.89	39.31
Case 2: One micron deep wet crack with 15-micron mesh size - 23503 elements- Process time 822 sec										
39918.86	0.250	0.250	38973.08	0.244	0.259	38974.22	0.244	0.259	39288.72	39.29
Case 3: One micron deep dry crack with 10-micron mesh size - 65323 elements - Process time 3349 sec										
39918.39	0.250	0.250	38915.33	0.244	0.259	38916.04	0.244	0.259	39249.92	39.25

Table E22: Shear modulus results for eight inclined 45-degree cracks RVE obtained using EasyPBC plugin in Abaqus for dry crack condition.

DRY CRACKS				
RVE with Single Crack (Inclined 45-degree cracks)				
G₁₂	G₁₃	G₂₃	E_{avg}	E_{avg}
(MPa)			(MPa)	(GPa)
20-micron mesh				
15713.606	15713.63	15534.762	15653.999	15.654
15-micron mesh				
15699.423	15966.481	15512.253	15726.052	15.726
10-micron mesh				
15681.904	15681.774	15485.725	15616.468	15.616

Table E23: Shear modulus results for eight inclined 45-degree cracks RVE obtained using EasyPBC plugin in Abaqus for saturated crack condition.

SATURATED CRACKS				
RVE with Single Crack (Inclined 45-degree cracks)				
G₁₂	G₁₃	G₂₃	E_{avg}	E_{avg}
(MPa)			(MPa)	(GPa)
20-micron mesh				
15728.063	15728.114	15835.924	15764.034	15.764
15-micron mesh				
15715.069	15715.094	15831.387	15753.850	15.754
10-micron mesh				
15698.838	15698.935	15823.813	15740.529	15.741

Details of 200*200*200 micron³ RVE with increasing order of cracks (one to eight cracks in a single RVE) – Dry crack

condition

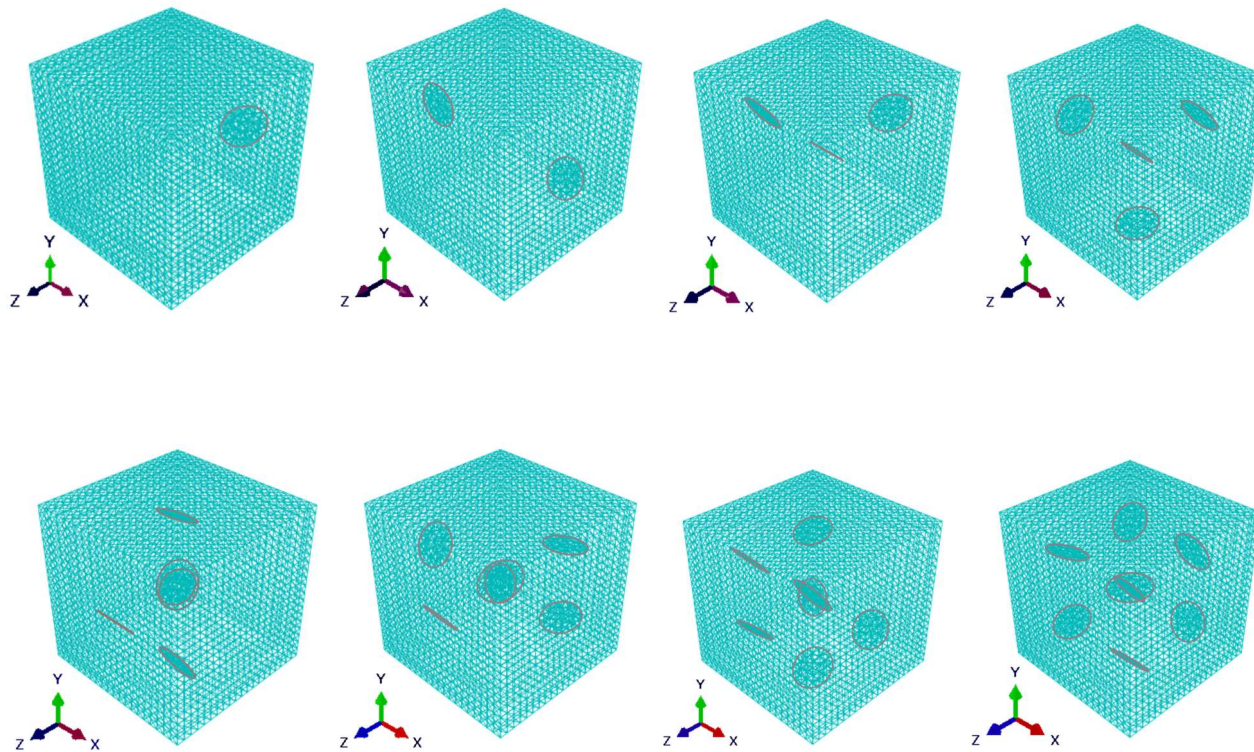


Table E24: Elastic properties for different RVEs using EasyPBC plugin.

DRY CRACKS										
E₁₁	v₁₂	v₁₃	E₂₂	v₂₁	v₂₃	E₃₃	v₃₁	v₃₂	E_{avg}	E_{avg}
(MPa)	-	-	(MPa)	-	-	(MPa)	-	-	(MPa)	(GPa)
200-micron RVE with single Random position dry crack, Rotation = -60 degrees and x, y, z = 150,150,50										
Case A: Single Random dry crack with 10-micron mesh size - 45966 elements - Process time 3552 sec										
39989.716	0.250	0.250	39701.532	0.248	0.249	39884.256	0.249	0.250	39858.501	39.859
200-micron RVE with two Random position dry cracks, Rotation = -30, 75 degrees and x, y, z = 150,150,50										
Case B: Two Random dry cracks with 10-micron mesh size - 51303 elements - Process time 1510 sec										
39979.400	0.250	0.250	39873.024	0.249	0.250	39324.840	0.246	0.246	39725.755	39.726
200-micron RVE with three Random position dry cracks, Rotation = 45, -60,30 degrees										
Case C: Three Random dry cracks with 10-micron mesh size - 55587 elements - Process time 2180 sec										
39969.112	0.250	0.250	39375.640	0.246	0.248	39374.736	0.246	0.248	39573.163	39.573
200-micron RVE with four Random position dry cracks, Rotation = 30, -50, 40, -80 degrees										
Case D: Four Random dry cracks with 10-micron mesh size - 58166 elements - Process time 2574 sec										
39958.816	0.250	0.250	39093.532	0.245	0.246	39252.816	0.246	0.247	39435.055	39.435
200-micron RVE with five Random position dry cracks, Rotation = 25, -35, -55, 65, 40 degrees										
Case E: Five Random dry cracks with 10-micron mesh size - 58279 elements - Process time 2396 sec										
39948.560	0.250	0.250	39020.124	0.244	0.246	38944.180	0.244	0.246	39304.288	39.304
200-micron RVE with six Random position dry cracks Rotation = -25, 35, -75, 80, -30, -60 degrees										
Case F: Six Random dry cracks with 10-micron mesh size - 61255 elements - Process time 1991 sec										
39938.296	0.250	0.250	38668.348	0.242	0.244	38952.592	0.244	0.246	39186.412	39.186
200-micron RVE with seven Random position dry cracks, Rotation = -20, 50, -70, 40, -40, -55, 30 degrees										
Case G: Seven Random dry cracks with 10-micron mesh size - 63989 elements - Process time 2459 sec										
39928.056	0.250	0.250	38626.996	0.242	0.244	38511.464	0.241	0.243	39022.172	39.022
200-micron RVE with eight Random position dry cracks, Rotation = 30, -65, -40, 70, -25, 45, -85, 15 degrees										
Case H: Eight Random dry cracks with 10-micron mesh size - 66877 elements - Process time 2816 sec										
39917.800	0.250	0.250	38388.440	0.241	0.243	38442.368	0.241	0.243	38916.203	38.916

Table E25: Shear modulus results for RVEs with increasing order of cracks obtained using EasyPBC plugin in Abaqus for dry crack condition.

DRY CRACKS				
200x200x200 RVE with multiple cracks				
G₁₂	G₁₃	G₂₃	E_{avg}	E_{avg}
(MPa)			(MPa)	(GPa)
One Crack				
15942.419	15978.082	15933.626	15951.376	15.951
Two Cracks				
15973.837	15866.544	15857.854	15899.412	15.899
Three Cracks				
15880.415	15879.846	15804.957	15855.073	15.855
Four Cracks				
15824.952	15857.239	15733.429	15805.207	15.805
Five Cracks				
15805.547	15793.497	15667.442	15755.495	15.755
Six Cracks				
15729.614	15787.931	15584.674	15700.740	15.701
Seven Cracks				
15731.75	15707.937	15536.376	15658.688	15.659
Eight Cracks				
15674.368	15687.775	15447.748	15603.297	15.603

Details of 200*200*200 micron³ RVE with increasing order of cracks (one to eight cracks in a single RVE) – Saturated crack condition

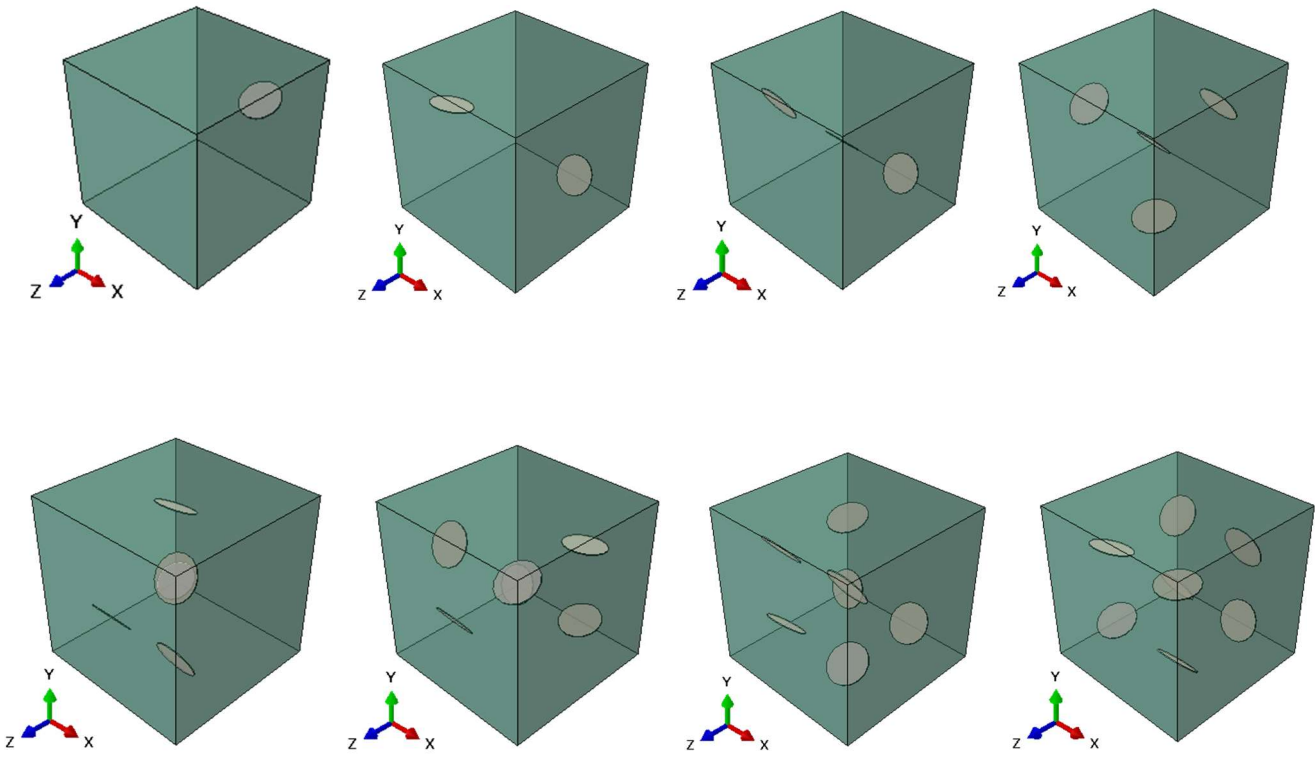


Table E26: Elastic properties for different RVEs using EasyPBC plugin.

SATURATED CRACKS										
E₁₁	v₁₂	v₁₃	E₂₂	v₂₁	v₂₃	E₃₃	v₃₁	v₃₂	E_{avg}	E_{avg}
(MPa)	-	-	(MPa)	-	-	(MPa)	-	-	(MPa)	(GPa)
200-micron RVE with single with Random position Wet crack, Rotation = -60 degrees and x,y,z = 150,150,50										
Case A: Single Random dry crack with 10-micron mesh size - 46525 elements - Process time 1963 sec										
39989.776	0.250	0.250	39853.632	0.249	0.251	39905.816	0.249	0.251	39916.408	39.916
200-micron RVE with two Random position wet cracks Rotation = -30, 75 degrees and x,y,z = 150,150,50										
Case B: Two Random dry cracks with 10-micron mesh size - 50753 elements - Process time 1574 sec										
39979.536	0.250	0.250	39778.872	0.249	0.251	39817.872	0.249	0.251	39858.760	39.859
200-micron RVE with three Random position wet cracks Rotation = 45,-60,30 degrees										
Case C: Three Random dry cracks with 10-micron mesh size - 54666 elements - Process time 2258 sec										
39969.360	0.250	0.250	39671.288	0.248	0.253	39566.600	0.248	0.253	39735.749	39.736
200-micron RVE with four Random position wet cracks Rotation = 30, -50, 40, -80 degrees										
Case D: Four Random wet cracks with 10-micron mesh size - 58788 elements - Process time 2851 sec										
39959.076	0.250	0.250	39511.160	0.247	0.253	39557.136	0.248	0.253	39675.791	39.676
200-micron RVE with five Random position wet cracks Rotation = 25, -35, -55, 65, 40 degrees										
Case E: Five Random wet cracks with 10-micron mesh size - 59956 elements - Process time 2442 sec										
39948.900	0.250	0.250	39405.336	0.247	0.254	39385.320	0.247	0.254	39579.852	39.580
200-micron RVE with six Random position wet cracks Rotation = -25, 35, -75, 80, -30, -60 degrees										
Case F: Six Random wet cracks with 10-micron mesh size - 62151 elements - Process time 2018 sec										
39938.716	0.250	0.250	39335.232	0.247	0.253	39420.032	0.247	0.254	39564.660	39.565
200-micron RVE with seven Random position wet cracks Rotation = -20, 50, -70, 40, -40, -55, 30 degrees										
Case G: Seven Random wet cracks with 10-micron mesh size - 65481 elements - Process time 2543 sec										
39928.544	0.250	0.250	39181.392	0.246	0.256	39148.280	0.245	0.256	39419.405	39.419
200-micron RVE with eight Random position wet cracks Rotation = 30, -65, -40, 70, -25, 45, -85, 15 degrees										
Case H: Eight Random wet cracks with 10-micron mesh size - 67839 elements - Process time 2941 sec										
39918.352	0.250	0.250	39154.028	0.246	0.255	39173.816	0.246	0.255	39415.399	39.415

Table E27: Shear modulus results for RVEs with increasing order of cracks obtained using EasyPBC plugin in Abaqus for saturated crack condition.

SATURATED CRACKS				
200x200x200 RVE with multiple cracks				
G₁₂	G₁₃	G₂₃	E_{avg}	E_{avg}
(MPa)			(MPa)	(GPa)
One Crack				
15945.457	15979.104	15965.609	15963.390	15.963
Two Cracks				
15911.894	15936.811	15906.512	15918.406	15.918
Three Cracks				
15920.278	15852.975	15909.77	15894.341	15.894
Four Cracks				
15834.409	15864.792	15853.518	15850.906	15.851
Five Cracks				
15816.116	15804.922	15835.888	15818.975	15.819
Six Cracks				
15744.978	15799.9	15735.659	15760.179	15.760
Seven Cracks				
15746.864	15724.514	15765.748	15745.709	15.746
Eight Cracks				
15692.149	15705.244	15654.673	15684.022	15.684

Details of 200*200*200 micron³ RVE with 24 randomly oriented cracks

Dry crack condition

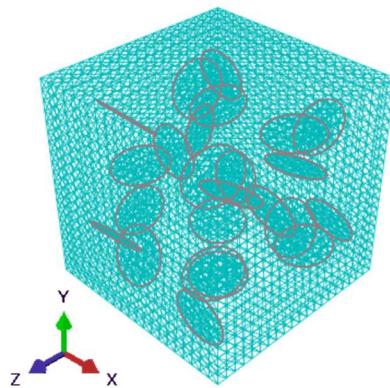
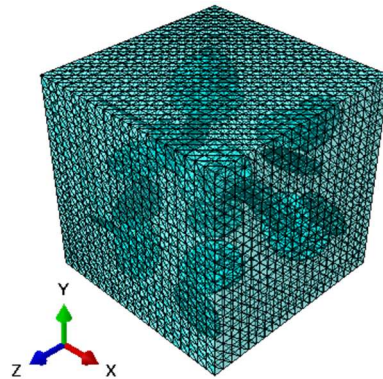
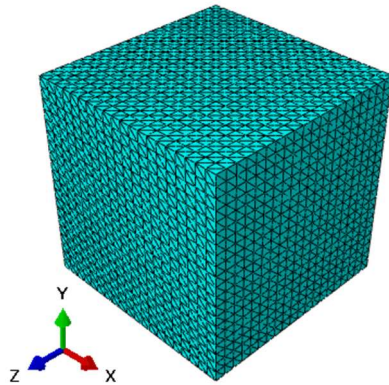
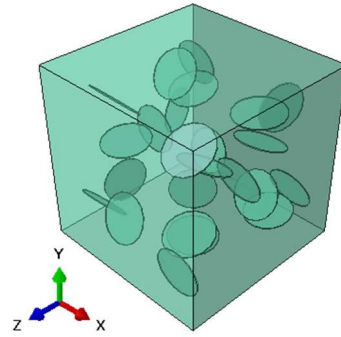
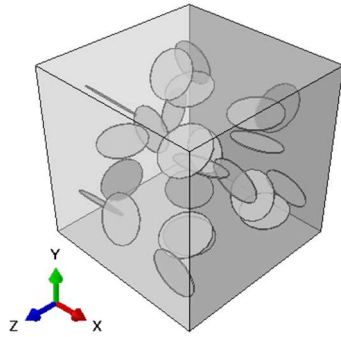


Table E28: Elastic properties for RVEs with 24 randomly oriented cracks

DRY CRACKS										
200*200*200 micron³ RVE with 24 dry Random Cracks (CDP = 0.1)										
Case 1b: RVE with 24 Random dry cracks (radius=32.182) with 10-micron mesh - 77875 elements - Process time 4414 sec										
E₁₁	v₁₂	v₁₃	E₂₂	v₂₁	v₂₃	E₃₃	v₃₁	v₃₂	E_{avg}	E_{avg}
(MPa)	-	-	(MPa)	-	-	(MPa)	-	-	(MPa)	(GPa)
36610.916	0.231	0.234	32947.698	0.207	0.212	31971.270	0.204	0.205	33843.295	33.843
200*200*200 micron³ RVE with 24 dry Random Cracks (CDP = 0.2)										
Case 2b: RVE with 24 Random dry cracks (radius=40.548) with 10-micron mesh - 83834 elements - Process time 5868 sec										
36365.644	0.251	0.251	24749.992	0.158	0.177	26405.774	0.168	0.188	29173.803	29.174
200*200*200 micron³ RVE with 24 dry Random Cracks (CDP = 0.3)										
Case 3b: RVE with 24 Random dry cracks (radius=46.415) with 10-micron mesh - 87006 elements - Process time 1953 sec										
39169.624	0.251	0.251	21055.326	0.135	0.163	21184.580	0.137	0.164	27136.510	27.137
200*200*200 micron³ RVE with 24 dry Random Cracks (CDP = 0.4)										
Case 4b: RVE with 24 Random dry cracks (r=51.087) with 10-micron mesh - 87635 elements - Process time 1666 sec										
39004.044	0.251	0.251	18330.774	0.118	0.153	19267.544	0.124	0.161	25534.121	25.534
200*200*200 micron³ RVE with 24 dry Random Cracks (CDP = 0.5)										
Case 5b: RVE with 24 Random dry cracks (r=55.032) with 10-micron mesh - 92957 elements - Process time 3486 sec										
38841.080	0.250	0.250	17773.500	0.114	0.194	17853.658	0.115	0.195	24822.746	24.823
200*200*200 micron³ RVE with 24 dry Random Cracks (CDP = 0.6)										
Case 6b: RVE with 24 Random dry cracks (r=58.480) with 10-micron mesh - 92850 elements - Process time 1572 sec										
38696.180	0.249	0.250	15932.287	0.103	0.154	16494.084	0.107	0.159	23707.517	23.708
200*200*200 micron³ RVE with 24 dry Random Cracks (CDP = 0.7)										
Case 7b: RVE with 24 Random dry cracks (radius=66.943) with 10-micron mesh - 93497 elements - Process time 1583 sec										
38552.896	0.250	0.249	15189.011	0.098	0.140	16208.278	0.105	0.149	23316.728	23.317
200*200*200 micron³ RVE with 24 dry Random Cracks (CDP = 0.8)										
Case 8b: RVE with 24 Random dry cracks (r=64.366) with 10-micron mesh - 96096 elements - Process time 1595 sec										
38423.184	0.249	0.249	15566.982	0.101	0.158	16936.712	0.110	0.172	23642.293	23.642
200*200*200 micron³ RVE with 24 dry Random Cracks (CDP = 0.9)										
Case 9b: RVE with 24 Random dry cracks (r=66.943) with 10-micron mesh - 96550 elements - Process time 1490 sec										
38292.496	0.248	0.248	15212.125	0.099	0.147	15498.770	0.100	0.150	23001.130	23.001
200*200*200 micron³ RVE with 24 dry Random Cracks (CDP = 1.0)										
Case 10b: RVE with 24 Random dry cracks (r=69.336) with 10-micron mesh - 94653 elements - Process time 1540 sec										
38234.960	0.248	0.248	15640.032	0.101	0.156	15602.144	0.101	0.156	23159.045	23.159

Table E29: Shear modulus results for RVEs with 24 randomly oriented cracks obtained using EasyPBC plugin in Abaqus for dry crack condition.

DRY CRACKS				
RVE with 24 Randomly oriented cracks				
G₁₂	G₁₃	G₂₃	E_{avg}	E_{avg}
(MPa)			(MPa)	(GPa)
CDP = 0.1				
13965.6	13822.155	13212.539	13666.765	13.667
CDP = 0.2				
12126.796	12609.148	9718.307	11484.750	11.485
CDP = 0.3				
11001.143	11040.896	8035.6255	10025.888	10.026
CDP = 0.4				
9622.426	10162.423	6686.592	8823.814	8.824
CDP = 0.5				
8927.583	9126.587	6341.834	8132.001	8.132
CDP = 0.6				
7616.8825	8110.6775	4975.228	6900.929	6.901
CDP = 0.7				
7334.5815	7596.4845	4907.8085	6612.958	6.613
CDP = 0.8				
6924.5595	7442.1775	5107.3635	6491.367	6.491
CDP = 0.9				
6510.997	6711.223	4724.131	5982.117	5.982
CDP = 1.0				
6576.3785	6309.0405	4601.187	5828.869	5.829

Details of 200*200*200 micron³ RVE with 24 randomly oriented cracks
Saturated crack condition

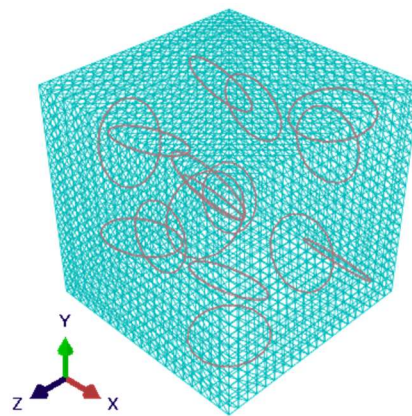
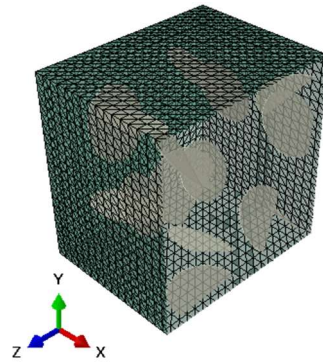
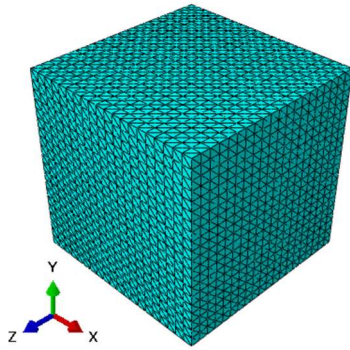
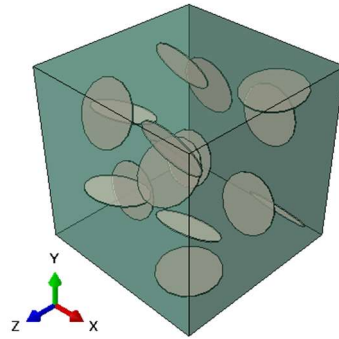
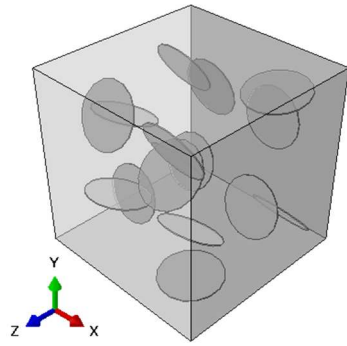


Table E30: Elastic properties for RVEs with 24 randomly oriented cracks

SATURATED CRACKS										
200*200*200 micron³ RVE with 24 dry Random Cracks (CDP = 0.1)										
Case 1b: RVE with 24 Random wet cracks (r=32.182) with 10-micron mesh - 84932 elements - Process time 4861 sec										
E₁₁	v₁₂	v₁₃	E₂₂	v₂₁	v₂₃	E₃₃	v₃₁	v₃₂	E_{avg}	E_{avg}
(MPa)	-	-	(MPa)	-	-	(MPa)	-	-	(MPa)	(GPa)
38247.044	0.243	0.261	38383.208	0.232	0.273	35562.152	0.243	0.267	37397.468	37.397
200*200*200 micron³ RVE with 24 dry Random Cracks (CDP = 0.2)										
Case 2b: RVE with 24 Random wet cracks (r=40.580) with 10-micron mesh - 94967 elements - Process time 10637 sec										
39369.584	0.253	0.253	32350.928	0.208	0.308	32622.106	0.210	0.310	34780.873	34.781
200*200*200 micron³ RVE with 24 dry Random Cracks (CDP = 0.3)										
Case 3b: RVE with 24 Random wet cracks (r=46.415) with 10-micron mesh - 101964 elements - Process time 3670 sec										
39174.580	0.254	0.254	29823.992	0.193	0.339	29811.912	0.193	0.339	32936.828	32.937
200*200*200 micron³ RVE with 24 dry Random Cracks (CDP = 0.4)										
Case 4b: RVE with 24 Random wet cracks (r=46.415) with 10-micron mesh - 88917 elements - Process time 3821 sec										
39010.820	0.255	0.254	27883.412	0.182	0.353	28437.544	0.185	0.360	31777.259	31.777
200*200*200 micron³ RVE with 24 dry Random Cracks (CDP = 0.5)										
Case 5b: RVE with 24 Random wet cracks (r=55.032) with 10-micron mesh - 116731 elements - Process time 5777 sec										
38850.856	0.255	0.255	26864.820	0.176	0.370	26952.790	0.177	0.372	30889.489	30.889
200*200*200 micron³ RVE with 24 dry Random Cracks (CDP = 0.6)										
Case 6b: RVE with 24 Random wet cracks (r=58.480) with 10-micron mesh - 119355 elements - Process time 4046 sec										
38707.336	0.256	0.256	25360.720	0.168	0.385	25634.488	0.169	0.389	29900.848	29.901
200*200*200 micron³ RVE with 24 dry Random Cracks (CDP = 0.7)										
Case 7b: RVE with 24 Random wet cracks (r=61.563) with 10-micron mesh - 124494 elements - Process time 4832 sec										
38567.200	0.257	0.256	24283.386	0.162	0.397	24571.244	0.163	0.402	29140.610	29.141
200*200*200 micron³ RVE with 24 dry Random Cracks (CDP = 0.8)										
Case 8b: RVE with 24 Random wet cracks (r=64.366) with 10-micron mesh - 146290 elements - Process time 5890 sec										
33728.204	0.263	0.252	26299.490	0.205	0.322	27262.236	0.203	0.333	29096.643	29.097
200*200*200 micron³ RVE with 24 dry Random Cracks (CDP = 0.9)										
Case 9b: RVE with 24 Random wet cracks (r=66.94329) with 10-micron mesh - elements - Process time sec										
-	-	-	-	-	-	-	-	-	0	0
200*200*200 micron³ RVE with 24 dry Random Cracks (CDP = 1.0)										
Case 10b: RVE with 24 Random wet cracks (r=69.336) with 10-micron mesh - elements - Process time sec										
-	-	-	-	-	-	-	-	-	0	0

Table E31: Shear modulus results for RVEs with 24 randomly oriented cracks obtained using EasyPBC plugin in Abaqus for saturated crack condition.

SATURATED CRACKS				
RVE with 24 Randomly oriented cracks				
G₁₂	G₁₃	G₂₃	E_{avg}	E_{avg}
(MPa)			(MPa)	(GPa)
CDP = 0.1				
14108.943	14281.945	14186.891	14192.593	14.193
CDP = 0.2				
12498.036	12911.142	12707.129	12705.436	12.705
CDP = 0.3				
11509.814	11510.517	11244.893	11421.741	11.422
CDP = 0.4				
10295.639	10837.180	10399.371	10510.730	10.511
CDP = 0.5				
9790.75	9915.570	9879.745	9862.022	9.862
CDP = 0.6				
8554.805	9104.190	8700.929	8786.641	8.787
CDP = 0.7				
8376.62	8772.93	8393.273	8514.274	8.514
CDP = 0.8				
7908.513	8290.490	7483.046	7894.016	7.894
CDP = 0.9				
-	-	-	0.000	0.000
CDP = 1.0				
-	-	-	0.000	0.000

Note: The elastic properties for CDP 0.9 and 1.0 were not obtained due to meshing issue which occurred due to multiple cracks overlapping with each other.

Young's Modulus Results for Three Different RVE Cases and Different Crack Numbers in 200*200*200 micron³ RVE with CDPs from 0.1 to 1.0

Table E32: Young's modulus values of 8 cracks in RVE with three different cases

CDP	E, GPa						Avg	Avg	STD	STD
	Dry-Case 1	Dry-Case 2	Dry-Case 3	Skd-Case 1	Skd-Case 2	Skd-Case 3	Dry	Skd	Dry	Skd
0	40	40	40	40	40	40	40	40	0	0
0.1	33.841	33.662	33.491	36.901	36.580	36.932	33.665	36.804	0.175	0.195
0.2	28.791	28.466	28.218	35.405	34.032	34.678	28.492	34.705	0.287	0.687
0.3	27.207	27.206	25.278	34.537	33.025	33.211	26.563	33.591	1.113	0.824
0.4	26.488	26.129	23.153	33.913	32.667	31.476	25.257	32.685	1.831	1.218
0.5	26.138	22.065	22.683	31.989	30.747	31.476	23.629	31.404	2.195	0.624
0.6	25.428	22.012	20.752	31.557	31.093	28.689	22.731	30.446	2.419	1.539
0.7	25.063	23.887	19.900	31.338	30.131	29.879	22.950	30.449	2.706	0.780
0.8	24.199	18.584	18.275	30.779	28.691	28.570	20.352	29.347	3.335	1.242
0.9	23.028	18.070	16.166	30.409	28.624	28.119	19.088	29.051	3.543	1.203
1	22.911	16.859	15.770	28.200	27.593	28.119	18.513	27.971	3.847	0.329

Table E33: Normalized Young's modulus plot values for 8 cracks in RVE with three different cases

CDP	E, GPa						Avg	Avg	STD	STD
	Dry-Case 1	Dry-Case 2	Dry-Case 3	Skd-Case 1	Skd-Case 2	Skd-Case 3	Dry	Skd	Dry	Skd
0	1	1	1	1	1	1	1	1	0	0
0.1	0.846	0.842	0.837	0.923	0.914	0.923	0.842	0.920	0.004	0.005
0.2	0.720	0.712	0.705	0.885	0.851	0.867	0.712	0.868	0.007	0.017
0.3	0.680	0.680	0.632	0.863	0.826	0.830	0.664	0.840	0.028	0.021
0.4	0.662	0.653	0.579	0.848	0.817	0.787	0.631	0.817	0.046	0.030
0.5	0.653	0.552	0.567	0.800	0.769	0.787	0.591	0.785	0.055	0.016
0.6	0.636	0.550	0.519	0.789	0.777	0.717	0.568	0.761	0.060	0.038
0.7	0.627	0.597	0.498	0.783	0.753	0.747	0.574	0.761	0.068	0.020
0.8	0.605	0.465	0.457	0.769	0.717	0.714	0.509	0.734	0.083	0.031
0.9	0.576	0.452	0.404	0.760	0.716	0.703	0.477	0.726	0.089	0.030
1	0.573	0.421	0.394	0.705	0.690	0.703	0.463	0.699	0.096	0.008

Table E34: Details of crack radius used to model RVE with 8, 16 and 24 cracks

S.No	CDP	Volume (V)	No. of Cracks (n)	Crack radius (a)	No. of Cracks (n)	Crack radius (a)	No. of Cracks (n)	Crack radius (a)
-	-	$(200)^3 \text{ micron}^3$	-	micron	-	micron	-	micron
1	0.1	8000000	8	46.416	16	36.840	24	32.183
2	0.2	8000000	8	58.480	16	46.416	24	40.548
3	0.3	8000000	8	66.943	16	53.133	24	46.416
4	0.4	8000000	8	73.681	16	58.480	24	51.087
5	0.5	8000000	8	79.370	16	62.996	24	55.032
6	0.6	8000000	8	84.343	16	66.943	24	58.480
7	0.7	8000000	8	88.790	16	70.473	24	61.564
8	0.8	8000000	8	92.832	16	73.681	24	64.366
9	0.9	8000000	8	96.549	16	76.631	24	66.943
10	1	8000000	8	100	16	79.370	24	69.336